Estimation and detection of transmission line characteristics in the copper access network

Lindqvist, Fredrik

2011

Citation for published version (APA):
Lindqvist, F. (2011). *Estimation and detection of transmission line characteristics in the copper access network*. [Doctoral Thesis (compilation), Department of Electrical and Information Technology].

Total number of authors:
1

Estimation and Detection of Transmission Line Characteristics in the Copper Access Network

Fredrik Lindqvist

Doctoral Dissertation

October 2011

LUND UNIVERSITY

Department of Electrical and Information Technology

Abstract

The copper access-network operators face the challenge of developing and maintaining cost-effective digital subscriber line (DSL) services that are competitive to other broadband access technologies. The way forward is dictated by the demand of ever increasing data rates on the twisted-pair copper lines. To meet this demand, a relocation of the DSL transceivers in cabinets closer to the customers are often necessary combined with a joint expansion of the accompanying optical-fiber backhaul network. The equipment of the next generation copper network are therefore becoming more scattered and geographically distributed, which increases the requirements of automated line qualification with fault detection and localization.

This scenario is addressed in the first five papers of this dissertation where the focus is on estimation and detection of transmission line characteristics in the copper access network. The developed methods apply model-based optimization with an emphasis on using low-order modeling and a priori information of the given problem. More specifically, in Paper I a low-order and causal cable model is derived based on the Hilbert transform. This model is successfully applied in three contributions of this dissertation. In Paper II, a class of low-complexity unbiased estimators for the frequency-dependent characteristic impedance is presented that uses one-port measurements only. The so obtained characteristic impedance paves the way for enhanced time domain reflectometry (*a.k.a.* TDR) on twisted-pair lines. In Paper III, the problem of estimating a nonhomogeneous and dispersive transmission line is investigated and a space-frequency optimization approach is developed for the DSL application. The accompanying analysis shows which parameters are of interest to estimate and further suggests the introduction of the concept *capacitive length* that overcomes the necessity of a priori knowledge of the physical line length. In Paper IV, two methods are developed for detection and localization of load coils present in so-called loaded lines. In Paper V, line topology identification is addressed with varying degree of a priori information. In doing so, a model-based optimization approach is employed that utilizes multi-objective evolutionary computation based on one/two-port measurements.

A complement to transceiver relocation that potentially enhance the total data throughput in the copper access network is dynamic spectrum management (DSM). This promising multi-user transmission technique aims at maximizing the transmission rates, and/or minimizing the power consumption, by mitigating or cancelling the dominating crosstalk interference between twisted-pair lines in the same cable binder. Hence the spectral utiliza-

tion is improved by optimizing the transmit signals in order to minimize the crosstalk interference. However, such techniques rely on accurate information of the (usually) unknown crosstalk channels.

This issue is the main focus of Paper VI and VII of this dissertation in which Paper VI deals with estimation of the crosstalk channels between twisted-pair lines. More specifically, an unbiased estimator for the square-magnitude of the crosstalk channels is derived from which a practical procedure is developed that can be implemented with standardized DSL modems already installed in the copper access network. In Paper VII the impact such a non-ideal estimator has on the performance of DSM is analyzed and simulated. Finally, in Paper VIII a novel echo cancellation algorithm for DMT-based DSL modems is presented.

Contents

Preface

This doctoral dissertation consists of an introductory chapter and the following eight papers describing an approach to cable modeling and various signal processing methods applied to the transmission lines in the copper access network:

I. F. Lindqvist, P.O. Börjesson, P. Ödling, S. Höst, K. Ericson, and T. Magesacher, "Low-order and causal twisted-pair cable modeling by means of the Hilbert transform," *AIP Conference Proceeding*, vol. 1106, pp. 301-310, 2008.

II. F. Lindqvist, P.O. Börjesson, P. Ödling, K. Ericson, and T. Magesacher, "Estimation of twisted-pair characteristic impedance from one-port measurements," To be submitted.

III. F. Lindqvist and P.O. Börjesson, "Estimation of nonhomogeneous and dispersive twisted-pair transmission lines," Submitted to *IEEE Transactions on Instrumentation and Measurement*, Oct. 2011.

IV. F. Lindqvist and A. Fertner, "Detection and localization of load coils from one-port measurements," *IEEE Transactions on Instrumentation and Measurement*, vol. 59, no. 7, pp. 1972-1982, Jul. 2010.

V. C. Sales, R. Rodrigues, F. Lindqvist, J. Costa, A. Klautau, K. Ericson, J. Rius i Riu, and P.O. Börjesson, "Line topology identification using multi-objective evolutionary computation," *IEEE Transactions on Instrumentation and Measurement*, vol. 59, no. 3, pp. 715-729, Mar. 2010.

VI. F. Lindqvist, N. Lindqvist, B. Dortschy, P. Ödling, P.O. Börjesson, K. Ericson, and P. Evaldo, "Crosstalk channel estimation via standardized two-port measurements," *EURASIP Journal on Advances in Signal Processing*, vol. 2008, Article ID 916865, 14 pages, 2008.

VII. N. Lindqvist, F. Lindqvist, M. Monteiro, B. Dortschy, E. Pelaes, and A. Klautau, "Impact of crosstalk channel estimation on the DSM performance for DSL networks," *EURASIP Journal on Advances in Signal Processing*, vol. 2010, Article ID 935076, 11 pages, 2010.

VIII. F. Lindqvist, A. Fertner, and P. Frenger, "Frequency domain echo canceller," *patent application*, PCT/SE01/01242, filed 1 Jun. 2000, WO 01/93448 A2, pub. date 6 Dec. 2001.

In Paper I–IV and VI, the author of this dissertation performed the analysis, developed the simulation programs, evaluated the methods, and prepared the manuscripts. For Paper V and VII the author was one of the promoters of the used approach, with a major contribution to the analysis and the manuscripts. The technology in Paper VIII was invented in a joint effort where the author of this dissertation also created the simulation programs and evaluated the method(s).

The following patent applications contain some of the presented results or are connected to the topic of the dissertation, but are not included:

- F. Lindqvist and A. Fertner, "Method and localization unit for detecting and locating load coils in a transmission line," *patent application*, filed 5 Jun. 2009, US 2010/0156553 A1, pub. date 24 Jun. 2010.

- F. Lindqvist, B. Dortschy, A. Klautau, N. Lindqvist, and E. Pelaes, "A method and system for management of transmission resources in digital communication systems," *patent application*, WO 2010/060446 A1, pub. date 3 Jun. 2010.

- F. Lindqvist, "Estimation of transmission line insertion loss," *patent application*, PCT/SE2007/000446, filed 8 May 2007, WO 2008/008015 A2, pub. date 17 Jan. 2008.

- F. Lindqvist, A. Fertner, and P.O. Börjesson, "A method and a system for cable or subscriber loop investigation performing loop topology identification," *patent application*, PCT/SE2006/000134, filed 31 Jan. 2006, WO 2007/089173 A1, pub. date 9 Aug. 2007.

- A. Fertner, F. Lindqvist, and P.O. Börjesson, "Load coil detection and localization," *patent application*, PCT/IB2006/003724, filed 20 Dec. 2006, WO 2007/072191 A1, pub. date 28 Jun. 2007.

- F. Lindqvist, J. Rius i Riu, J. Costa, and C. Sales, "Method and arrangement for loop qualification in a digital subscriber line (DSL) system," *patent application*, PCT/SE2006/050417, filed 20 Oct. 2006, WO 2008/048156 A1, pub. date 24 Apr. 2008.

- F. Lindqvist and B. Dortschy, "Method for determining automatically a FEXT/NEXT transfer function," *patent application*, PCT/SE2006/001017, filed 5 Sep. 2006, WO 2008/030145 A1, pub. date 13 Mar. 2008.

- S. Allevad, P. Ödling, A. Fertner, H. Back, F. Lindqvist, P.O. Börjesson, and J. Rius i Riu, "Method, device and program product for estimating

properties of a telecommunication transmission line," *patent application*, PCT/SE2005/001619, filed 27 Oct. 2005, WO 2007/050001 A1, pub. date 3 May 2007.

- F. Lindqvist and P.O. Börjesson, "Characteristics determination of a digital subscriber line," *patent application*, PCT/IB2004/003955, filed 1 Dec. 2004, WO 2006/059175 A1, pub. date 8 Jun. 2006.

- A.F. Jensen, F. Lindqvist, and A. Wiå, "Method and arrangement for estimation of line properties," *patent application*, PCT/SE04/00718, filed 11 May 2004, US 2007/0014393 A1, pub. date 18 Jan. 2007.

- J. Rosenberg, F. Lindqvist, A. Wiå, A. Fertner, A.F. Jensen, P.O. Börjesson and Per Ödling, "Method and arrangement for signal loop test," *patent application*, PCT/SE04/00296, filed 4 Mar. 2004, US 2005/00274563 A1, pub. date 3 Feb. 2005.

The following list of publications partly contains some of the presented results or address methods relevant to this dissertation, but are not included:

- F. Lindqvist and A. Fertner, "Frequency Domain Echo Canceller for DMT-based Systems," Accepted in Oct. 2011 for publication in *IEEE Signal Processing Letters*.

- S. Höst, F. Lindqvist, A. Fertner, K. Ericson, M. Berg, I. Pappa, and P.O. Börjesson, "Low complexity computation of the BT0 Hilbert twisted pair cable model," *15th International OFDM-Workshop (InOWo'10)*, pp. 195-199, Hamburg, Germany, Sep. 2010.

- E. Medeiros, N. Lindqvist, M. Monteiro, H. Abrahim, F. Lindqvist, B. Dortschy, and A. Klautau, "DSM performance on practical DSL systems based on estimated crosstalk channel information," *17th European Signal Processing Conference 2009*, Glasgow, Scotland, United Kingdom, Aug. 2009.

- N. Lindqvist, F. Lindqvist, B. Dortschy, E. Pelaes, and A. Klautau, "Impact of crosstalk estimation on the dynamic spectrum management performance," *in Proc. of IEEE Global Communication Conference (GLOBECOM 2008)*, New Orleans, USA, Nov. 2008.

- J. Rius i Riu, J. Rosenberg, F. Lindqvist, M. Tilocca, C. Bianco, B. van den Heuvel, P. Ödling, T. Magesacher, M. Berg, J. Sorio, A. Uvliden,

and P.O. Börjesson, "The IST-MUSE approach to DSL loop qualification and monitoring," *Proc. 3rd Broadband Europe Conference*, Geneva, Switzerland, Dec. 2006.

- J. Costa, J. Reis, I. Negrao, A. Castro, L. de Souza, K. Ericson, F. Lindqvist, and J. Rius i Riu, "Characterization of subscriber local loop by measures and analysis of frequency and impulse responses," *SPIE Optics East Broadband Access Communication Technologies*, Boston, MA, USA, Oct. 2006.

- J. Reis, A. Castro, J. Costa, J. Rius i Riu, and F. Lindqvist, "Characterization of subscriber local loop by measures of frequency response and TDR," *XVIII IMEKO World Congress Metrology for a Sustainable Development*, Rio de Janeiro, Brazil, Sep. 2006.

- J. Dias, I. Negrao, A. Castro, J. Costa, G. Cavalcante, J. Rius i Riu, K. Ericson, and F. Lindqvist, "Improving the performance evaluation of ADSL systems by using a modem diagnosis methodology," *XXII Simpósio Brasileiro de Microondas e Optoeletronica Congresso Brasileiro de Eletromagnetismo*, Campinas, SP, Brazil, Aug. 2006.

- L. Alcantara, R. Rodrigues, C. Sales, A. Castro, J. Costa, F. Lindqvist, and J. Rius i Riu, "Single-ended transfer function estimation of telephone links for deployment of xDSL services," *XXII Simpósio Brasileiro de Telecomunicaçōes - SBrT 2005*, Campinas, SP, Brazil, Sep. 2005.

Acknowledgments

I first met Professor Per Ödling and Professor Per Ola Börjesson about ten years ago, as part of a research cooperation between Ericsson's DSL research laboratory and Lund University (LTH). A significant part of this doctoral dissertation can be traced back to this fruitful and successful cooperation. As a new DSL research engineer, I soon realized how instructive and stimulating it is to work with two such skilled and experienced researchers. Throughout the years, this reflection and insight has struck me many times. It is therefore not an overstatement to declare that it has been a true privilege to be part of this cooperation, and that I owe much to my two mentors and supervisors; Per and Per Ola.

Despite the interesting and successful research work, the next logical step for me at the mid of year 2006 was to join the part of Ericsson that works with wireless communication. Having made this change of working area, it looked as if my DSL journey had ended. However, in the beginning of year 2007, the LTH Professors Per and Per Ola offered me the opportunity to finalize and publish some of the ideas we had been working with. I of course accepted the offer, and the accompanying challenge, which marks the continuation of the halted DSL journey. I am therefore also deeply grateful to Per and Per Ola for having me in their research group and for providing a creative and scientific environment.

I wish to thank my supervisor Dr. Thomas Magesacher, also at the Broadband Communication group at Lund University (LTH), for providing valuable guidance and excellent technical feedback at various stages of this dissertation, in addition to plenty of proof reading. Although seldom located in the same city, or on the same continent for that matter, I wish to mention our interesting and fruitful discussions, often via emails or video/chat conference systems.

I wish to express my deep gratitude to my colleague Dr. Antoni Fertner, at Ericsson Research, for the outstanding cooperation throughout the years, and for the inspiration and all technical conversations, in addition to the humble encouragement to make this dissertation.

A big thanks goes to all the colleagues at the Broadband Communication group at Lund University (LTH), with a special thanks to Dr. Stefan Höst for all the good advice and for the LaTex tips, and to M.Sc. Pernilla Schuber for providing an inspiring atmosphere in addition to always being helpful. As I have been stationed in Stockholm, some 600 km from Lund, I would also like to thank the administrative personnel at LTH for all the help.

I wish to thank all the staff at the DSL laboratory, Ericsson Research, for the interesting discussions and for the friendship. I am in particular grateful to my colleagues Dr. Klas Ericson and to M.Sc. Boris Dortschy.

I am thankful to my current manager, and previous managers, at Ericsson AB for giving me the opportunity of working part-time for LTH to pursue my Licentiate and PhD studies. I am also thankful to my colleagues at LTE System, Ericsson AB, Stockholm, for their smooth cooperation despite my part-time off leave. Furthermore, I would like to take the opportunity to thank the DSL research group at the Federal University of Para (UFPA), Brazil, with a special thanks to M.Sc. Eduardo Medeiros and M.Sc. Marcio Monteiro for among other things teaching me those delicate expressions in Portuguese.

Finally and most of all, I wish to thank my family including my wife Dr. Neiva Lindqvist. I am immensely grateful to Neiva for our excellent cooperation, and more importantly, for her love and encouragement.

Fredrik Lindqvist
Stockholm
October 2011

Introduction

Broadband communication via the telephone lines is an important part of the everyday life for millions of people around the world and will (likely) continue to be so for many years to come. This cost-effective broadband access is made possible in numerous societies by installing broadband transceivers in the already existing copper access-network. With established means for efficient and reliable communication between companies and their customers, and between citizens and authorities, incentives for economical growth and wealth are provided. In fact, this telecommunication infrastructure is today taken for granted in many countries. Moreover, wireline broadband access continues to expand and evolve as more and new services are requested at the same time as competitive access technologies are being developed and launched.

This doctoral dissertation focuses on digital signal processing methods for estimating and detecting various kinds of line characteristics in the copper access network. The so obtained information about the lines can be divided into two categories. The first category is related to line qualification including fault detection and localization, required for access network operation and maintenance. The second category of line characteristics allows the network operator and the service provider to enhance the performance of the transmission lines by applying new emerging signal processing techniques.

This first introductory chapter provides an overview of the copper access network with an emphasis on the addressed transmission line characteristics. This is accompanied by a brief description of transmission line modeling and the transceiver measurements that facilitate a practical deployment of the proposed methods. Finally, the scientific contributions of the dissertation are summarized.

1   Historical Retrospect

The foundation of the copper access network started at the end of the 19th century with the deployment of telephone lines. These lines consist of twisted-pair copper cables that connect the subscribers to the (nearest) Central Office. At each line-end, a transceiver unit, *e.g.* a telephone, provides means for transmission and reception of the information flow conveyed via electro-magnetic propagation to and from the intended user(s).

The craft of manufacturing the equipment for the copper access network has been developed to a fine art for more than hundred years. The original use of the network was of course for analogue telephony, often referred to as plain old telephone service (POTS), which is routed through the vast public switched telephone network (PSTN). The telecom operators continue to offer and maintain the POTS which millions of customers use every day, even though the number of subscribers is decreasing in favor of mobile telephony and voice over IP subscriptions. During the 1970's, 1980's and the 1990's the fax-machine and several types of voice-band modems found their way to the mass-market and provided analog access to local networks and eventually access to the mighty Internet. All of these analog access-technologies utilize the same frequency band, namely the POTS-band, from about $300\,\mathrm{Hz}$ up to $4000\,\mathrm{Hz}$. However, it soon became evident that there was a great interest and need for significantly higher bit rates than the $33-56\,\mathrm{Kbps}$ possible with the most sophisticated voice-band modems utilizing the POTS frequency band.

The industry and the academic world mobilized during the 1980's and the 1990's to take the next step; developing the *digital subscriber line* (DSL) technology, where the analog access over the telephone line is replaced by a digital pipeline. However, the digital era started prior to this with the telecom operators digitizing the so-called trunk lines between the Central Offices and other network installations [1]. Hence the backbone of the PSTN was first digitized and prepared for handling the coming digital services.

The main DSL deployment targeted services that are available and wide-spread today such as e-mail, teleconferencing, web browsing, video-on-demand, voice over IP and IP-TV. The DSL development led to the standardization of several DSL technologies; ISDN, HDSL, SHDSL, ADSL, ADSL2/2+ and VDSL/VDSL2 [1,2]. Today, ADSL and ADSL2/2+ are the most widely used of these technologies, where the asymmetric frequency band-plan reflects the original application foreseen in the beginning of the 1990's, namely, video-on-demand. In this application, a larger frequency band is required by the downstream transmission, compared to the upstream transmission, in order to convey the high-speed data transmission from the network to the customer. However, during the last years it has become important for ADSL operators

to offer improved upstream transmission as up-loading of *e.g.* music and video-clips is becoming more popular.

The copper access network was predicted, by some, to be doomed during the 1990's due to the expected mass-deployment of the superior optical fiber. Although there is no doubt that the optical fiber is better suited for high-capacity data transmission than the twisted-pair copper cable, the mass replacements of the telephone lines has so far not occurred. The main reason for this is the high cost involved, especially when the fiber deployment comes closer to the customers were the lines typically branch off substantially, and therefore, require a lot of digging to lay the fibers.

2   The Copper Access Network

Fig. 1 shows a simplified picture of the copper access network and its main components. A Central Office typically serves between 20.000 and 100.000 lines via large *feeder* cables that contain up to 10.000 twisted-pair lines per feeder [1].
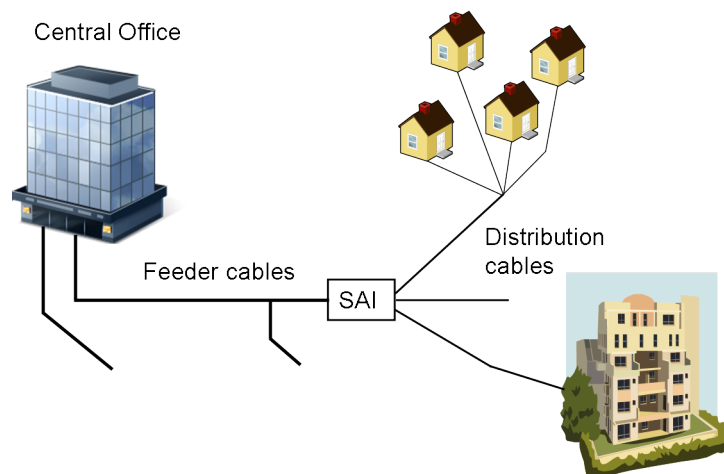
Figure 1: Illustration of the copper access network.

The feeders are terminated at the serving area interface (SAI) [1], also called the primary cross-connection point, from which the lines branch off in *distribution* cables containing 25 to a few hundred twisted-pair lines per cable. In practice, there are often many intermediate steps as well. Typically 1500 to 3000 customers are served per SAI. The length of the distribution

cables is often less than $1 \, \mathrm{km}$, while the feeder cables can be up to $4-6 \, \mathrm{km}$ or more [1]. However, the lengths depend strongly on the country, the region, and the type of area *e.g.* urban or rural. The average line length in Europe is around $1.5 \, \mathrm{km}$ while in North America this figure is closer to $2 \, \mathrm{km}$ [1]. The lines inside the feeders and the distribution cables are normally grouped, or bundled, into binder groups of *e.g.* 25, 50 or 100 lines as illustrated in Fig. 2. Within a binder group, the twisted-pairs are twisted together with other pairs in the binder to reduce the overall electromagnetic interference (crosstalk), to and from the other lines. Due to the separation of the binders, the unwanted residual crosstalk between lines is in general more prominent for lines belonging to the same binder group.

The interfering crosstalk from neighboring systems is one of the main impairments for high-speed DSL modems that share the same spectrum. Both near-end crosstalk (NEXT) and far-end crosstalk (FEXT) occur, as illustrated in Fig. 3, where NEXT refers to the crosstalk caused by the transmitter(s) on the *same side* of the line while FEXT denotes the crosstalk from the transmitter(s) on the *opposite side* of the line. The characteristics of the NEXT and FEXT channels depend on several factors such as cable type, length, twisting, grouping, etc., and are often unknown to the network operator. The estimation of these NEXT and FEXT channels are the subject of Paper VI [3] and Paper VII [4].

The ambition of many copper access-network operators is to replace the feeders by optical fiber cables that enable DSL transceiver deployment at the SAI or at street cabinets closer to the customers. However, the electrical power supply to the SAI and to the cabinets are still a necessity that the Central Office with its battery back-up typically needs to provide.
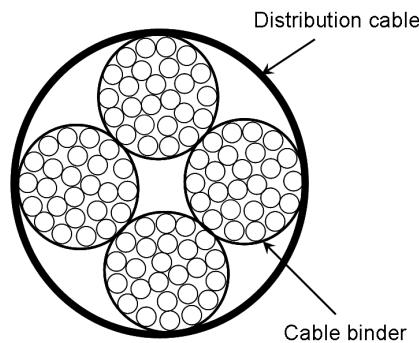
Figure 2: Cross-section of a distribution cable with 100 twisted-pairs in four binder groups. Each pair is represented by a small circle.
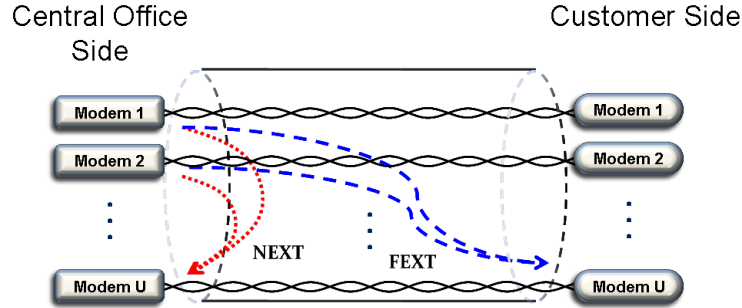
Figure 3: Illustration of far-end crosstalk (FEXT) and near-end crosstalk (NEXT) in a cable binder with U number of lines.

2.1   The Twisted-Pair Copper Line

The twisted-pair cable used for the telephone lines consists typically of two unshielded and isolated cylindrical metal wires twisted together in order to reduce the susceptibility to external electromagnetic interference, created by for instance lightning, radio transmitters, or household devices [1, 2]. The wires are normally made of copper even though aluminum and steel have been used in the past to lower the weight and the cost, but with the added drawback of increased line attenuation. Today the most common isolation material is plastic, in particular polyethylene (PE) and polyvinylchloride (PVC). The latter has the advantage of being more fire resistant than PE, and is therefore preferred for indoor wiring, but has the disadvantage of reduced electrical isolation. Cables with paper isolation are still found in the copper access network as it was commonly used in the past.

The distance between the Central Office and the customer limits the capacity of the telephone line since the attenuation of the copper cable increases with cable length. To overcome this drawback, cables with thicker wire-diameter, *i.e.*, lower attenuation per unit length, are often deployed further away from the Central Office in order to keep the overall line attenuation low. For instance, a PE cable with $0.4\,$mm wire-diameter has a typical attenuation of $12-14\,$dB/km at $300\,$kHz and a $0.9\,$mm cable has a corresponding attenuation of around $7\,$dB/km. Hence the telephone lines are built as multi-section cables, also called multi-section lines, as depicted in Fig. 4. The topology identification of such transmission lines and the estimation of characterizing line parameters (electrical/physical) are addressed by several prior work *e.g.* [5–10], and by Paper II [11], Paper III [12], and Paper V [13].

In some countries, for instance in USA and Canada, the lines can have so called *bridged-taps* which are an unterminated cable, typically $100 - 500\,\mathrm{m}$ long, spliced to the line to create an additional connection point. Such a bridged-tap line is shown in Fig. 4. These unused stubs create dips in the channel frequency response and hence decrease the transmission capacity of the line in addition to making the design of *e.g.* effective equalization and echo cancellation more challenging [1]. The detection and localization of bridged-taps are addressed in *e.g.* [5, 14] and Paper V [13].

To supply POTS further out from the Central Offices, lines longer than about $5.5\,\mathrm{km}$ were in the past equipped with *load coils* [1] in some countries. Such a loaded line is illustrated in Fig. 4. The load coil is an inductive device that reduces the line attenuation in the POTS band. However, on these loaded lines the attenuation is increased for frequencies above the POTS band to such an extent that (ordinary) DSL services can not operate. The detection and localization of load coils is considered in *e.g.* [15–20] and Paper IV [21].
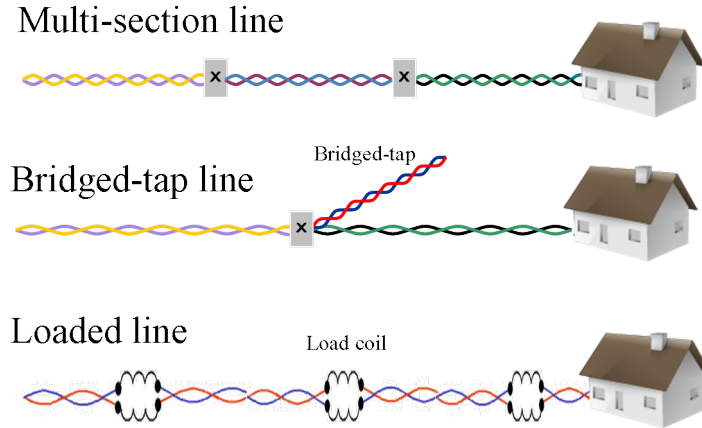
Figure 4: Different line configurations found in the copper access network.

2.2   Line Faults and Line Qualification

The twisted-pair lines of the copper access network are often several decades old and far from faultless. A common problem is oxidation of wire splices. This occurs when two wires are not tightly bonded. The oxidation affects the transmission signal in an often non-linear and possibly time-varying way that

can cause a significant increase in line resistance with a substantial signal loss as a consequence. A POTS line typically has fewer of these problems since the high ringing voltage tends to break-down the oxidation layer. Hence lines only used for DSL communication, with voice over IP instead of POTS, may degrade faster unless a DC current is provided once in a while to prevent oxidation [1]. Other common problems in the copper access network are: incorrectly spliced wires, loose wire contacts, split wire-pairs, DC/AC current leakage to ground or to other pairs, moisture or water penetration into the cables, and line unbalancing resulting in increased electromagnetic ingress and egress [1, 2].

A major challenge for the copper access-network operator is to maintain a high quality of the transmission link [22]. Whenever a customer reports a failing service, or complains about intermittent errors, the countermeasure in terms of fault detection and localization must be rapid and cost-effective. This can be achieved by utilizing the already installed transceivers for monitoring and diagnosing the transmission link by means of analyzing the received disturbances combined with transmission of one or more test-signals over the line for the purpose of detecting any anomaly of the line characteristics, *cf.* [6–8, 22–32], Paper II [11] and Paper III [12]. The same or similar techniques can also be used for line pre-qualification where the DSL operator estimates the capacity of the lines in order to check what kind of broadband services can be offered to the customer of a particular line [5, 9, 10, 33–36], Paper III–Paper V [12, 13, 21].

3   Next Generation Network

The new trends for the copper networks are dictated by the increasing capacity demands on the DSL broadband access, leading to the deployment of transceiver equipment at the SAI or in cabinets (a.k.a. remote terminals) even further away from the Central Office. The purpose of these relocations is to place the DSL transceivers (modems) closer to the customers, often within $0.5\,\text{km}$, and hence increase the capacity of the copper link. In addition, the lines between the Central Office and the cabinets have to be complemented, or replaced, by *e.g.* one or few optical fibers to carry the aggregated high-speed data. The cabinets are therefore sometimes referred to as optical network units (ONU). The recently standardized VDSL2 technology [37] is intended for cabinet deployment and is expected to become the next major improvement to the DSL network as it will increase the bit rate per subscriber line from $8 - 24\,\text{Mbps}$ with ADSL2/2+ [38, 39] to $25 - 100\,\text{Mbps}$ with VDSL2.

Although a relocation of the DSL transceivers closer to the customers

results in lower signal attenuation and larger available bandwidths other obstacles such as the "near-far" problem are introduced. That is, any adjacent transmitter located near the considered receiver could disturb the desired signal from the more distant transmitter, since the signal power decreases with distance and frequency in the direct transmission channel, while the FEXT power typically increases up to some peak frequency before dropping again. This scenario often occurs if some of the lines are served from the Central Office while other lines of the same binder originate from a remote terminal, as shown in Fig. 5. The crosstalk generated from the remote terminal can in such cases severely impair the highly attenuated downstream signal from the Central Office unless crosstalk mitigation/cancellation is utilized. Such techniques are known as *dynamic spectrum management* (DSM) and are briefly described in Section 4.

The fourth generation broadband concept (4GBB) is introduced in [40] which presents a possible next step in the evolution of the copper access network. The throughput predictions in [40], for various deployment scenarios and physical layer techniques, indicate that the data rates of the 4GBB copper network will reach hundreds of Mbps, and under certain conditions, exceed 1 Gbps.
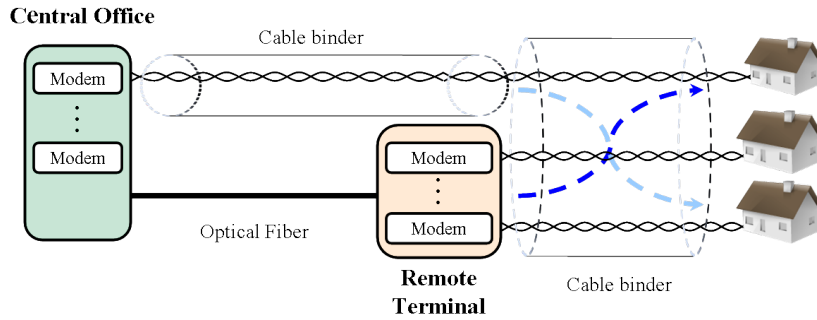
Figure 5: A network scenario with partly relocated DSL modems in a cabinet (remote terminal) closer to the customers. The undesirable FEXT channels are illustrated by the dashed arrows where the darker color indicates a higher FEXT level.

4   Dynamic Spectrum Management

Traditional DSL systems employ static spectrum management (SSM) which ensures that all lines present in the same cable binder are spectrally compatible. In doing so, SSM assumes a worst-case crosstalk scenario without taking into account the slowly time-varying channel conditions. In other words SSM relies on fixed spectral allocation and flat power back-off across all frequencies, as illustrated in the left figure of Fig. 6, which unfortunately wastes channel capacity.

Dynamic spectrum management (DSM) has been proposed in *e.g.* [2, 41–50] to more efficiently deal with the frequency-dependent nature of the crosstalk, whose magnitude is typically 10-20 dB higher than the background noise level. This promising technique aims at maximizing the total data throughput, and/or minimizing the power consumption, of all DSL lines by optimizing the transmit spectra in order to minimize the crosstalk interference. This is schematically illustrated in the right figure of Fig. 6 for a near-far scenario where User 2 is connected to a much closer located cabinet while User 1 is served from the CO.

Two such alternative approaches are *Vectoring* (a.k.a. vectored DSL) and *spectrum balancing* which nowadays are both referred to as DSM. With Vectoring the DSL network is often treated as a multiple-input multiple-output (MIMO) system where the transmitted signals are co-ordinated in order to reduce the undesirable crosstalk by means of precoding/decoding. To realize this in practice requires a system with high computational power in addition to both amplitude and phase information of the frequency-dependent crosstalk channels. This approach is not pursued further in this dissertation, but it should be noted that Vectoring has recently being standardized and
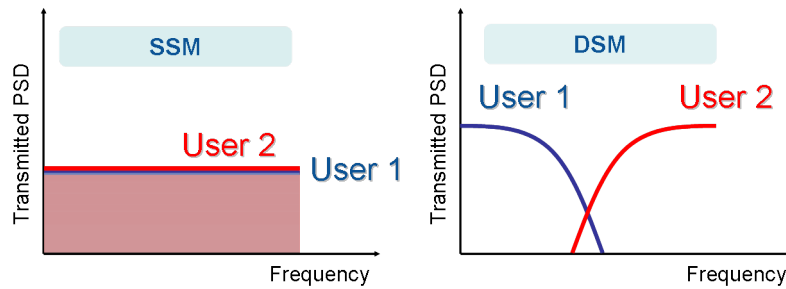
Figure 6: Illustration of spectral allocation with static/dynamic spectrum management (SSM/DSM).

demonstrated on real cables with impressive performance gains.

In contrast to Vectoring, spectrum balancing methods essentially treat the crosstalk interference as noise. In doing so, the optimized spectrum allocations attempt to *avoid* the crosstalk into other lines while at the same time maximize the total data throughput subjected to the system resource constraints. The required level of co-ordination depends on the used algorithm.

One of the first described spectrum balancing method is the famous Iterative Water-filling (IWF) algorithm [1], where each individual line autonomously maximizes its own data rate by "waterfilling" its transmit spectrum over the received interference plus noise. The IWF can achieve near optimum performance in certain weak crosstalk-scenarios but is suboptimum in the typical near-far scenario with mixed Central Office and remote terminal transceivers (*cf.* Fig. 5).

Two proposed *optimum* DSM algorithms are the Optimal Spectrum Balancing (OSB) algorithm [43] and the Iterative Spectrum Balancing (ISB) algorithm [42] where the former has an exponential complexity in the number of users while ISB has a corresponding quadratic complexity. In addition to the high complexity, both of these algorithms are centralized in the sense that they rely on a so-called network management center to optimize the power spectral density (PSD) of all the transceivers at the same time. To accomplish this requires knowledge of the crosstalk channels between the lines. However, such measurements are not supported by the existing DSL standards. In [44] a semi-centralized DSM algorithm denoted SCALE is proposed. This algorithm achieves better performance than IWF with comparable complexity, but is not autonomous and requires message exchange between the modems at the customer side via a central unit. Both SCALE and ISB are used in Paper VII [4].

An autonomous DSM algorithm is described in [46]. This so-called ASB algorithm can be applied in a distributed fashion across users with no requirements of real-time exchange of information. The ASB algorithm is also of relatively low complexity and is proved to be convergent under certain sufficient conditions on the channel gains [46].

Vital for a successful application of all of these spectrum balancing methods is the availability of information of the (usually) unknown crosstalk channels. The estimation of these channels and the resulting impact on the DSM performance are considered in *e.g.* [45, 48], Paper VI [3] and Paper VII [4]. It should be emphasized that this dissertation is not directly concerned with the DSM optimization problem, but with the issue of how to practically estimate the crosstalk channels.

5 The DSL Transceiver

Fig. 7 shows a simplified block diagram of a generic DSL transceiver with the transmitter (Tx) and the receiver (Rx) parts connected to the line via a three-port hybrid. The hybrid is an analogue circuit that enables simultaneous transmission and reception, *i.e.*, duplex transmission [1]. The hybrid is normally integrated on the same circuit board as the Tx and the Rx. In practice, the hybrid is never perfectly matched to the (unknown) line, which causes the transmitted signal to partly leak back to the receiver. This so called *echo signal* is often significantly stronger than the received far-end signal [1]. In case the transmission system employs frequency division duplex (FDD), where the downstream and upstream spectra do not overlap, the echo is normally not of major concern provided filtering is employed to reduce the out-of-band echo leakage. However, for systems using overlapping spectra, as optional for *e.g.* ADSL modems [38, 39], echo cancellation is needed to mitigate the destructive echo signal [1, 2, 51–53], Paper VIII [54].
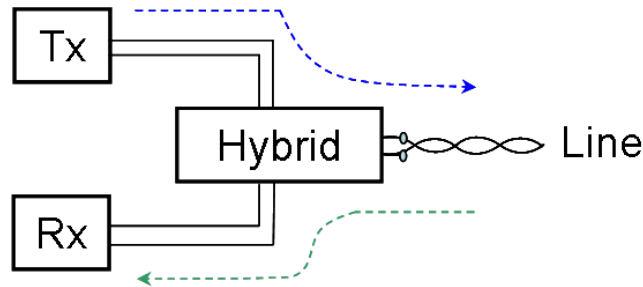
Figure 7: A DSL transceiver with its receiver (Rx), transmitter (Tx), and analogue hybrid circuit connected to the line.

5.1 Measuring Line Input Impedance

For the purpose of estimating the properties of the transmission lines in a cost-effective way, the DSL transceiver can be used to measure the line input impedance Z_{in} [24, 25] or the scattering parameter S_{11} [55, 56]. However, these quantities cannot be measured directly by the DSL transceiver. Instead, the echo transfer function from Tx to Rx, see Fig. 7, is usually measured by transmitting a known test-signal and at the same time measuring the received frequency-domain echo signal. The echo transfer function can then be obtained as $H_{echo}(\omega) = Y(\omega)/X(\omega)$, for the angular frequency $\omega = 2\pi f$ of the

considered bandwidth, where $X(\omega)$ and $Y(\omega)$ denote the Fourier transform of the transmitted and received signal, respectively [1,25,52,53], Paper VIII [54]. For a DSL modem utilizing discrete multitone (DMT) modulation [1], the implementation of the echo measurement can be simplified by employing a wide-band test signal with a period time equal to the DMT symbol time. Furthermore, it can be shown [25] that the echo transfer function of a DSL modem can be expressed as a function of the angular frequency by

$$H_{echo}(\omega) = \frac{H_\infty(\omega)Z_{in}(\omega) + Z_{h0}(\omega)}{Z_{in}(\omega) + Z_{hyb}(\omega)}. \tag{1}$$

Here $Z_{hyb}(\omega)$ is the impedance of the transceiver seen from the line, $H_\infty(\omega)$ is the echo transfer function when $Z_{in}(\omega) \to \infty$, and $Z_{h0}(\omega) = H_0(\omega)Z_{hyb}(\omega)$ with $H_0(\omega)$ being the echo transfer function when $Z_{in}(\omega) \to 0$. From (1) we note that the line input impedance $Z_{in}(\omega)$ can be obtained from the measured $H_{echo}(\omega)$ as

$$Z_{in}(\omega) = \frac{Z_{h0}(\omega) - Z_{hyb}(\omega)H_{echo}(\omega)}{H_{echo}(\omega) - H_\infty(\omega)}. \tag{2}$$

Equation (1) can also be written as

$$H_{echo}(\omega)Z_{in}(\omega) + H_{echo}(\omega)Z_{hyb}(\omega) - H_\infty(\omega)Z_{in}(\omega) - Z_{h0}(\omega) = 0, \tag{3}$$

which in matrix form yields

$$\begin{bmatrix} 1 & -H_{echo}(\omega) & Z_{in}(\omega) \end{bmatrix} \begin{bmatrix} Z_{h0}(\omega) \\ Z_{hyb}(\omega) \\ H_\infty(\omega) \end{bmatrix} = H_{echo}(\omega)Z_{in}(\omega). \tag{4}$$

The complex-valued transceiver parameters $Z_{hyb}(\omega)$, $Z_{h0}(\omega)$ and $H_\infty(\omega)$ can be determined by a set of calibration measurements where the transceiver is connected to known terminations, *e.g.* resistors of different values. More specifically, $H_{echo}^{(n)}(\omega)$ is measured at calibration time $n = 1, 2, ..., N$ with impedance $Z_{in}^{(n)}(\omega)$ terminating the transceiver. Hence with N number of calibration measurements (4) can be expressed as

$$\mathbf{A}(\omega)\bar{z}(\omega) = \bar{b}(\omega), \tag{5}$$

where matrix $\mathbf{A}(\omega)$ is of size $N \times 3$, the vector $\bar{z}(\omega)$ is of size 3×1, and $\bar{b}(\omega)$ is of size $N \times 1$, *i.e.*,

$$\begin{aligned} \mathbf{A}(\omega) &= \begin{bmatrix} \bar{1} & -\bar{H}_{echo}(\omega) & \bar{Z}_{in}(\omega) \end{bmatrix} \\ \bar{z}(\omega) &= [Z_{h0}(\omega)\, Z_{hyb}(\omega)\, H_\infty(\omega)]^T \\ \bar{b}(\omega) &= diag\left(\bar{H}_{echo}(\omega)\right) \bar{Z}_{in}(\omega) \end{aligned}$$

and

$$\bar{H}_{echo}(\omega) = \left[H_{echo}^{(1)}(\omega)\,H_{echo}^{(2)}(\omega)\,\cdots\,H_{echo}^{(N)}(\omega)\right]^{T}$$
$$\bar{Z}_{in}(\omega) = \left[Z_{in}^{(1)}(\omega)\,Z_{in}^{(2)}(\omega)\,\cdots\,Z_{in}^{(N)}(\omega)\right]^{T}.$$

Here $diag\left(\bar{H}_{echo}(\omega)\right)$ denotes the $N \times N$ diagonal matrix with vector $\bar{H}_{echo}(\omega)$ along its main diagonal. Thus, the transceiver parameters can be estimated as the least-squares (LS) solution to (5) based on at least three calibration measurements ($N \geq 3$), that is,

$$\bar{z}_{LS}(\omega) = \left(\mathbf{A}^{H}(\omega)\mathbf{A}(\omega)\right)^{-1}\mathbf{A}^{H}(\omega)\bar{b}(\omega), \tag{6}$$

where ^{H} denotes the conjugate transpose.

Equation (6) assumes that $\mathbf{A}(\omega)$ has full rank, *i.e.*, that $\mathbf{A}^{H}(\omega)\mathbf{A}(\omega)$ is invertible. If this assumption is not satisfied other methods such as the Moore-Penrose pseudo inverse can be used to calculate $\bar{z}_{LS}(\omega)$. It is important to note that (6) is typically performed only one time per *transceiver type* and the parameters of $\bar{z}_{LS}(\omega)$ can be pre-stored in software [25]. Once the DSL transceiver has been deployed and installed in the access network, the input impedance $Z_{in}(\omega)$ of the line can be calculated from the measured $H_{echo}(\omega)$ by using (2) and the transceiver parameters of $\bar{z}_{LS}(\omega)$.

6 Transmission Line Analysis and Modeling

This section summarizes the fundamentals of cable modeling and introduces important concepts used for analysis and modeling of transmission lines. Since this is a vast field with a rich literature the description herein is by no means complete and focuses merely on the parts relevant to this dissertation. In the first subsection, dispersive and homogeneous cables are treated. In the second subsection, piecewise-homogeneous transmission lines are analyzed and the two-port network theory with $ABCD$ modeling [1,51] is presented.

6.1 Cable Modeling

Accurate and for the purpose adequate cable models are essential for estimating or predicting the transmission line characteristics in the copper access network [1,2,5,6,8–10,23,57,58], see also Paper I–V [11–13,21,59]. The fundamentals of cable modeling can be found in many books on electromagnetic theory.
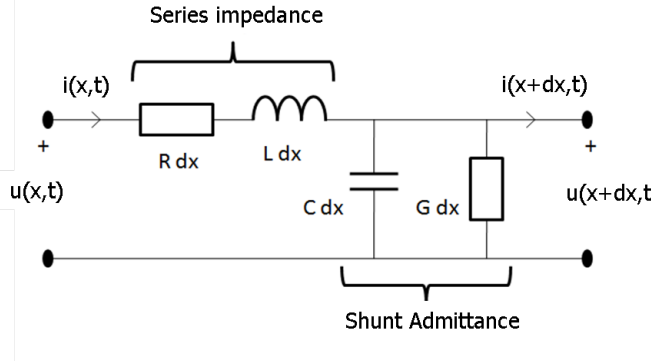
Figure 8: An infinitesimal homogeneous cable segment of length dx.

A twisted-pair cable can be modeled as a cascade of infinitesimal homogeneous segments. As illustrated in Fig. 8, each such segment of length dx can be treated as a circuit consisting of a series resistance R, a series inductance L, a shunt capacitance C, and a shunt conductance G, all expressed per unit length [1, 2]. By applying Kirchhoff's voltage and current laws for the circuit depicted in Fig. 8, we can derive a set of partial differential equations that relate the voltage $u(x, t)$ with $u(x + dx, t)$ and the current $i(x, t)$ with $i(x + dx, t)$. That is, at a position x and time t, we get the relations

$$\frac{u(x + \mathrm{d}x, t) - u(x, t)}{\mathrm{d}x} = -R\, i(x, t) - L\frac{\partial i(x, t)}{\partial t} \tag{7}$$

$$\frac{i(x + \mathrm{d}x, t) - i(x, t)}{\mathrm{d}x} = -G\, u(x + \mathrm{d}x, t) - C\frac{\partial u(x + \mathrm{d}x, t)}{\partial t}. \tag{8}$$

Further in the limit letting d$x \to 0$ in (7)–(8), the *general transmission line equations* are obtained, *i.e.*,

$$\frac{\partial u(x, t)}{\partial x} = -R\, i(x, t) - L\frac{\partial i(x, t)}{\partial t} \tag{9}$$

$$\frac{\partial i(x, t)}{\partial x} = -G\, u(x, t) - C\frac{\partial u(x, t)}{\partial t}. \tag{10}$$

By assuming a harmonic time dependence and employing phasors [1], (9)–(10) can be simplified to ordinary differential equations. Hence, by setting *e.g.*

$$u(x, t) = \Re\left\{U(x)e^{j\omega t}\right\} \tag{11}$$

$$i(x, t) = \Re\left\{I(x)e^{j\omega t}\right\}, \tag{12}$$

and substituting these two equations in (9)–(10) we obtain

$$\frac{\mathrm{d}U(x)}{\mathrm{d}x} = -\left(R + j\omega L\right)I(x) \tag{13}$$

$$\frac{\mathrm{d}I(x)}{\mathrm{d}x} = -\left(G + j\omega C\right)U(x). \tag{14}$$

In (11)–(12), ω and $\Re\{.\}$ denote the angular frequency and the real part of the argument, respectively. The coupled *time-harmonic transmission line equations* in (13)–(14) can be combined to a pair of second-order differential equations, *i.e.,*

$$\frac{\mathrm{d}^2 U(x)}{\mathrm{d}x^2} = \gamma^2 U(x) \tag{15}$$

$$\frac{\mathrm{d}^2 I(x)}{\mathrm{d}x^2} = \gamma^2 I(x), \tag{16}$$

where the *propagation constant* γ is defined by

$$\gamma = \sqrt{ZY} = \sqrt{\left(R + j\omega L\right)\left(G + j\omega C\right)}. \tag{17}$$

Here Z is the series impedance and Y is the shunt admittance, both shown in Fig. 8. Equations (13)–(16) are sometimes referred to as the Telegrapher's equations. It is easily verified that the two following expressions are solutions to (15) and (16), respectively,

$$U(x) = U_0^+ e^{-\gamma x} + U_0^- e^{\gamma x} \tag{18}$$

$$I(x) = I_0^+ e^{-\gamma x} + I_0^- e^{\gamma x}. \tag{19}$$

Equation (18) and (19) can be seen as a sum of two voltage and current waves that traverse the line in opposite directions. The voltage and current wave-amplitudes are represented by U_0^+, U_0^- and I_0^+, I_0^- respectively. It can be shown that the ratio of the positive-going voltage to the positive-going current is equal to the length-independent *characteristic impedance* Z_0, defined by (20). In addition, Z_0 is equal to the negative ratio of the negative-going voltage to the negative-going current, *i.e.,*

$$Z_0 = \frac{U_0^+}{I_0^+} = -\frac{U_0^-}{I_0^-} = \sqrt{\frac{Z}{Y}} = \sqrt{\frac{R + j\omega L}{G + j\omega C}}. \tag{20}$$

Twisted-pair cables for DSL transmission are highly *dispersive* since $R, L, C,$ and G are in general frequency dependent. For the commonly used polyethylene cables, C is approximately constant with frequency while G is often

considered negligible due to low dielectric losses. In any case, γ and Z_0 are frequency dependent for twisted-pair cables wherefore this is explicitly stated in the following.

Any dispersive and homogeneous cable is completely characterized by the frequency-dependent *secondary parameters* $Z_0(\omega)$ and $\gamma(\omega)$ for a given cable length. Hence these quantities constitute a cable model. A common way to estimate these cable model parameters in practice is to twice measure the input impedance on a short cable section, *e.g.* 10 m, first with an open far-end and then with a short-circuit far-end. In this way, the characteristic impedance $Z_0(\omega)$ and the propagation constant $\gamma(\omega)$ can be obtained as

$$Z_0(\omega) = \sqrt{Z_{oc}(\omega)Z_{sc}(\omega)} \qquad (21)$$

$$\gamma(\omega) = \frac{1}{l}\tanh^{-1}\sqrt{\frac{Z_{sc}(\omega)}{Z_{oc}(\omega)}}, \qquad (22)$$

where $Z_{sc}(\omega)$ and $Z_{oc}(\omega)$ denote the measured input impedance of the cable of length l with short-circuit and open-circuit far-end termination, respectively. The length of the measured cable section affects the estimation results and is a trade-off since a too short cable gives low parameter values that could be susceptible to noise while a too long cable typically violates the assumption of a homogeneous cable due to *e.g.* non-perfect twisting in the manufacturing [60].

Some cable models instead characterize the cable in terms of the *primary parameters* $R(\omega), L(\omega), C(\omega), G(\omega)$, and it is straightforward to derive the following relations from (17) and (20)

$$R(\omega) = \Re\left\{\gamma(\omega)Z_0(\omega)\right\} \qquad (23)$$

$$L(\omega) = \frac{1}{\omega}\Im\left\{\gamma(\omega)Z_0(\omega)\right\} \qquad (24)$$

$$C(\omega) = \frac{1}{\omega}\Im\left\{\frac{\gamma(\omega)}{Z_0(\omega)}\right\} \qquad (25)$$

$$G(\omega) = \Re\left\{\frac{\gamma(\omega)}{Z_0(\omega)}\right\}, \qquad (26)$$

where $\Re\{.\}$ and $\Im\{.\}$ denote the real and the imaginary part of the argument. It should be emphasized that different parameterized expressions (models) for the secondary and primary parameters have been used, leading to different types of cable models [23, 58, 61–63], Paper I [59].

6.2 Transmission Line Analysis

Fig. 9 depicts a homogeneous and dispersive transmission line connected to a voltage source U_S with source impedance Z_S at $x = 0$. At the far-end the line is connected to a termination impedance Z_T at $x = \ell$. All of these quantities are in general frequency dependent, but this is for notational simplicity omitted herein.

At a position $x \in [0, \ell]$ along the line the voltage is denoted $U(x)$ and the current $I(x)$. With the help of (18)–(20) the *wave impedance* $Z(x)$ and the *reflection response* $\Gamma(x)$ can be defined at position x as

$$Z(x) = \frac{U(x)}{I(x)} = Z_0 \frac{U_0^+ e^{-\gamma x} + U_0^- e^{\gamma x}}{U_0^+ e^{-\gamma x} - U_0^- e^{\gamma x}}, \quad \Gamma(x) = \frac{U_0^- e^{\gamma x}}{U_0^+ e^{-\gamma x}}. \qquad (27)$$

By combining these two definitions the following two relations are obtained

$$Z(x) = Z_0 \frac{1 + \Gamma(x)}{1 - \Gamma(x)}, \quad \Gamma(x) = \frac{Z(x) - Z_0}{Z(x) + Z_0}. \qquad (28)$$

In particular, at $x = 0$ the ratio between the left-side reflected wave to the incident wave is given by

$$\Gamma(0) = \frac{Z_{in} - Z_0}{Z_{in} + Z_0}, \qquad (29)$$
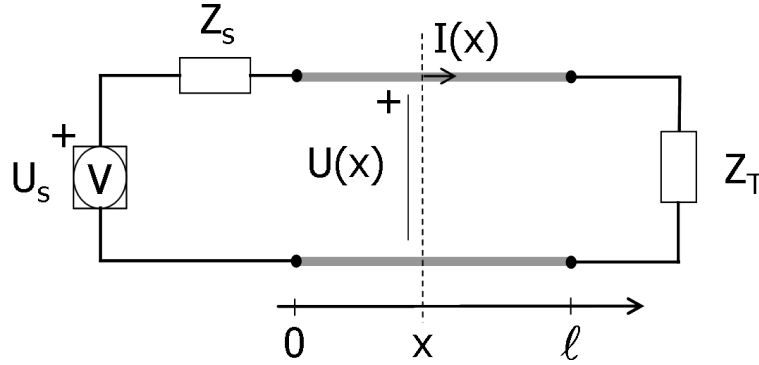
Figure 9: A homogeneous and dispersive transmission line of length ℓ connected to a voltage source $U_S(\omega)$ with source impedance $Z_S(\omega)$ at $x = 0$. A termination impedance $Z_T(\omega)$ is connected at the far-end at $x = \ell$.

where the all-important *line input impedance* $Z_{in} = Z(0)$. The definition of $\Gamma(0)$ in (29) equals that of the scattering parameter S_{11} with an associated reference impedance chosen as Z_0. The scattering parameter S_{11} is used in *e.g.* [5] and Paper V [13].

It is sometimes appropriate to work with the *voltage reflection coefficient* which is commonly defined at the source $(x = 0)$ and at the termination impedance $(x = \ell)$, seen from the left-side, as

$$\Gamma_S = \frac{Z_S - Z_0}{Z_S + Z_0}, \quad \Gamma_T = \frac{Z_T - Z_0}{Z_T + Z_0}. \tag{30}$$

From (30) it can be deduced that an open-ended line with $Z_T \to \infty$ provides $\Gamma_T = 1$, *i.e.*, complete reflection, while $Z_T = Z_0$ gives $\Gamma_T = 0$ resulting in no far-end reflection and therefore no left-propagating wave. For DSL transceivers, $Z_S \neq Z_0$ in practice whereupon it follows from (30) that $\Gamma_S \neq 0$. Hence a reflection of the transmitted signal is created at $x = 0$. The impact and utilization of this typically strong and slowly decaying reflection is discussed in Paper II [11].

With reference to Fig. 9 the two following boundary conditions can be stated

$$U(0) = U_S - Z_S I(0), \quad U(\ell) = Z_T I(\ell). \tag{31}$$

By using (18)–(19) with (20), we obtain for $x = \ell$ the following relations

$$U_0^+ \;\; = \;\; \frac{1}{2}\Big(U(\ell) + Z_0 I(\ell)\Big)e^{+\gamma\ell} \tag{32}$$

$$U_0^- \;\; = \;\; \frac{1}{2}\Big(U(\ell) - Z_0 I(\ell)\Big)e^{-\gamma\ell}. \tag{33}$$

Similarly, for $x = 0$ we obtain

$$U(0) \;\; = \;\; U_0^+ + U_0^- \tag{34}$$

$$I(0) \;\; = \;\; \frac{U_0^+}{Z_0} - \frac{U_0^-}{Z_0}. \tag{35}$$

By combining the relations in (32)–(35) we find after some manipulations a matrix equation that relates the voltages and currents at the line ends, *i.e.*,

$$\left[\begin{array}{c} U(0) \\ I(0) \end{array}\right] = \left[\begin{array}{cc} \cosh(\gamma\ell) & Z_0\sinh(\gamma\ell) \\ \frac{\sinh(\gamma l)}{Z_0} & \cosh(\gamma\ell) \end{array}\right] \left[\begin{array}{c} U(\ell) \\ I(\ell) \end{array}\right]. \tag{36}$$

In the two-port theory, these matrix elements characterize the transmission line, as depicted in Fig. 10, and are commonly referred to as *ABCD* parameters, that is,

$$\left[\begin{array}{c} U(0) \\ I(0) \end{array}\right] = \left[\begin{array}{cc} A & B \\ C & D \end{array}\right] \left[\begin{array}{c} U(\ell) \\ I(\ell) \end{array}\right]. \tag{37}$$

The $ABCD$-matrix is often referred to as the *transmission matrix* from which it (once again) can be deduced that a dispersive and homogeneous line is completely characterized by Z_0, γ, and the line length ℓ.

From (36)–(37) and (31) it follows that the line input impedance can be expressed as

$$Z_{in} = \frac{U(0)}{I(0)} = Z_0 \frac{Z_T \cosh(\gamma\ell) + Z_0 \sinh(\gamma\ell)}{Z_T \sinh(\gamma\ell) + Z_0 \cosh(\gamma\ell)} = \frac{Z_T A + B}{Z_T C + D}, \qquad (38)$$

where for the often considered case with an open-ended line, *i.e.*, when $Z_T \to \infty$,

$$Z_{in} = Z_0 \coth(\gamma\ell) = \frac{A}{C}. \qquad (39)$$

Dividing all terms in (38) with $\cosh(\gamma\ell)$ yields

$$Z_{in} = Z_0 \frac{Z_T + Z_0 \tanh(\gamma\ell)}{Z_T \tanh(\gamma\ell) + Z_0}. \qquad (40)$$

From (40) it can be observed that $Z_{in} \to Z_0$ as $\tanh(\gamma\ell) \to 1$, which is valid as the line length goes to infinity. That is, the line input impedance is approximately the characteristic impedance of a long line irrespectively of the termination impedance.

With reference to Fig. 10, the frequency-dependent *transfer function H* is commonly defined as

$$H = \frac{U(\ell)}{U_S}. \qquad (41)$$
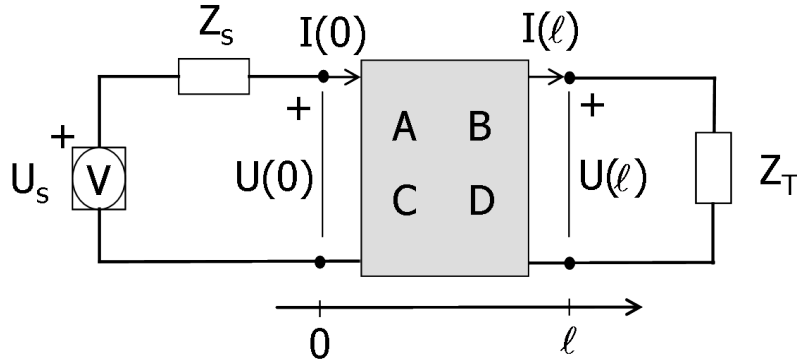
Figure 10: A transmission line of length ℓ characterized by its $ABCD$-matrix according to the two-port theory.

By exploiting (37) with the boundary conditions in (31), it is straightforward to express (41) in terms of the $ABCD$ parameters together with the source and the termination impedances, *i.e.*,

$$H = \frac{U(\ell)}{Z_S\left(CU(\ell) + D\frac{U(\ell)}{Z_T}\right) + AU(\ell) + B\frac{U(\ell)}{Z_T}} = \frac{Z_T}{Z_S\left(CZ_T + D\right) + AZ_T + B}.$$
(42)

For analysis of twisted-pair cables in the copper access network, one often assumes $Z_S = Z_T = Z_0$ which with the definition of the $ABCD$ parameters substituted in (42) gives

$$H = \frac{1}{2}e^{-\gamma\ell}.$$
(43)

This corresponds to the transfer function of a perfectly matched single-section dispersive and homogeneous transmission line. With a perfectly matched source impedance ($Z_S = Z_0$) and open far-end ($Z_T = \infty$), it can be noted from (42) that the transfer function yields

$$H = e^{-\gamma\ell}.$$
(44)

To analyze a *piecewise-homogeneous* twisted-pair line composed of N homogeneous cable sections spliced together, the chain rule [1] can be applied. This important rule states that the overall response of the multi-section line is obtained by the matrix multiplication of each section's $ABCD$-matrix, as illustrated in Fig. 11. Hence the *total* transmission matrix $\mathbf{M}$ that characterizes the overall line can be expressed as

$$\mathbf{M} = \mathbf{M}^{(1)} \times \mathbf{M}^{(2)} \cdots \times \mathbf{M}^{(N)},$$
(45)
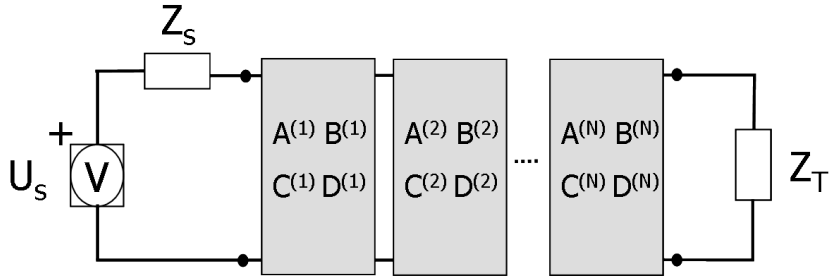
Figure 11: A multi-section line composed of N homogeneous cable sections where each section is characterized by its $ABCD$-matrix according to the two-port theory.

where line section number s is represented by its transmission matrix $\mathbf{M}^{(s)}$ defined by the $ABCD$ parameters in (36)–(37) denoted as

$$\mathbf{M}^{(s)} = \left[\begin{array}{cc} A^{(s)} & B^{(s)} \\ C^{(s)} & D^{(s)} \end{array} \right] . \tag{46}$$

Since the matrix multiplication is not commutative, the forward (left-to-right) transmission matrix is in general not equal to the backward (right-to-left) transmission matrix unless the transmission line happens to be symmetric. In other words, the total transmission matrix is dependent on the sequence of order of the cable sections. Moreover, the chain rule also allows representing lines containing bridged-taps or load coils by simply including the corresponding $ABCD$-matrix [1].

Of fundamental importance is the relation between the one-port impedance measurement Z_{in} and the transfer function H. For a general open-ended non-homogeneous and dispersive transmission line, we find from (31), (37), (39), and (41) that

$$H = \frac{U(\ell)}{U_S} = \frac{U(\ell)}{U(0)} \cdot \frac{Z_{in}}{Z_{in} + Z_S} = \frac{1}{A} \cdot \frac{Z_{in}}{Z_{in} + Z_S} = \frac{1}{C} \cdot \frac{1}{Z_{in} + Z_S}, \tag{47}$$

where A and C are the total matrix elements obtained through (45). Thus, for an open-ended line (47) shows that H depends on both Z_{in} and A or C, depending on the expression used. Note that Z_S is considered known as it is located in the voltage source. Since Z_{in} depends on only the ratio between A and C, as seen in (39), it can be concluded that the one-port impedance measurement with $Z_T \to \infty$ does not provide (in general) sufficient information to also determine the transfer function. This is also true for a single-section homogeneous line. In essence, one can not in general expect to obtain the complete transmission characteristics of a line from a one-port impedance measurement only. This important fact is reflected in Paper V [13] where the criteria function utilizes both Z_{in} and H, if available, in order to estimate the topology of the transmission line. However, under certain circumstances the transfer function can be accurately estimated based on a one-port impedance measurement as demonstrated in *e.g.* Paper III [12].

Finally, it should be mentioned that the $ABCD$ parameters, mainly used in this dissertation, are only one possible way to model or analyze transmission line properties. Other approaches employ for instance S-parameters, Z-parameters, Y-parameters, or T-parameters.

7   Contributions of This Doctoral Dissertation

In the first five papers of this dissertation the main focus is on estimation and detection of transmission line characteristics in the copper access network. The developed methods apply model-based optimization with an emphasis on using low-order modeling and a priori information of the given problem. The subsequent two papers deal with estimation of crosstalk channels between twisted-pair cables in a cable binder. The impact such a non-ideal estimator has on the performance of dynamic spectrum management (DSM) is analyzed and simulated. In the final paper a novel echo cancellation algorithm for DMT-based DSL modems is described.

In the following respective subsection a summary of each paper is presented and the key points of each contribution are highlighted.

7.1   Paper I

The *BT0* cable model is standardized by ETSI [64] to represent the twisted-pair copper lines in the European access networks. With this cable model, the line resistance and the line inductance are treated as mutually independent. This, however, leads to a non-causal model as reported in [58] and a higher model order than necessary. The lack of causality of the *BT0* model corresponds in the frequency domain to violating the Hilbert transform-relation between the real and the imaginary part of the series impedance [65].

In Paper I we analyze the necessary requirements for a general frequency-dependent impedance to comply with the causal conditions stated by the Hilbert transform. In the analysis we slightly extend the basic form of the Hilbert transform defined in *e.g.* [65]. With the understanding of the extended form a new twisted-pair cable model is derived that is both causal and has fewer parameters than prior art. The new cable model, denoted $BT0_H$, consists of only four cable-dependent parameters which should be compared to the original *BT0* model that consists of seven parameters.

7.2   Paper II

Paper II presents a class of estimators for the frequency-dependent characteristic impedance of a twisted-pair cable based on one-port measurements only. The so obtained characteristic impedance paves the way for enhanced time domain reflectometry (TDR). In contrast to previously published time-domain methods [9, 10, 24], no *a priori* information about the line is required such as a cable data base. Thereto, the proposed estimators are unbiased as opposite to a prior art frequency-domain method [66]. In general the prior

works require a multi-dimensional optimization when employing the cable models in *e.g.* [63], which typically leads to a nonlinear and non-convex optimization problem. The high complexity in minimizing the state of the art criteria is partly avoided in [9, 10] by restricting the sought parameters to a finite set of values stored in a cable data base. However, this requires up-to-date and accurate *a priori* information about the used cables. In Paper II we overcome the high complexity by instead proposing a time domain criterion based on the squared line input impedance.

By applying the cable model derived in Paper I, we obtain the low-complexity *Estimator I* that solves the resulting *non-linear* least-square (LS) problem by means of a one-dimensional grid search and a linear LS solver. Similarly, by applying the VUB0 or MAR2 cable model [23, 58], *Estimator II* is obtained that solves the resulting *non-linear* least-square (LS) problem by means of a two-dimensional grid search and a linear LS solver.

The two derived estimators are evaluated with both simulated cables and laboratory measurements on twisted-pair cables. The results show that a significant TDR enhancement can be achieved by subtracting the estimated (squared) characteristic impedance. With real measurements the estimation results were somewhat degraded due to inhomogeneities of the cables resulting in model errors.

7.3   Paper III

In this paper we analyze how the one-port impedance measurement depends on the properties of the transmission line, and the relevant electrical parameters possible to estimate from such a measurement are identified. The analysis in Paper III shows that the ratios R/C and L/C, and the total line capacitance, are of prime interest for the present application rather than R, L, and C. This is in contrast to several prior works focusing on estimating R, L, C, and G. The analysis further suggests the introduction of *capacitive length* defined in Paper III as

$$y(x) = \int_0^x C_\infty(x')\mathrm{d}x', \tag{48}$$

where x is the spatial variable in unit meter, and C_∞ is a model for the nonhomogeneous and frequency-independent capacitance. From (48) it follows that the *total* line capacitance of a nonhomogeneous and dispersive twisted-pair line of length ℓ can be expressed as

$$y(\ell) = \int_0^\ell C_\infty(x')\mathrm{d}x', \tag{49}$$

which is a quantity that (often) can be measured by a POTS transceiver
and/or estimated by a DSL modem.

Based on this insight, we adopt and develop a space-frequency optimiza-
tion approach [67] that is made feasible without explicit knowledge of ℓ.
In doing so, the invariant imbedding equations are solved in the frequency
domain based on the measured total line capacitance and the known termi-
nation impedance. The derived high-frequency MODEL II contains only two
parameters compared to three in prior art. By applying the cable model
presented in Paper I the enhanced MODEL III is developed which contains
three parameters. This latter model captures also the lower frequencies. For
both models, analytical gradients of the objective function with respect to the
sought model parameters are derived which allows computationally efficient
gradient-based optimization.

The simulation results indicate that both parameters of MODEL II can be
fairly accurately estimated with only one-port reflection data for the homo-
geneous lines up to about 1000 m, and up to about 200 m for the considered
nonhomogeneous lines. The results further suggest that the variances of the
estimated parameters increase with the line length but decrease with the ca-
ble diameter. For the nonhomogeneous lines with lengths beyond 200 m, the
true parameter profiles are typically not obtained with MODEL II despite
minimizing the objective function, probably due to local optima and/or due
to the non-uniqueness of the solution. With two-port reflection data the re-
sults are not (significantly) improved on the longer lines since MODEL II is
not valid at the required low frequencies. Hence, for longer lines MODEL III
is preferable. The simulation results indicate that two-port reflection data are
needed to estimate all three parameters of MODEL III. Moreover, exhaustive
simulations show that a gradually increased bandwidth is vital for a successful
optimization, provided sufficiently close start values. In the DSL application,
the latter can be obtained from *e.g.* a cable data base or measurements.

For all considered lines the transfer function is quite accurately estimated
with only one-port reflection data even though the obtained parameter pro-
files do not (typically) resemble the true ones for the longer lines. This im-
portant result is a merit of having sufficiently close start values, since it can
easily be proved that the one-port reflection data do not uniquely determine
the sought parameters nor the transfer function.

7.4   Paper IV

This paper deals with detection and localization of load coils in the copper
access network. It is shown that the input impedance of a line containing N
load coils can be approximated by a *continued fraction expansion (CFE)* for

the considered POTS frequency band. That is, the line can be viewed as a series of periodically repeated cells of impedances. Moreover, by detecting and counting the number of *resonant frequencies* in the POTS-band of the line impedance (spectrum), the presence of load coils and the number of them can be detected. In the paper, a relation between the resonant frequencies and the distance to the first coil is derived. It is furthermore shown that the *pole* corresponding to the highest resonant frequency is present for all N, *i.e.*, irrespectively of the number of load coils. Consequently, when determining the location of the first load coil of a line with N load coils, only the highest resonant frequency needs to be considered. These properties are exploited by the proposed low-complexity CFE-based location algorithm for *symmetric* loaded lines.

To handle non-symmetric lines, a model-based approach is proposed that minimizes the least-square (LS) error in the frequency domain between the measured line input impedance and a corresponding model. The sought model parameters represent line properties such as the number of line sections, the section lengths, and the cable types. Although a stochastic optimization algorithm is employed, the minimization poses a challenge due to the multi-dimensional criterion function with multiple local optima. Paper IV uses the following strategy to lower the complexity of the problem. By utilizing the detected number of load coils with the CFE-based method, the *structure* of the line topology is known prior to the minimization. It thus remains to estimate the section lengths and the type of cables of the loaded line. With an assumed cable data base, the number of unknown parameters is further reduced to one integer-value per cable type and one length-parameter per line section.

The two described methods are compared and evaluated by computer simulations and by laboratory measurements on real transmission lines. The estimation results indicate that up to five load coils can robustly be detected and located with the proposed methods.

7.5   Paper V

A method for line topology identification is described in Paper V where either one-port measurements (SELT) or both one-port and two-port (DELT) measurements are utilized. The new method, denoted TIMEC, uses the SELT measured scattering parameter $\hat{S}_{11}$ and the DELT measured transfer function $\hat{H}$. In case only SELT measurements are available, the transfer function and associated formulas are not used. The task is to estimate the set of parameters Θ that characterize a given line. More specifically, for a multi-section line, $\Theta = \left\{ \theta^{(1)}, \theta^{(2)}, ..., \theta^{(n_s)} \right\}$ is a set of subsets where $\theta^{(k)} = \left\{ l^k, g^k, b^k \right\}$

contains the length, gauge and type (serial/bridged-tap) of the kth section.

Since two objective functions are used, denoted $V_{S_{11}}(\Theta)$ and $V_H(\Theta)$, multi-objective optimization is performed. To deal with the potentially conflicting objective functions, the multi-objective optimization algorithm NSGA-II [68] is adopted which provides a set of (optimum) solutions that reflects the interaction between the different objectives. The NSGA-II is based on Pareto front selection [68]. The sorting of solutions in Pareto fronts is a useful formalism for letting the optimum solutions evolve along the optimization process. Therefore, at the end of the optimization, a set Ψ corresponding to the solutions in the first Pareto front is selected, and a decision rule is employed to choose the final solution.

In Paper V, the following strategy is adopted. Firstly, the best candidate solution associated with each objective function is selected from all candidates Θ_r belonging to the first Pareto front. That is,

$$\Theta_H^* = \arg \min_{r=1,2,\ldots\,|\Psi|} V_H(\Theta_r)$$

and

$$\Theta_{S_{11}}^* = \arg \min_{r=1,2,\ldots\,|\Psi|} V_{S_{11}}(\Theta_r).$$

Then, the final solution is chosen as the one among these two options that has the smallest sum of the objective functions, $i.e.$,

$$\Theta^* = \arg \min_{\Theta=\Theta_H^*,\Theta_{S_{11}}^*} \Big(V_H(\Theta) + V_{S_{11}}(\Theta) \Big). \tag{50}$$

The performance of the TIMEC method is evaluated by computer simulations with varying degree of information. A comparison with a state of the art method indicates that TIMEC achieves better results, for all the tested lines, when only one-port measurements are used. The results are improved when employing both one-port and two-port measurements. If a rough estimate of the total length is also used, near-perfect estimation is obtained for all tested lines.

7.6   Paper VI

Paper VI investigates how to simultaneously estimate the square-magnitude of the multiple-input multiple-output (MIMO) NEXT and FEXT channels of a copper access cable binder with standardized and already deployed equipment, $i.e.$, discrete multitone (DMT) based DSL modems. Thus, the target user is a network operator which can (normally) only access/control the power spectral density (PSD) of received/transmitted signals. A PSD-based

estimator is therefore suggested. To comply with the standardized DSL systems [37–39], only the time domain can be utilized for signal separation. Hence, by sequentially activating one transmitter at a time, all channels (elements) of the MIMO channel matrix $|\mathbf{H}|^{\mathbf{2}}$ are excited. The so obtained single-input multiple-output (SIMO) sequential-transmission scheme is exploited by the proposed estimator.

Although the paper derives and reviews the optimum minimum variance unbiased estimator for the considered SIMO scenario, its inapplicability for the target network operator overshadows its usefulness. With no statistical *a priori* information about the noise we resort to least-square (LS) estimation. However, it is shown that a PSD-based LS estimate $\widehat{|\mathbf{H}|}^{\mathbf{2}}$ becomes biased even if the noise can be considered uncorrelated, normally distributed, and with a mean value of zero. To circumvent this, it is assumed that the noise PSD is stationary over a time span of at least two measurement intervals. That is, before activating transmitter m, the noise PSD is measured with all transmitters silent. The so obtained (background) noise PSD is denoted $\mathbf{P}_z(m_0)$. Transmitter m is thereafter activated and transmits a known signal with the PSD $\mathbf{P}_x(m)$ resulting in $\mathbf{P}_y(m)$ being measured at the receiver(s). Due to the assumed temporarily-stationary condition we have $\mathbf{P}_z(m) \approx \mathbf{P}_z(m_0)$. An unbiased PSD-based estimate $\widetilde{|\mathbf{H}|}^{\mathbf{2}}(m)$ can be formulated by modifying the LS estimator accordingly

$$
\begin{aligned}
\widetilde{|\mathbf{H}|}^{\mathbf{2}}(m) &= \widehat{|\mathbf{H}|}^{\mathbf{2}}(m) - \mathbf{P}_x(m)^{-1}\mathbf{P}_z(m_0) \\
&= |\mathbf{H}|^{\mathbf{2}}(m) - \mathbf{P}_x(m)^{-1}\Big(\mathbf{P}_z(m) - \mathbf{P}_z(m_0)\Big) \\
&= \mathbf{P}_x(m)^{-1}\Big(\mathbf{P}_y(m) - \mathbf{P}_z(m_0)\Big).
\end{aligned}
\tag{51}
$$

The temporary stationarity assumption is reasonable from at least two aspects: in the SIMO case no other active disturber is present, and the twisted-pair channel is non time-varying. The estimate in (51) and the accompanying procedure can be implemented with standardized ADSL/VDSL modems. Note that a similar PSD-based estimator can be derived for the NEXT channels.

The method is evaluated by laboratory experiments on FEXT channels of a cable binder. A comparison with reference measurements indicates that the mean deviation of the estimator is less than $3\,\mathrm{dB}$ for most frequencies. The accompanying error analysis suggests that the FEXT channel estimation error $\widetilde{\Delta}$ is uniformly distributed within $[-3, 3]$ dB. The analysis further shows that the estimation error increases more than linearly when the level of the background noise $P_z(m_0)$ approaches $P_y(m)$. When the difference between

$P_y(m)$ and $P_z(m_0)$ becomes larger than $5\,\mathrm{dBm/Hz}$ the estimation error is approximately linear with the measurement error.

7.7   Paper VII

A practical implementation of DSM algorithms must cope with inaccuracies in the crosstalk channel estimation. Motivated by this fact, Paper VII investigates the impact of non-ideal crosstalk channel estimation on the DSM performance. For this purpose, the crosstalk channel estimator presented in Paper VI is considered.

In order to gain insight of how the bitloading [1] and the data rate are affected by the FEXT channel estimation error, a statistical sensitivity analysis of the achievable bitloading as a function of the FEXT channel estimation error $\widetilde{\Delta}$ is presented. More specifically, in Paper VII the probability density function (PDF) of the achievable bitloading as a function of the random variable $\widetilde{\Delta}$ is derived followed by the derivation of the PDF for the data rate. In doing so, a relation between the bitloading and $\widetilde{\Delta}$ is obtained that reveals the variation in the assignment of bits per frequency caused by the non-perfect crosstalk channel estimation. Such a variation in the number of bits is also reflected in the final solutions of the DSM algorithms in terms of a spread in the achievable data rate.

A key assumption in the analysis is the modeling of the FEXT channel estimation error $\widetilde{\Delta}$ as uniformly distributed within $[-3, 3]$ dB, which is motivated by the results of Paper VI. Another key assumption is the approximation of the data rate PDF by the Gaussian distribution in accordance with the Central Limit Theorem. The validation of this second assumption is numerically verified by comparing the derived PDF with corresponding Monte Carlo simulations for measured FEXT channels of an ordinary twisted-pair cable binder.

The impact of the crosstalk channel estimation on the DSM performance is evaluated by means of computer simulations of two DSM algorithms (ISB and SCALE). The results indicate that the error introduced by the adopted estimation procedure does not compromise the performance of the DSM techniques, *i.e.*, the considered crosstalk channel estimator provides enough means for a practical implementation of DSM.

7.8   Paper VIII

This paper addresses echo cancellation for DSL communications with discrete multitone (DMT) modulation. The described adaptive echo canceller operates entirely in the frequency domain. The method allows estimation

and subtraction of an echo signal impaired by intercarrier and intersymbol interference (*i.e.*, ICI and ISI) present when the impulse response of the echo channel is longer than the cyclic prefix. With adaptive coefficient-matrices the echo canceller can track a slowly changing echo channel due to *e.g.* temperature changes. Implementation aspects for symmetric and asymmetric DMT-based systems are described together with various ways to reduce the computational complexity. The method is verified by computer simulations. The number of required matrix coefficients of the echo canceller depends on *e.g.* the echo channel and is a trade-off between desired level of echo suppression and computational complexity. In a practical implementation, fast initialization methods combined with time-variable and/or subcarrier dependent step sizes [69, 70] should be employed to avoid starting the adaptation from zero initialization and improving the rate of convergence.

References

[1] T. Starr, J.M. Cioffi, and P.J. Silverman, *Understanding digital subscriber line technology*, Prentice Hall, Upper Saddle River, 1999.

[2] T. Starr, M. Sorbara, J.M. Cioffi, and P.J. Silverman, *DSL Advances*, Prentice-Hall, 2003.

[3] F. Lindqvist, N. Lindqvist, B. Dortschy, P. Ödling, P.O. Börjesson, K. Ericsson, and E. Pelaes, "Crosstalk channel estimation via standardized two-port measurements," *EURASIP Journal on Advances in Signal Processing*, vol. 2008, Article ID 916865, 14 pages, 2008.

[4] N. Lindqvist, F. Lindqvist, M. Monteiro, B. Dortschy, E. Pelaes, and A. Klautau, "Impact of crosstalk channel estimation on the DSM performance for DSL networks," *EURASIP Journal on Advances in Signal Processing*, vol. 2010, Article ID 935076, 11 pages, 2010.

[5] T. Bostoen, P. Boets, M. Zekri, L. Van Biesen, T. Pollet, and D. Rabijns, "Estimation of the transfer function of a subscriber loop by means of one-port scattering parameter measurement at the central office," *IEEE Journal of Selected Areas in Communications*, vol. 20, No. 5, pp. 936–948, June 2002.

[6] T. Vermeiren, T. Bostoen, F. Louage, P. Boets, and X.O. Chehab, "Subscriber loop topology classification by means of time-domain reflectometry," *IEEE International Conference on Communications*, Anchorage, USA, 11-15 May, 2003.

[7] P. Boets, L. Van Biesen, T. Bostoen, and D. Gardan, "Single-ended line testing - a white box approach," *Proceedings of the 4th IASTED International Multi-Conference, Wireless and Optical Communications*, July 8-10, 2004, Banff, Canada.

[8] L. Van Biesen, P. Boets, F. Louage, and T. Bostoen, "Expert system for the identification and classification of the local loop," *10th IMEKO TC7 International Symposium*, Saint-Petersburg, Russia, June 30-July 2, 2004.

[9] K. Kerpez and S. Galli, "Single-ended loop make-up identification. Part I: A method of analyzing TDR measurements," *IEEE Transactions on Instrumentation and Measurement*, vol. 55, no. 2, pp. 528–537, Apr. 2006.

[10] K. Kerpez and S. Galli, "Single-ended loop make-up identification. Part II: Improved algorithms and performance results," *IEEE Transactions on Instrumentation and Measurement*, vol. 55, no. 2, pp. 538–549, Apr. 2006.

[11] F. Lindqvist, P.O. Börjesson, P. Ödling, K. Ericson, and T. Magesacher, "Estimation of twisted-pair characteristic impedance from one-port measurements," *To be submitted.*

[12] F. Lindqvist and P.O. Börjesson, "Estimation of nonhomogeneous and dispersive twisted-pair transmission lines," *Submitted to IEEE Transactions on Instrumentation and Measurement*, Oct. 2011.

[13] C. Sales, R.M. Rodrigues, F. Lindqvist, J. Costa, A. Klautau, K. Ericson, J. Rius i Riu, and P.O. Börjesson, "Line topology identification using multi-objective evolutionary computation," *IEEE Transactions on Instrumentation and Measurement*, vol. 59, no. 3, pp. 715–729, Mar. 2010.

[14] J.L. Fang, C. Zeng, and J.M. Cioffi, "Bridged tap location estimation," *preprint.*

[15] Godwin et al., "Method and apparatus to determine whether a subscriber line is loaded or non-loaded," US patent number 4620068, 1986.

[16] Jai H. Eu, "Digital measurement of amplitude and phase of sinusoidal signal and detection of load coil based on said measurement," US patent number 5404388, 1995.

[17] J. Kamali and B.H. Khalaj, "Single ended line probing in DSL system," US patent number 6668041, 2003.

[18] Sunrise Telecom Incorporated, "SunSet xDSL application series: load coil testing, publication number APP-XDSL-012 Rev.B," 2001.

[19] V. Demjanenko and A. Torres, "ITU - Telecommunication standardization sector temporary document WH-095," Study Group 15, Waikiki, Hawaii, USA, 29 June - 3 July, 1998.

[20] W.T. Bisignani, "Automated loaded transmission-line testing using pattern recognition techniques," *IEEE Transaction on Instrumentation and Measurement*, vol. IM-24, No.1, pp. 1–4, 1975.

[21] F. Lindqvist and A. Fertner, "Detection and localization of load coils from one-port measurements," *IEEE Transactions on Instrumentation and Measurement*, vol. 59, no. 7, pp. 1972–1982, Jul. 2010.

[22] J. Rius i Riu, J. Rosenberg, F. Lindqvist, M. Tilocca, C. Bianco, B. van den Heuvel, P. Ödling, T. Magesacher, M. Berg, J. Sorio, A. Uvliden, and P. O. Börjesson, "The IST-MUSE approach to DSL loop qualification and monitoring," *Proc. 3rd Broadband Europe Conference*, Geneva, Switzerland, Dec., 2006.

[23] P. Boets, *Frequency domain identification of transmission lines from time domain measurements*, Ph.D. thesis, Vrije Universiteit Brussel, Dept. ELEC, Pleinlaan 2, 1050 Brussels, June 1997.

[24] S. Galli and D.L. Waring, "Loop makeup identification via single ended testing: beyond mere loop qualification," *IEEE Journal of Selected Areas in Communications*, vol. 20, No. 5, pp. 923–935, June 2002.

[25] J. Rosenberg, F. Lindqvist, A. Wiå, A. Fertner, A.F. Jensen, P.O. Börjesson and P. Ödling, "Method and arrangement for signal loop test," patent application, PCT/SE04/00296, filed 4 Mars 2004, US 2005/00274563 A1, pub. date 3 Feb. 2005.

[26] A.F. Jensen, F. Lindqvist, and A. Wiå, "Method and arrangement for estimation of line properties," patent application, PCT/SE04/00718, filed 11 May 2004, US 2007/0014393 A1, pub. date 18 Jan. 2007.

[27] F. Lindqvist and P.O. Börjesson, "Characteristics determination of a digital subscriber line," patent application, PCT/IB2004/003955, filed 1 Dec. 2004, WO 2006/059175 A1, pub. date 8 June 2006.

[28] S. Allevad, P. Ödling, A. Fertner, H. Back, F. Lindqvist, P.O. Börjesson, and J. Rius i Riu, "Method, device and program product for estimating properties of a telecommunication transmission line," patent application, PCT/SE2005/001619, filed 27 Oct. 2005, WO 2007/050001 A1, pub. date 3 May 2007.

[29] F. Lindqvist, A. Fertner, and P.O. Börjesson, "A method and a system for cable or subscriber loop investigation performing loop topology identification," patent application, PCT/SE2006/000134, filed 31 Jan. 2006, WO 2007/089173 A1, pub. date 9 Aug. 2007.

[30] J. Dias, I. Negrao, A. Castro, J. Costa, G. Cavalcante, J. Rius i Riu, K. Ericson, and F. Lindqvist, "Improving the performance evaluation of ADSL systems by using a modem diagnosis methodology," *XXII Simpósio Brasileiro de Microondas e Optoeletronica Congresso Brasileiro de Eletromagnetismo*, Campinas, SP, Brazil, Aug. 2006.

[31] J. Reis, A. Castro, J. Costa, J. Rius i Riu, and F. Lindqvist, "Characterization of subscriber local loop by measures of frequency response and TDR," *XVIII IMEKO World Congress Metrology for a Sustainable Development*, Rio de Janeiro, Brazil, Sep. 2006.

[32] J. Costa, J. Reisa, I. Negrao, A. Castro, L. de Souza, K. Ericson, F. Lindqvist, and J. Rius i Riu, "Characterization of subscriber local loop by measures and analysis of frequency and impulse responses," *SPIE Optics East Broadband Access Communication Technologies*, Boston, MA, USA, Oct. 2006.

[33] L. Alcantara, R. Rodrigues, C. Sales, A. Castro, J. Costa, F. Lindqvist, and J. Rius i Riu, "Single-ended transfer function estimation of telephone links for deployment of xDSL services," *XXII Simpósio Brasileiro de Telecomunicações - SBrT 2005, Campinas, SP, Brazil*, Sep. 2005.

[34] A. Fertner, F. Lindqvist, and P.O. Börjesson, "Load coil detection and localization," patent application, PCT/IB2006/003724, filed 20 Dec. 2006, WO 2007/072191 A1, pub. date 28 Jun. 2007.

[35] F. Lindqvist and A. Fertner, "Method and localization unit for detecting and locating load coils in a transmission line," patent application, filed 5 Jun. 2009, US 2010/0156553 A1, pub. date 24 Jun. 2010.

[36] F. Lindqvist, "Estimation of transmission line insertion loss," patent application, PCT/SE2007/000446, filed 8 May 2007, WO 2008/008015 A2, pub. date 17 Jan. 2008.

[37] ITU-T G.993.2, "Very high speed digital subscriber line transceivers 2 (vdsl2)," 2006.

[38] ITU-T G.992.3, "Asymmetric digital subscriber line transceivers 2 (adsl2)," 07/2002.

[39] ITU-T G.992.5, "Asymmetric digital subscriber line transceivers - extended bandwidth (adsl2plus)," 05/2003.

[40] P. Ödling, T. Magesacher, M. Berg, S. Höst, E.A. Sanchez, and P.O. Börjesson, "The 4th generation broadband concept," *IEEE Communications Magazine*, vol. 47, no. 1, pp. 63–69, Jan. 2009.

[41] K.B. Song, S.T. Chung, G. Ginis, and J.M. Cioffi, "Dynamic spectrum management for next-generation DSL systems," *IEEE Communications Magazine*, vol. 40, no. 10, pp. 101–109, 2002.

[42] R. Cendrillon and M. Moonen, "Iterative spectrum balancing for digital subscriber lines," *IEEE International Communications Conference (ICC)*, May 2005.

[43] R. Cendrillon, W. Yu, M. Moonen, J. Verlinden, and T. Bostoen, "Optimal multiuser spectrum balancing for digital subscriber lines," *IEEE Trans. Commun.*, vol. 54, no. 5, pp. 922–933, May 2006.

[44] J. Papandriopoulos and J.S. Evans, "Low-complexity distributed algorithms for spectrum balancing in multi-user DSL networks," *IEEE International Conference on Communications (ICC)*, Jun. 2006.

[45] F. Lindqvist and B. Dortschy, "Method for determining automatically a FEXT/NEXT transfer function," patent application, PCT/SE2006/001017, filed 5 Sep. 2006, WO 2008/030145 A1, pub. date 13 Mar. 2008.

[46] R. Cendrillon, J. Huang, M. Chiang, and M. Moonen, "Autonomous spectrum balancing for digital subscriber lines," *IEEE Transactions on Signal Processing*, vol. 55, no. 8, pp. 4241–4257, Aug. 2007.

[47] "Dynamic Spectrum Management Technical Report," *ATIS Committee NIPP Pre-published document ATIS-PP-0600007*, May 2007.

[48] ITU-T Study Group 15, "G.vector: Draft Recommendation," Dec. 2008.

[49] M. Monteiro, N. Lindqvist, and A. Klautau, "Spectrum balancing algorithms for power minimization in DSL networks," *IEEE International Conference on Communications ICC '09. Dresden, Germany*, 2009.

[50] E. Medeiros, N. Lindqvist, M. Monteiro, H. Abrahim, F. Lindqvist, B. Dortschy, and A. Klautau, "DSM performance on practical DSL systems based on estimated crosstalk channel information," in *17th European Signal Processing Conference 2009*, Glasgow, Scotland, United Kingdom, Aug. 2009.

[51] P. Golden, H. Dedieu, and K. Jacobsen, *Fundamentals of DSL technology*, Auerbach Publications, Taylor & Francis Group, 2006.

[52] M. Ho, J.M. Cioffi, and J. Bingham, "Discrete multitone echo cancelation," *IEEE Transactions on Communications*, vol. 44, pp. 817–825, Jul 1996.

[53] F. Lindqvist and A. Fertner, "Frequency domain echo canceller for DMT-based systems," *Accepted in Oct. 2011 for publication in IEEE Signal Processing Letters.*

[54] F. Lindqvist, A. Fertner, and P. Frenger, "Frequency domain echo canceller," patent application, PCT/SE01/01242, filed 1 Jun. 2000, WO 01/93448 A2, pub. date 6 Dec. 2001.

[55] T. Pollet, "How to capture the most information about a subscriber line through selt: measuring the one-port scattering parameter," ITU - Telecommunication Standardization Sector, Temporary Document OJ-090, Osaka, Japan, 21-25 Oct., 2002.

[56] T. Pollet, "How is g.selt to specify s11 (calibrated measurements)?," Tech. Rep., ITU - Telecommunication Standardization Sector, Temporary Document OJ-090, Osaka, Japan, 21-25 Oct., 2002.

[57] L. Heylen and J. Musson, "Cable models predict physically impossible behaviour in time domain," *ETSI TM6 contribution* , Amsterdam, Holland, 29 Nov - 1 Dec, 1999.

[58] J. Musson, "Maximum likelihood estimation of the primary parameters of twisted pair cables," Tech. Rep., ETSI STC contribution TD8, TM6 meeting, Madrid Spain, Jan 26-30 1998.

[59] F. Lindqvist, P.O. Börjesson, P. Ödling, S. Höst, K. Ericson, and T. Magesacher, "Low-order and causal twisted-pair cable modeling by means of the hilbert transform," *RVK08 - The twentieth Nordic Conference on Radio Science and Communications*, Växjö, Sweden, June 9-11, 2008. AIP Conference Proceeding, vol. 1106, pp 301-310.

[60] IEC/CEI 61156-1, "International standard, multicore and symmetrical pair/quad cables for digital communications, part 1: Generic specification," 2002.

[61] J. Cook, "Parametric modeling of twisted pair cables for VDSL," ANSI contribution, T1E1.4/96-15, Irvine, CA, USA, 22-25 Jan, 1996.

[62] J. Cook, "Minor Correction to T1E1.4/96-15, parametric modeling of twisted pair cables for VDSL," ANSI contribution, T1E1.4/96-15, Colorado Springs, CO, USA, 22-24 April, 1996.

[63] R.F.M. van den Brink, "Cable reference models for simulating metallic access networks," Tech. Rep., ETSI STC TM6 Permanent document TM6(97)02, June 1998.

[64] ITU-T G.996.1, "Test procedures for digital subscriber line (dsl) transceivers," 02/2001.

[65] A. Papoulis, *The Fourier integral and it's application*, McGraw-Hill Book Company, Inc., 1987.

[66] P. Boets, T. Bostoen, L. Van Biesen, and T. Pollet, "Preprocessing of signals for single-ended subscriber line testing," *IEEE Transactions on Instrumentation and Measurement*, vol. 55, no. 5, pp. 1509–1518, Oct. 2006.

[67] M. Norgren and S. He, "An optimization approach to the frequency-domain inverse problem for a nonuniform LCRG transmission line," *IEEE Transaction On Microwave Theory and Techniques*, vol. 44, pp. 1503–1507, 1996.

[68] K. Deb, A. Pratap, S. Agarwal, and T. Meyarivan, "A fast and elitist multiobjective genetic algorithm: NSGA-II," *IEEE Transactions on Evolutionary Computation*, vol. 6, no. 2, pp. 182–197, Apr. 2002.

[69] M. Ho, "Multicarrier echo cancellation and multichannel equalization," *Ph.D. dissertation, Stanford University*, June, 1995.

[70] M. Ho, J.M. Cioffi, and J.A.C. Bingham, "Discrete multitone echo cancelation," *IEEE Transactions on Communications*, vol. 44, pp. 817–825, July, 1996.

Paper I

Paper I

Low-Order and Causal Twisted-Pair Cable Modeling by Means of the Hilbert Transform

Abstract

A new low-order and causal twisted-pair cable model for the copper access network is derived. From the series resistance of the widely used, but non-causal, *BT0* model, the series inductance is computed via the Hilbert transform. By doing so, a causal cable model is obtained containing fewer parameters compared to the *BT0* model. The deviation between the two models is evaluated for the standardized ETSI cables.

1 Introduction

Cable models representing the twisted-pair copper lines in the European access networks are standardized by ETSI [1]. These models are widely used to compare the performance of DSL transceivers from different vendors and to specify requirements for DSL systems. Hence, the so-called ETSI cables [1], which are based on the *BT0* cable model [2,3], constitute the norm for DSL cable modeling. However, as reported in [4], the *BT0* model has a non-physical behavior in the time domain since it violates the law of causality. The lack of causality of the *BT0* model corresponds in the frequency domain to violating the Hilbert transform-relation between the real and the imaginary part of the series impedance [5]. In this paper, we analyze the necessary requirements for a general frequency-dependent impedance to comply with the causal conditions stated by the Hilbert transform. In the analysis we slightly extend the basic form of the Hilbert transform defined in *e.g.* [5]. We derive a new twisted-pair cable model, denoted $BT0_H$, that is both causal and has fewer parameters than the standardized *BT0* model. The reduction of model order is made possible by relating the real part to the imaginary part of the series impedance via the Hilbert transform. In other words, unlike *BT0*, the new model does *not* treat the series resistance and the series inductance as mutually independent. The merit of low order is important for DSL line qualification methods described in *e.g.* [6] where the transfer function of a multi-section line is estimated with model-based optimization. The criteria functions used in this type of applications typically have many local optima. Hence, it is desirable to employ a parameterized cable model of low order to decrease the search space dimension and thereby reduce the complexity of finding the global optimum.

The outline of the paper is as follows. In Section 2, the causality conditions for a general frequency-dependent impedance are described. The new $BT0_H$ cable model is introduced in Section 3. A parameter optimization of the $BT0_H$ model for the ETSI cables is described in Section 4. In Section 5, the *BT0* and the $BT0_H$ model are compared for the ETSI cables. Finally, conclusions are presented in Section 6.

2 Causality Conditions

Consider a general frequency-dependent (passive) impedance $\tilde{Z}(\omega) = \tilde{R}(\omega) + j\omega\tilde{L}(\omega)$, where $\tilde{R}(\omega)$ and $\tilde{L}(\omega)$ are the resistance and the inductance, respectively, at angular frequency $\omega = 2\pi f$. The tilde-sign distinguish these quantities from the extended impedance used later on in this section.

Let $\tilde{z}(t)$ denote the inverse Fourier transform of $\tilde{Z}(\omega)$. Assume that the time domain response $\tilde{z}(t)$ is real-valued and causal. Further assume that both $\tilde{R}(\omega) \to 0$ and $\omega\tilde{L}(\omega) \to 0$ as $\omega \to \infty$. Under these conditions, $\tilde{z}(t)$ has no (Dirac) impulses at $t = 0$ and it can be shown by decomposition of $\tilde{z}(t)$ into its *even* and *odd* parts that the following relations between $\tilde{R}(\cdot)$ and $\tilde{L}(\cdot)$ hold [5]:

$$\tilde{R}(\omega) = \frac{1}{\pi} \int_{-\infty}^{\infty} \frac{x\tilde{L}(x)}{\omega - x} \mathrm{d}x \qquad (1)$$

$$\omega\tilde{L}(\omega) = -\frac{1}{\pi} \int_{-\infty}^{\infty} \frac{\tilde{R}(x)}{\omega - x} \mathrm{d}x \qquad (2)$$

Equations (1) and (2) are known as the *Hilbert transform* [5] and assure that $\tilde{z}(t) = 0$ for $t < 0$. Next, we extend (1) and (2) to the slightly more general case where the resistance and the inductance are permitted to approach constant values as $\omega \to \infty$. As will be described in Section 3 this extension has interesting properties applicable to cable modeling. Assume now that we add a constant resistance ΔR to $\tilde{Z}(\omega)$. Denote the new total resistance by $R(\omega) = \tilde{R}(\omega) + \Delta R$. Adding ΔR to the frequency response corresponds to adding the impulse $\Delta R\delta(t)$ to $\tilde{z}(t)$. Hence, the condition $\tilde{z}(t) = 0$ for $t < 0$ is still satisfied. Similarly, we add the constant $j\omega\Delta L$ to $\tilde{Z}(\omega)$, which corresponds to the addition of $\Delta L\delta'(t) = \Delta L\frac{\mathrm{d}\delta(t)}{\mathrm{d}t}$ to $\tilde{z}(t)$. Consequently, $\tilde{z}(t)$ remains causal also in this case where we denote the new total inductance by $L(\omega) = \tilde{L}(\omega) + \Delta L$. Here we have defined the first derivative of $\delta(t)$ as in [5], where $\int_{-\infty}^{\infty} \frac{\mathrm{d}\delta(t-\tau)}{\mathrm{d}t} f(t)\mathrm{d}t = -\frac{\mathrm{d}f(\tau)}{\mathrm{d}t}$, and $f(t)$ is an arbitrary function.

Let us now take a second look at the relation between the real part and the imaginary part of the slightly extended impedance $Z(\omega) = R(\omega) + j\omega L(\omega)$, as defined above. Since the real and the imaginary part of $Z(\omega)$ correspond to the even and the odd part of its time-domain transform [5], respectively, $z(t)$ can be expressed as

$$\begin{aligned} z(t) &= z_e(t) + z_o(t) \\ &= (\tilde{z}_e(t) + \Delta R\delta(t)) + (\tilde{z}_o(t) + \Delta L\delta'(t)), \end{aligned} \qquad (3)$$

where $\tilde{z}_e(t)$ and $\tilde{z}_o(t)$ are the even and the odd parts of $\tilde{z}(t)$. By introducing the signum-function $sgn(t)$ [5], the even and the odd part of $z(t)$ in (3) can be written as

$$z_e(t) = \tilde{z}_o(t)sgn(t) + \Delta R\delta(t) \qquad (4)$$
$$z_o(t) = \tilde{z}_e(t)sgn(t) + \Delta L\delta'(t). \qquad (5)$$

Hence, the Fourier transform of $z_e(t)$ and $z_o(t)$ yields

$$R(\omega) = \frac{1}{2\pi} j\omega \tilde{L}(\omega) * \frac{2}{j\omega} + \Delta R \tag{6}$$

$$j\omega L(\omega) = \frac{1}{2\pi} \tilde{R}(\omega) * \frac{2}{j\omega} + j\omega \Delta L, \tag{7}$$

where $*$ is the continuous-time convolution operator. It now follows that the relation between $R(\omega)$ and $L(\omega)$ can be expressed as follows by replacing $*$ with the convolution integral

$$R(\omega) = \frac{1}{\pi} \int_{-\infty}^{\infty} \frac{x\tilde{L}(x)}{\omega - x} \mathrm{d}x + \Delta R \tag{8}$$

$$\omega L(\omega) = -\frac{1}{\pi} \int_{-\infty}^{\infty} \frac{\tilde{R}(x)}{\omega - x} \mathrm{d}x + \omega \Delta L, \tag{9}$$

where $\tilde{R}(\omega) = R(\omega) - \Delta R$ and $\tilde{L}(\omega) = L(\omega) - \Delta L$. Here, ΔR and ΔL are chosen such that $\tilde{R}(\omega) \to 0$ and $w\tilde{L}(\omega) \to 0$ as $\omega \to \infty$. Thus, by allowing impulses at $t = 0$, the Hilbert transform of (1)–(2) has been extended to the slightly more general case. With the assumed conditions we can state the following based on (8)–(9). For a given causal impedance with inductance $L(\omega)$, we can only determine the total resistance in (8) within a constant ΔR. Similarly, given $R(\omega)$ of a causal impedance, we can only determine the total inductance in (9) within a constant ΔL. This uncertainty has implications to cable modeling as described in the following section.

3 Cable Modeling Application

A twisted-pair cable can be modeled as a cascade of infinitesimal homogeneous segments of length dx. Each segment can be treated as a circuit [7] consisting of a series impedance $Z(\omega) = R(\omega)dx + j\omega L(\omega)dx$ and a shunt admittance $Y(\omega) = G(\omega)dx + j\omega C(\omega)dx$. Here, $R(\omega), L(\omega), G(\omega)$, and $C(\omega)$ are the series resistance, the series inductance, the shunt conductance, and the shunt capacitance, respectively, which are all frequency-dependent and expressed per unit length. Different parameterized expressions (models) for these quantities can be found, leading to different cable models [8]. The standardized *BT0* cable model [1–3] defines the line resistance and the line inductance as

$$R(f) = \sqrt[4]{r_{oc}^4 + a_c f^2} \tag{10}$$

and

$$L(f) = \frac{L_0 + L_\infty (\frac{f}{f_m})^b}{1 + (\frac{f}{f_m})^b}, \tag{11}$$

where $r_{oc}, a_c, L_0, L_\infty, f_m, b$ are all model parameters [1]. Moreover, *BT0* models the line capacitance as constant with regards to frequency and the conductance is set to zero (approximation). (From now on we use frequency $f = \omega/2\pi$ instead of ω in order to comply with [1,2]. This would have been less convenient when working with the Hilbert transforms in Section 2). In order to obtain a causal model with fewer model parameters than *BT0*, we rewrite the line resistance in (10) as

$$R(f) = R_0 \sqrt[4]{1 + (f/\nu)^2} = R_0 Q(f/\nu), \tag{12}$$

where $R_0 = r_{oc}$ and $\nu = \sqrt{\frac{r_{oc}^4}{a_c}}$. Furthermore, instead of using (11) we model $L(f)$ by means of the Hilbert transform as

$$L(f) = \frac{R_0}{2\pi f} \Lambda(f/\nu) + L_\infty^{(H)}, \tag{13}$$

where $\Lambda(f/\nu)$ is the Hilbert transform of $Q(f/\nu)$ and $L_\infty^{(H)}$ is another cable-dependent parameter that cannot be determined via the Hilbert transform as described in Section 2. In (12), $R(f) \nrightarrow 0$ as $f \to \infty$ and the Hilbert integral for calculating $\Lambda(f/\nu)$ is not absolute-convergent. However, the Cauchy principle value of the integral is convergent and we interpret the integral in this way. Another consequence of using the Cauchy principle value is that there is no need to subtract ΔR from $R(\omega)$ as in (9).

As for the *BT0* model we assume that the line capacitance, denoted $C_\infty^{(H)}$, is constant with frequency and that the line conductance is zero. Thus, our new causal cable model, denoted $BT0_H$, consists of only four cable-dependent parameters represented by $R_0, \nu, L_\infty^{(H)}, C_\infty^{(H)}$. This should be compared to the original *BT0* model in (10)–(11) that consists of seven parameters where $G(f) = 0$ and $C(f) = C_\infty$.

4   Parameter Optimization

The ETSI cables in [1] are defined for five different cable diameters: 0.32, 0.40, 0.50, 0.63 and 0.90 mm. Numerical values for the model parameters are specified in [1] for each cable (diameter). In order to represent the ETSI cables with the $BT0_H$ model, the parameters are identified for each cable.

Since the series resistance and the shunt capacitance for the two models are the same, it is appropriate to set $R_0 = r_{oc}$, $\nu = \sqrt{\frac{r_{oc}^4}{a_c}}$, and $C_\infty^{(H)} = C_\infty$. With this choice, only the parameter $L_\infty^{(H)}$ has to be optimized. Inspired by [2], we minimize the difference between the series inductance of the two models. The applied least-squares (LS) criterion can be formulated as

$$J(L_\infty^{(H)}) = \min_{L_\infty^{(H)}} \sum_{f_k=f_{\text{low}}}^{f_{\text{high}}} \left(L(f_k) - L_{BT0_H}(f_k, L_\infty^{(H)}) \right)^2, \qquad (14)$$

where $L(f_k)$ denotes the series inductance of the *BT0* model defined by (11) and $L_{BT0_H}(f_k, L_\infty^{(H)})$ is the inductance according to (13). Here, f_k denotes the kth discrete frequency point where $f_k \in [f_{\text{low}}, f_{\text{high}}]$. The optimum LS solution of (14) is found by the first derivative of (14) with respect to $L_\infty^{(H)}$. This leads to the LS solution

$$L_\infty^{(H)} = \frac{1}{N} \sum_{f_k=f_{\text{low}}}^{f_{\text{high}}} \left(L(f_k) - \frac{R_0}{2\pi f_k} \Lambda(f_k/\nu) \right), \qquad (15)$$

where $N = f_{\text{high}} - f_{\text{low}} + 1$.

For the evaluation of the parameter optimization in Section 5, we consider the relative deviation of the series inductance (in percent) between *BT0* and *BT0_H*. We define this deviation as

$$L_{dev}(f_k) = 100 \; \frac{L(f_k) - L_{BT0_H}(f_k, L_\infty^{(H)})}{L(f_k)}. \qquad (16)$$

Another important performance measure of the model is the *insertion loss* (*IL*), which is used for *e.g.* computing the DSL channel capacity. The frequency-dependent *IL* is a measure of the channel attenuation that is defined (in dB) by, [7],

$$IL = -20 \log_{10} \left| \frac{Z_L + Z_s}{AZ_L + B + Z_s(CZ_L + D)} \right|, \qquad (17)$$

where A, B, C, D are the elements of the so-called *ABCD* matrix [7]. Furthermore, Z_S and Z_L are the source and load impedance, respectively, here approximated by $100\,\Omega$ pure resistance. Note that the elements of the *ABCD* matrix depend on both the frequency and the cable length, which has been omitted in the notation. In Section 5 we compare the relative deviation (in percent) of the insertion loss defined in an analogous way to (16).

5   Model Comparison

In this section, we evaluate the differences between the *BT0* and the *BT0$_H$* cable model. The following subsections compare the model deviation of the series inductance, the insertion loss (IL) and the causality of the impulse response.

5.1   *BT0$_H$* Parameter Optimization

The LS criterion defined in (14) is minimized for each European test cable [1] in order to find the LS optimum $L_\infty^{(H)}$ parameter of the *BT0$_H$* model. The optimal values are computed using (15) with a total of 4096 equally spaced frequency points from 10 kHz to 30 MHz. The start frequency has been chosen to avoid the errors of the *BT0* model at low frequencies, described in [2]. The stop frequency corresponds to the highest frequency used by the VDSL2 standard [9]. The Hilbert transform in (15) is computed via numerical integration. The results of the LS optimized $L_\infty^{(H)}$, rounded to one decimal, are listed in Table 1 together with the corresponding values of the *BT0* model.

Table 1: Parameter $L_\infty^{(H)}$ optimization results

Wire diameter	*BT0* L_∞ [μH/km]	*BT0$_H$* $L_\infty^{(H)}$ [μH/km]
0.32 mm	382.2	460.0
0.40 mm	426.0	405.3
0.50 mm	532.7	515.1
0.63 mm	477.2	462.6
0.90 mm	520.5	508.6

5.2   Evaluation of the Series Inductance

Fig. 1 and Fig. 2 show the results of the LS optimization for the ETSI cables in terms of a comparison between the *BT0* and *BT0$_H$* series inductance and the relative deviation defined in (16). Note that the figures compare the results up to 100 MHz even though only the frequency range from 10 kHz to 30 MHz is used in the optimization. From Fig. 2 it can be seen that the relative deviation is larger for lower frequencies.

Moreover, the 0.32 mm cable type sticks out by having a significantly larger deviation. This cable type is, however, less common and is used only
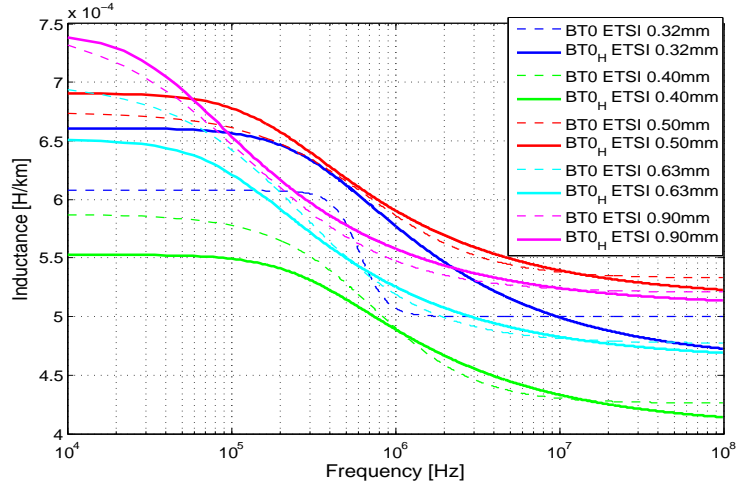
Figure 1: Series inductance for the *BT0* and the *BT0_H* cable model of different ETSI cables.
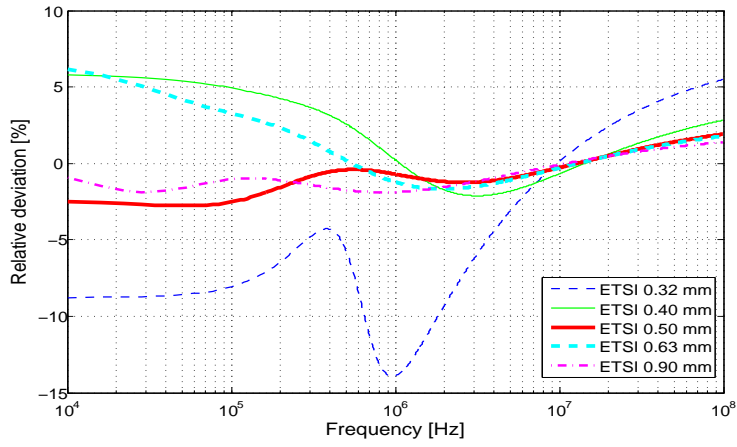
Figure 2: Deviation between the *BT0* and the *BT0_H* series inductance of different ETSI cables.

for short distances ($< 300\,$m) due to its high IL. Above $20\,$kHz the deviation is less than $\pm 6\,\%$ for all cable types except for the $0.32\,$mm. Above $400\,$kHz the deviation is less than $\pm 3\,\%$ except for the $0.32\,$mm type. It should be mentioned that the deviation can be reduced for the $0.32\,$mm cable by using a lower frequency range in the computation of (15). However, this has the effect of increasing the deviation for higher frequencies.

5.3   Evaluation of the Insertion Loss

Given the optimal parameters in the LS sense shown in Table 1, the insertion loss (IL) of the two cable models is compared for different cable lengths. Fig. 3 depicts the relative IL deviation as a function of frequency for ETSI $0.40\,$mm. In line with [2] frequencies up to $100\,$MHz are compared (16384 points). As for the four other ETSI cable types, the spread (variance) of the relative deviation at frequencies above $500\,$kHz is much lower than the mean value of the deviations for the different cable lengths. The maximum magnitude of the relative deviation of the IL is shown in Fig. 4 for all the five ETSI cables with cable lengths 0.1, 0.5, 1.0, 1.5 and 3.0 km.
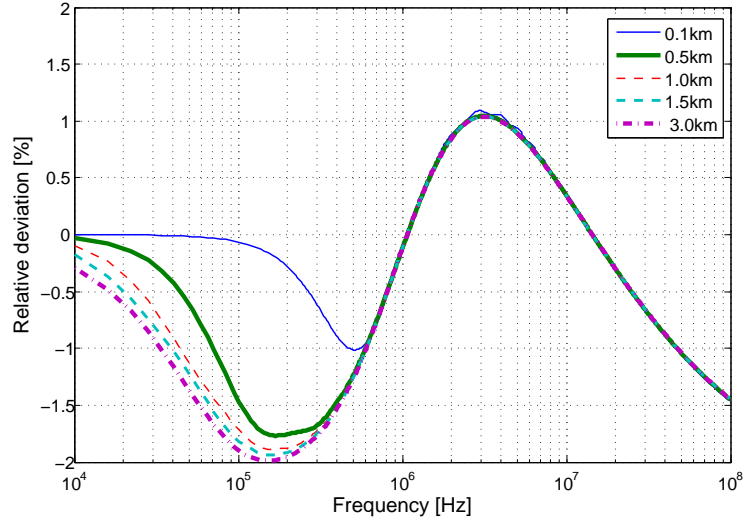
Figure 3: Relative insertion loss deviation between ETSI $0.40\,$mm *BT0* and *BT0$_H$* for different cable lengths.
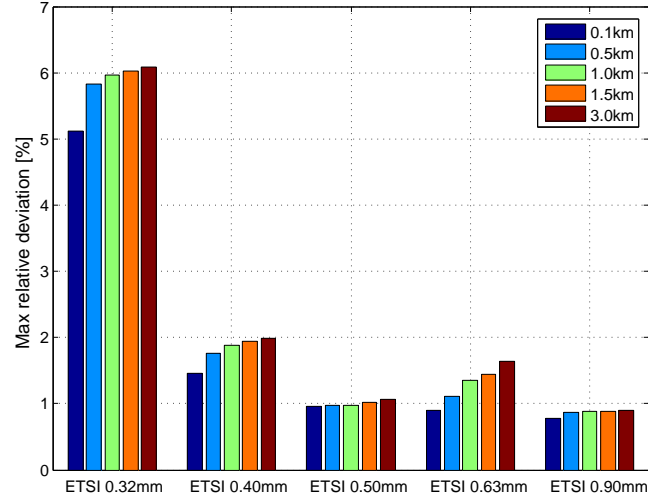
Figure 4: Maximum magnitude of the relative insertion loss deviation between *BT0* and *BT0_H* for the ETSI cables of different lengths.

It can be noted from Fig. 4 that the deviation is below 2 % for all cables except for the 0.32 mm type, which is due to the larger deviation of the series inductance. As expected, the (maximum) relative deviation increases slightly for longer cables.

5.4   Evaluation of Causality

For time-domain applications it is vital that the impulse response of the cable model behaves as for real twisted-pair cables. A characteristic feature of a real impulse response is the delay-time it takes for an impulse to travel from the near-end to the far-end side of a cable. During this time period, the response measured at the far-end must be zero to obey the law of causality. In other words, an effect must not proceed its cause. The velocity of propagation (VOP) is frequency dependent for real twisted-pair cables and is inversely proportional to the square-root of LC [7]. Consequently, the theoretical *minimum* delay-time can be calculated from the *maximum* VOP for a given cable length.

For the *BT0* model and for twisted-pair cables [7], the minimum delay-time for a given cable length is proportional to the square-root of $L_\infty C_\infty$, since L decreases with frequency and C is (approximately) constant.

Fig. 5 shows the impulse responses from the near-end to the far-end of a cable based on the *BT0* and on the *BT0$_H$* cable model. The figure also shows the calculated minimum delay-times for *BT0* and *BT0$_H$*. It is clear from Fig. 5 that the impulse response of the *BT0* model starts before the minimum delay-time, and hence, violates the law of causality. It can also be observed that the start of the impulse response of *BT0$_H$* complies well with the minimum delay-time.
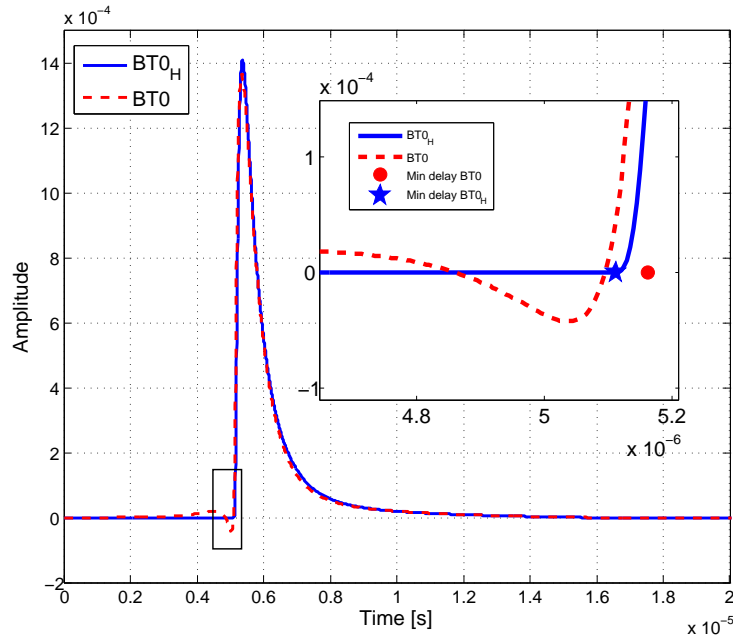
Figure 5: Impulse response from the near-end to the far-end of a 1 km ETSI 0.5 mm cable modeled with the *BT0* and the *BT0$_H$* cable model. The filled-circle shows the (theoretical) min-delay time of *BT0* and the filled-star shows the min-delay time of *BT0$_H$*.

6   Discussion and Conclusions

For a general complex-valued impedance, the Hilbert transform-relation between its real part and its imaginary part, as defined in *e.g.* [5], was extended to the slightly more general case by allowing the Dirac-impulse and

its first-order derivative in the time domain at origo. An application to cable modeling was presented where the standardized non-causal $BT0$ model was converted to a causal and low-order model denoted $BT0_H$. The derived $BT0_H$ model contains only four parameters compared to the seven parameters of the $BT0$ model. A least-squares parameter optimization was described targeting a representation of the standardized ETSI cables with the $BT0_H$ model. The optimized parameters provide fairly low deviations of the series inductance and, more specifically, result in a relative insertion loss deviation of less than $\pm 2\,\%$. Only the ETSI $0.32\,\mathrm{mm}$ cable type showed larger deviation, which might be due to the ETSI-defined parameters for this particular cable type. The improved causality of the $BT0_H$ model compared to $BT0$ was demonstrated by studying the impulse response from the near-end to the far-end side of the ETSI cable. The theoretical minimum-delay time for each model was compared with the impulse response of the model. It can be concluded that the $BT0_H$ model provides a causal time-domain behavior in contrast to $BT0$.

References

[1] ITU-T G.996.1, "Test procedures for digital subscriber line (dsl) transceivers," 02/2001.

[2] J. Cook, "Parametric modeling of twisted pair cables for VDSL," ANSI contribution, T1E1.4/96-15, Irvine, CA, USA, 22-25 Jan, 1996.

[3] J. Cook, "Minor Correction to T1E1.4/96-15, parametric modeling of twisted pair cables for VDSL," ANSI contribution, T1E1.4/96-15, Colorado Springs, CO, USA, 22-24 April, 1996.

[4] J. Musson, "Maximum likelihood estimation of the primary parameters of twisted pair cables," Tech. Rep., ETSI STC contribution TD8, TM6 meeting, Madrid Spain, Jan 26-30 1998.

[5] A. Papoulis, *The Fourier integral and it's application*, McGraw-Hill Book Company, Inc., 1987.

[6] T. Bostoen, P. Boets, M. Zekri, L. Van Biesen, T. Pollet, and D. Rabijns, "Estimation of the transfer function of a subscriber loop by means of one-port scattering parameter measurement at the central office," *IEEE Journal of Selected Areas in Communications*, vol. 20, No. 5, pp. 936–948, June 2002.

[7] T. Starr, J.M. Cioffi, and P.J. Silverman, *Understanding digital subscriber line technology*, Prentice Hall, Upper Saddle River, 1999.

[8] R.F.M. van den Brink, "Cable reference models for simulating metallic access networks," Tech. Rep., ETSI STC TM6 Permanent document TM6(97)02, June 1998.

[9] ITU-T G.993.2, "Very high speed digital subscriber line transceivers 2 (vdsl2)," 2006.

Paper II

Paper II

Estimation of Twisted-pair Characteristic Impedance from One-Port Measurements

Abstract

This paper presents a class of estimators for the characteristic impedance of a twisted-pair cable based on data obtained from one-port measurements only. The so obtained characteristic impedance paves the way for enhanced time domain reflectometry (TDR). In contrast to previously published time-domain methods, no *a priori* information about the line is required such as a cable data base. Thereto, the proposed estimators are unbiased as opposite to a prior art frequency-domain method. The structure of the estimators is motivated by analyzing the reflections occurring on a single-section cable. By basing the estimators on the squared line input impedance, and applying low-order causal cable modeling, a class of low-complex least squares estimators is derived. The performance is evaluated by means of computer simulations and by measurements on telecommunication cables.

1   Introduction

Accurate knowledge of transmission-line properties is necessary for maintaining a high quality copper access network. Specific tasks include service provisioning, trouble-shooting failing services, and predicting possible consequences of any modification to the existing access network. Far from all telecom operators have complete knowledge of their transmission lines (loops) between the Central Office (CO) and the customers, which constitutes an important part of their broadband access network. The original lines have often been installed decades ago and various kinds of modifications have been made throughout the years such as replacements of individual cable sections and topology changes [1]. Hence, the accompanying documentation is seldom complete and not necessarily updated. Up-to-date and accurate line information is of great importance and can be retrieved by using low-cost one-port measurements referred to as Single-Ended Line Testing (SELT). To save cost, the SELT function may be integrated into new or already installed Digital Subscriber Line (DSL) equipment. Through a mere software update, the DSL transceiver units become the "eyes and ears", *i.e.* the sensors, of a DSL management and monitoring system. This function integration also provides means for reducing the labor-intensive work associated with manual testing using hand-held SELT equipment.

Two-port measurements conducted synchronously from both sides of the line have been standardized in *e.g.* [2]. This technique is referred to as Loop Diagnostic (LD) in [2] and is obviously only applicable when modems are present on both sides of the line and both modems support LD. During pre-qualification of DSL services, the modem at the customer side has normally not yet been installed, and hence, LD cannot be utilized. Furthermore, LD cannot be applied in case of a cable break. Thus, LD should be seen as a complement to SELT, where the latter provides a tool for both pre-qualification of DSL lines and automatic fault localization irrespectively of the type of customer equipment.

An important technique used in SELT is time domain reflectometry (TDR) whose working principle is similar to that of RADAR: a waveform is transmitted on the line and the received echo signal is analyzed. That is, the received signal contains one or several echoes caused by imperfect far-end termination, cable gauge changes (splices causing impedance changes), or bridged-taps. One limiting factor for TDR applied on twisted-pair lines, which have severe time dispersion and attenuation, is the strong echo reflection caused by the impedance mismatch between the SELT equipment and the cable [3]. Thus, in order to extract useful information about the twisted-pair transmission line, a signal processing effort following the TDR measurement is necessary.

A similar method to TDR is FDR (Frequency Domain Reflectometry) which is often used in practice by *e.g.* DSL transceivers for SELT. In FDR the line is excited with one or several sinusoids covering the frequency band of interest whereupon the reflected *stationary* response is recorded. The so obtained high-resolution measurement captures the full-length impedance response of the line and permits the calculation of the echo-path channel [4], the scattering parameter S_{11} [5], or the line input impedance. From any of these quantities various kinds of *off-line* TDR responses can be obtained.

Galli and Waring describe in [3] how the impedance mismatch between the SELT equipment and the line creates a so-called slowly decaying signal (SDS) that limits the resolution and the range of TDR on twisted-pair cables. An analytical expression for the SDS is presented which shows that the SDS is determined by the line's characteristic impedance we set out to find in this paper. In [3] the analytical expression is further used for subtraction of the SDS from the measured signal whereupon the obtained TDR enhancements are validated by means of experiments. However, no detailed description is given of how to determine the SDS for an unknown line so that the method can be employed without *a priori* information. In [6, 7] the principles of [3] are applied to address SELT estimation of the transfer function and the determination of the loop topology of a multi-section transmission line. More specifically, the developed method utilizes the subtraction technique in the time-domain combined with hypothesis testing of different loop discontinuities represented by auxiliary topologies. In doing so, the method employs a cable data base assumed available *a priori*. However, a static data base typically overlooks temperature changes and aging effects. Thereto, it has been reported in [5] that the variation of *e.g.* the characteristic impedance within the same cable (*i.e.,* the deviation in a 20-pair 0.5 mm PE cable) can vary $50\,\Omega$ at $10\,\text{kHz}$ and $5\,\Omega$ at $100\,\text{kHz}$.

Boets *et al.* describe in [8–10] how a TDR response is pre-processed and signal-features extracted in order to perform loop topology estimation with a rule-based interpreting system. These kind of systems require that the SDS at the measurement plane is mitigated or removed from the TDR response. The proposed methods solve this by fitting an ad-hoc decaying function to the SDS [11], or by identifying the characteristic impedance with a parametric model [8, 10]. More specifically, [10] minimizes the sum-of-square differences in the frequency domain between the line input impedance and a parameterized model of the characteristic impedance, with respect to the sought parameters. This requires however a nonlinear and non-convex multi-dimensional optimization where the rather computationally complex Levenberg-Marquard minimizer is employed in [10]. Although the approach was found to be robust, the method has a systematic model error since the line input impedance

does not equal the characteristic impedance unless the line is infinitely long.

This paper presents a class of unbiased estimators for the characteristic impedance of a cable via one-port measurements, *i.e.* via SELT, without assuming *a priori* information or an infinitely long line. The determined characteristic impedance can then be used with the methods in *e.g.* [3, 6–10] to enhance the TDR response of a twisted-pair copper line. The proposed class of estimators is derived by minimizing a time-domain error criterion similar to the state of the art criterion used in [6, 7]. Different estimators within the class are obtained by applying different models of the (squared) characteristic impedance. The complexity of the estimators is determined by the order of the applied model. In particular two estimators that provide low-complexity least-squares solutions are studied and evaluated.

The remainder of the paper is organized as follows. Section 2 introduces the SELT system. In Section 3 an analysis of the reflections occurring on a single-section line is presented, which motivates the employed error criterion that the proposed class of low-complexity estimators is derived from. Section 4 compares the state of the art error criterion with the proposed criterion. Section 5 introduces two low-order models of the (squared) characteristic impedance, which are applied in Section 6 to derive two low-complexity least squares estimators. Section 7 and 8 provide estimation results based on computer simulations and laboratory measurements. Finally, conclusions are presented in Section 9.

2   Single-Ended Line Testing (SELT)

The SELT system considered in this paper is depicted in Fig. 1. A test head, here in form of a DSL transceiver, is connected to a twisted-pair copper line. The line is terminated by a far-end impedance (load) that is generally unknown, but is often classified as infinite, short-circuited ($0\,\Omega$), or matched to the line (*e.g.* around $100\,\Omega$). Without loss of generality, the termination impedance is here assumed to be infinite which corresponds to an open-end line and is a common approximation of an on-hook POTS (plain old telephone service) phone or a cable break. In general the line consists of multiple cable *sections* of different wire diameters (gauges) spliced together [4]. During a SELT session, the transceiver employs FDR and transmits one or more waveforms onto the line and records the received echo signal. The recorded signal is used by the transceiver to calculate the line input impedance $Z_{in}(f)$ where f denotes the frequency measured in Hz. Some transceivers measure the scattering parameter $S_{11}(f)$ instead, but in this paper we will only consider $Z_{in}(f)$ since it reduces the computational complexity of the proposed class

of estimators as described in Section 4.

The measured input impedance of a transmission line can be expressed as a function of the $ABCD$ parameters, [4], *i.e.*,

$$Z_{in}(f) = \frac{A(f)\ Z_T(f) + B(f)}{C(f)\ Z_T(f) + D(f)}, \tag{1}$$

where $Z_T(f)$ is the far-end termination impedance, and the $ABCD$ parameters for a *single-section* homogeneous line yield

$$\begin{aligned} A(f) &= D(f) = \cosh(\gamma(f)d), \\ B(f) &= Z_0(f)\ \sinh(\gamma(f)d), \\ C(f) &= \frac{\sinh(\gamma(f)d)}{Z_0(f)}. \end{aligned} \tag{2}$$

Here $Z_0(f)$ is the characteristic impedance of the line, $\gamma(f)$ is the propagation constant, and d is the length of the line. In case of a *multi-section* line, the $ABCD$ parameters in (2) correspond to the elements of the total transmission matrix which can be calculated by multiplying the cascaded segments' $ABCD$-matrices of the line [4]. Hence, in general $Z_{in}(f)$ depends on the side from which the measurement is performed.

The measured signal $Z_{in}(f)$ contains, in general, an unknown number of echoes with unknown arrival times, amplitudes, and shapes. The reflection pattern contained in the line input impedance of a single-section line is analyzed hereafter.
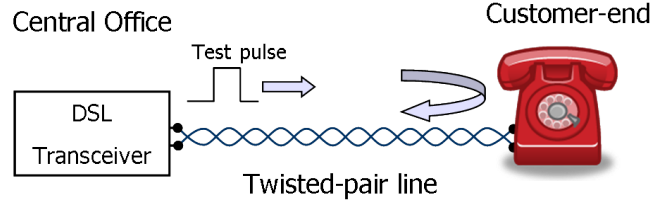
Figure 1: SELT system with DSL transceiver test head.

3   Reflection Analysis

The following analysis complements to some extent the experimental results disclosed in [3], and more importantly, explains the rational behind the proposed error criterion in Section 4 and the derived estimators in Section 6.

The measured input impedance is proportional to the output voltage response occurring when a current Dirac-pulse is applied onto the line. In fact, the input impedance for an open-ended single-section line can be expressed straightforwardly as

$$
\begin{aligned}
Z_{in}(f) &= Z_0(f) \coth(\gamma(f)d) = Z_0(f)\frac{1 + e^{-2\gamma(f)d}}{1 - e^{-2\gamma(f)d}} \\
&= Z_0(f) \left(1 + e^{-2\gamma(f)d}\right) \sum_{n=0}^{\infty} (e^{-2\gamma(f)d})^n \\
&= Z_0(f) + 2Z_0(f)e^{-2\gamma(f)d} + 2Z_0(f)e^{-4\gamma(f)d} \dots
\end{aligned}
\tag{3}
$$

The propagation constant $\gamma(f) = \alpha(f) + j\beta(f)$ consists of the attenuation constant $\alpha(f)$ and the phase constant $\beta(f)$ [4]. The geometric series in (3) converges since $\alpha(f)d$ is always greater than zero for real cables. For the purpose of illustration it is assumed in this section (and only here) that the single-way line delay $\tau_d = \frac{d}{v_p}$ is constant with frequency, where v_p is the phase velocity (velocity of propagation) [4], and hence, β is a linear function of frequency where $\beta(f) = \frac{2\pi f \tau_d}{d}$. With this assumption we obtain $\gamma(f) = \alpha(f) + j\frac{2\pi f \tau_d}{d}$. Hence (3) can be written as

$$
\begin{aligned}
Z_{in}(f) &= Z_0(f) + 2Z_0(f)e^{-2\alpha(f)d}e^{-j2\pi f(2\tau_d)} \\
&+ 2Z_0(f)e^{-4\alpha(f)d}e^{-j2\pi f(4\tau_d)} + \dots \\
&= Z_0(f) + 2Z_0(f)G(f)e^{-j2\pi f(2\tau_d)} \\
&+ 2Z_0(f)G^2(f)e^{-j2\pi f(4\tau_d)} + \dots,
\end{aligned}
\tag{4}
$$

where $G(f) = e^{-2\alpha(f)d}$. It follows that the corresponding time-domain representation of the input impedance is given by

$$
\begin{aligned}
z_{in}(t) &= z_0(t) + 2z_0(t) * g(t - 2\tau_d) \\
&+ 2z_0(t) * g(t - 4\tau_d) * g(t - 4\tau_d) + \dots
\end{aligned}
\tag{5}
$$

where t is the time in seconds, $*$ denotes the continuous-time convolution, and $z_0(t)$ and $g(t)$ are the inverse Fourier transforms of $Z_0(f)$ and $G(f)$, respectively. Thus, the line input impedance consists of a sum of reflections where the first term, *i.e.* $z_0(t)$, occurs at time zero while the other reflections have propagated back and forth on the line one or several times, *i.e.,* first-order and higher-order reflections occur.

By subtracting $z_0(t)$ from (5), or equivalently $Z_0(f)$ from (4), we get

$$
\begin{aligned}
z_{in}(t) - z_0(t) &= 2z_0(t) * g(t - 2\tau_d) \\
&+ 2z_0(t) * g(t - 4\tau_d) * g(t - 4\tau_d) + \dots
\end{aligned}
\tag{6}
$$

From (6) we observe that the time response of $z_{in}(t)-z_0(t)$ starts at $2\tau_d$ rather than at time zero. Hence, the resulting signal is zero for $t \in [0, 2\tau_d)$. Note that the time interval $[0, 2\tau_d)$ covers the time from zero just until the arrival of the first reflection. The subtraction in (6) corresponds to the TDR enhancement used in [3] for removing the superimposed slowly decaying signal. In [3] this subtraction-technique is performed in the frequency domain and works with $Z_{in}(f)/(Z_{in}(f) + Z_{ref}(f))$ instead of $Z_{in}(f)$, where $Z_{ref}(f)$ is a reference impedance. The principle is however the same. It can be demonstrated by *e.g.* simulations that $z_{in}(t) - z_0(t)$ is zero for $t \in [0, 2\tau_d)$ also for cables with frequency-dependent τ_d. The key feature exploited by the proposed estimators is the zero-response of $z_{in}(t) - z_0(t)$ for $t \in [0, 2\tau_d)$, obtained with the true characteristic impedance.

However, in a practical SELT application $Z_{in}(f)$ and $Z_0(f)$ can only be measured within a limited frequency band, *i.e.,* for $f \in [f_{low}, f_{high}]$ where f_{low} and f_{high} denotes the lowest and highest frequency, respectively. The so obtained bandlimited signals are denoted with a tilde-sign and yield

$$
\tilde{Z}_{in}(f) = Z_{in}(f)H_{win}(f)
\tag{7}
$$

and

$$
\tilde{Z}_0(f) = Z_0(f)H_{win}(f),
\tag{8}
$$

where $H_{win}(f)$ is the rectangular window-function defined by

$$
H_{win}(f) = \begin{cases} 1 & \text{if } f_{low} \leq f \leq f_{high}; \\ 0 & \text{otherwise.} \end{cases}
\tag{9}
$$

Consequently, for the bandlimited case the subtraction in (6) can be expressed as

$$
\begin{aligned}
\tilde{z}_{in}(t) - \tilde{z}_0(t) &= 2z_0(t) * h_{win}(t) * g(t - 2\tau_d) \\
&+ 2z_0(t) * h_{win}(t) * g(t - 4\tau_d) * g(t - 4\tau_d) \\
&+ \dots,
\end{aligned}
\tag{10}
$$

where the inverse Fourier transform of $H_{win}(f)$ is denoted $h_{win}(t)$, which is a non-causal sinc-function of the form $\sin(t)/t$ valid for $t \in [-\infty, \infty]$.

It can be observed that (10) equals (6) only for infinite bandwidth since $h_{win}(t)$ then corresponds to a Dirac signal $\delta(t)$. Thus, it follows from (10), in the bandlimited case, that the result of the subtraction is *not* zero for $t \in [0, 2\tau_d)$ due to the non-causal response of $h_{win}(t)$.

With the purpose of minimizing the undesirable non-causal effect of $h_{win}(t)$, and retain a zero-response for $t \in [0, 2\tau_d)$, we introduce a filter $P(f)$ and perform the subtraction in the frequency domain, *i.e.,*

$$
\begin{aligned}
E(f) &= P(f)\Big(Z_{in}(f)H_{win}(f) - Z_0(f)H_{win}(f)\Big) \\
&= P(f)\Big(\tilde{Z}_{in}(f) - \tilde{Z}_0(f)\Big).
\end{aligned} \tag{11}
$$

By letting $H(f) = P(f)H_{win}(f)$, where $P(f)$ is controllable, the time domain transform of (11) can be expressed with (10) as

$$
\begin{aligned}
e(t) &= 2z_0(t) * h(t) * g(t - 2\tau_d) \\
&+ 2z_0(t) * h(t) * g(t - 4\tau_d) * g(t - 4\tau_d) \\
&+ \ldots,
\end{aligned} \tag{12}
$$

where $e(t)$ and $h(t)$ is the inverse Fourier transform of $E(f)$ and $H(f)$, respectively. Equation (12) shows the ideal case for a single-section line where the complete reflection at time zero has been canceled. The success of obtaining a zero-response for $t \in [0, 2\tau_d)$ still depends on the filter $P(f)$. The optimum design of filter $P(f)$ is out of the scope of this paper, but the results of Section 7 and 8 indicate that the employed (ad-hoc) filters are not performance-limiting factors of the proposed estimators. The requirements on $P(f)$ and the used filter structure is further discussed in Appendix A. In the next sections we will show that the computational complexity of the proposed estimators can be reduced by squaring $\tilde{Z}_{in}(f)$ and $\tilde{Z}_0(f)$ in (11). The squaring-operation is only a minor modification that does not change the main results of the analysis presented above.

An analysis of the reflection pattern of the bandlimited $\tilde{Z}_{in}$ for a *multi-section* line reveals that the first reflection is determined completely and conclusively by the characteristic impedance of the *first* section. This is exemplified in Fig. 2 which illustrates how the (TDR) signal $P(f)\tilde{Z}_{in}(f) = P(f)H_{win}(f)Z_{in}(f)$ can be enhanced by subtracting $P(f)\tilde{Z}_0(f)$, *i.e.,* using the signal in (11). In Fig. 2 the 200 m splice is masked by the tail from the previous reflection and becomes visible (detectable), as seen in the inlay of the figure, due to the subtraction. For the purpose of illustration, the filter $P(f)$ is here a Butterworth low-pass filter of second-order. Obviously, the filter choice impacts the shape of the TDR response as discussed in Appendix A.

Fig. 2 thus demonstrates that the subtraction technique provides an almost perfect zero-response until the arrival of the first splice reflection at 200 m.

We emphasize that the benefit of subtracting the characteristic impedance of the first cable section is threefold: (a) it enables detection of weaker reflections, as also described in *e.g.* [3], (b) it provides an easier interpretation of the TDR response, and (c) the requirements on the test pulse spectrum, *i.e.* the TDR filter, is relaxed since the reflection at time zero is already removed and does therefore not interfere with other reflections.
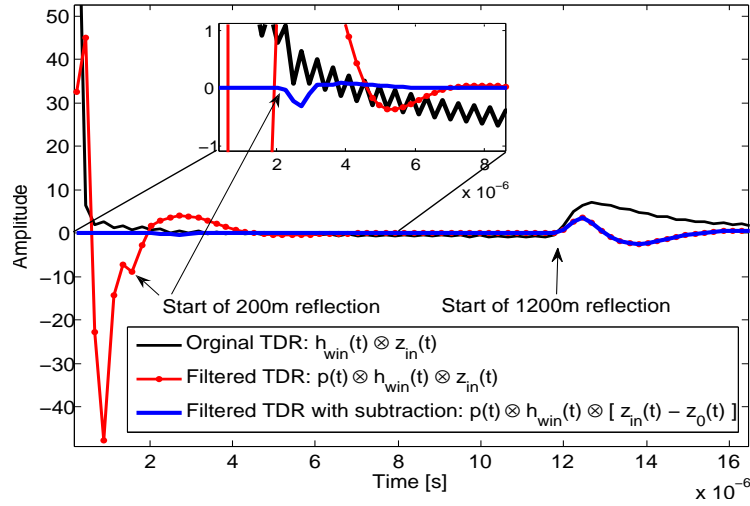
Figure 2: TDR response of a two-section line consisting of a 200 m 0.50 mm cable cascaded with a 1000 m 0.63 mm cable. A Butterworth low-pass filter of second-order is here employed to mitigate the high-frequency ripples of the signal. Subtraction of $z_0(t)$ allows for detection of the 200 m reflection.

4   Error Criteria

The rational behind the parameterized Z_0-estimators comes from (6), which shows that the observed signal $z_{in}(t)$ becomes zero in the time interval $[0, 2\tau_d)$ if $z_0(t)$ of the first section is subtracted from $z_{in}(t)$. In what follows we first review the state of the art estimator used for loop-makeup identification in [6,7]. Secondly, we formulate the proposed error criterion utilized by the new class of estimators.

It should be stressed that both the state of the art estimator and the new class minimize an error-signal in the time interval $[0, 2\tau_d)$. In practice, however, τ_d is unknown and a "step-forward" process is therefore proposed where an initial value of τ_d is first used in the error criteria. The initial value corresponds to the shortest considered (first) cable section. Unless the magnitude of the error criteria is satisfactory, the value of τ_d is increased and the error criteria is computed again in an iterative manner until the stop condition is reached. A natural stop condition is the dramatic increase in the error criteria occurring when τ_d exceeds the first section.

4.1   State of the Art

Consider the SELT system and the single-section line depicted in Fig. 1. Let $Z_{out}(f)$ denote the frequency-dependent output impedance of the SELT equipment, *i.e.,* the output impedance of the DSL transceiver. The estimator in [6, 7] essentially uses the following frequency-domain error signal

$$S(f, \boldsymbol{\theta}) = \frac{Z_{in}(f)}{Z_{in}(f) + Z_{out}(f)} - \frac{Z_0(f, \boldsymbol{\theta})}{Z_0(f, \boldsymbol{\theta}) + Z_{out}(f)}, \qquad (13)$$

where $Z_0(f, \boldsymbol{\theta})$ is a model of the characteristic impedance of the first cable section, and the parameter vector $\boldsymbol{\theta}$ is to be estimated. The corresponding time-domain error energy is minimized within the time interval $[0, 2\tau_d)$ which gives the error criteria

$$J(\boldsymbol{\theta}) = \sum_{n=0}^{\lfloor 2\tau_d/T_s \rfloor} \Big(\Re^2 \{ s(n, \boldsymbol{\theta}) \} + \Im^2 \{ s(n, \boldsymbol{\theta}) \} \Big), \qquad (14)$$

where n denotes discrete-time with sampling period T_s, and $s(n, \boldsymbol{\theta})$ is the inverse discrete-time Fourier transform of $S(f, \boldsymbol{\theta})$. Moreover, $\Re\{.\}$ and $\Im\{.\}$ denote the real and imaginary part of the argument, respectively.

The minimization of (14) requires, in general, multi-dimensional optimization when employing the cable models in *e.g.* [12], which typically leads to a nonlinear and non-convex optimization problem. The high complexity in minimizing (14) is partly avoided in [6, 7] by restricting $\boldsymbol{\theta}$ to a finite set of values stored in a cable data base. However, this requires up-to-date and accurate *a priori* information about the used cables.

4.2   Proposed Criterion

By returning to (6) and basing the error criterion on Z_{in}^2, the proposed criterion overcomes the high complexity in the minimization of (14). This further

leads to a class of unbiased estimators of low complexity when applying cable models of low order as described in Section 6.

More specifically, the proposed criterion utilizes the following frequency-domain error signal

$$E(f, \boldsymbol{\theta}) = Z_{in}(f)Z_{in}(f) - Z_0(f, \boldsymbol{\theta})Z_0(f, \boldsymbol{\theta}), \tag{15}$$

which is obtained by squaring Z_{in} and Z_0. As before, $Z_0(f, \boldsymbol{\theta})$ denotes the model of the characteristic impedance of the first cable section, where the parameter vector $\boldsymbol{\theta}$ is to be estimated. The purpose of squaring in (15) is to cancel the square-root of Z_0 defined for several cable models as will be explained in the next section. It follows from (3)–(5) that the time-domain transform of the error signal in (15) is zero in the time interval $[0, 2\tau_d]$ if $\boldsymbol{\theta}$ represents the true $Z_0(f)$ of the first cable section.

In order to define a time-domain criterion, the general filter $H(f) = P(f)H_{win}(f)$ is introduced with the same purpose as in Section 3. That is, filter $H_{win}(f)$ accounts for the limited measurement bandwidth and filter $P(f)$ provides the necessary band-limitation of the squared signals in (15), as discussed in Appendix A. The filtered error signal $\tilde{E}(f, \boldsymbol{\theta}) = H(f)E(f, \boldsymbol{\theta})$ yields

$$\tilde{E}(f, \boldsymbol{\theta}) = H(f)Z_{in}(f)Z_{in}(f) - H(f)Z_0(f, \boldsymbol{\theta})Z_0(f, \boldsymbol{\theta}). \tag{16}$$

The proposed time-domain error criterion minimizes the energy of the inverse discrete Fourier transform of (16) with respect to $\boldsymbol{\theta}$ within the time interval $[0, 2\tau_d)$, i.e.,

$$J(\boldsymbol{\theta}) = \sum_{n=0}^{\lfloor 2\tau_d/T_s \rfloor} \left| z_m(n) - h(n) \otimes z_0(n, \boldsymbol{\theta}) \otimes z_0(n, \boldsymbol{\theta}) \right|^2, \tag{17}$$

where $h(n)$ is the discrete-time response of $H(f)$ and $z_m(n) = h(n) \otimes z_{in}(n) \otimes z_{in}(n)$ is the filtered version of the observed signal, and $\otimes$ denotes the discrete-time convolution operator. The new class of estimators minimizes the error criterion in (17) where different models of the characteristic impedance provide a variety of estimators within the same class. To keep the complexity of the estimators low, a low-order and causal model of the characteristic impedance is required, which is the focus of the next section. We return to the minimization of (17) in Section 6 where the models derived in the next section are applied, which leads to the wanted class of low order and low complexity least squares (LS) estimators.

It should be emphasized that the error criterion in (17) is in principle independent of the filter choice $h(n)$, i.e., the design of $p(n)$, but the estimation performance is not.

5   Characteristic Impedance Modeling

In the literature, *e.g.* [12–19], several twisted-pair models have been derived and fitted to measurement data with the aim of modeling either the cable primary parameters, the secondary parameters, or the series line impedance and shunt admittance. The characteristic impedance Z_0 can be calculated from any of these models. Since the error criterion in (17) is defined in the time domain, it is important that the applied model is *causal*. The model should also be of low-order to reduce the complexity in the minimization of (17).

In the following we derive two types of models for the squared characteristic impedance, denoted *Model I* and *Model II*, based on the BT0$_H$ and VUB0 cable models in [19, 20], respectively. These two cable models fulfill our requirements of being causal and of low order. It is important to note here that the two different models applied in (17) lead to two slightly different estimators in Section 6, but still within the same class of estimators defined by the error criterion in (17). Furthermore, it is important to distinguish the set of parameters that defines the cable model(s) from the set of parameters that defines our model(s) of the (squared) characteristic impedance.

5.1   Model I

For the squared characteristic impedance modeling we consider the frequency dependent function

$$Z_0^2(f, \boldsymbol{\theta}) = Z_0(f, \boldsymbol{\theta}) Z_0(f, \boldsymbol{\theta}), \tag{18}$$

where $\boldsymbol{\theta}$ is the model parameter vector. The characteristic impedance is generally defined by its primary parameters according to [4]:

$$Z_0(f) = \sqrt{(R + j2\pi f L)/(G + j2\pi f C)}. \tag{19}$$

In [19] the series line resistance per unit length of the BT0$_H$ cable model is represented as

$$R(f) = R_0 Q(f, \nu), \tag{20}$$

where R_0 is a cable dependent parameter and Q is a known function of both frequency f and parameter ν. The series line inductance per unit length is modeled in [19] as

$$L(f) = \frac{R_0}{2\pi f} \Lambda(f, \nu) + L_\infty^{(H)}, \tag{21}$$

where $\Lambda(f, \nu)$ is the Hilbert transform of $Q(f, \nu)$ and $L_\infty^{(H)}$ is another parameter of the BT0$_H$ cable model. For the shunt admittance, the line capacitance

per unit length is $C(f) = C_\infty$ which is constant with frequency, and the line conductance per unit length $G(f)$ is modeled as zero, *i.e., G(f)* is neglected. In summary, the BT0$_\mathrm{H}$ cable model consists of the four cable-dependent parameters $R_0, \nu, L_\infty^{(H)}$ and $C_\infty^{(H)}$ [19].

By substituting (19)–(21) in (18), we get with $C(f) = C_\infty^{(H)}$ and $G(f) = 0$:

$$Z_0^2(f, \boldsymbol{\theta}) = \frac{R_0 Q(f, \nu) + j2\pi f(\frac{R_0}{2\pi f}\Lambda(f, \nu) + L_\infty^{(H)})}{j2\pi f C_\infty^{(H)}}. \tag{22}$$

The expression above can be further simplified by introducing the two parameters $\alpha_1 = \frac{R_0}{C_\infty^{(H)}}$ and $\alpha_2 = \frac{L_\infty^{(H)}}{C_\infty^{(H)}}$. After some straightforward manipulations, (22) yields

$$Z_0^2(f, \boldsymbol{\theta}) = \alpha_1 (\frac{Q(f, \nu)}{j2\pi f} + \frac{\Lambda(f, \nu)}{2\pi f}) + \alpha_2 = \alpha_1 \Phi(f, \nu) + \alpha_2, \tag{23}$$

where we have introduced the function

$$\Phi(f, \nu) = \frac{Q(f, \nu)}{j2\pi f} + \frac{\Lambda(f, \nu)}{2\pi f}. \tag{24}$$

Thus, for *Model I* the squared characteristic impedance is represented by (23) with parameter vector $\boldsymbol{\theta}_{BT0_H} = [\nu\ \alpha_1\ \alpha_2\ ]^T$, where the subscript denotes the cable model it is based on. The introduced parameters give the following relations

$$\begin{aligned} R_0/C_\infty^{(H)} &= \alpha_1 \\ L_\infty^{(H)}/C_\infty^{(H)} &= \alpha_2, \end{aligned} \tag{25}$$

which connects the BT0$_\mathrm{H}$ *cable model* parameters with the parameters of the *characteristic impedance model.*

5.2   Model II

Another model of the squared characteristic impedance can be derived from the model adapted for twisted-pair cables in [15], referred to as VUB0 in [20] (but with slightly different definitions of parameter a_1 and a_4). In order to get a distance-independent model, the parameter a_1 is here normalized with the squared cable length, that is, we set $\tilde{a}_1 = a_1/d^2$. Hence, the squared

(normalized) characteristic impedance can be expressed as

$$
\begin{aligned}
Z_0^2(f, \boldsymbol{\theta}) &= \frac{\gamma^2(f)}{(j2\pi f C_\infty)^2} \\
&= \frac{a_4}{C_\infty^2} + \frac{\tilde{a}_1}{C_\infty^2} \left(\frac{\sqrt{-j2\pi f}}{j2\pi f} \frac{J_0}{J_1} + \frac{a_3}{2} \Psi(f, a_2, a_3) \right) \\
&= \beta_1 \Theta(f, \boldsymbol{\xi}) + \beta_2,
\end{aligned}
\tag{26}
$$

where the notation is borrowed from [15] with the addition of $\beta_1 = \tilde{a}_1/C_\infty^2$ and $\beta_2 = a_4/C_\infty^2$. Furthermore, C_∞ is the capacitance per unit length, assumed constant with frequency, and $\Theta(f, \boldsymbol{\xi})$ is a known function of both frequency and the vector $\boldsymbol{\xi} = [\xi_1\ \xi_2\ ]^T$. Thus, for *Model II* the squared characteristic impedance is represented by (26) with parameter vector $\boldsymbol{\theta}_{VUB0} = [\beta_1\ \beta_2\ \xi_1\ \xi_2\ ]^T$.

It should be noted that the normalized VUB0 cable model is parameterized by $\tilde{a}_1, a_2, a_3, a_4$, and that these *cable parameters* are in turn dependent on the electromagnetic and geometric properties of the cable [15]. More specifically, with the notation used in [15] and [20], these electromagnetic and geometric parameters are: $a, D, \sigma, \mu, C_\infty$. It follows straightforwardly from (26) and [15] that the relation between the *cable parameters* and the parameters of $\boldsymbol{\theta}_{VUB0}$ are:

$$
\begin{aligned}
\tilde{a}_1 &= \beta_1 C_\infty^2 = \frac{C_\infty}{a\pi} \sqrt{\mu/\sigma} \\
a_2 &= \xi_1 = (a/D)^2 \\
a_3 &= \xi_2 = a\sqrt{\mu\sigma} \\
a_4 &= \beta_2 C_\infty^2 = \tilde{a}_1 a_3 \ln(1/\sqrt{a_2}).
\end{aligned}
\tag{27}
$$

It is worth pointing out that *Model II* defined by (26) can be seen as a general model. That is, the squared characteristic impedance can also be based on *e.g.* the MAR2 cable model in [16] whereupon one can show that the squared characteristic impedance can be described with the same structure as in (26), but with a different expression for the cable dependent function $\Theta(f, \boldsymbol{\xi})$.

6   Least Squares Estimator

We now return to the minimization of the error criterion in (17) and apply *Model I* and *Model II* of the previous section. This leads to two different low-complexity least squares (LS) Z_0-estimators denoted *Estimator I* and *Estimator II*. Lower-case and upper-case boldfaced letters are used in the following to denote vectors and matrices, respectively.

6.1   Estimator I

From (16) we note that the frequency-domain signals are filtered by $H(f)$. With this filter included, *Model I* in (23) becomes

$$H(f)Z_0^2(f, \boldsymbol{\theta}_{BT0_H}) = \alpha_1 H(f)\Phi(f, \nu) + \alpha_2 H(f). \tag{28}$$

By introducing $\psi(n, \nu) = h(n) \otimes \phi(n, \nu)$ where $h(n)$ and $\phi(n, \nu)$ are the discrete-time transforms of $H(f)$ and $\Phi(f, \nu)$, respectively, the inverse discrete-time Fourier transform of (28) gives us the desired time-domain filtered model of the squared characteristic impedance, *i.e.,*

$$h(n) \otimes z_0(n, \boldsymbol{\theta}_{BT0_H}) \otimes z_0(n, \boldsymbol{\theta}_{BT0_H}) = \alpha_1 \psi(n, \nu) + \alpha_2 h(n), \tag{29}$$

where $\otimes$ denotes the discrete-time convolution operator. Substituting (29) in (17) then yields the error criterion to be minimized as

$$J(\nu, \alpha_1, \alpha_2) = \sum_{n=0}^{\lfloor 2\tau_d/T_s \rfloor} \left| z_m(n) - \alpha_1 \psi(n, \nu) - \alpha_2 h(n) \right|^2, \tag{30}$$

where $z_m(n) = h(n) \otimes z_{in}(n) \otimes z_{in}(n)$.

With vector notation, equation (30) can be expressed as

$$J(\nu, \alpha_1, \alpha_2) = (\boldsymbol{r} - \boldsymbol{A}(\nu)\boldsymbol{\alpha})^T (\boldsymbol{r} - \boldsymbol{A}(\nu)\boldsymbol{\alpha}), \tag{31}$$

where

$$\begin{aligned}
\boldsymbol{r} &= [z_m(0) \ z_m(1) \ \cdots \ z_m(\lfloor 2\tau_d/T_s \rfloor)]^T \\
\boldsymbol{A}(\nu) &= \begin{bmatrix} \psi(0, \nu) & h(0) \\ \vdots & \vdots \\ \psi(\lfloor 2\tau_d/T_s \rfloor, \nu) & h(\lfloor 2\tau_d/T_s \rfloor) \end{bmatrix} \\
\boldsymbol{\alpha} &= [\alpha_1 \ \alpha_2]^T.
\end{aligned}$$

The minimization of $J(\nu, \alpha_1, \alpha_2)$ constitutes a linear LS problem for a fixed value of parameter ν, that is,

$$\boldsymbol{\alpha}(\nu) = \left[\Re \left\{ \boldsymbol{A}(\nu)^H \boldsymbol{A}(\nu) \right\} \right]^{-1} \Re \left\{ \boldsymbol{A}(\nu)^H \boldsymbol{r} \right\}, \tag{32}$$

where ^{H} denotes conjugate transpose.

Without loss of generality it will be assumed, for simplicity, that matrix $\boldsymbol{A}$ and vector $\boldsymbol{r}$ are real valued. The complex case can be handled similarly by introducing the real-operator $\Re\{\}$ as above. By fixing parameter ν,

the problem has been reduced to one dimension, which can easily be solved with low complexity. For example, parameter ν can be set to span the region from ν_{min} to ν_{max} and the solution that yields the minimum value of $J(\nu, \alpha_1(\nu), \alpha_2(\nu))$ in (31) can be selected. In general this non-linear LS problem can be formulated and solved as follows

$$\nu_{LS} = \arg \min_{\nu} \; J(\nu, \alpha_1(\nu), \alpha_2(\nu)), \tag{33}$$

where ν_{LS} is used to calculate the linear LS solution

$$\boldsymbol{\alpha}_{LS} = \left[\boldsymbol{A}(\nu_{LS})^T \boldsymbol{A}(\nu_{LS}) \right]^{-1} \boldsymbol{A}(\nu_{LS})^T \boldsymbol{r}. \tag{34}$$

To summarize, *Estimator I* provides a solution to (17) by applying *Model I*. The resulting LS solution in (33)–(34) is computed and the output of *Estimator I* is the parameter vector $\boldsymbol{\theta}_{BT0_H} = [\nu \; \alpha_1 \; \alpha_2 \;]^T$, which together with (23) gives the estimated (squared) characteristic impedance.

6.2   Estimator II

In line with the steps taken to derive *Estimator I* we here apply *Model II* of (26) in (17). By introducing the time-domain function $\tilde{\psi}(n, \boldsymbol{\xi}) = h(n) \otimes \vartheta(n, \boldsymbol{\xi})$, where $\vartheta(n, \boldsymbol{\xi})$ is the inverse Fourier transform of $\Theta(f, \boldsymbol{\xi})$, we can write the error criterion to be minimized in (17) as

$$J(\boldsymbol{\xi}, \beta_1, \beta_2) = \sum_{n=0}^{\lfloor 2\tau_d/T_s \rfloor} \left| z_m(n) - \beta_1 \tilde{\psi}(n, \boldsymbol{\xi}) - \beta_2 h(n) \right|^2. \tag{35}$$

Applying the same analysis as for *Estimator I*, we obtain the following LS solution

$$\boldsymbol{\xi}_{LS} = \arg \min_{\boldsymbol{\xi}} \; J(\boldsymbol{\xi}, \beta_1(\boldsymbol{\xi}), \beta_2(\boldsymbol{\xi})), \tag{36}$$

which is used to calculate

$$\boldsymbol{\beta}_{LS} = \left[\boldsymbol{B}(\boldsymbol{\xi}_{LS})^T \boldsymbol{B}(\boldsymbol{\xi}_{LS}) \right]^{-1} \boldsymbol{B}(\boldsymbol{\xi}_{LS})^T \boldsymbol{r} \tag{37}$$

where

$$\boldsymbol{B}(\boldsymbol{\xi}) = \begin{bmatrix} \tilde{\psi}(0, \boldsymbol{\xi}) & h(0) \\ \vdots & \vdots \\ \tilde{\psi}(\lfloor 2\tau_d/T_s \rfloor, \boldsymbol{\xi}) & h(\lfloor 2\tau_d/T_s \rfloor) \end{bmatrix}$$

$$\boldsymbol{\beta} = [\beta_1 \; \beta_2]^T.$$

The minimization of (36) is in this case carried out over two dimensions instead of just one. However, this is still a low-complexity operation compared to the multi-dimensional nonlinear optimization required in (14).

Thus, *Estimator II* solves (17) by applying *Model II* which leads to the LS solution formulated in (36)–(37). The output of *Estimator II* is the parameter vector $\boldsymbol{\theta}_{VUB0} = [\beta_1\ \beta_2\ \xi_1\ \xi_2\ ]^T$, which together with (26) provides the estimated (squared) characteristic impedance.

7   Computer Simulations

This section presents performance results of *Estimator I* and *Estimator II* on simulated twisted-pair cables.

7.1   Setup

For all cases, 512 frequency points are simulated between $4.3125\,\text{kHz}$ and $2.208\,\text{MHz}$ which corresponds to the ADSL2+ bandwidth and carrier spacing [2]. A sampling frequency of $4.4\,\text{MHz}$ is used for the time-domain processing. All conversions from frequency domain to time domain are implemented as inverse fast Fourier transforms (IFFTs) with Hermitian extension to obtain real-valued time-domain signals. A filter with the z-transform $P(z) = (1+z^{-1})^M(1-z^{-1})^N$ is used to filter the measurement points, where the design parameters $\{M, N\}$ are integer values set to $\{4, 9\}$ and $\{10, 30\}$ for *Estimator I* and *Estimator II*, respectively. These values were found empirically and provide a satisfying trade-off between mitigation of the non-causal behavior and a short pulse-duration, as discussed in Section 3 and Appendix A. For the criterion calculation in (30) and (35) a summation interval of $[0, 1.3\tau_d/T_s]$ is used, which provides an additional margin until the arrival of the first far-end reflection, where τ_d is the single-way line delay of the cable. The cables are simulated using the models listed in Table 6 in Appendix B.

7.2   Performance Measure

As performance measures we consider the relative error of the estimated parameters, and a signal reduction measure (SRM) of the reflection occurring in the summation interval, *i.e.,* the reduction of the SDS. We define the SRM for *Estimator I* and *Estimator II* as the ratio of the residual estimation error and the error criterion without any model, *i.e.,*

$$SRM_1 = J(\nu, \alpha_1, \alpha_2)/J(0, 0, 0) \tag{38}$$

$$SRM_2 = J(\boldsymbol{\xi}, \beta_1, \beta_2)/J(\mathbf{0}, 0, 0), \tag{39}$$

respectively. For the calculation of the SRM, the summation interval in (30) and (35) is set to $[0, 1.6\tau_d/T_s]$, *i.e.* 80 % of the roundtrip line delay. In some of the figures we include a comparison with the *average* $Z_0(f)$ defined as the arithmetic mean value of BT0$_H$ cable type 0.32 mm, 0.40 mm and 0.50 mm, which would be likely candidates for the first cable section.

7.3   Estimation Results

In order to evaluate *Estimator I*, the true $\boldsymbol{\theta}_{BT0_H} = [\nu \ \alpha_1 \ \alpha_2]^T$ is calculated based on the BT0$_H$ cable model via (25) and a comparison with the estimated parameters are conducted. In Table 1 the so obtained relative estimation errors are listed. From Table 1 we conclude that *Estimator I* is able to accurately estimate the model parameters and the characteristic impedance, where the latter is further manifested by Fig. 3. The estimation errors are dominated by numerical algorithm limitations and numerical round-off errors.

Table 1: Estimation results for *ESTIMATOR I* on simulated BT0$_H$ cables.

Length [km]	Diameter [mm]	Rel. error α_1, α_2 [%]	Rel. error ν [%]	SRM_1 [dB]
0.5	0.32	-9.3E-7, -9.5E-8	4.3E-6	141
1.0	0.40	-7.9E-8, -5.8E-9	3.5E-7	192
1.0	0.50	-6.5E-8, -1.3E-9	2.7E-7	202
1.0	0.63	-6.4E-8 -5.3E-10	2.6E-7	160
1.0	0.90	6.1E-6, 8.6E-9	-2.5E-5	138

For all the simulated cases, the criterion function of *Estimator I* is convex and contains only one sharp deep global optimum, as depicted in Fig. 4. This results in less stringent requirements for the optimization algorithm. The estimation becomes less accurate for shorter cables as shown in Table 2. However, by increasing the measurement bandwidth, and hence the sampling frequency, the accuracy can be improved for shorter cables. For instance, by increasing the bandwidth by a factor of two, while still using 512 measurement points, a reduction of the relative estimation error by a factor of 100 is obtained for the 0.15 km case (not shown in Table 2).

Table 2: Length-dependence of *ESTIMATOR I* on simulated BT0$_\mathrm{H}$ cables.

Length [km]	Diameter [mm]	Rel. error α_1, α_2 [%]	Rel. error ν [%]	SRM_1 [dB]
0.15	0.40	4.8E-1, 3.7E-2	-2.6	73
0.30	0.40	1.2E-4, 1.6E-5	-6.1E-4	115
0.50	0.40	-1.9E-6, -1.5E-7	8.6E-6	133
3.00	0.40	-7.9E-8, -5.8E-9	3.5E-7	215
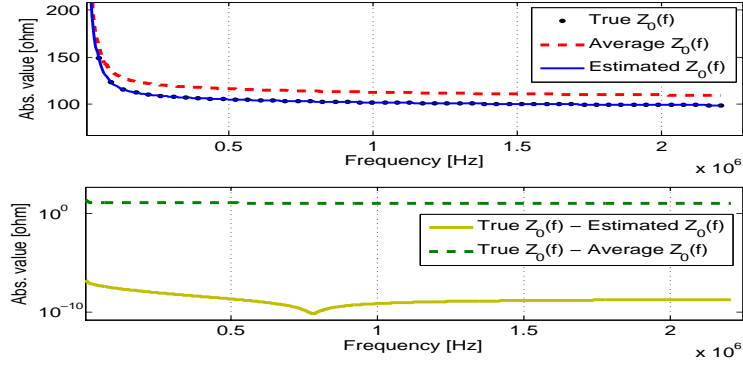
Figure 3: Characteristic impedance estimation for *Estimator I* with 1 km 0.40 mm BT0$_\mathrm{H}$ cable model.
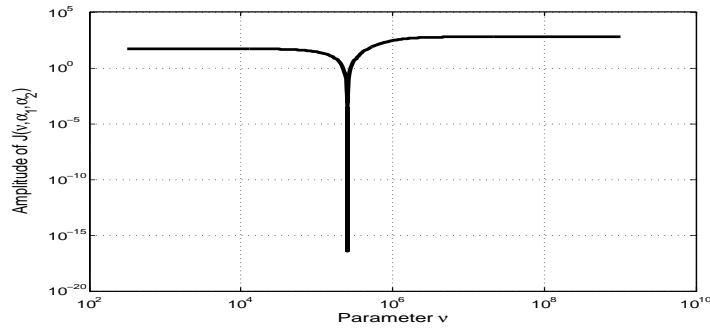
Figure 4: Criterion function for *Estimator I* with 1km 0.4mm BT0$_\mathrm{H}$ cable.

To evaluate the sensitivity to measurement noise, $Z_{in}(f)$ is here disturbed with additive white Gaussian noise (AWGN). That is, for each frequency point f_x we form

$$Z_{in}^{dist}(f_x) = Z_{in}(f_x) + W(f_x),$$

where

$$W(f_x) = W_{re}(f_x) + jW_{im}(f_x),$$

and

$$W_{re}(f_x), W_{im}(f_x) \text{ are independent } \mathcal{N}(0, \sigma^2).$$

Table 3 shows the statistical mean results of a Monte Carlo simulation for *Estimator I*. As expected, the mean SRM decreases as the noise variance is increased. It can be noted by comparing the results of Table 3 with Table 1 that the results are now limited by the added noise rather than numerical algorithm limitations or numerical round-off errors.

For *Estimator II* the true vector $\boldsymbol{\theta}_{VUB0} = [\beta_1 \ \beta_2 \ \xi_1 \ \xi_2]^T$ is calculated based on the corresponding normalized VUB0 cable model via (27), and the evaluation is conducted by comparing with the estimated parameters. The so obtained relative estimation errors are listed in Table 4. The results in Table 4 demonstrate that *Estimator II* is able to accurately estimate the model parameters and the characteristic impedance of the different cables. The two-dimensional *inverse* criterion function is depicted in Fig. 5 for the 1 km 0.40 mm VUB0 cable case. The global optimum is clearly visible as the highest peak, as is also one of the present local optima.

Table 3: Estimation results for *ESTIMATOR I* with AWGN on a simulated BT0$_H$ cable of length 1 km.

Diameter [mm]	AWGN σ^2	Mean error α_1, α_2 [%]	Mean error ν [%]	Mean SRM_1 [dB]
0.40	1E-5	1.1E-2, 1.0E-3	4.8E-2	97
0.40	1E-4	3.7E-2, 4.0E-3	1.7E-1	87
0.40	1E-3	1.2E-1, 1.2E-2	5.4E-1	77
0.40	1E-2	3.7E-1, 4.1E-2	1.7	67

Table 4: Estimation results for *ESTIMATOR II* on simulated VUB0 cables with length 1 km.

Diameter [mm]	Rel. error β_1, β_2 [%]	Rel. error ξ_1, ξ_2 [%]	SRM_2 [dB]
0.40	-1.3E-8, 4.8E-9	1.4E-7, -1.0E-8	252
0.50	1.6E-8, -4.9E-9	-1.4E-7, 2.6E-8	241
0.63	1.9E-8, -4.9E-9	-1.9E-7, 3.7E-8	244
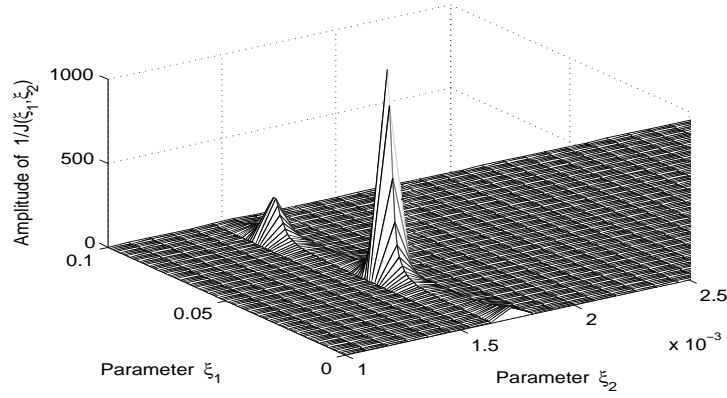
Figure 5: Inverse criterion function for *Estimator II* with the 1 km 0.40 mm VUB0 cable model.

8 Laboratory Measurements

In this section, we investigate the performance of *Estimator I* for real twisted-pair cables. It turns out that the corresponding performance of *Estimator II* is similar and is therefore omitted.

8.1 Setup

The same setup as in Section 7 is used, but with the line input impedance measured with an HP4192A impedance analyzer. The cables were rolled up on drums and have the properties listed in Table 5.

Table 5: Laboratory twisted-pair cables.

Cable	Identity	Length [km]	Wire diameter [mm]
C4	ELALE, TEL, 3100115/0010	0.45	0.50
C8	EULEV, THE, 2401402/010	0.50	0.40
C14	EULEV, THE, 2401402/010	0.20	0.40

8.2　Characteristic Impedance Estimation

For evaluation purposes the characteristic impedances of the cables are calculated from conventional *open-end* and *short-circuited* termination measurements (see *e.g.* [4]). The estimation results for cable C4 and C8 are shown in Fig. 6 to Fig. 9. In order to compare with the *a priori* data base approach in [6, 7], we select the cable in Table 6 that yields the best least squares fit of $Z_0(f)$ to the measurement data. In this way, the 0.90 mm cable was selected for the measurement on C4 and the 0.32 mm cable was selected for C8. From the results of Fig. 6 to Fig. 9 we conclude that the estimated $Z_0(f)$ yields a lower estimation error than the average Z_0 and the selected data base cable. The cable data base is in this case limited, but the selected 0.90 mm cable in Fig. 6 still provides a close match to the measurement data. However, the line resistance of the 0.90 mm cable is much lower than the line resistance of the real 0.40 mm cable used in the test. This indicates that the line inductance and/or capacitance of the data base cable compensates for the resistance mismatch, resulting in an overall close match.

From Fig. 6 to Fig. 9 it can also be observed that the measured characteristic impedance contains significant ripples along the frequency axis. One further concludes that the shape of these ripples will not be possible to capture with the characteristic impedance models applied in this paper, or likely any of the models in *e.g.* [12]. Despite this drawback, the absolute error is for most frequencies lower than 5 Ω. More importantly, the TDR (band-pass) filter will suppress the low and high frequencies where the error is largest. As another reference for comparison we consider [17] where the characteristic impedance was measured and the parameters of an applied *rational function* identified. The maximum approximation errors were in this case in the order of $2 - 5\,\Omega$. As stated in [17], rational functions are: *flexible and accurate but not well suited if inherent cable behavior is required as for*
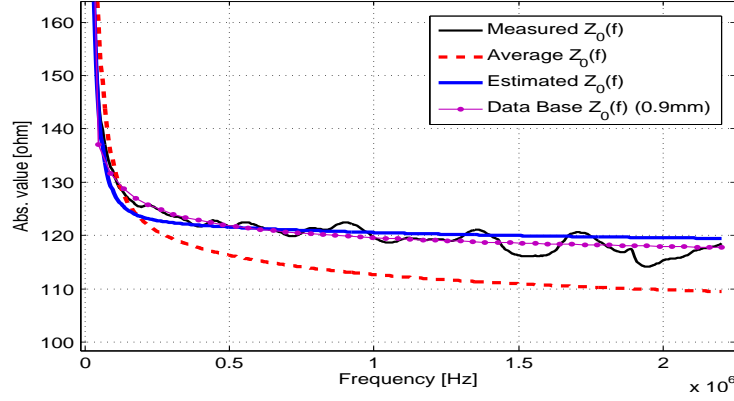
Figure 6: Measured and estimated characteristic impedance for cable C4.
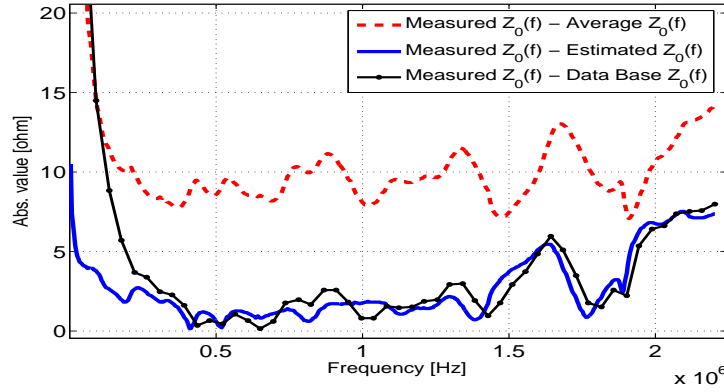
Figure 7: Estimation error of the characteristic impedance for cable C4.

SELT application. Thus, we remark that our low-complexity LS SELT estimator targets another goal than the model identification in [17]. In other words, our estimated parameters are part of a physical cable model, and hence should be more suitable for *e.g.* frequency extrapolation and estimation of the transfer function or other related quantities. In fact, there is no guarantee that a flexible rational function model, applied in the approach of this paper, will behave physically outside the limited criterion region.

The estimated Z_0 for cable C4 and C8 give a SRM_1 of $44\,\mathrm{dB}$ and $38\,\mathrm{dB}$,
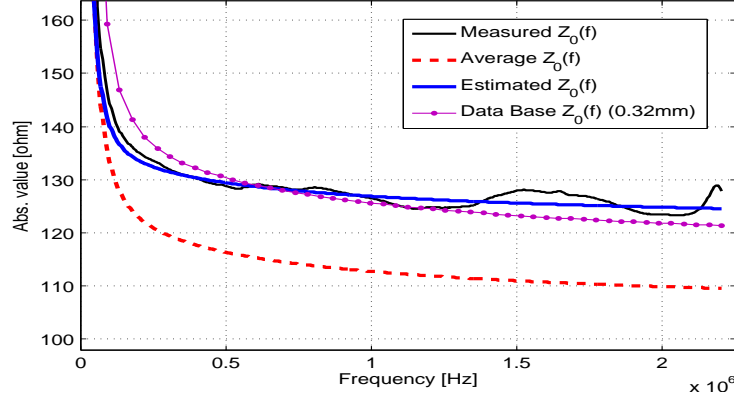
Figure 8: Measured and estimated characteristic impedance for cable C8.
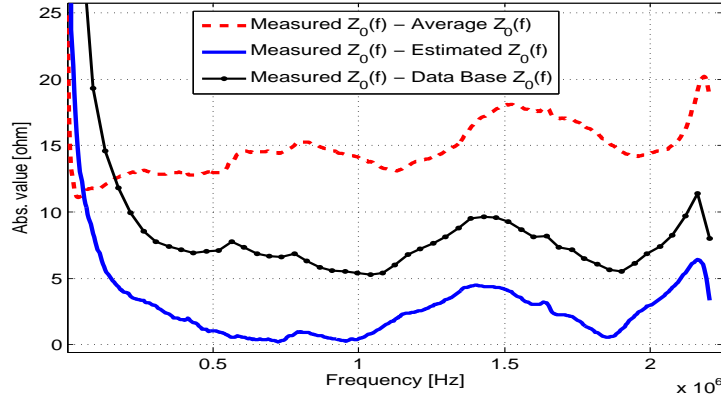
Figure 9: Estimation error of the characteristic impedance for cable C8.

which should be compared to the measured Z_0 having a SRM_1 of 56 dB and 71 dB, respectively. Given that the measured Z_0 on both C4 and C8 contains significant ripples, and has low SRM compared to the simulated cables, it is reasonable to assume that the estimation errors are dominated by model errors that are much larger than the measurement errors. In fact, our measurements of Z_0 on very short cables, *e.g.* 10 m, give no, or very little frequency domain ripples. This further indicates that the cables are nonhomogeneous along the line, as also pointed out in [17]. This phenomena

occurring on nonhomogeneous cables are also described in [21], where it is referred to as *structural effects*.

Finally, it is worth mentioning that the performance of *Estimator II* on cable C4, C8, and C14 is similar to that of *Estimator I*.

8.3   TDR Enhancement

As an additional performance comparison, Fig. 10 shows the TDR enhancement of *Estimator I* when applied on a two-section line where the results of subtracting the average and the estimated Z_0 are depicted. That is, the figure shows $z_m(n) - h(n) \otimes z_0(n) \otimes z_0(n)$ for the three cases: with no information of Z_0 (original TDR), with average cable data base Z_0, and with estimated Z_0. The two-section line consists of cable C14 and C4 in cascade. From Fig. 10 we observe that the splice reflection at 200 m, *i.e.,* the negative peak, becomes easier to detect with the proposed estimator since the reflection is not being confused with the strong ringing originating from time zero. Furthermore, the solid blue line indicates that no more splice points are present in the first 200 m of the line.

Figure 10: Original TDR signal on a two-section line consisting of cable C14 cascaded with C4 (200 m and 450 m), and the enhancement obtained when subtracting the average Z_0 and *Estimator I* obtained Z_0.

9   Discussion and Conclusions

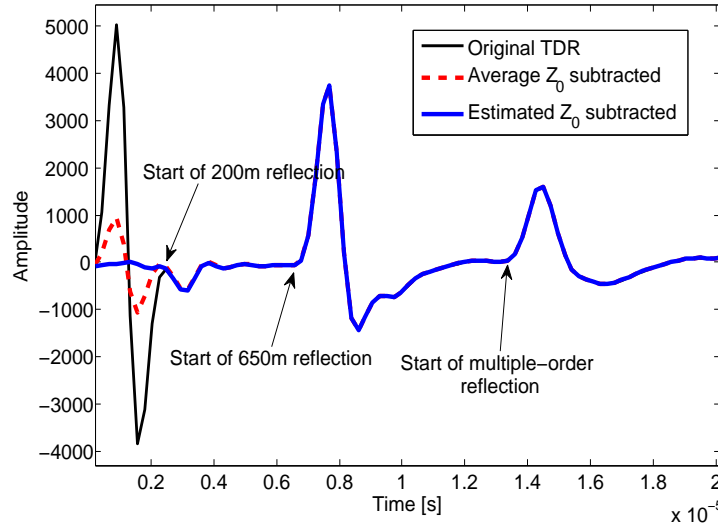This paper deals with estimation of the characteristic impedance based on data obtained from SELT measurements only. State of the art estimators assume either *a priori* information in an accurate cable data base, or an infinitely long cable. The latter assumption results in a systematic model error, *i.e.,* the estimator is biased, unless the line is (infinitely) long. Both prior art approaches require a computationally complex nonlinear and non-convex multi-dimensional optimization. By instead basing the estimator on the squared line input impedance, and applying low-order and causal cable modeling, a class of low-complexity least squares (LS) estimators is derived that involve only a one- or two-dimensional grid search and a linear LS solver.

The simulation results show that both *Estimator I* and *II* are able to accurately estimate the sought parameters and hence the twisted-pair characteristic impedance. Laboratory measurements on twisted-pair cables show that the characteristic impedance contains ripples along the frequency axis due to inhomogeneities in the cable, which the applied models are not able to capture. Consequently, the estimation results obtained with real measurements were somewhat degraded compared to using simulated data due to model errors. Nonetheless, significant TDR enhancement was achieved by subtracting the estimated (squared) characteristic impedance leading to reduced interference from the reflection at the measurement plane, in addition to improved detection of weak reflections. The enhancement also allows a straightforward interpretation of the TDR response for both a naked eye and for an automatic interpreting system.

Moreover, the described estimators can also be used in the identification of a multi-section line according to the principles in [6, 7] but now without *a priori* information. Thereto, the estimators can be applied in an iterative estimation procedure where the measurement plane of a multi-section line is virtually moved closer and closer to the far-end as disclosed in [22].

Appendix A

The proposed estimators are based on squaring $\tilde{Z}_{in}(f)$ and $\tilde{Z}_0(f)$ in (11), and applying the filter $P(f)$, which gives the frequency domain signal

$$\tilde{E}(f) = P(f)\Big(\tilde{Z}_{in}^2(f) - \tilde{Z}_0^2(f)\Big),$$

where $\tilde{Z}_{in}(f)$ and $\tilde{Z}_0(f)$ are the bandlimited input impedance and the characteristic impedance of the line, respectively, defined in Section 3.
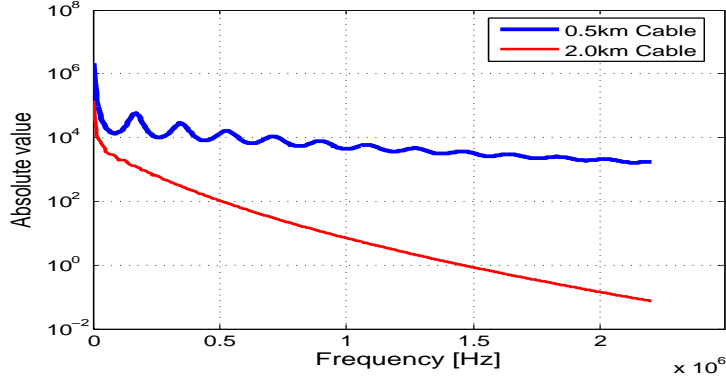
Figure 11: Frequency domain signal $\tilde{E}(f)$ for two twisted-pair cables of length $0.5\,\text{km}$ and $2.0\,\text{km}$, respectively.

Fig. 11 shows $\tilde{E}(f)$ with $P(f) = 1$, *i.e.,* without filtering, for a typical twisted-pair cable of length $0.5\,\text{km}$ and $2\,\text{km}$. From this figure it is clear that the dynamic range of $\tilde{E}(f)$ can be large if $P(f) = 1$. That is, at low frequencies the amplitude of $\tilde{Z}_{in}^2(f) - \tilde{Z}_0^2(f)$ reaches high values while at high frequencies the amplitude tends to level out at a lower value. Since this signal is to be used in the time domain criterion defined by (17), filter $P(f)$ is required to bandlimit the signal before applying the inverse Fourier transform. In the following we denote the inverse Fourier transform of $\tilde{E}(f)$ with $\tilde{e}(t)$. We further assume in this appendix that $\tilde{Z}_0^2(f)$ is known. The design of filter $P(f)$ has two main requirements: (a) provide a zero-response of $\tilde{e}(t)$ for time $t \in [0, 2\tau_d)$, and (b) provide an impulse response $p(t)$ that is shorter than the shortest considered first cable section.

To meet these requirements, we choose an (ad-hoc) filter structure with the z-transform $P(z) = (1 + z^{-1})^M (1 - z^{-1})^N$, where $\{M, N\}$ are integer-valued filter design parameters. Fig. 12 depicts the frequency response of this filter for three different settings of $\{M, N\}$, *i.e.,* with $\{1, 1\}$, $\{2, 2\}$ and $\{5, 5\}$ for Filter I, II and III, respectively. The time domain signal $\tilde{e}(t)$ for the three different filters are shown in Fig. 13 and Fig. 14, in linear and logarithmic amplitude-scale, for a typical twisted-pair cable of length $0.5\,\text{km}$.

From Fig. 12, Fig. 13 and Fig. 14, it can be observed that a higher-order filter gives an increased attenuation of the lower and higher frequencies, as expected, leading to more band-limitation of the signal $\tilde{E}(f)$. As a consequence, the mitigation of the non-causal effect of $\tilde{e}(t)$, caused by the ban-
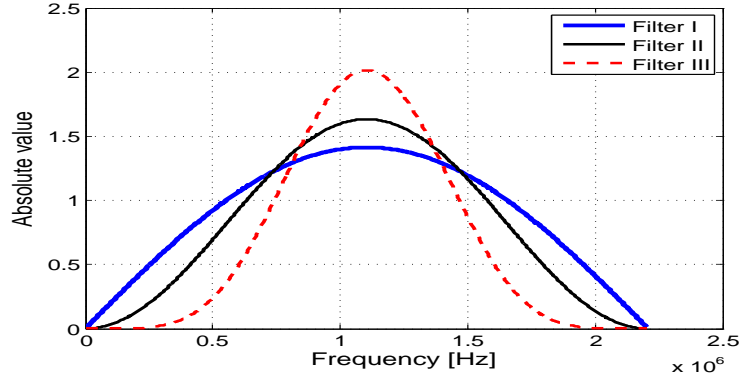
Figure 12: Frequency response of $P(z) = (1 + z^{-1})^M (1 - z^{-1})^N$ for different sets of $\{M, N\}$ for Filter I, II and III, respectively.
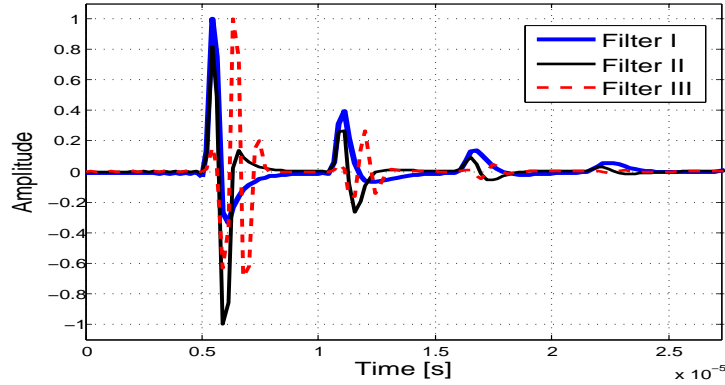
Figure 13: Time domain signal $\tilde{e}(t)$, in linear amplitude-scale, with Filter I, II and III for a twisted-pair cable of length $0.5\,\mathrm{km}$.

dlimited measurements, is improved for higher filter-orders. The latter is especially visible in Fig. 14 where a more bandlimited $\tilde{E}(f)$ provides a more attenuated signal $\tilde{e}(t)$ for time $t \in \left[0, 5 \cdot 10^{-6}\right)$ s. Here, $5 \cdot 10^{-6}$ corresponds (approximately) to the round-trip time, in seconds, for the far-end reflection. However, the higher-order filter also gives a longer impulse response which increases the risk of interference with the second reflection, $e.g.$ from the sec-
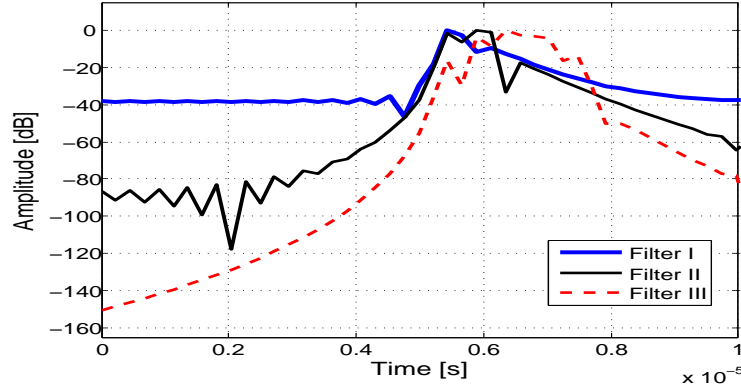
Figure 14: Time domain signal $|\tilde{e}(t)|$ with Filter I, II and III, in logarithmic amplitude-scale, for a twisted-pair cable of length $0.5\,\text{km}$.

ond cable-section (if any), when performing the filtering. Thus, there exist a trade-off between mitigating the non-causal behavior of $\tilde{e}(t)$ and avoiding a too long filter impulse response.

Appendix B

This appendix defines the electromagnetic and geometrical parameters of the cable models used for performance evaluation of *Estimator I* and *Estimator II*. For the BT0$_\text{H}$ model [19], the ETSI parameters defined in [18] are employed, but with the inductance modeled according to the BT0$_\text{H}$ model in order to avoid non-causal behavior. For the normalized VUB0 model, described in Section 5, the $0.5\,\text{mm}$ cable type has parameters taken from [20], while the other cable types contain fictive values. In Table 6, the elementary constants have the values $\epsilon_0 = \frac{10^{-9}}{36\pi}$ F/m and $\mu_0 = 4\pi 10^{-7}$ H/m. The listed units of $R_0, \nu, L_\infty^{(H)}$, and $C_\infty^{(H)}$ are $\Omega/\text{km}, \text{Hz}, \mu\text{H/km}$, and nF/km, respectively. Parameters a and D are both in mm, and σ is expressed in S/m.

Table 6: Electromagnetic and geometric parameters of simulated cables.

Diameter [mm]	BT0$_{\mathrm{H}}$ $R_0, \nu, L_\infty^{(H)}, C_\infty^{(H)}$	Normalized VUB0 $a, D, \sigma, \epsilon, \mu, C_\infty$
0.32	$409, 2.71 \cdot 10^5,$ $582.6, 40$	–
0.40	$280, 2.52 \cdot 10^5,$ $484.7, 50$	$0.19, 0.8, 5.6938 \cdot 10^7,$ $0.226\epsilon_0, \mu_0, 50$
0.50	$179.2, 1.36 \cdot 10^5,$ $584.5, 50$	$0.25, 1, 5.81 \cdot 10^7,$ $2.26\epsilon_0, \mu_0, 50$
0.63	$113, 7.97 \cdot 10^4,$ $520.0, 45$	$0.28, 1.05, 5.9262 \cdot 10^7,$ $2.486\epsilon_0, \mu_0, 45$
0.90	$55.1, 3.13 \cdot 10^4,$ $553.9, 40$	–

References

[1] P. Ödling, B. Mayr, and S. Palm, "The technical impact of the un-bundling process and regulatory action," *ComMag*, vol. 38, No. 5, pp. 74–80, May 2000.

[2] ITU-T G.992.3, "Asymmetric digital subscriber line transceivers 2 (adsl2)," 07/2002.

[3] S. Galli and D.L. Waring, "Loop makeup identification via single ended testing: beyond mere loop qualification," *IEEE Journal of Selected Areas in Communications*, vol. 20, No. 5, pp. 923–935, June 2002.

[4] T. Starr, J.M. Cioffi, and P.J. Silverman, *Understanding digital subscriber line technology*, Prentice Hall, Upper Saddle River, 1999.

[5] P. Boets, T. Bostoen, L. Van Biesen, and T. Pollet, "Measurement, calibration and pre-processing of signals for single-ended subscriber line identification," *Instrumentation and Measurement Technology Conference - IMTC 2003*, Vail, CO, USA, 20-22 May 2003.

[6] K. Kerpez and S. Galli, "Single-ended loop make-up identification. Part I: A method of analyzing TDR measurements," *IEEE Transactions on Instrumentation and Measurement*, vol. 55, no. 2, pp. 528–537, Apr. 2006.

[7] K. Kerpez and S. Galli, "Single-ended loop make-up identification. Part II: Improved algorithms and performance results," *IEEE Transactions on Instrumentation and Measurement*, vol. 55, no. 2, pp. 538–549, Apr. 2006.

[8] P. Boets, L. Van Biesen, T. Bostoen, and D. Gardan, "Single-ended line testing - a white box approach," *Proceedings of the 4th IASTED International Multi-Conference, Wireless and Optical Communications*, July 8-10, 2004, Banff, Canada.

[9] L. Van Biesen, P. Boets, F. Louage, and T. Bostoen, "Expert system for the identification and classification of the local loop," *10th IMEKO TC7 International Symposium*, Saint-Petersburg, Russia, June 30-July 2, 2004.

[10] P. Boets, T. Bostoen, L. Van Biesen, and T. Pollet, "Preprocessing of signals for single-ended subscriber line testing," *IEEE Transactions on Instrumentation and Measurement*, vol. 55, no. 5, pp. 1509–1518, Oct. 2006.

[11] T. Vermeiren, T. Bostoen, F. Louage, P. Boets, and X.O. Chehab, "Subscriber loop topology classification by means of time-domain reflectometry," *IEEE International Conference on Communications*, Anchorage, USA, 11-15 May, 2003.

[12] R.F.M. van den Brink, "Cable reference models for simulating metallic access networks," Tech. Rep., ETSI STC TM6 Permanent document TM6(97)02, June 1998.

[13] J. Cook, "Parametric modeling of twisted pair cables for VDSL," ANSI contribution, T1E1.4/96-15, Irvine, CA, USA, 22-25 Jan, 1996.

[14] J. Cook, "Minor Correction to T1E1.4/96-15, parametric modeling of twisted pair cables for VDSL," ANSI contribution, T1E1.4/96-15, Colorado Springs, CO, USA, 22-24 April, 1996.

[15] P. Boets, *Frequency domain identification of transmission lines from time domain measurements*, Ph.D. thesis, Vrije Universiteit Brussel, Dept. ELEC, Pleinlaan 2, 1050 Brussels, June 1997.

[16] J. Musson, "Maximum likelihood estimation of the primary parameters of twisted pair cables," Tech. Rep., ETSI STC contribution TD8, TM6 meeting, Madrid Spain, Jan 26-30 1998.

[17] P. Boets and L. Van Biesen, "Metallic 2-wire parametric line models - a survey," *XVIII IMEKO world congress, Metrology for Sustainable Development*, Rio de Janeiro, Brazil, Sept. 17-22, 2006.

[18] ITU-T G.996.1, "Test procedures for digital subscriber line (dsl) transceivers," 02/2001.

[19] F. Lindqvist, P.O. Börjesson, P. Ödling, S. Höst, K. Ericson, and T. Magesacher, "Low-order and causal twisted-pair cable modeling by means of the hilbert transform," *RVK08 - The twentieth Nordic Conference on Radio Science and Communications*, Växjö, Sweden, June 9-11, 2008. AIP Conference Proceeding, vol. 1106, pp 301-310.

[20] T. Bostoen, P. Boets, M. Zekri, L. Van Biesen, T. Pollet, and D. Rabijns, "Estimation of the transfer function of a subscriber loop by means of one-port scattering parameter measurement at the central office," *IEEE Journal of Selected Areas in Communications*, vol. 20, No. 5, pp. 936–948, June 2002.

[21] IEC/CEI 61156-1, "International standard, multicore and symmetrical pair/quad cables for digital communications, part 1: Generic specification," 2002.

[22] F. Lindqvist, A. Fertner, and P.O. Börjesson, "A method and a system for cable or subscriber loop investigation performing loop topology identification," patent application, PCT/SE2006/000134, filed 31 Jan. 2006, WO 2007/089173 A1, pub. date 9 Aug. 2007.

Paper III

Paper III

Estimation of Nonhomogeneous and Dispersive Twisted-pair Transmission Lines

Abstract

For the emerging and future copper access network a higher transmission bandwidth will be utilized on significantly shorter twisted-pair cables than common today. These preconditions also apply to urban mobile backhauling of fourth generation radio access systems on already existing copper lines. Hence it is of great interest to address methods that can obtain accurate and for the purpose relevant transmission line information on these relatively short cables. In this paper, we adopt and develop a space-frequency model-based optimization approach originally targeting parameter reconstruction in microwave applications. In doing so, we explore the line parameters of interest and introduce the concept of capacitive length that overcomes the necessity of *a priori* knowledge of physical length. This also allows reducing the number of sought model parameters compared to prior art. The first obtained high-frequency model is furthermore enhanced for the lower frequencies used by existing digital subscriber line (DSL) services. Analytical gradients of the objective function with respect to sought model parameters are derived for both models, which enables computationally efficient gradient-based optimization. The performance and limitations of the method in terms of parameter estimation and transfer function estimation are evaluated by means of computer simulations with either one-port or two-port reflection data.

1   Introduction

A cost-effective way to retrieve transmission line information utilizes one/two-port measurements from already installed equipment, *e.g.*, DSL modems and/or POTS (plain old telephone service) transceivers. The so obtained line information enables pre-qualification and assessments of the line condition in addition to fault localization. In general this corresponds to solving the *inverse problem* with the aim to determine the unknown transmission line parameters based on known one/two-port measurements. The opposite is referred to as solving the *direct problem*. In the area of DSL several solutions to the inverse problem have been proposed. One such solution is based on time domain reflectometry (TDR) [1–7]. Another solution, which may be combined with TDR, is model-based optimization where the transmission line is parameterized with one or more cable models from which a measured quantity to be modeled is obtained via classic two-port network theory followed by optimization of a suitable criterion [4, 5, 8–10]. These model-based methods assume a continuous frequency dependence but only constant spatial dependence within each cable type. In addition, these methods generally target relatively long lines used by current DSL services.

In order to substantially improve the transmission capacity on already deployed lines, the DSL operators are forced to move the transceivers closer to each other (*e.g.* cabinet deployment) preferably combined with Vectoring [11]. The reduced target line length stretches from tens of meters up to several hundreds of meters. For these relatively short lines, methods that address electromagnetic scattering in a nonhomogeneous medium, *e.g.*, [12, 13], are becoming attractive also for the DSL application. However, the scattering methods are often developed for microwave frequencies [14] where the typical target device (*e.g.* a filter) has a physical extension fraction of a meter. Furthermore, since the target is different the assumed a priori information does not necessarily comply with the given problem, as will be evident later on.

A review of several scattering methods is found in *e.g.* [14] of which we in the sequel point out three of particular interest for our purpose. In [15] and [16] electrical parameters of a (RLCG) transmission line are reconstructed starting out from the telegrapher's equations formulated in the time domain. The method used involves wave-splitting and the compact Green functions technique. The method in [17] treats essentially the same problem in the frequency domain. That is, by applying the wave-splitting technique, imbedding equations for the reflection and transmission coefficients are derived. This together with the known boundary condition provides a solution to the direct problem, repeatedly solved when minimizing the objective

function in the accompanying inverse problem. A comparison between [16] and [17] is found in [18]. A main result of [16], confirmed by simulation results in [17], is the non-uniqueness of the solution to the inverse problem for a general (RLCG) transmission line. Under the given circumstances [16] and [17] show that with one-port reflection data, only one electrical parameter (R,L,C or G) can successfully be determined, while with two-port reflection data various pairs of parameters can be reconstructed. In addition, [17] reports that three parameters can be reconstructed with two-port reflection data provided sufficiently close start values.

Working entirely in the frequency domain as in [17] appears beneficial when the bandlimited reflection data is also measured in the frequency domain. Since all widely used models for twisted-pair cables [19, 20] are conveniently represented in the frequency domain, such an approach avoids the inherent difficulties of transforming bandlimited signals/models to the time domain which would be an alternative. Hence our needs coincide with how the inverse problem is formulated in [17].

In the present paper, we adopt and develop the approach in [17] for the DSL application with nonhomogeneous and dispersive transmission lines. In doing so, the described method takes advantage of formulating the inverse problem with imbedding equations which enables derivation of analytical gradients for the objective function. Hence, the used approach allows gradient-based optimization. This is in contrast to *e.g.* [8, 10] which instead exploit numerical perturbation inherent in the employed optimization algorithm. Numerical perturbations typically increase the computational complexity significantly compared to using analytical gradients.

The paper is organized as follows. In Section 2 and 3 the direct and inverse problems are described. In Section 4 we analyze how the one-port impedance measurement depends on the properties of the transmission line and explore what electrical parameters are relevant to estimate. In Section 5 the concept of capacitive length is introduced and MODEL II is derived (where MODEL I refers to prior art). In Section 6 MODEL III is presented. A description of how the transfer function can be obtained is provided in Section 7 followed by details of the numerical implementation in Section 8. In Section 9 the computer simulations are presented. Finally, conclusions are given in Section 10.

2   The Direct Problem

A nonhomogeneous and dispersive transmission line can be modeled as a cascade of infinitesimal homogeneous segments [21]. Each such segment of length dx can be treated as a circuit depicted in Fig. 1.
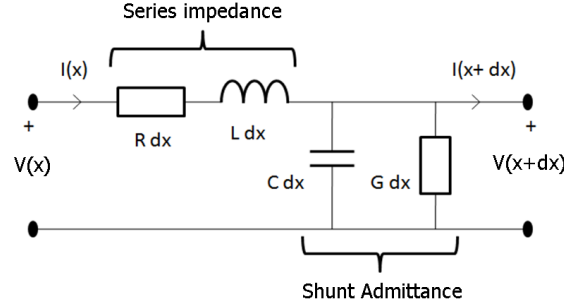
Figure 1: An infinitesimal homogeneous cable segment of length dx.

Here $R(x,\omega), L(x,\omega), C(x,\omega)$, and $G(x,\omega)$ denote respectively the series resistance, the series inductance, the shunt capacitance, and the shunt conductance which are all in general space-frequency dependent and expressed per unit length. By assuming a harmonic time dependence $\exp(j\omega t)$ and applying the Kirchhoff's voltage and current laws for the circuit depicted in Fig. 1, we obtain the telegrapher's equations that relate the voltage V and the current I for a nonhomogeneous and dispersive line, *i.e.*,

$$\frac{\partial}{\partial x}V(x,\omega) = -\Big(R(x,\omega) + j\omega L(x,\omega)\Big)I(x,\omega) \tag{1}$$

$$\frac{\partial}{\partial x}I(x,\omega) = -\Big(G(x,\omega) + j\omega C(x,\omega)\Big)V(x,\omega). \tag{2}$$

With the wave-splitting transform[1] defined in [17], one can derive from (1)–(2) the following system of equations for the so-called split components

$$\frac{\partial}{\partial x}\left[\begin{array}{c} V^+(x,\omega) \\ V^-(x,\omega) \end{array}\right] = \left[\begin{array}{cc} -a & -b \\ b & a \end{array}\right]\left[\begin{array}{c} V^+(x,\omega) \\ V^-(x,\omega) \end{array}\right] \tag{3}$$

where $a(x,\omega)$ and $b(x,\omega)$ are conveniently defined as

$$a(x,\omega) = \frac{1}{2}\Big[j\omega\Big(C\tilde{Z}_0 + L\tilde{Z}_0^{-1}\Big) + \Big(G\tilde{Z}_0 + R\tilde{Z}_0^{-1}\Big)\Big] \tag{4}$$

$$b(x,\omega) = \frac{1}{2}\Big[j\omega\Big(C\tilde{Z}_0 - L\tilde{Z}_0^{-1}\Big) + \Big(G\tilde{Z}_0 - R\tilde{Z}_0^{-1}\Big)\Big]. \tag{5}$$

Here, $\tilde{Z}_0$ denotes the characteristic impedance of a homogeneous line attached to the left side of the transmission line where the latter occupies the

---

[1]This corresponds to the definition of the voltage waves in [8] with $Z_{ref1} = \tilde{Z}_0$.

one-dimensional region $[0, \ell]$, *i.e.*, the homogeneous line is connected at $x = 0$. In general $\tilde{Z}_0$ may be frequency dependent, but is assumed known. Without much loss of generality it is here assumed, as in [17], that the line is terminated by an open-end, *i.e.,* the far-end impedance $Z_T = \infty$. In the DSL application this assumption corresponds to a cable break or (approximately) to a line termination with an on-hook POTS phone. The reflection and transmission coefficients for the transmission line can be determined by an invariant imbedding approach. This approach [17] considers a subline $[x, \ell]$ of the complete line and assumes that the subline is temporarily terminated at the left side by $\tilde{Z}_0$. With this in mind, it is appropriate to define the reflection coefficient[2] $r(x, \omega)$ and the transmission coefficient $t(x, \omega)$ accordingly

$$r(x, \omega) \;=\; \frac{V^-(x, \omega)}{V^+(x, \omega)} \tag{6}$$

$$t(x, \omega) \;=\; \frac{V(\ell, \omega)}{V^+(x, \omega)}, \tag{7}$$

where $V(\ell, \omega) = V^+(\ell, \omega) + V^-(\ell, \omega)$. By substituting (6) in (3) a Riccati differential equation can be formulated which yields

$$\frac{\partial}{\partial x} r(x, \omega) = 2a(x, \omega) r(x, \omega) + b(x, \omega) \Big(1 + r^2(x, \omega) \Big). \tag{8}$$

Since the termination impedance is assumed known, the following boundary condition can be stated

$$r(\ell, \omega) = \frac{Z_T(\omega) - \tilde{Z}_0(\omega)}{Z_T(\omega) + \tilde{Z}_0(\omega)}. \tag{9}$$

The solution to the direct problem with reflection data is found by integrating (8) in the negative x-direction starting out from (9). The so obtained solution corresponds to the *physical* reflection coefficient $r(0, \omega)$.

Similarly, by substituting (7) in (3) one can obtain the following differential equation for the transmission coefficient

$$\frac{\partial}{\partial x} t(x, \omega) = \Big(a(x, \omega) + b(x, \omega) r(x, \omega) \Big) t(x, \omega), \tag{10}$$

where the boundary condition yields

$$t(\ell, \omega) = \frac{2 Z_T(\omega)}{Z_T(\omega) + \tilde{Z}_0(\omega)}. \tag{11}$$

The solution to the direct problem with transmission data can be found by integrating (10) in the negative x-direction starting out from (11). This provides the sought *physical* transmission coefficient $t(0, \omega)$.

---

[2]This quantity corresponds at $x = 0$ to the scattering parameter S_{11} used in *e.g.* [8].

3   The Inverse Problem

In order to determine the unknown line parameters based on one/two-port measurements, an objective function is defined that represents the difference between the measured quantity and a parameterized model. By minimizing this difference, *i.e.*, the error, the sought model parameters are (hopefully) obtained. Inspired by [17], we define the objective function with the one-port measurement as

$$J(p) = \sum_{\omega=\omega_{min}}^{\omega_{max}} W_r(\omega)\Big|r(0,\omega) - r_m(\omega)\Big|^2,\qquad(12)$$

where $W_r(\omega)$ is a weight function and $r_m(\omega)$ denotes the *measured* physical reflection coefficient. The model $r(0,\omega)$ for the reflection coefficient at $x = 0$ has an implicit dependence on the parameter vector $p = [p_1(x)\,p_2(x)\,...\,p_M(x)]$ which contains M model parameters, expressed as a function of the spatial dimension. With a two-port measurement consisting of both the left-side and the right-side physical reflection coefficients, the objective function is modified accordingly

$$J_2(p) = J(p) + \sum_{\omega=\omega_{min}}^{\omega_{max}} W_r(\omega)\Big|r^{(2)}(\ell,\omega) - r_m^{(2)}(\omega)\Big|^2,\qquad(13)$$

where $r_m^{(2)}(\omega)$ is the measured physical *right-side* reflection coefficient and $r^{(2)}(\ell,\omega)$ is the corresponding model at measurement point $x = \ell$. Note that also $r^{(2)}(\ell,\omega)$ has an implicit dependence on the parameter vector p. Since all derived expressions for the left-side reflection coefficient have an analogous right-side counterpart, we mainly focus on (12) and assume one-port reflection data unless otherwise stated. In [17] with a dispersive surface impedance four parameters ($M = 4$) are used, defined as

$$\begin{aligned}
R(x,\omega) &= (1+j)\sqrt{\omega}R_\nu(x)\\
L(x,\omega) &= L_\infty(x)\\
C(x,\omega) &= C_\infty(x)\\
G(x,\omega) &= G_0(x),
\end{aligned}\qquad(14)$$

where R includes the internal inductance. With this model, which we refer to as MODEL I, [17] defines the sought parameters as $p = [R_\nu(x)\,L_\infty(x)\,C_\infty(x)\,G_0(x)]$. Here the first parameter has been renamed (compared to [17]) due to conflicting variable names, and L_∞ and C_∞ have been introduced to comply

with the cable parameter notations commonly used within the DSL community [19, 20]. Moreover, for twisted-pair cables in the copper access network (*i.e.,* of category 3 or higher) the conductance can often be neglected. Throughout the rest of the paper we therefore make the following assumption

$$G(x, \omega) = 0. \tag{15}$$

When solving the inverse problem by minimizing (12) (or (13)), the solution to the direct problem in Section 2 is required. Without an analytical solution to the direct problem one may iteratively minimize (12). Since solving the direct problem is fairly costly in terms of number of computations, a gradient-based optimization is preferred over numerical perturbation techniques. It can be concluded that (12) based on (14) depends only implicitly on the parameters. Therefore, analytical gradients with respect to the parameters can conveniently be obtained by the introduction of auxiliary functions as shown in [17] (and similarly in [15]). The solution to the inverse problem in [17] (and [15]) requires knowledge of ℓ, *i.e.,* the line length is assumed known a priori. In the DSL application the physical line length is in general not known. However, a length estimate can be obtained by using *e.g.* TDR, but that requires knowledge of the (unknown) velocity of propagation. Therefore, an alternative formulation to prior art is proposed in Section 5 which better fits the DSL application with unknown physical line length. First, however, a motivation for using this alternative approach is given in the coming section.

4   One-port Measurements

This section reviews how the one-port impedance measurement depends on the properties of the transmission line and what electrical parameters are possible and relevant to estimate from such a measurement. We start out considering a homogeneous cable (*i.e.,* without x-dependence) in order to obtain analytical and fruitful results. Thereafter is the more difficult case of a nonhomogeneous line considered which is exemplified by a cascade of different homogeneous cables. It is assumed that the one-port measurement constitutes the line input impedance $Z_{in}(\omega)$ or, similarly, the physical reflection coefficient in (6) whose relations at $x = 0$ can be expressed as

$$r(0, \omega) = \frac{Z_{in}(\omega) - Z_S(\omega)}{Z_{in}(\omega) + Z_S(\omega)}, \tag{16}$$

where Z_S denotes the known source impedance of *e.g.* a DSL modem connected to the line at $x = 0$. The input impedance of a homogeneous single-

section line expressed as a function of the $ABCD$ parameters [21] yields

$$Z_{in}(\omega) = \frac{A(\omega)Z_T(\omega) + B(\omega)}{C(\omega)Z_T(\omega) + D(\omega)}, \tag{17}$$

where the chain matrix elements are defined as

$$\begin{aligned}
A(\omega) &= D(\omega) = \cosh(\gamma(\omega)\ell) \\
B(\omega) &= Z_0(\omega)\sinh(\gamma(\omega)\ell) \\
C(\omega) &= \sinh(\gamma(\omega)\ell)/Z_0(\omega).
\end{aligned} \tag{18}$$

Here $Z_0(\omega)$ is the characteristic impedance of the line, $\gamma(\omega)$ is the propagation constant, and ℓ is the length of the line. Hence for an open-ended line, *i.e.*, when $Z_T \to \infty$, it follows from (17)–(18) that the input impedance is given by

$$Z_{in}(\omega) = Z_0(\omega)\coth\Big(\gamma(\omega)\ell\Big). \tag{19}$$

The frequency dependent $RLCG$ parameters are related to $Z_0(\omega)$ and $\gamma(\omega)$ through, [21],

$$Z_0(\omega) = \sqrt{\frac{R + j\omega L}{G + j\omega C}}, \ \gamma(\omega) = \sqrt{\Big(R + j\omega L\Big)\Big(G + j\omega C\Big)}. \tag{20}$$

By substituting (14)–(15) and (20) in (19), $Z_{in}(\omega)$ can be rewritten as

$$Z_{in}(\omega) = \sqrt{\frac{1-j}{\sqrt{\omega}}\rho_1 + \rho_2}\coth\Big(j\omega\rho_0\sqrt{\frac{1-j}{\sqrt{\omega}}\rho_1 + \rho_2}\Big), \tag{21}$$

where the following quantities have been defined

$$\rho_0 = C_\infty \ell, \ \ \rho_1 = R_\nu/C_\infty, \ \ \rho_2 = L_\infty/C_\infty. \tag{22}$$

From (21) it can be concluded that $Z_{in}(\omega)$ depends in a nonlinear way on ρ_0, ρ_1, ρ_2, and that at most three line quantities can be determined per frequency. It can also be concluded that if R, L, C are all increased/decreased by an arbitrary factor while ℓ is decreased/increased by the same factor, $Z_{in}(\omega)$ is unchanged. Thus, different points in the set $\{R, L, C, \ell\}$ may correspond to the same one-port measurement. Although the one-port measurement remains in general non-unique with the parameterization in (21)–(22), the number of unknowns is reduced by one. In addition, $\rho_0 = C_\infty \ell$, which

may be viewed as total *capacitive length*, corresponds to the total line capacitance. This quantity can (often) be measured by a POTS transceiver and/or estimated by a DSL modem. Hence with ρ_0 known *a priori*, $Z_{in}(\omega)$ depends on only two line parameters. For high frequencies $\frac{\rho_1}{\sqrt{\omega}} \approx 0$ whereupon $Z_{in}(\omega) \approx -j\sqrt{\rho_2}\cot\left(\omega\rho_0\sqrt{\rho_2}\right)$. From this approximation it can be seen that the one-port measurement $Z_{in}(\omega)$ depends primarily on ρ_2 for high frequencies while both ρ_1 and ρ_2 affect $Z_{in}(\omega)$ for lower frequencies. Furthermore, as the line length and/or the frequency increases $\coth(\gamma(\omega)\ell) \to 1$ in (19) whereupon $Z_{in}(\omega) \to Z_0(\omega)$. Thus, for a long line and/or high frequency mainly one line quantity impacts the one-port measurement since $Z_{in}(\omega) \approx \sqrt{\rho_2} = \sqrt{L_\infty/C_\infty}$. The understanding of these dependencies are useful when interpreting the results in Section 9.

An all-important line property is the *transfer function* which for a homogeneous single-section line with $Z_S = Z_0$ and $Z_T = \infty$ yields, [21],

$$H(\omega) = e^{-\gamma(\omega)\ell} = e^{-\sqrt{(R+j\omega L)(G+j\omega C)}\,\ell}. \tag{23}$$

By using the parameterization in (21)–(22) the transfer function in (23) can be expressed as

$$H(\omega) = e^{-j\omega\rho_0\sqrt{\frac{1-j}{\sqrt{\omega}}\rho_1+\rho_2}}. \tag{24}$$

From (24) it can be noted that the transfer function is determined by the capacitive length ρ_0 and the two parameters ρ_1 and ρ_2. That is, the transfer function is not explicitly dependent on the line length ℓ or the velocity of propagation. It can also be seen that the impact of ρ_2 on the transfer function increases with frequency. Thus, according to the parameterization in (21)–(22) it is the ratios of R/C, L/C, and $C\ell$ that are of prime interest to estimate rather than R, L and C.

For a multi-section line composed of n_s number of homogeneous cables, which exemplifies a nonhomogeneous line, the chain rule [21] can be applied to obtain the total transmission matrix $\mathbf{M}$, *i.e.*,

$$\mathbf{M} = \mathbf{M}^{(1)} \times \mathbf{M}^{(2)} \cdots \times \mathbf{M}^{(n_s)}, \tag{25}$$

where line section number s is represented by its transmission matrix $\mathbf{M}^{(s)}$ defined by the $ABCD$ parameters in (18), *i.e.*,

$$\mathbf{M}^{(s)} = \begin{bmatrix} A^{(s)} & B^{(s)} \\ C^{(s)} & D^{(s)} \end{bmatrix}. \tag{26}$$

In this case, (16) and (17) are still valid but now $ABCD$ are obtained via the matrix product (25) and hence represent the *overall* line. For example, with $n_s = 2$ we find for the two-section line that

$$Z_{in}(\omega) = -jZ_0^{(1)} \frac{\cos\theta^{(1)}\cos\theta^{(2)} - \frac{Z_0^{(1)}}{Z_0^{(2)}}\sin\theta^{(1)}\sin\theta^{(2)}}{\sin\theta^{(1)}\cos\theta^{(2)} + \frac{Z_0^{(1)}}{Z_0^{(2)}}\cos\theta^{(1)}\sin\theta^{(2)}}, \qquad (27)$$

where the first section is represented by $\left\{Z_0^{(1)}, \theta^{(1)}\right\}$ and the second section by $\left\{Z_0^{(2)}, \theta^{(2)}\right\}$, which are related through

$$\theta^{(1)}(\omega) = \omega\rho_0^{(1)}\sqrt{\frac{1-j}{\sqrt{\omega}}\rho_1^{(1)} + \rho_2^{(1)}} = \omega\rho_0^{(1)}Z_0^{(1)}(\omega)$$

$$\theta^{(2)}(\omega) = \omega\rho_0^{(2)}\sqrt{\frac{1-j}{\sqrt{\omega}}\rho_1^{(2)} + \rho_2^{(2)}} = \omega\rho_0^{(2)}Z_0^{(2)}(\omega).$$

In order to gain better understanding of how these line quantities affect the inverse problem at hand, the objective function in (12) is visualized in Fig. 2 in terms of contour plots for a nonhomogeneous line comprising two cascaded (homogeneous) twisted-pair cables. Here (12) is evaluated for typical values of $\rho_2^{(1)}$ and $\rho_2^{(2)}$ while the other parameters are fixed. The one-port measurement in (16) is calculated via the analytical expression in (27) with $Z_S = 50\,\Omega$. In total 100 equidistant frequency points are used within the bandwidth $[0.5, 15]\,\mathrm{MHz}$ (upper figure) or $[2, 15]\,\mathrm{MHz}$ (lower figure). The lengths of the first and second cables are $1/3$ and $2/3$ of the total line length of $400\,\mathrm{m}$, respectively. By comparing the upper and lower plots of Fig. 2, it can be seen that both plots show one global optimum and that the exclusion of the lower frequencies give several local optima. It can also be seen, especially in the lower figure, that the objective function is less sensitive to a change in $\rho_2^{(2)}$ than to a change in $\rho_2^{(1)}$ which indicates that the first section dominates, as expected. With a shorter line length (not shown) mainly one global optimum is visible also for the bandwidth $[2, 15]\,\mathrm{MHz}$. For a typical single-section line with one homogeneous cable section, only one global optimum is observed when evaluating (12) as a function of $\rho_1^{(1)}$ and $\rho_2^{(1)}$.

Thus from these experiments it can be deduced that the objective function in (12) appears to be an (approximately) convex function for homogeneous lines but non-convex for nonhomogeneous lines. For the considered two-section line, the convexity depends on both the used bandwidth and on

the line length where a shorter line tend to make the objective function more convex. By repeating the experiments and studying the contour plots of the objective function in (13) with *two-port* reflection data, all the performed experiments suggest that only one optimum is present for both considered bandwidths. Hence, with two-port reflection data the convexity of the optimization problem can be improved in this case.
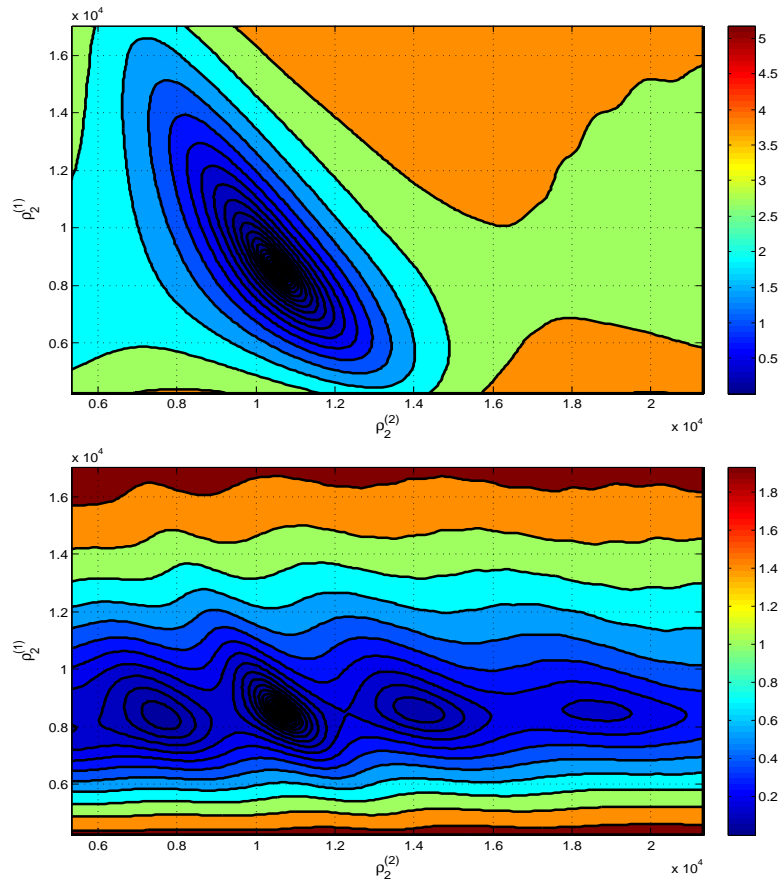

Figure 2: Contour plots of (12) for a two-section line comprising two homogeneous cables with total line length of $400\,\mathrm{m}$. The bandwidth is $[0.5, 15]\,\mathrm{MHz}$ in upper figure and $[2, 15]\,\mathrm{MHz}$ in lower figure. The true values are $\rho_2^{(1)} = 0.85 \cdot 10^4$ $[\Omega/\mathrm{F}]$ and $\rho_2^{(2)} = 1.07 \cdot 10^4$ $[\mathrm{H/F}]$.

5   Utilizing Capacitive Length

Instead of relying on the physical line length ℓ we utilize the concept *capacitive length* introduced in the previous section. In doing so, a new set of parameters is defined which in addition reduces the number of parameters by one compared to [17], and therefore decreases the dimension of the optimization problem. We define the capacitive length as

$$y(x) = \int_0^x C(x',\omega)\mathrm{d}x' = \int_0^x C_\infty(x')\mathrm{d}x', \tag{28}$$

where the model in (14) is applied. The *a priori* known (*e.g.* measured) total line capacitance can therefore be expressed as

$$y(\ell) = \int_0^\ell C_\infty(x')\mathrm{d}x'. \tag{29}$$

By making the variable substitution $\mathrm{d}y = C_\infty(x)\mathrm{d}x$ that follows from (28), and using (15), (8) can be rewritten[3] as

$$\frac{\partial}{\partial y}r(y,\omega) = 2\frac{a(y,\omega)}{C_\infty(y)}r(y,\omega) + \frac{b(y,\omega)}{C_\infty(y)}\Big(1 + r^2(y,\omega)\Big). \tag{30}$$

For convenience we define $A(y,\omega) = \frac{a(y,\omega)}{C_\infty(y)}$ and $B(y,\omega) = \frac{b(y,\omega)}{C_\infty(y)}$, which inserted in (30) gives

$$\frac{\partial}{\partial y}r(y,\omega) = 2A(y,\omega)r(y,\omega) + B(y,\omega)\Big(1 + r^2(y,\omega)\Big), \tag{31}$$

and the boundary condition $r(y(\ell),\omega) = 1$ for an open-ended line. It follows from (4)–(5) and (14), with Z_S attached at $y = 0$, that $A(y,\omega)$ and $B(y,\omega)$ can be expressed accordingly

$$
\begin{aligned}
A(y,\omega) &= \frac{1}{2}\Big[j\omega\Big(Z_S + \frac{L_\infty(y)}{C_\infty(y)}Z_S^{-1} + \frac{R_\nu(y)Z_S^{-1}}{C_\infty(y)\sqrt{w}}\Big) \\
&\quad + \frac{R_\nu(y)\sqrt{w}}{C_\infty(y)}Z_S^{-1}\Big].
\end{aligned}
\tag{32}
$$

$$
\begin{aligned}
B(y,\omega) &= \frac{1}{2}\Big[j\omega\Big(Z_S - \frac{L_\infty(y)}{C_\infty(y)}Z_S^{-1} - \frac{R_\nu(y)Z_S^{-1}}{C_\infty(y)\sqrt{w}}\Big) \\
&\quad - \frac{R_\nu(y)\sqrt{w}}{C_\infty(y)}Z_S^{-1}\Big].
\end{aligned}
\tag{33}
$$

---

[3]Here a slight abuse of notation is used since in general $r(x,\omega) \neq r(y,\omega)$.

If we now redefine the line parameters as

$$p_1(y) = \frac{R_\nu(y)}{C_\infty(y)} \tag{34}$$

$$p_2(y) = \frac{L_\infty(y)}{C_\infty(y)}, \tag{35}$$

then (32) and (33) can be rewritten as

$$
\begin{aligned}
A(y,\omega) &= \frac{1}{2}\Big[j\omega\Big(Z_S + p_2(y)Z_S^{-1} + \frac{p_1(y)}{\sqrt{w}}Z_S^{-1}\Big) \\
&\quad + p_1(y)\sqrt{w}Z_S^{-1}\Big] \tag{36} \\
B(y,\omega) &= \frac{1}{2}\Big[j\omega\Big(Z_S - p_2(y)Z_S^{-1} - \frac{p_1(y)}{\sqrt{w}}Z_S^{-1}\Big) \\
&\quad - p_1(y)\sqrt{w}Z_S^{-1}\Big]. \tag{37}
\end{aligned}
$$

We refer to (34) and (35) as the model parameters of MODEL II, where the first model corresponds to prior art described in Section 3. Thus, with the introduction of capacitive length according to (28) the number of parameters has been reduced from three to two (assuming (15)) and the physical line length ℓ is no longer required. The solution to the direct problem is readily obtained by integrating (31) in the negative y-direction starting out from the given boundary condition. As the parameters in (34) and (35) do not change the structure of the equations compared to using physical line length, the expressions for the analytical gradients remain the same. That is, $\frac{\partial J(p)}{\partial p_1}(y)$ and $\frac{\partial J(p)}{\partial p_2}(y)$ can readily be obtained from the results of [17], *i.e.*,

$$
\begin{aligned}
\frac{\partial J}{\partial p_1}(y) &= \Re \sum_{\omega=\omega_{min}}^{\omega_{max}} \Big(1+j\Big)\sqrt{\omega}Z_S^{-1}(\omega)\Big(1-r(y,\omega)\Big)^2 \\
&\quad \cdot U(y,\omega) \tag{38} \\
\frac{\partial J}{\partial p_2}(y) &= \Re \sum_{\omega=\omega_{min}}^{\omega_{max}} j\omega Z_S^{-1}(\omega)\Big(1-r(y,\omega)\Big)^2 U(y,\omega), \tag{39}
\end{aligned}
$$

where $\Re\{.\}$ denotes the real part of the argument and $U(y,\omega)$ corresponds to the auxiliary function defined in [17], but here expressed as a function of capacitive length.

6　Improvements for Low Frequencies

The parameterized model in (14) is a high-frequency model that accounts for the skin effect but is not accurate for the lower part of the spectrum used by DSL transmission, *e.g.,* the lower ADSL2+/VDSL2 frequencies [22, 23]. In this section we extend the model in (14) in order to better prescribe the lower frequencies. The extension is described for the case using capacitive length. A similar extension can be performed for the case using physical length.

　　The low-order and causal cable model derived in [24] is valid for both the lower and upper part of the ADSL2+/VDSL2 spectrum. This model expresses the resistance and inductance (per unit length) of a homogeneous and dispersive line as

$$R = R_0 \sqrt[4]{1 + (f/\nu)^2} = R_0 Q(f/\nu) \tag{40}$$

$$L = \frac{R_0}{2\pi f} \Lambda(f/\nu) + L_\infty, \tag{41}$$

where R_0, ν, and L_∞ are model parameters and $\Lambda(f/\nu)$ denotes the Hilbert transform of $Q(f/\nu)$, see [24] for details. As before, the capacitance is denoted C_∞ and is constant with frequency. The conductance G is assumed zero as in (15).

　　In the following we allow these parameters to vary along the spatial dimension in order to represent a nonhomogeneous and dispersive line, *i.e.,* $R_0 = R_0(y)$, $\nu = \nu(y)$, and $L_\infty = L_\infty(y)$. By substituting (40)–(41) in (4)–(5), and exploiting (14) with Z_S attached at $y = 0$, we obtain

$$
\begin{aligned}
A(y,\omega) &= \frac{1}{2}\Big[j\omega\Big(Z_S + \frac{L_\infty(y)}{C_\infty(y)}Z_S^{-1}\Big) + \frac{R_0(y)}{C_\infty(y)}\Big(Q(\frac{f}{\nu(y)}) \\
&+ j\Lambda(\frac{f}{\nu(y)})\Big)Z_S^{-1}\Big].
\end{aligned}
\tag{42}
$$

$$
\begin{aligned}
B(y,\omega) &= \frac{1}{2}\Big[j\omega\Big(Z_S - \frac{L_\infty(y)}{C_\infty(y)}Z_S^{-1}\Big) - \frac{R_0(y)}{C_\infty(y)}\Big(Q(\frac{f}{\nu(y)}) \\
&+ j\Lambda(\frac{f}{\nu(y)})\Big)Z_S^{-1}\Big].
\end{aligned}
\tag{43}
$$

If we redefine the line parameters as

$$\tilde{p}_1(y) = \frac{R_0(y)}{C_\infty(y)} \tag{44}$$

$$\tilde{p}_2(y) = \nu(y) \tag{45}$$

$$\tilde{p}_3(y) = \frac{L_\infty(y)}{C_\infty(y)}, \tag{46}$$

then (42) and (43) can be expressed as

$$
\begin{aligned}
A(y,\omega) &= \frac{1}{2}\Big[j\omega\Big(Z_S + \tilde{p}_3(y)Z_S^{-1}\Big) + \tilde{p}_1(y)\Big(Q(\frac{f}{\tilde{p}_2(y)}) \\
&+ j\Lambda(\frac{f}{\tilde{p}_2(y)})\Big)Z_S^{-1}\Big].
\end{aligned}
\tag{47}
$$

$$
\begin{aligned}
B(y,\omega) &= \frac{1}{2}\Big[j\omega\Big(Z_S - \tilde{p}_3(y)Z_S^{-1}\Big) - \tilde{p}_1(y)\Big(Q(\frac{f}{\tilde{p}_2(y)}) \\
&+ j\Lambda(\frac{f}{\tilde{p}_2(y)})\Big)Z_S^{-1}\Big].
\end{aligned}
\tag{48}
$$

We refer to (44)–(46) as the model parameters of MODEL III. The solution to the inverse problem with this extended model involves the same steps as with MODEL II. The main difference is the Hilbert transform $\Lambda(\frac{f}{\tilde{p}_2(y)})$. As described in [25], the computation of this Hilbert transform can be performed with low complexity by using *e.g.* a polynomial approximation.

6.1 Analytical Gradients

In order to use computationally efficient gradient-based optimization, analytical gradients of the objective function are derived with respect to the new parameters in (44) and (45), *i.e.*, $\frac{\partial J}{\partial \tilde{p}_1}(y)$ and $\frac{\partial J}{\partial \tilde{p}_2}(y)$. Since $\tilde{p}_3(y)$ and $p_2(y)$ are equally defined we have $\frac{\partial J}{\partial \tilde{p}_3}(y) = \frac{\partial J}{\partial p_2}(y)$. The details of the analysis are shown in Appendix A from which we find

$$
\begin{aligned}
\frac{\partial J}{\partial \tilde{p}_1}(y) &= \Re \sum_{\omega=\omega_{min}}^{\omega_{max}} Z_S^{-1}(\omega)\Big[Q(\frac{f}{\tilde{p}_2(y)}) + j\Lambda(\frac{f}{\tilde{p}_2(y)}) \Big] \\
&\cdot \Big(1 - r(y,\omega)\Big)^2 U(y,\omega)
\end{aligned}
\tag{49}
$$

$$
\begin{aligned}
\frac{\partial J}{\partial \tilde{p}_2}(y) &= \Re \sum_{\omega=\omega_{min}}^{\omega_{max}} Z_S^{-1}(\omega)\Big[Q'(\frac{f}{\tilde{p}_2(y)}) + j\Lambda'(\frac{f}{\tilde{p}_2(y)}) \Big] \\
&\cdot \tilde{p}_1(y)\Big(1 - r(y,\omega)\Big)^2 U(y,\omega)
\end{aligned}
\tag{50}
$$

Here $\Re\{.\}$ denotes the real part of the argument and $U(y,\omega)$ corresponds to the auxiliary function defined in [17], but here expressed as a function of capacitive length. Furthermore, in (50) $Q'(\frac{f}{\tilde{p}_2(y)}) \equiv \frac{\partial}{\partial \nu}Q(\frac{f}{\nu(y)})$ and $\Lambda'(\frac{f}{\tilde{p}_2(y)}) \equiv \frac{\partial}{\partial \nu}\Lambda(\frac{f}{\nu(y)})$. The first derivative is straightforward as concluded from the definition of Q in (40). The derivative of the Hilbert transform requires some

more care. It can for instance be calculated by utilizing numerical integration preferably with the variable substitution stated in [25], or with reduced computational complexity by analytically taking the derivative of a polynomial approximation of Λ [25]. In Section 9 the latter method is employed.

6.2   Combining Models

MODEL II and III can at least in theory be utilized in a combined way. The idea is as follows. First, the high-frequency model (MODEL II) is applied with the advantage of only optimizing two parameters. In this case, low frequencies must be excluded from the objective function, $i.e.$, $w_{min} \gg 0$ in (12). Since parameter $p_2(y) = \tilde{p}_3(y)$, the optimized value of $p_2(y)$ can be reused as a fixed value for $\tilde{p}_3(y)$ when optimizing the remaining parameters of MODEL III, including lower frequencies. This procedure has the advantage that only two parameters have to be optimized at any given time. Alternatively, the optimized value of $p_2(y)$ is only used as start value for $\tilde{p}_3(y)$ when optimizing all three parameters of MODEL III.

The procedure can be refined by noting that $\tilde{p}_1(y) = p_1(y)\sqrt{\tilde{p}_2(y)}$ and subsequently only optimizing $\tilde{p}_2(y)$ for MODEL III, which corresponds to a one-dimensional parameter optimization. This of course presumes that $p_1(y)$ and $p_2(y)$ are accurately estimated with MODEL II in the first place.

7   Transfer Function

In what follows we describe how the frequency-dependent transfer function can be determined from the results obtained when solving the direct and inverse problems of Section 2 and 3. To better follow the previous notations, the spatial variable corresponds herein to the physical length rather than the capacitive length, but the end result ($i.e.$, (58)) is the same. Let us assume that a voltage source $V_S(\omega)$ with a source impedance $Z_S(\omega)$ is connected to the line input at $x = 0$. This results in a voltage $V_T(\omega)$ over the termination impedance $Z_T(\omega)$ at $x = \ell$. Hence the transfer function is defined as

$$H(\omega) = \frac{V_T(\omega)}{V_S(\omega)}. \tag{51}$$

If $Z_{in}(\omega)$ denotes the input impedance of the line measured at $x = 0$, the voltage at the line input yields

$$V_{in}(\omega) = V_S(\omega)\frac{Z_{in}(\omega)}{Z_{in}(\omega) + Z_S(\omega)}. \tag{52}$$

Substitution of (16) in (52) provides

$$V_{in}(\omega) = V_S(\omega)\Big(\frac{1 + r(0, \omega)}{2}\Big), \qquad (53)$$

which with (51) gives

$$H(\omega) = \frac{V_T(\omega)}{V_{in}(\omega)}\Big(\frac{1 + r(0, \omega)}{2}\Big). \qquad (54)$$

Since the voltage along the line, $V(x, \omega)$, is the sum of the split components defined in Section 2 we have

$$V_{in}(\omega) = V^+(0, \omega) + V^-(0, \omega), \qquad (55)$$
$$V_T(\omega) = V^+(\ell, \omega) + V^-(\ell, \omega). \qquad (56)$$

By using (55)–(56) and (6) we find after some manipulations

$$H(\omega) = \frac{1}{2}\frac{V^+(\ell, \omega)}{V^+(0, \omega)}\Big(1 + r(\ell, \omega)\Big). \qquad (57)$$

For the assumed open-ended line, the boundary condition $r(\ell, \omega) = 1$ leads to

$$H(\omega) = \frac{V^+(\ell, \omega)}{V^+(0, \omega)} = \frac{t(0, \omega)}{t(\ell, \omega)}, \qquad (58)$$

where in the last step we used the definition of the transmission coefficient in (7). Equation (58) shows that the transfer function can be determined from the transmission coefficient evaluated at $x = 0$ and $x = \ell$, as expected.

To summarize, based on a one-port measurement of the physical reflection coefficient the inverse problem is first solved in order to obtain the parameter vector p. This in turn enables solving the direct problem in (10)–(11) yielding the transmission coefficient from which the transfer function can be estimated via (58).

8   Numerical Implementation

The numerical algorithms used to solve the direct and inverse problems are described in this section. The actual implementation is verified in Section 9 by means of computer simulations.

To solve the direct problem we apply the Trapezoidal rule and integrate (31) from the known boundary condition $r(y(\ell), \omega) = 1$ towards $r(0, \omega)$. The spatial dimension $y \in [0, y(\ell)]$ is discretized into a grid of $M + 1$ equidistant

points by $y_m = m\,h$ for $m = 0, 1, ..., M$ where $h = \frac{y(\ell)}{M}$. With the assumed discretization the following second order equation can be derived from (31)

$$c_2 r^2(y_m, \omega) + c_1 r(y_m, \omega) + c_0 = 0, \qquad (59)$$

where the coefficients are

$$c_2 = \frac{h}{2} B(y_m, \omega) \qquad (60)$$

$$c_1 = h A(y_m, \omega) + 1 \qquad (61)$$

$$c_0 = \frac{h}{2} \Big[2A(y_{m+1}, \omega) r(y_{m+1}, \omega) + B(y_{m+1}, \omega)$$

$$\cdot \Big(1 + r^2(y_{m+1}, \omega) \Big) + B(y_m, \omega) \Big] - r(y_{m+1}, \omega). \qquad (62)$$

Since (59) is quadratic there are two roots at each discrete point, *i.e.*,

$$r(y_m, \omega) = \frac{-c_1 \pm \sqrt{c_1^2 - 4c_2 c_0}}{2c_2}. \qquad (63)$$

However, only the root with the + sign satisfies the requirement $|r(y_m, \omega)| \leq 1$ for the considered lines. Equation (59) is valid for angular frequency ω within the measurement bandwidth $\omega \in [\omega_{min}, \omega_{max}]$. This bandwidth is discretized into N frequency points which are summed up in the objective function. Thus, with P number of model parameters (*i.e.* $P = 2$ for MODEL II and $P = 3$ for MODEL III) there are in total $M \cdot P$ variables to optimize. The far-end spatial point y_M corresponds to the boundary value and is therefore not accounted for.

In contrast to the frequency dimension, the spatial dimension may contain one or more step functions due to *e.g.* different cable types which requires a large M in order to preserve high accuracy in the numerical solution to the direct problem. It is therefore undesirable to explicitly store and optimize each spatial variable. In the following subsection we consider spatial modeling as a way to reduce the number of spatial variables. The numerical optimization algorithm is described thereafter.

8.1   Spatial Modeling

8.1.1   Linear Modeling

Two types of linear spatial modeling are considered, namely, *piecewise-constant* and *linear interpolation*. For both types the parameter $p_i(y)$ is represented with K number of spatial variables where $K \ll M$ and (for simplicity)

M/K is chosen to be an integer. With piecewise-constant spatial modeling the direct problem is solved with $p_i(y_k)$ for $k = \lfloor m\frac{K}{M} \rfloor$ where $m = 0, 1, ..., M - 1$. However, the optimization only stores and updates $p_i(y_k)$ for $k = 0, \frac{M}{K} - 1, ..., (K - 1)\frac{M}{K} - 1$ where $m = M$ corresponds to the far-end. Similarly, with linear interpolation the optimization only uses $p_i(y_k)$ for $k = 0, \frac{M}{K} - 1, ..., (K - 1)\frac{M}{K} - 1$ where these K variables are linearly interpolated to form $M + 1$ values used when solving the direct problem.

8.1.2 Modeling with Orthonormal Basis

In case a model parameter $p_i(y)$ is known to follow some deterministic shape in the spatial dimension it is reasonable to impose this restriction on $p_i(y)$. To generalize, we let the spatial variation be represented by a K-dimensional weighted orthonormal basis expressed as

$$p_i(y) = \sum_{k=0}^{K-1} \alpha_{ik}\Phi_k(y), \qquad (64)$$

where $\Phi_k(y)$ is the kth basis function and α_{ik} is the kth real-valued coefficient associated with the ith model parameter. The basis functions are assumed to be orthonormal within the spatial region $y \in [0, y(\ell)]$, *i.e.*,

$$\int_0^{y(\ell)} \Phi_k(y')\Phi_j^*(y')\mathrm{d}y' = \begin{cases} 1 & \text{if } k = j, \\ 0 & \text{otherwise.} \end{cases} \qquad (65)$$

In Appendix B the analytical gradient $\frac{\partial J}{\partial \alpha_{ik}}$ of the objective function with respect to coefficient α_{ik} is derived. In the present paper, we consider in particular the set of orthonormal basis comprising a linear combination of sine and cosine functions with a fundamental period twice the (capacitive) length of the line. With the discretization defined previously these basis functions are defined for $m = 0, 1, ..., M$ and $k = 0, 1, ..., K - 1$ as

$$\Phi_k(y_m) = \begin{cases} \sqrt{\frac{2}{M}}\cos(\frac{2\pi mk}{2M}) & \text{if } k \text{ even,} \\ \sqrt{\frac{2}{M}}\sin(\frac{2\pi mk}{2M}) & \text{if } k \text{ odd.} \end{cases} \qquad (66)$$

For $k = 0$ the even basis function is used which leads to a constant basis that allows capturing the spatial mean value of the parameter profile. By using a fundamental period greater than M, *e.g.* $2M$ as used here, arbitrary parameter values can be represented at the near-end and far-end of the line.

8.2   Numerical Optimization

For the non-linear optimization the Quasi-Newton (QN) algorithm is employed as the search directions do not require computation of the Hessian matrix and yet still attain a superlinear rate of convergence [26]. Hence, at the nth iteration the update of the parameter vector p yields

$$p_{n+1} = p_n + \lambda_n s_n, \tag{67}$$

where s_n denotes the search direction and λ_n is the step length. Before the update in (67), the search direction is calculated according to QN, *i.e.*,

$$s_n = B_n^{-1} \nabla J_n, \tag{68}$$

where ∇J_n is the analytical gradient of the objective function with respect to the sought parameter vector, and B_n is a symmetric positive definite matrix that approximates the Hessian matrix $\nabla^2 J_n$. For the update of B_n we resort to the *BFGS* method where the inverse B_n^{-1} is updated. For the step length λ_n we use an inexact line search that fulfills the Wolfe condition [26].

9   Computer Simulations

In this section we evaluate the performance of parameter estimation and transfer function estimation on simulated twisted-pair lines. The simulated system employs the described optimization approach where (12) is minimized with one-port reflection data, and (13) is minimized with two-port reflection data. The analytical gradients based on MODEL II or MODEL III are utilized. The numerical implementation is according to Section 8.

9.1   Setup

The considered reflection measurement has a maximum bandwidth from 20 kHz to 30 MHz with N frequency points separated in a logarithmic scale. In a DSL application, such a measurement can be performed by *e.g.* a VDSL2 transceiver [23]. For all computer simulations the standardized ETSI cables in [19] are used. However, these cables are described by the *BT* cable model which has a non-causal behavior. To circumvent this shortcoming, the line inductance is replaced by the inductance of the $BT0_H$ cable model in [24]. The physical reflection coefficient $r_m(\omega)$, which represents a measurement, is calculated according to (16) where the line input impedance is obtained from the following recursive formula [21] utilizing spatial discretization with

$M + 1$ equidistant points, *i.e.*,

$$Z_{in}(x_i) = Z_0(x_i) \frac{Z_{in}(x_{i+1}) + Z_0(x_i) \tanh\Big(\gamma(x_i)\Delta x\Big)}{Z_0(x_i) + Z_{in}(x_{i+1}) \tanh\Big(\gamma(x_i)\Delta x\Big)} \tag{69}$$

where $x_i = i\frac{\ell}{M}$ for $i = M - 1, M - 2, ..., 0$ and $\Delta x = x_{i+1} - x_i$. By definition $Z_{in}(x_M) = Z_T$. The simulated measurement is therefore not obtained in the same way as when solving the direct problem. The explicit notation of frequency dependence has been omitted in (69). It is assumed that the termination impedance $Z_T = \infty$ (open-end) and the source impedance $Z_S = 50\,\Omega$ (arbitrary). As described in Section 8 there are in total $K \cdot P$ number of parameter values to optimize, where P denotes the number of model parameters and $K \ll M$ is the number of (optimized) spatial variables per model parameter. Since the objective function in (12) may be non-convex and have large plateaus, as exemplified in Fig. 2, the success of a gradient-based local minimizer depends on how close the start values are to the (global) optimum. However, the electrical parameters of the twisted-pair cables are not completely unknown and (hopefully) complies with the manufacturing requirements. Therefore, typical values can be obtained from *e.g.* [19] or from a cable database. Since the sought parameters differs by several orders of magnitude the optimization problem is poorly scaled. The simulator therefore works (internally) with normalized values which are, for convenience, also used when plotting the estimated profiles. In this context, the considered ETSI $0.4, 0.5$, and $0.63\,\text{mm}$ cables [19] have a normalized parameter range between 0.4 and 1.3, from which we choose the (approximate) median value of 1 as the start value for all parameters, *i.e.*, $p_i(y_k) = 1\,\forall i, k$, at the start of the optimization.

The simulated reflection coefficient as a function of both frequency and spatial dimension is depicted in Fig. 3 and Fig. 4 for a homogeneous single-section line with length $100\,\text{m}$ and $500\,\text{m}$, respectively. The direct problem is in this case solved with the true parameter profiles in order to provide insight to how the cable length and attenuation affect the reflection coefficient. It can be observed from Fig. 3 that the spatial variation of the reflection coefficient increases for higher frequencies. This behavior suggests that for a given spatial resolution, the numerical errors occurring when estimating the higher frequencies typically impact the objective function more. It is therefore appropriate to use a low-pass weight function that de-emphasize the higher frequencies. We use $W_r(\omega) = 100^{-(\omega/\omega_{max})^2}$ as in [17]. Fig. 3 also suggests that hardly no variation of the reflection coefficient occurs close to the far-end independent of frequency. Hence the parameter gradients are small in

Figure 3: Reflection coefficient for ETSI 0.5 mm cable of length 100 m evaluated with $M = 5000$ spatial points and $N = 200$ frequency points from 20 kHz to 10 MHz.
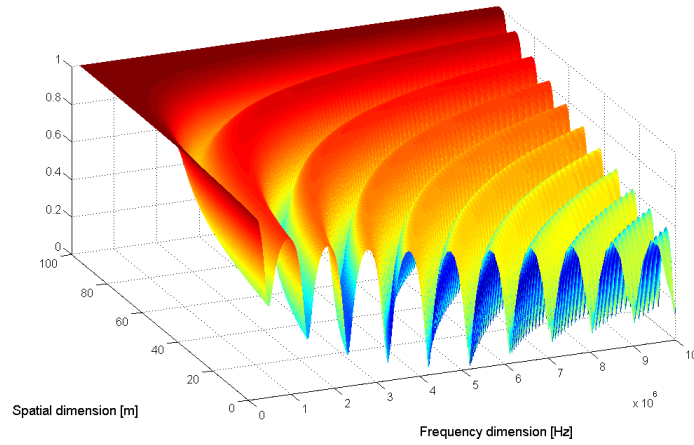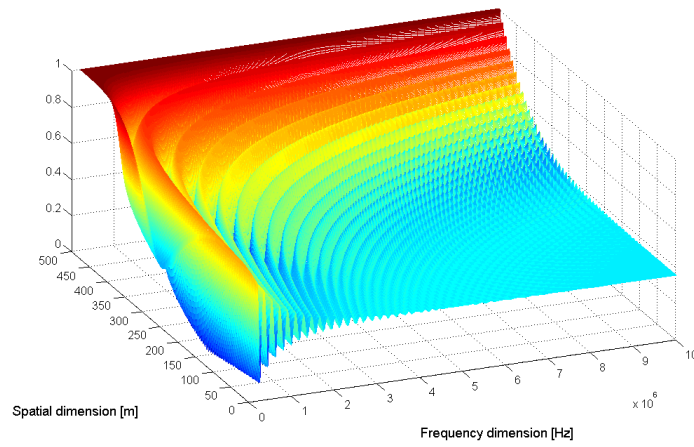

Figure 4: Reflection coefficient for ETSI 0.5 mm cable of length 500 m evaluated with $M = 5000$ spatial points and $N = 200$ frequency points from 20 kHz to 10 MHz.

the vicinity of the far-end which give rise to difficulties when estimating the line parameters. However, as will be seen later on, a relatively large parameter error close to the far-end tend to have a minor influence on the objective function and on the transfer function. From Fig. 4 it can be observed that a longer cable has a reflection coefficient with more rapid and attenuated oscillations that essentially levels out to a constant level for higher frequencies. This corresponds to $\coth(\gamma(\omega)\ell) \to 1$ in (19) and $Z_0(\omega) \to \sqrt{\frac{L_\infty}{C_\infty}}$. Thus from (16) it follows that the reflection coefficient $r(0,\omega) \to \frac{\sqrt{\frac{L_\infty}{C_\infty}} - Z_S}{\sqrt{\frac{L_\infty}{C_\infty}} + Z_S}$ which is around 0.4 in Fig. 4. This confirms that mainly $\frac{L_\infty}{C_\infty}$ impacts the reflection coefficient and thereby the objective function as the line length and/or the frequency increase.

The accuracy of the parameter estimation generally increases with higher values of M, K and N due to better numerical approximations and a denser space-frequency grid. However, this also implies increased computational complexity. In addition, an increase in K (and/or P) typically leads to slower rate of convergence since more variables need to be optimized. It is therefore instructive to first assess the errors caused by non-perfect numerical approximations and inherent structural errors due to simplistic modeling (*i.e.*, MODEL II). This also provides a way to heuristically determine adequate upper limits for K and M. In the simulator this is accomplished by solving the direct problem using the true parameter profiles with MODEL II and MODEL III, respectively. The so obtained $r(0, w)$ is compared with the (true) physical reflection coefficient $r_m(\omega)$ in order to calculate the difference, *i.e.*, the error, which is depicted in Fig. 5 and Fig. 6 for various cable lengths.

From Fig. 5 it can be observed that the error increases significantly with the line length for lower frequencies ($< 1\,\mathrm{MHz}$). This behavior is reasonable since MODEL II only models the resistivity as proportional to $\sqrt{\omega}$ which is not valid for the lower frequencies as the line length increases. This is in contrast to MODEL III in Fig. 6 where the error is less length dependent at lower frequencies. With both models the numerical error decreases at higher frequencies for a long line since the reflection coefficient becomes rather flat, *cf.* Fig. 3 and Fig. 4. The impact of increasing the spatial resolution can be seen by comparing the curves with $M = 1000$ and $M = 5000$. Although the numerical noise can be reduced even further for higher frequencies with $M > 5000$, the overall gain of the present system is small. Hence, we can heuristically state that $K = 2$ and $M \approx 5000$ are adequate upper limits for the homogeneous lines when solving the direct problem with the linear spatial modeling methods. Similarly, $K \approx 50$ and $M \approx 5000$ are sufficient for the

Figure 5: Absolute error in reflection coefficient $r(0, \omega)$ with MODEL II and ETSI 0.5 mm for various lengths. Linear interpolation with $K = 50$, $N = 500$, and $M = 1000$ or $M = 5000$.
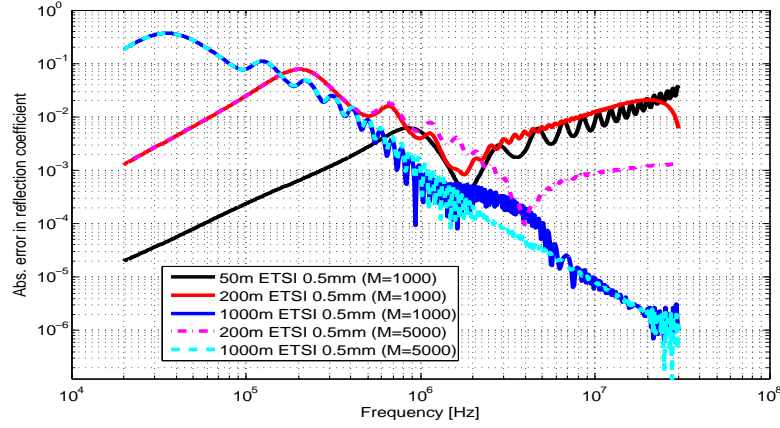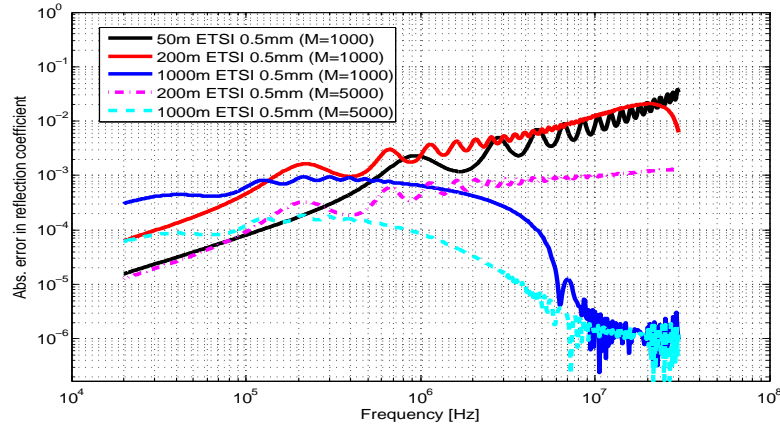

Figure 6: Absolute error in reflection coefficient $r(0, \omega)$ with MODEL III and ETSI 0.5 mm for various lengths. Linear interpolation with $K = 50$, $N = 500$, and $M = 1000$ or $M = 5000$.

nonhomogeneous lines considered in this section while for spatial modeling with orthonormal basis $K \approx 20$ and $M \approx 5000$ are reasonable moderate upper limits.

9.2   Parameter Estimation with MODEL II

9.2.1   Homogeneous Lines

The herein considered transmission lines consists of only one ETSI cable type and are thus homogeneous along the spatial dimension. The results of estimating one parameter is shown in Fig. 7 for various bandwidths. In this case p_2 is optimized while p_1 is assumed known. The line is an ETSI 0.5 mm cable of length 100 m. The bandwidth contains $N = 100$ frequency points from 1 MHz up to 2, 4, or 8 MHz. The results are shown after convergence and indicate that the periodicity of the estimated profiles increase with the bandwidth. Approximately a two-times increase in the periodicity can be observed as the highest frequency is doubled. This periodicity, also visible in the experiments in [17], seems to originate from the numerical approximation. In fact, by starting the optimization with the same settings but with the true p_2 as start value, the same periodicity can be observed after some iterations since the algorithm tries to minimize the residual numerical noise occurring when solving the direct problem. Furthermore, it can be deduced from the simulation results that $K = 50$ provides better performance than $K = 2$ although $K = 2$ should theoretically be sufficient for homogeneous lines. The reason for this can be seen in Fig. 7 which shows that the estimation error tend to decrease for higher bandwidths except near the far-end. The latter is a consequence of tiny gradients when $r(y, \omega) \approx 1$ giving $\frac{\partial J}{\partial p_2}(y) \approx 0$ close to the far-end. Therefore, linear interpolation with $K > 2$ allows more accurate profiles close to the far-end. The results also suggest that the estimated profiles become slightly biased due to compensation for the incorrect far-end values. In fact, by using two-port reflection data it can be observed that the bias disappears and the parameter profiles become symmetrical.

The results of estimating both parameters are exemplified in Fig. 8 and Fig. 9 for an ETSI 0.5 mm cable of length 200 m and 1000 m, respectively. By comparing these two figures it can be seen that the variances of the parameters are larger for the longer line, as expected, and that the estimation error increases near the far-end for both lines. It can also be observed, especially for the longer line, that the profiles are tilted (biased) due to the tiny gradients close to the far-end. Interestingly, the spatial mean value of each estimated profile corresponds accurately to the true value, *i.e.*, within the second decimal. It should be noted that the results in Fig. 8 and Fig. 9 are shown after
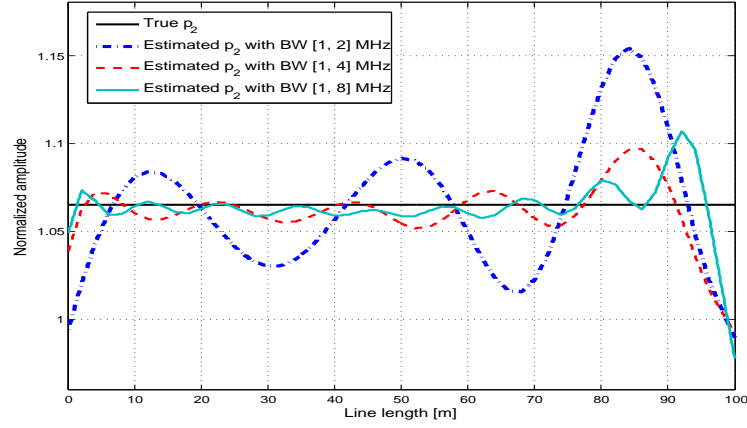
Figure 7: Parameter estimation with MODEL II using one-port reflection data on ETSI 0.5 mm of length 100 m. Linear interpolation with $K = 50, M = 1000, N = 100$ and various bandwidths.
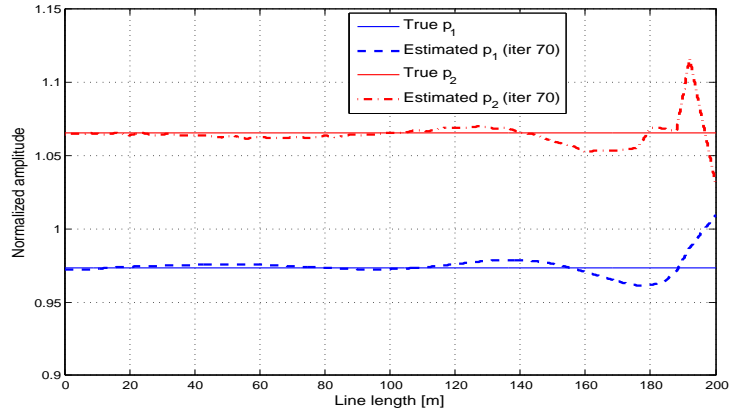
Figure 8: Parameter estimation with MODEL II using one-port reflection data on ETSI 0.5 mm of length 200 m. Linear interpolation with $K = 50, M = 5000, N = 100$ and bandwidth $[2, 10]$ MHz.
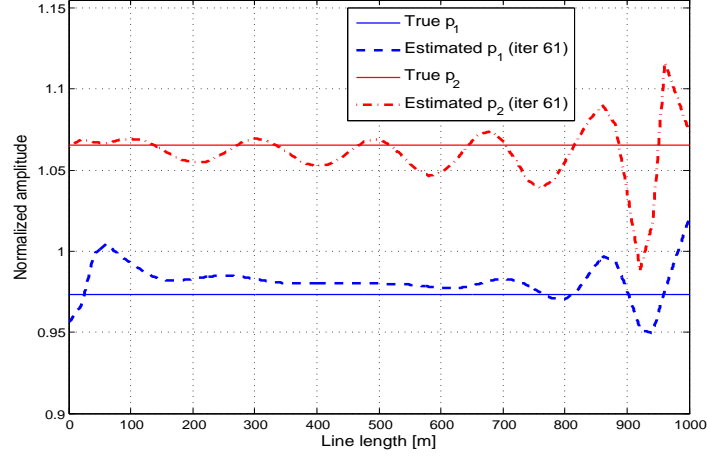
Figure 9: Parameter estimation with MODEL II using one-port reflection data on ETSI $0.5\,\text{mm}$ of length $1000\,\text{m}$. Linear interpolation with $K = 50, M = 5000, N = 100$ and bandwidth $[1,5]\,\text{MHz}$.

70 and 61 optimization iterations and that no significant improvements occur with more iterations nor by increasing any of K, M and/or N. Similar estimation results are obtained with ETSI $0.4\,\text{mm}$ and ETSI $0.63\,\text{mm}$ where the parameter error is typically less than 0.05 up to $1000\,\text{m}$. The results further suggest that the variances of the parameters generally increases with the line length and decline somewhat with increased cable diameter.

Moreover, it can be concluded from exhaustive simulations that the outcome of the estimation is dependent on the bandwidth, *i.e.,* $[\omega_{min}, \omega_{max}]$. In fact, the selection of the bandwidth is a trade-off. On the one hand, it is natural to exclude the lower frequencies with MODEL II as previously discussed. On the other hand, the simulation results clearly indicate that the optimization tend to fail, especially for longer lines, if the optimization starts with a too high value of ω_{min} and/or if the used bandwidth is too large. This behavior can be understood by comparing the contour plots in Fig. 2 where it is seen that the convexity of the objective function is improved by using a bandwidth with lower frequencies. Thus, instead of using a fixed bandwidth a better strategy is to successively increase ω_{min} and/or ω_{max} during the optimization. A too high value of ω_{max} is however undesirable as the numerical noise typically increase.

9.2.2 Nonhomogeneous Lines

In this subsection we consider lines where the sought parameters have a spatial dependence. The outcome of such a parameter estimation on a fictitious single-section nonhomogeneous line is depicted in Fig. 10 where the true parameters have a sinusoidal shape. This shape simulates a non-ideal twist along the cable although the assumed periodicity and amplitude are ad hoc chosen. From Fig. 10 it can be observed that both parameters are quite accurately estimated from the one-port reflection data with a larger error at the edges. For this experiment the bandwidth is first $[0.8, 10]$ MHz and after 40 iterations changed to $[2, 20]$ MHz at the same time as M is increased from 1000 to 5000. Linear interpolation is used with $K = 50$ and $N = 100$. If the line length is increased to 200 m the accuracy of the estimation deteriorates with only one-port reflection data.

Next we consider homogeneous cable types spliced together, *i.e.*, piecewise-homogeneous parameters along the spatial dimension. The outcome of such a parameter estimation is shown in Fig. 11 and Fig. 12 for a three-section line after convergence in 50 and 90 iterations, respectively. By comparing Fig. 11 and Fig. 12 it can be noted that the estimation error increases with the line length and that the far-end proves more difficult to estimate accurately.
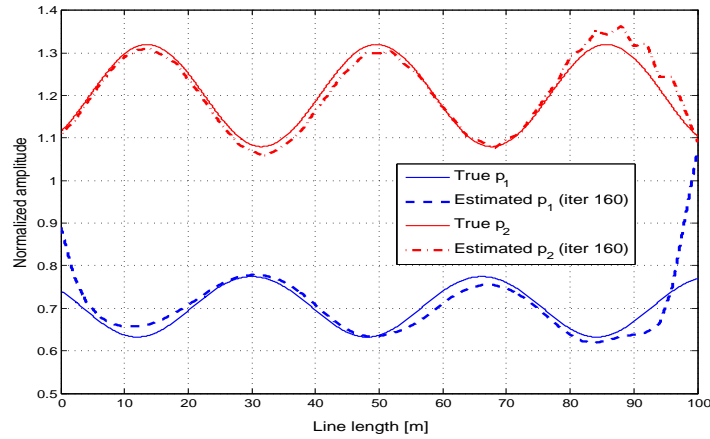
Figure 10: Parameter estimation with MODEL II using one-port reflection data on a single-section nonhomogeneous line with a total line length of 100 m. Linear interpolation is used with $K = 50, M = 5000, N = 100$ and bandwidth $[2, 20]$ MHz.

Figure 11: Parameter estimation with MODEL II using one-port reflection data on a three-section line $(0.4, 0.63, 0.5\,\text{mm})$ with a total line length of $50\,\text{m}$. Linear interpolation is used with $K = 50, M = 1000, N = 100$ and bandwidth $[2, 25]\,\text{MHz}$.

Figure 12: Parameter estimation with MODEL II using one-port reflection data on a three-section line $(0.4, 0.63, 0.5\,\text{mm})$ with a total length of $200\,\text{m}$. Linear interpolation is used with $K = 50, M = 5000, N = 200$ and bandwidth $[2, 20]\,\text{MHz}$.

Figure 13: Parameter estimation with MODEL II using one-port reflection data on a three-section line $(0.4, 0.63, 0.5 \, \text{mm})$ with a total length of $200 \, \text{m}$. Spatial modeling with orthonormal basis using $K = 21, M = 5200, N = 100$ and bandwidth $[2, 20] \, \text{MHz}$.

For the $50 \, \text{m}$ case, the bandwidth is first $[0.8, 10] \, \text{MHz}$ and after 30 iterations changed to $[2, 25] \, \text{MHz}$ while N is increased from 50 to 100. For the $200 \, \text{m}$ case, the bandwidth is first $[0.5, 5] \, \text{MHz}$ and after 30 iterations changed to $[2, 20] \, \text{MHz}$ with $N = 200$. For both cases, linear interpolation with $K = 50$ and $M = 1000$ are used except during the last iterations where M is increased to 5000 for the longer line in order to enhance the estimated profiles. The results of parameter estimation exploiting spatial modeling with the orthonormal basis is shown in Fig. 13. Here the $200 \, \text{m}$ case is once more used with $M = 2100$ and $K = 21$. By comparing Fig. 12 and Fig. 13 it can be noted that the orthonormal basis give similar results as with linear interpolation although K is less than half. With increased K and M essentially no further improvements occur. Despite seemingly large oscillations of the estimated profiles in Fig. 11, Fig. 12 and Fig. 13 the spatial mean value of each profile is accurately estimated (within the second decimal). For the three-section line with a line length beyond $200 \, \text{m}$, for instance $500 \, \text{m}$, the estimated profiles do not typically resemble the true profiles although the objective function is minimized. This result suggests that the non-uniqueness of the solution prevents trustful parameter estimation on longer lines with only one-port reflection data. Moreover, for the longer lines the estimation results are not necessarily improved with two-port reflection data since MODEL II is not valid at the lower frequencies needed to estimate p_1.

9.3   Parameter Estimation with MODEL III

With MODEL III lower frequencies can be included in the objective function which proves critical for longer lines as previous results show. For shorter lines, however, the resistive parameter $\tilde{p}_1$ is small and has only a minor impact on the objective function. Hence MODEL III is preferred on longer lines. A disadvantage with MODEL III compared to MODEL II is that one more model parameter has to be optimized, *i.e.*, one more profile with K variables.

9.3.1   Homogeneous Lines

For long homogeneous lines, say $> 800\,\text{m}$, the simulation results indicate that the method is not always capable of estimating all three parameters of MODEL III with only one-port reflection data. In a successful case with $1\,\text{km}$ ETSI $0.5\,\text{mm}$ cable, the estimation error is less than 0.05 for $\tilde{p}_1$ and $\tilde{p}_3$ while for $\tilde{p}_2$ the error is up to 0.1. At the last $150\,\text{m}$ the error is significantly larger due to the far-end problem previously discussed.

9.3.2   Nonhomogeneous Lines

With only one-port reflection data, the estimated profiles for the nonhomogeneous lines do not (typically) represent the true profiles if more than one model parameter is optimized (the other assumed known), although the objective function is significantly minimized. With two-port reflection data, the estimation results are improved as depicted in Fig. 14 for a piecewise homogeneous three-section line of length $900\,\text{m}$. The simulation results also indicate that for lines longer than about $300\,\text{m}$, linear spatial modeling is preferred over orthonormal basis, probably due to higher requirements on precision when projecting the spatial dependent gradients onto the basis, *cf.* (85). The results of the parameter estimation on a cascade of two fictitious nonhomogeneous lines are shown in Fig. 15, from which it can be noted that near perfect estimation of $\tilde{p}_3$ is achieved. For $\tilde{p}_1$ and $\tilde{p}_2$ the error is up to 0.1 and worse in the vicinity of the splice point around $165\,\text{m}$. The spatial mean value of each estimated profile are equally accurate for all three parameters. By increasing any of K, M and/or N no major improvements can be observed. The reason for the significantly larger error in $\tilde{p}_1$ and $\tilde{p}_2$ can be understood by recognizing the minor impact these two parameters have on the line resistance R for higher frequencies, and thereby on the objective function. By instead looking at the high-frequency asymptote of R, which yields $\frac{R_0}{C_\infty \sqrt{\nu}} = \frac{\tilde{p}_1}{\sqrt{\tilde{p}_2}}$, it can be noted from Fig. 16 that this parameter better
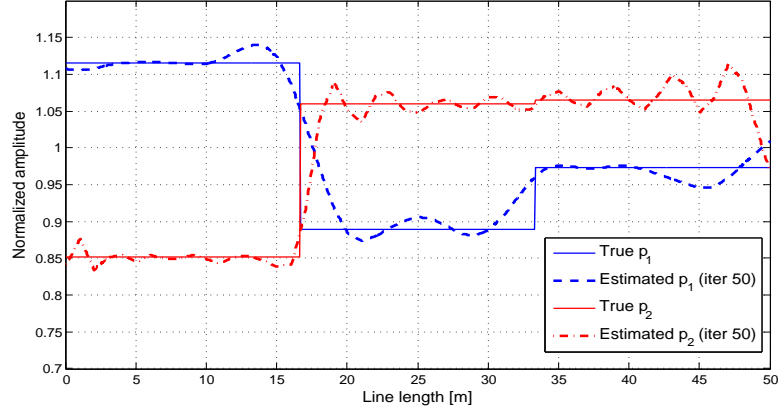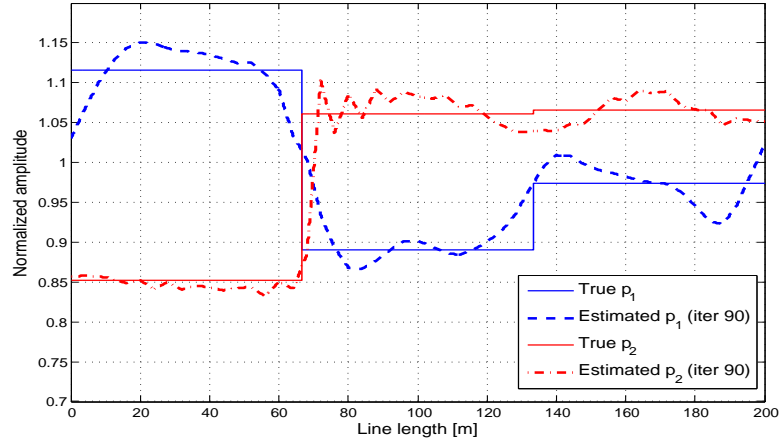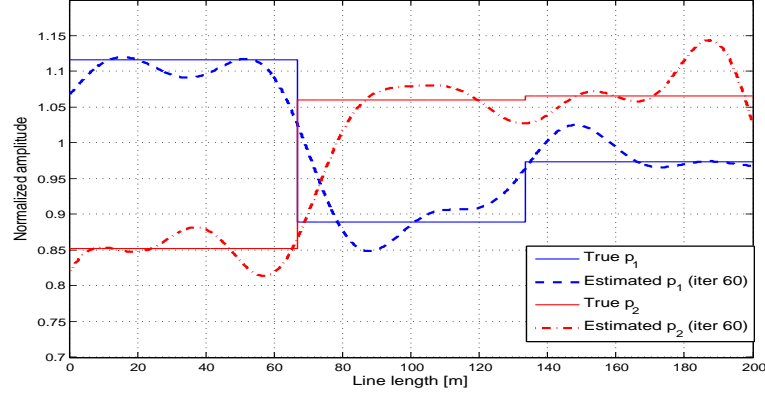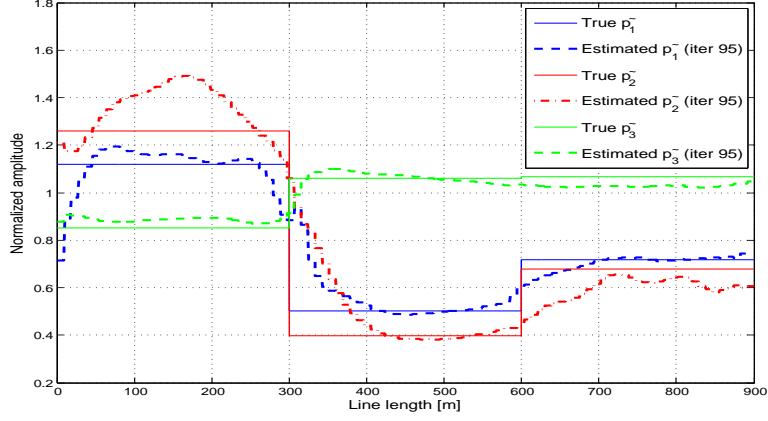
Figure 14: Parameter estimation with MODEL III using two-port reflection data on a three-section line $(0.4, 0.63, 0.5\,\text{mm})$ with a total length of $900\,\text{m}$. Linear interpolation with $K = 100, M = 1000, N = 100$, and bandwidth $[0.02, 5]\,\text{MHz}$.
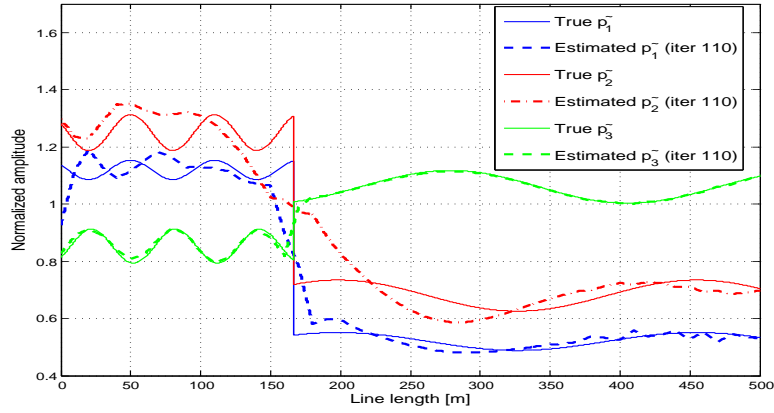
Figure 15: Parameter estimation with MODEL III using two-port reflection data on a two-section fictitious line with a total length of $500\,\text{m}$. Linear interpolation with $K = 50, M = 8000, N = 100$, and bandwidth $[0.02, 10]\,\text{MHz}$.

follows the step at the splice point since this contains mainly high frequency components.
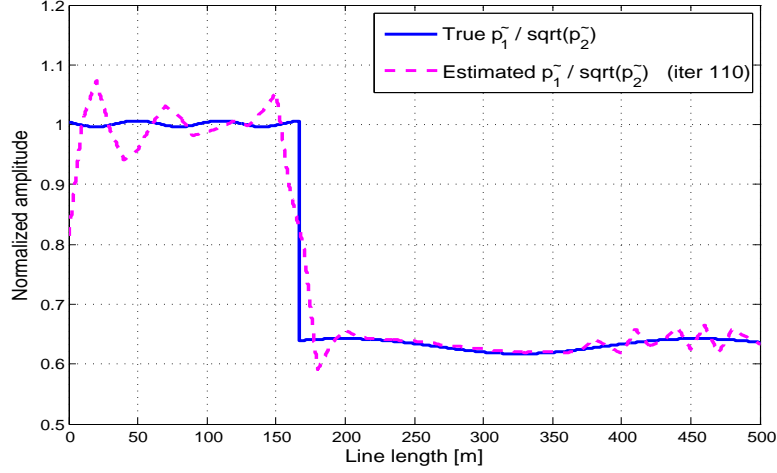
Figure 16: Parameter estimation with MODEL III using two-port reflection data on a two-section fictitious line with a total length of 500 m. Linear interpolation with $K = 50, M = 8000, N = 100$, and bandwidth $[0.02, 10]$ MHz.

9.4 Transfer Function Estimation

In Fig. 17 the estimated transfer function is shown for a two-section line consisting of ETSI 0.4 mm and ETSI 0.5 mm with a total line length of 1 km. Only one-port reflection data is used during the parameter estimation. The so obtained profiles minimize the objective function but do not resemble the true profiles, as expected from previous results. For comparison, the transfer function corresponding to the start values is also shown in Fig. 17, *i.e.*, without optimization. The estimation error is depicted in Fig. 18 which shows that the absolute error, *i.e.*, the absolute difference, is less than 6 dB for MODEL II and less than 1 dB for MODEL III in the frequency range between 20 kHz and 20 MHz. For this line the attenuation exceeds 100 dB beyond 20 MHz. It should be emphasized that both the amplitude and the phase are estimated. Similar results are obtained with the other test lines considered in this section.
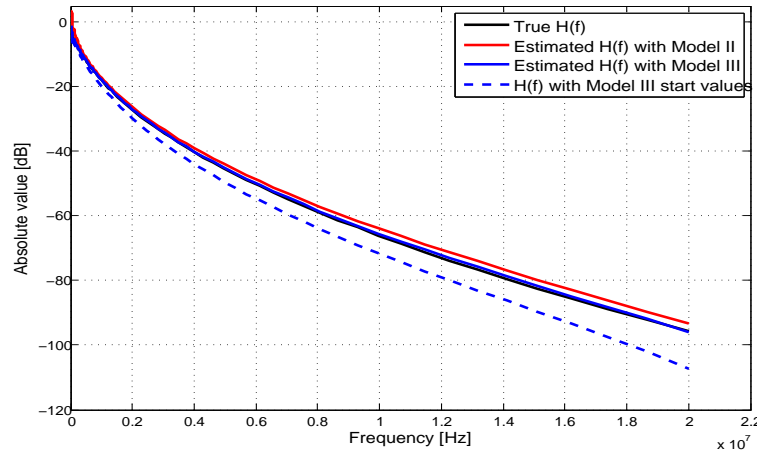
Figure 17: Transfer function $H(f)$ of a two-section line consisting of ETSI 0.4 mm and ETSI 0.5 mm with a total line length of 1 km.
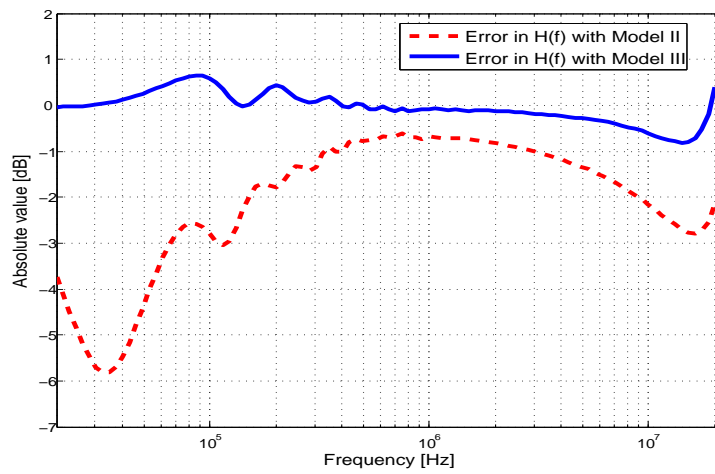
Figure 18: Estimation error in transfer function with MODEL II and MODEL III. The two-section line consists of ETSI 0.4 mm and ETSI 0.5 mm with a total line length of 1 km.

10   Discussion and Conclusions

By analyzing how the one-port impedance measurement depends on the properties of the transmission line, the relevant electrical parameters possible to estimate from such a measurement are identified. The analysis shows that the ratios R/C and L/C, and the total line capacitance, are of prime interest for the present application rather than R, L and C. This is in contrast to several prior works focusing on estimating R, L, C and G. The analysis further suggests the introduction of *capacitive length* in (28) that in addition to reducing the dimension of the optimization problem overcomes the necessity of a priori knowledge of physical length ℓ. Based on this insight, we adopt and develop a space-frequency optimization approach [17] that is made feasible without explicit knowledge of ℓ. The derived high-frequency MODEL II has the advantage of containing only two parameters compared to three in prior art. By applying this model in (12), it can be deduced from studying contour plots of the objective function that the convexity typically deteriorates with increased line length and/or if the measurement bandwidth excludes lower frequencies. It can also be deduced that the convexity may be improved by using two-port reflection data with (13).

The simulation results indicate that both parameters of MODEL II can be fairly accurately estimated (*i.e.*, error typically < 0.05) with only one-port reflection data for the homogeneous lines up to about 1000 m, and up to about 200 m for the considered nonhomogeneous lines. The results further suggest that the variances of the estimated parameters increase with the line length but decrease with the cable diameter. For the nonhomogeneous lines with lengths beyond 200 m, the true parameter profiles are typically not obtained with MODEL II despite minimizing the objective function in (12), probably due to local optima and/or due to the non-uniqueness of the solution. With two-port reflection data the results are not (significantly) improved on the longer lines since MODEL II is not valid at the required low frequencies.

The enhanced MODEL III is obtained by applying the $BT0_H$ cable model [24] whereupon the lower frequencies are also captured. The simulation results indicate that two-port reflection data are needed to estimate all three parameters of MODEL III where parameter $\tilde{p}_3 = L_\infty/C_\infty$ is most accurately estimated, especially at splice-points. The latter is due to the minor influence the resistive parameters have on the objective function at high frequencies, as concluded by studying the estimated high-frequency asymptote of R. Exhaustive simulations show that a gradually increased bandwidth is vital for a successful optimization, provided sufficiently close start values. In the DSL application, the latter can be obtained from *e.g.* a cable data base or measurements.

For all considered lines the transfer function is quite accurately estimated with only one-port reflection data even though the obtained parameter profiles do not (typically) resemble the true ones for the longer lines. This important result is a merit of having sufficiently close start values, since it can easily be proved that the one-port reflection data do not uniquely determine the sought parameters nor the transfer function.

Future work includes evaluation of the method with real measurements on telecommunication cables. It should be noted though that the adopted optimization approach has been verified in *e.g.* [17] with noisy data.

Appendix A. Analytical Gradients of Objective Function with Linear Spatial Modeling

Analytical gradients of the objective function in (12) with respect to the parameters in (44) and (45) are derived in the following. Completely analogous expressions are obtained for the objective function in (13) with two-port reflection data wherefore these are omitted. For simplicity the used notation omits dependence on y and ω. From the analysis in [17] it is known that an increment in the objective function $\delta J(p) = J(p + \delta p) - J(p)$, due to a small increment δp in the parameter vector, can be expressed as

$$\delta J(p) = -2 \int_0^\ell \Re \sum_{\omega=\omega_{min}}^{\omega_{max}} \left[2r\delta a + \left(1 + r^2\right)\delta b \right] U \mathrm{d}x + o(\delta p), \qquad (70)$$

where $\Re$ denotes the real-part operator, U is an auxiliary function, and where δa and δb are the corresponding increments of a and b defined in (4) and (5), respectively. Only reflection data is assumed. With MODEL III in Section 6, a corresponding increment δp in the parameter vector $p = [\tilde{p}_1, \tilde{p}_2, \tilde{p}_3]$ can similarly be expressed in terms of the increments of A and B in (47)–(48), *i.e.*,

$$\begin{aligned} \delta J(p) &= -2 \int_0^{y(\ell)} \Re \sum_{\omega=\omega_{min}}^{\omega_{max}} \left[2r\delta A + \left(1 + r^2\right)\delta B \right] U \mathrm{d}y \\ &+ o(\delta p), \end{aligned} \qquad (71)$$

where δA and δB can be formulated as

$$\delta A = \frac{\partial A}{\partial \tilde{p}_1}\delta \tilde{p}_1 + \frac{\partial A}{\partial \tilde{p}_2}\delta \tilde{p}_2 + \frac{\partial A}{\partial \tilde{p}_3}\delta \tilde{p}_3, \qquad (72)$$

$$\delta B = \frac{\partial B}{\partial \tilde{p}_1}\delta \tilde{p}_1 + \frac{\partial B}{\partial \tilde{p}_2}\delta \tilde{p}_2 + \frac{\partial B}{\partial \tilde{p}_3}\delta \tilde{p}_3. \qquad (73)$$

More specifically, from (47) and (48) we obtain

$$\frac{\partial A}{\partial \tilde{p}_1} = \frac{1}{2}\Big(Q(\frac{f}{\tilde{p}_2}) + j\Lambda(\frac{f}{\tilde{p}_2})\Big)Z_S^{-1} \tag{74}$$

$$\frac{\partial A}{\partial \tilde{p}_2} = \frac{1}{2}\tilde{p}_1\Big(Q'(\frac{f}{\tilde{p}_2}) + j\Lambda'(\frac{f}{\tilde{p}_2})\Big)Z_S^{-1} \tag{75}$$

$$\frac{\partial B}{\partial \tilde{p}_1} = -\frac{1}{2}\Big(Q(\frac{f}{\tilde{p}_2}) + j\Lambda(\frac{f}{\tilde{p}_2})\Big)Z_S^{-1} \tag{76}$$

$$\frac{\partial B}{\partial \tilde{p}_2} = -\frac{1}{2}\tilde{p}_1\Big(Q'(\frac{f}{\tilde{p}_2}) + j\Lambda'(\frac{f}{\tilde{p}_2})\Big)Z_S^{-1}, \tag{77}$$

where $Q'(\frac{f}{\tilde{p}_2(y)}) \equiv \frac{\partial}{\partial \nu}Q(\frac{f}{\nu(y)})$ and $\Lambda'(\frac{f}{\tilde{p}_2(y)}) \equiv \frac{\partial}{\partial \nu}\Lambda(\frac{f}{\nu(y)})$. Since all parameters are nondispersive, *i.e.*, frequency independent, $\delta J(p)$ in (71) can also be expressed in the following inner product form

$$\delta J(p) = \int_0^{y(\ell)} \frac{\partial J}{\partial \tilde{p}_1}\delta\tilde{p}_1 \mathrm{d}y + \int_0^{y(\ell)} \frac{\partial J}{\partial \tilde{p}_2}\delta\tilde{p}_2 \mathrm{d}y$$

$$+ \int_0^{y(\ell)} \frac{\partial J}{\partial \tilde{p}_3}\delta\tilde{p}_3 \mathrm{d}y + o(\delta p). \tag{78}$$

By substituting (72)–(77) into (71) and comparing the resulting expression with (78), the sought analytical gradients can be identified, *i.e.*,

$$\frac{\partial J}{\partial \tilde{p}_1}(y) = \Re \sum_{\omega=\omega_{min}}^{\omega_{max}} Z_S^{-1}(\omega)\Big[Q(\frac{f}{\tilde{p}_2(y)}) + j\Lambda(\frac{f}{\tilde{p}_2(y)})\Big]$$

$$\cdot \Big(1 - r(y,\omega)\Big)^2 U(y,\omega) \tag{79}$$

$$\frac{\partial J}{\partial \tilde{p}_2}(y) = \Re \sum_{\omega=\omega_{min}}^{\omega_{max}} Z_S^{-1}(\omega)\Big[Q'(\frac{f}{\tilde{p}_2(y)}) + j\Lambda'(\frac{f}{\tilde{p}_2(y)})\Big]$$

$$\cdot \tilde{p}_1(y)\Big(1 - r(y,\omega)\Big)^2 U(y,\omega), \tag{80}$$

where for the sake of completeness the dependence on the capacitive length y and the angular frequency ω are highlighted.

Appendix B. Analytical Gradients of Objective Function with Orthonormal Basis

By referring to the analysis in Appendix A, we consider a small increment $\delta p_i(y)$ in model parameter $p_i(y)$. It follows from (64) that this increment can

be written as

$$\delta p_i(y) = \sum_{k=0}^{K-1} \delta\alpha_{ik}\Phi_k(y), \tag{81}$$

where $\delta\alpha_{ik}$ is the corresponding increment in α_{ik}. With P number of model parameters the increment in the objective function, δJ, can be expressed by the following inner product form

$$\begin{aligned}
\delta J &= \int_0^{y(\ell)} \frac{\partial J}{\partial p_1}(y)\delta p_1(y)\mathrm{d}y + \int_0^{y(\ell)} \frac{\partial J}{\partial p_2}(y)\delta p_2(y)\mathrm{d}y \\
&\quad + \cdots + \int_0^{y(\ell)} \frac{\partial J}{\partial p_P}(y)\delta p_P(y)\mathrm{d}y + o(\delta p).
\end{aligned} \tag{82}$$

By substituting (81) into (82) we obtain

$$\begin{aligned}
\delta J &= \sum_{k=0}^{K-1} \Big(\int_0^{y(\ell)} \frac{\partial J}{\partial p_1}(y)\Phi_k(y)\mathrm{d}y\, \delta\alpha_{1k} + \cdots + \\
&\quad + \int_0^{y(\ell)} \frac{\partial J}{\partial p_P}(y)\Phi_k(y)\mathrm{d}y\, \delta\alpha_{Pk} \Big) + o(\delta p).
\end{aligned} \tag{83}$$

Since δJ can also be expressed as

$$\begin{aligned}
\delta J &= \sum_{k=0}^{K-1} \Big(\frac{\partial J}{\partial \alpha_{1k}}\delta\alpha_{1k} + \frac{\partial J}{\partial \alpha_{2k}}\delta\alpha_{2k} \\
&\quad + \cdots + \frac{\partial J}{\partial \alpha_{Pk}}\delta\alpha_{Pk} \Big) + o(\delta p),
\end{aligned} \tag{84}$$

the sought analytical gradients $\frac{\partial J}{\partial \alpha_{ik}}$ can be identified by comparing (83) and (84), that is,

$$\frac{\partial J}{\partial \alpha_{ik}} = \int_0^{y(\ell)} \frac{\partial J}{\partial p_i}(y)\Phi_k(y)\mathrm{d}y. \tag{85}$$

Thus, $\frac{\partial J}{\partial \alpha_{ik}}$ can be thought of as the projection of $\frac{\partial J}{\partial p_i}(y)$ onto the basis functions.

References

[1] S. Galli and D.L. Waring, "Loop makeup identification via single ended testing: beyond mere loop qualification," *IEEE Journal of Selected Areas in Communications*, vol. 20, No. 5, pp. 923–935, June 2002.

[2] T. Vermeiren, T. Bostoen, F. Louage, P. Boets, and X.O. Chehab, "Sub-scriber loop topology classification by means of time-domain reflectom-etry," *IEEE International Conference on Communications*, Anchorage, USA, 11-15 May, 2003.

[3] L. Van Biesen, P. Boets, F. Louage, and T. Bostoen, "Expert system for the identification and classification of the local loop," *10th IMEKO TC7 International Symposium*, Saint-Petersburg, Russia, June 30-July 2, 2004.

[4] K. Kerpez and S. Galli, "Single-ended loop make-up identification. Part I: A method of analyzing TDR measurements," *IEEE Transactions on Instrumentation and Measurement*, vol. 55, no. 2, pp. 528–537, Apr. 2006.

[5] K. Kerpez and S. Galli, "Single-ended loop make-up identification. Part II: Improved algorithms and performance results," *IEEE Transactions on Instrumentation and Measurement*, vol. 55, no. 2, pp. 538–549, Apr. 2006.

[6] P. Boets, T. Bostoen, L. Van Biesen, and T. Pollet, "Preprocessing of signals for single-ended subscriber line testing," *IEEE Transactions on Instrumentation and Measurement*, vol. 55, no. 5, pp. 1509–1518, Oct. 2006.

[7] C. Neus, P. Boets, and L. Van Biesen, "Feature extraction of one port scattering parameters for single ended line testing," *XVIII IMEKO World Congress*, 2006.

[8] T. Bostoen, P. Boets, M. Zekri, L. Van Biesen, T. Pollet, and D. Rabijns, "Estimation of the transfer function of a subscriber loop by means of one-port scattering parameter measurement at the central office," *IEEE Journal of Selected Areas in Communications*, vol. 20, No. 5, pp. 936–948, June 2002.

[9] F. Lindqvist and A. Fertner, "Detection and localization of load coils from one-port measurements," *IEEE Transactions on Instrumentation and Measurement*, vol. 59, no. 7, pp. 1972–1982, Jul. 2010.

[10] C. Sales, R.M. Rodrigues, F. Lindqvist, J. Costa, A. Klautau, K. Er-icson, J. Rius i Riu, and P.O. Börjesson, "Line topology identification using multi-objective evolutionary computation," *IEEE Transactions on Instrumentation and Measurement*, vol. 59, no. 3, pp. 715–729, Mar. 2010.

[11] G. Ginis and J.M. Cioffi, "Vectored transmission for digital subscriber line systems," *IEEE Journal on Selected Areas in Communications*, vol. 20, no. 5, pp. 1085–1104, June 2002.

[12] G. Kristensson and R.J. Krueger, "Direct and inverse scattering in the time domain for a dissipative wave equation. Part 1: Scattering operators," *Journal of Mathematical Physics*, vol. 27, no. 6, pp. 1667–1682, 1986.

[13] G. Kristensson and R.J. Krueger, "Direct and inverse scattering in the time domain for a dissipative wave equation. Part 2: Simultaneous reconstruction of dissipation and phase velocity profiles," *Journal of Mathematical Physics*, vol. 27, no. 6, pp. 1683–1693, 1986.

[14] S. He, S. Ström, and V.H. Weston, *Time Domain Wave-Splittings and Inverse Problems*, Oxford University Press, Oxford, 1998 (411 pages; ISBN 0198565496).

[15] J. Lundstedt and S. He, "A time-domain optimization technique for the simultaneous reconstruction of the characteristic impedance, resistance and conductance of a transmission line," *Journal of Electromagnetic Waves and Applications*, vol. 10(4), pp. 581–602, 1996.

[16] J. Lundstedt and S. Ström, "Simultaneous reconstruction of two parameters from the transient response of a nonuniform LCRG transmission line," *J. Electro. Waves Applic.*, vol. 10(1), pp. 19–50, 1996.

[17] M. Norgren and S. He, "An optimization approach to the frequency-domain inverse problem for a nonuniform LCRG transmission line," *IEEE Transaction On Microwave Theory and Techniques*, vol. 44, pp. 1503–1507, 1996.

[18] J. Lundstedt and M. Norgren, "Comparison between frequency domain and time domain methods for parameter reconstruction on nonuniform dispersive transmission lines," *Progress In Electromagnetic Research, PIER 43, 1-37, 2003.*

[19] ITU-T G.996.1, "Test procedures for digital subscriber line (dsl) transceivers," 02/2001.

[20] R.F.M. van den Brink, "Cable reference models for simulating metallic access networks," Tech. Rep., ETSI STC TM6 Permanent document TM6(97)02, June 1998.

[21] T. Starr, J.M. Cioffi, and P.J. Silverman, *Understanding digital subscriber line technology*, Prentice Hall, Upper Saddle River, 1999.

[22] ITU-T G.992.5, "Asymmetric digital subscriber line transceivers - extended bandwidth (adsl2plus)," 05/2003.

[23] ITU-T G.993.2, "Very high speed digital subscriber line transceivers 2 (vdsl2)," 2006.

[24] F. Lindqvist, P.O. Börjesson, P. Ödling, S. Höst, K. Ericson, and T. Magesacher, "Low-order and causal twisted-pair cable modeling by means of the hilbert transform," *RVK08 - The twentieth Nordic Conference on Radio Science and Communications*, Växjö, Sweden, June 9-11, 2008. AIP Conference Proceeding, vol. 1106, pp 301-310.

[25] S. Höst, F. Lindqvist, A. Fertner, K. Ericson, M. Berg, I. Pappa, and P.O. Börjesson, "Low complexity computation of the BT0 Hilbert twisted pair cable model," *15th International OFDM-Workshop (InOWo'10)*, pp. 195–199, Hamburg, Germany, Sep., 2010.

[26] Jorge Nocedal and Stephen J. Wright, *Numerical Optimization*, Springer-Verlag, 1999.

Paper IV

Paper IV

Detection and Localization of Load Coils from One-Port Measurements

Abstract

This paper deals with detection and localization of load coils in the copper access network. The load coil is a legacy device that must be removed before deploying broadband services on the twisted-pair transmission lines. The proposed methods do not require dedicated hardware but utilize the already installed transceivers for one-port measurements of the line input impedance. The number of load coils is detected by counting the number of resonance peaks in the line impedance spectrum. An approximative model of the symmetric loaded line is presented, from which a low-complexity load coil locator is derived. For non-symmetric lines, a load coil locator using model-based optimization is proposed. The two methods are compared and evaluated by computer simulations and by laboratory measurements on real transmission lines. The estimation results indicate that up to five load coils can be robustly detected and located with the proposed methods.

1   Introduction

Many copper-access network operators still have a considerable amount of customers subscribing only on telephony, *i.e.*, the plain old telephone service (POTS). Consequently, there is a great interest in estimating the suitability of the twisted-pair copper lines for broadband services, provided by state-of-the-art digital subscriber line (DSL) technologies as ADSL2+ and VDSL2 [1] [2]. Common impairments that hinders or reduces the full potential of broadband access over these lines are *e.g.* crosstalk ingress due to line impedance unbalance, bridged-taps, and load coils [3]. The far most severe impairment of these are the load coils, which are found on numerous lines in some countries.

The load coil is an inductive device that works like an impedance matching transformer. Telecom operators used to install load coils in order to provide telephony to customers located far from the Central Office (CO). However, at the same time as the load coil reduces the line attenuation at the voice frequencies, it drastically increases the attenuation at higher frequencies [3]. Thus, the load coils must be removed before the line can be deployed for broadband services using the higher frequencies [1] [2].

The operator has few options to *pre-qualify* the lines before investing in, and installing, broadband equipment. Essentially the options involve sending a technician into the field to conduct (expensive) manual testing, or to estimate the transmission line capacity from *e.g.* a database. However, since the original lines were installed decades ago, with various kinds of modifications made throughout the years, databases of the access lines are often non-existing or inaccurate. Hence, a more attractive option for the operator is to employ automated one-port measurements from the CO, referred to as single-ended line testing (SELT).

The existing POTS transceivers have been designed to monitor and diagnose the narrow voice-band $(0 - 4\,\text{kHz})$ by measuring elementary parameters such as DC/AC voltage, the resistance/capacitance at frequency zero between the wires of the line and between each wire and ground. These type of traditional measurements normally require *metallic access* to the line, which is commonly provided by expensive bypass-relays. Even so, far from all POTS transceivers are able to detect and locate load coils. Moreover, conventional DSL modems, with a built-in SELT function [4–10], are not designed to detect the load coils since the access to the lower voice frequencies is normally blocked by the *splitter filter*, required by the co-existence of POTS and DSL transmission [3]. As described in *e.g.* [11], pre-qualification with DSL modems typically fails to distinguish the load coil from a cable-break or the far-end line termination. Consequently, there is a substantial benefit in performing these measurements via the already installed (narrow band)

transceivers carrying POTS, *i.e.*, via the telephone line cards.

Concluding from the referred technical literature [12–17], the proposed methods are primarily oriented towards the detection of load coils while the localization has got less attention. The methods in [12–15] determines whether a line is equipped with load coil(s) or not, *i.e.*, loaded or not, by detecting characteristics in the magnitude or the phase of the measured line impedance. However, localization of the load coil(s) is not addressed. In [17], automated testing of loaded lines with pattern recognition is proposed. The method addresses load coil detection and localization by comparing the line under test with a pre-defined set of classes that represent possible line configurations. A decision space consisting of 20 regions (clusters) are utilized, each corresponding to one class. The mean-square distance to each line class is calculated based on extracted features from the measured line impedance. The line classification is then determined from the minimum class-distance. The number of pre-defined classes is kept low in [17] by assuming small deviation from the original load coil deployment rules. However, this assumption is not always valid due to changes of the access network by *e.g.* reconfigurations, displacement of CO:s and introduction of transceiver-cabinets closer to the customer [5, 18]. These (loaded) lines have more irregular topologies which require a wast number of line-classes to accurately predict the location of the load coils.

In this paper, we study load coil detection and localization based on one-port measurements of the line input impedance. The measurements do not require metallic access and can be performed by a conventional POTS transceiver [19] or by a DSL modem running in all-digital-loop (*e.g.* annexes I and J in [1]) with access to the POTS-band. We start out by presenting an approximative line model for the symmetric twisted-pair line equipped with load coils. The accompanying analysis show that the highest resonance peak of the line impedance spectrum is related to the distance between the CO and the first load coil. By exploiting this fact, a low-complexity load coil locator is obtained for the symmetric loaded lines. The number of present load coils is determined by detecting the number of resonance peaks in the line impedance spectrum. For the more general line topologies, *i.e.*, non-symmetric loaded lines, a load coil locator utilizing model-based optimization is proposed.

The remainder of the paper is organized as follows. Section 2 presents the legacy of the load coil and the deployment rules. Section 3 describes the approximative model of a transmission line with load coils. In Section 4.1 and in Appendix A we derive the low-complexity load coil detector and locator that utilizes the approximative line model. The load coil locator for the non-symmetric lines are described in Section 4.2. In Section 5, an indicator for the level of line symmetry is presented. Section 6 and 7 provide estimation results

from computer simulations and from laboratory measurements on real cables with a conventional POTS transceiver. Finally, a summary and conclusions are given in Section 8.

2   The Legacy of the Load Coil

Historically, the deployment of load coils in the copper access network can be traced back to M. I. Pupin's patent from year 1894, which disclose that load coils inserted periodically in series with a pair of wires reduces the attenuation at the voice frequencies. The common practice in the past, in *e.g.* the U.S., was that lines (loops) longer then 5.5 km (18 kft) were equipped with load coils, whereupon the lines were called *loaded lines*. The load coils were typically placed on the transmission lines at regular intervals of either 1.8 or 1.4 km (6 or 4.5 kft). The first load coil appeared about half of this distance from the CO and the last load coil was typically placed about 1 km (3 kft) from the customer premise (CP) site. The installed load coils were normally 88 or 66 mH inductors. The subscribers (and bridged-taps) were not placed between two load coils.

3   Modeling of Symmetric Loaded Lines

A twisted-pair transmission line is commonly modeled according to the two-port theory, where each section of the line is represented by its *ABCD*-matrix [3]. This type of modeling provides accurate results of *e.g.* the line input impedance and the transfer function, for a broad frequency range. For the low frequencies considered here, the line modeling can be simplified by approximating the line by a low-order electrical circuit with discrete components. Before presenting the approximative modeling in detail we describe the considered prerequisite of the symmetric line topology.

   We assume in this section, based on the deployment rules in Section 2, that the loaded lines are approximately symmetric and that the distance from the CO, and from the CP, to the nearest load coil is approximately half the length between two successive load coils. In case of only one load coil, it is assumed that the length from the CO, and from the CP, to the load coil is roughly equal. We further assume, in all sections of the paper, that the line is terminated by an on-hook POTS phone whose impedance can be considered infinite. Fig. 1 depicts a symmetric twisted-pair line with the load coils inserted periodically in series at definite spaced intervals. Due to the assumed symmetry, the transmission line in Fig. 1 can be seen as a series of

cascaded identical two-port *cells*, where each cell consists of a load coil with two line-sections of length $d/2$ connected at each side.
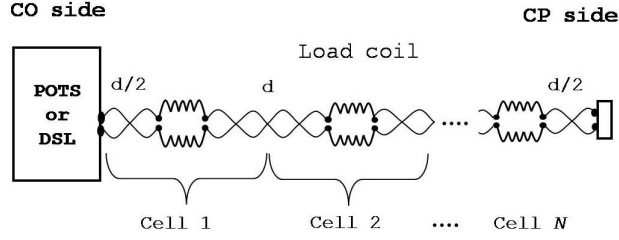
Figure 1: A symmetric twisted-pair line with periodically inserted load coils separated d km apart. The distance from the CO, and from the CP, to the nearest load coil is $d/2$ km.

For the low frequencies considered here, the input impedance of a line containing N load coils can be approximated by a *continued fraction expansion (CFE)* [20]. Subsequently, the line can be viewed as a series of periodically repeated cells of impedances, as illustrated in Fig. 2. In Fig. 2, Z_h denotes the
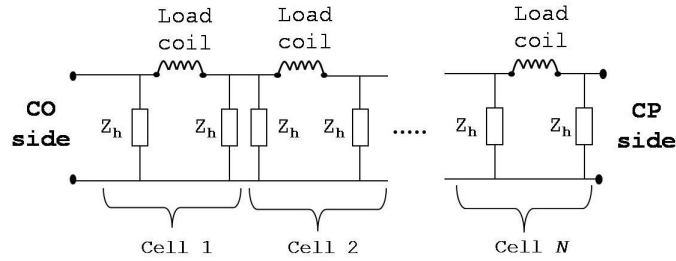
Figure 2: Illustration of a symmetric loaded line approximated by a continued fraction expansion (CFE) of the line input impedance, leading to periodically repeated cells of impedances.

first (and last) shunt impedance of each cell-circuit. The shunt impedance corresponds to the first (and last) line section of length $d/2$ km. Hence, the line section of length d between two successive load coils can be represented by the equivalent parallel-connected shunt impedance $Z_s = Z_h/2$. Without

much loss of generality, we assume here that the line sections are of same cable type. Thus, the input impedance of the N cascaded cells can be expressed as

$$Z_{in}^{(N)} = \cfrac{1}{\cfrac{1}{Z_h} + \cfrac{1}{jwL_c + \cfrac{1}{\frac{1}{Z_s} + \cfrac{1}{jwL_c + ... \frac{1}{jwL_c+Z_h}}}}}, \tag{1}$$

where L_c denotes the load coil inductance and $w = 2\pi f$ is the angular frequency in unit rad/s. It should be emphasized that the frequency dependence of $Z_{in}^{(N)}$, Z_h and Z_s is omitted in the description. As an example we consider the input impedance of a *single cell* ($N = 1$) which yields

$$Z_{in}^{(1)} = \frac{1}{\frac{1}{Z_h} + \frac{1}{jwL_c+Z_h}} = \frac{Z_h(jwL_c + Z_h)}{jwL_c + 2Z_h}. \tag{2}$$

For the general case with N cells, where $N > 1$, the following recursive formula can be derived from (1) after some straightforward manipulations

$$Z_{in}^{(N)} = \frac{1}{\frac{1}{Z_h} + \frac{1}{jwL_c+\frac{Z_h Z_{in}^{(N-1)}}{Z_h+Z_{in}^{(N-1)}}}}, \quad \text{for N = 2, 3, ... ,} \tag{3}$$

where $Z_{in}^{(1)}$ is given by (2). In the simplest form, the impedance Z_h (and Z_s) can be approximated for low frequencies by a line capacitance. Hence, by substituting

$$Z_h = \frac{1}{jwC_{km}(d/2)}, \tag{4}$$

in (3), where C_{km} denotes the line capacitance per km, it is possible to further simplify (3).

Fig. 3 shows the input impedance of a symmetric loaded line modeled according to the two-port theory and with the continued fraction expansion (CFE) in (1). The figure depicts the CFE with the true impedance Z_h and with the approximation in (4). The line consists in this case of a 0.5 mm cable ($C_{km} = 50$ nF/km) with three load coils ($N = 3, L_c = 88$ mH) separated by $d = 1.8$ km, and with a total line length of 5.4 km. From Fig. 3 we observe that the line impedance spectrum contains three significant peaks located in the $1.5 - 4$ kHz frequency band. We further note that the frequency position of the peaks is preserved with the two different CFE modelings, which is an important feature used for load coil localization in Section 4.1.
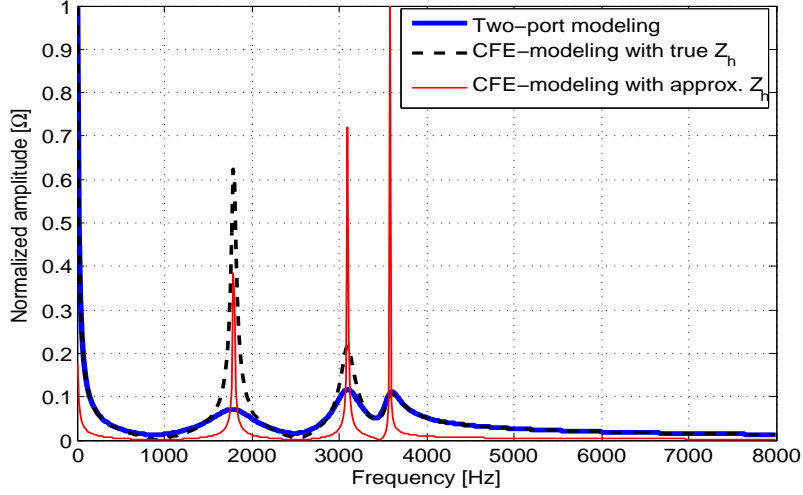
Figure 3: Input impedance of a symmetric twisted-pair line with three load coils, modeled with two-port theory and with the continued fraction expansion (CFE) in (1). Both the true shunt impedance Z_h and the approximation in (4) is shown. The total line length is $5.4\,\mathrm{km}$ and the distance between two neighboring load coils is $d = 1.8\,\mathrm{km}$.

4 Detection and Localization

In this section we first describe a load coil detector and locator for symmetrical lines constructed according to the building practices described in Section 2. In the second subsection we extend the locator by considering the more general case of non-symmetrical loaded lines.

4.1 Symmetric Loaded Lines

The peaks of the line impedance spectrum shown in Fig. 3 are not visible when load coils are not present. However, when load coils are present, the number of peaks in the $0 - 4\,\mathrm{kHz}$ POTS-band corresponds to the number of load coils. This property has also be reported in *e.g.* [12–14]. Hence, by detecting and counting the number of *resonant frequencies* in the POTS-band of the line impedance (spectrum), the presence of load coils and the number of them can be detected. In the following, a relation between the resonant frequencies and the distance from the CO to the first coil is given.

For the single-cell case ($N = 1$), the resonant frequency $f_{r1}^{(1)}$ is found by setting the denominator in (2) equal to zero, which with the approximation in (4) yields

$$f_{r1}^{(1)} = \frac{1}{2\pi} \sqrt{\frac{2}{L_c C_{km}(d/2)}}. \tag{5}$$

It follows from (5) that the distance $d/2$ or d can be estimated from the measured resonant frequency of the line input impedance, and hence, the location of the load coil can be determined. In Appendix A we derive the resonant frequencies for the *two-cells* ($N = 2$) and the *three-cells* ($N = 3$) cases, from which it can be concluded that the highest resonant frequency is identical for $N = 1, 2$ and 3. It is also shown in the Appendix that the *pole* corresponding to the highest resonant frequency is present for all N, *i.e.*, irrespectively of the number of load coils. Consequently, when determining the location of the first load coil of a line with N load coils, *i.e.*, the distance $d/2$, only the the highest resonant frequency need to be considered.

A low-complexity algorithm is proposed to synthesize the above described detection and localization. In summary, the algorithm works as follows. The line input impedance is measured by the transceiver [19]. A monotone decrease in the magnitude of the measured impedance, within the $0 - 4\,\text{kHz}$ frequency band, implies that no load coils are present. A peak in the impedance function indicates the presence of a load coil. The number of present load coils is determined by counting the number of peaks. From the highest measured resonant frequency, the distance $d/2$ from the CO to the first load coil is estimated. Due to the assumed line symmetry, the distance between two successive load coils follows from the estimated d. The proposed algorithm involves finding the maximums of the function $|Z_{in}(f)|$. The maximums of the magnitude function can also easily be determined by identifying the corresponding zero-crossings of the derivative with the following approximation

$$\frac{\partial |Z_{in}|}{\partial w} \approx \frac{\partial \Re\{Z_{in}\}}{\partial w} \Re\{Z_{in}\} + \frac{\partial \Im\{Z_{in}\}}{\partial w} \Im\{Z_{in}\}, \tag{6}$$

where $\Re\{.\}$ and $\Im\{.\}$ denotes the real and the imaginary-part of the argument, respectively. In practice, the derivative in (6) is implemented by finite differences.

4.2   Non-Symmetric Loaded Lines

In case the transmission lines have been modified such that the line-symmetry described in Section 2 is not valid, the accuracy of the CFE-based locator in Section 4.1 decreases. This is due to the frequency-shift of the resonant

peak(s), relative to the symmetric case. Therefore, a second locator algorithm is proposed to handle the non-symmetric lines by utilizing model-based optimization. This comes, however, at the cost of increased complexity. Before detailing the model-based locator, the consequences of applying the CFE-based locator to non-symmetric lines is briefly studied.

Fig. 4 compares the input impedance of a symmetric line with two corresponding non-symmetrical lines. In the two latter cases, the *first* and the *last* cables (seen from the CO) are 30% shorter than $d/2$, respectively. Here, the symmetric line has two load coils separated by $d = 1.8$ km and the total line length is 3.6 km. The two non-symmetric lines have $d = 1.8$ km and a total line length of 3.33 km. That is, the length of the first/last cable is $0.7d/2$ km. From Fig. 4 we observe that the frequencies of the resonant peaks are lower for the symmetric line than for the two non-symmetric lines. It can also be seen that the frequency of the highest resonant peak is the same for the two non-symmetric lines. Thus, for the two non-symmetric lines, the CFE-based locator gives the same (erroneous) estimate of the distance from the CO to
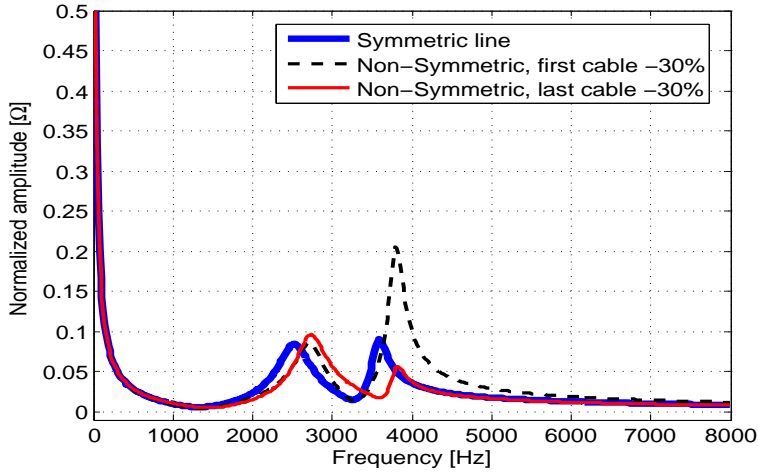
Figure 4: Line input impedance of a symmetric and two non-symmetric twisted-pair lines with two load coils. In first non-symmetric case (dashed), the length of the *first* cable is $0.7d/2$ km, *i.e.*, -30% compared to the symmetric line. In second non-symmetric case (solid thin), the length of the *last* cable is $0.7d/2$ km.

the first load coil.

The proposed load coil locator for non-symmetric lines employs line topology identification with model-based optimization, inspired by the approach in [4]. Here, an assumed cable data base is utilized, as in [5,6], which reduces the complexity of the method. More specifically, the proposed method minimizes the least-squares (LS) error between the measured line input impedance $Z_{in}(f)$ and a line model $Z_{model}(f, \boldsymbol{\theta})$, in order to estimate the *parameter vector* $\boldsymbol{\theta}$. The parameters of $\boldsymbol{\theta}$ represent line properties such as the number of line sections, the section lengths and the cable types. The LS error criterion can be formulated as

$$J(\boldsymbol{\theta}) = \sum_{f=f_{low}}^{f_{high}} \left| Z_{in}(f) - Z_{model}(f, \boldsymbol{\theta}) \right|^2, \tag{7}$$

where the lowest and the highest frequencies are f_{low} and f_{high}, respectively. The solution to this LS problem minimizes the value of $J(\boldsymbol{\theta})$, *i.e.*,

$$\boldsymbol{\theta}_{LS} = \arg\min_{\boldsymbol{\theta}} \; J(\boldsymbol{\theta}). \tag{8}$$

For the model $Z_{model}(f, \boldsymbol{\theta})$ we resort to the previously mentioned two-port theory, where a cable section is modeled by its frequency-dependent *ABCD*-matrix [3]. That is, a serial section is modeled by the matrix

$$\mathbf{M}_s = \begin{bmatrix} A & B \\ C & D \end{bmatrix} = \begin{bmatrix} \cosh(\gamma l) & Z_0 \sinh(\gamma l) \\ \dfrac{\sinh(\gamma l)}{Z_0} & \cosh(\gamma l) \end{bmatrix}, \tag{9}$$

while a load-coil with inductance L_c is modeled by

$$\mathbf{M}_c = \begin{bmatrix} A & B \\ C & D \end{bmatrix} = \begin{bmatrix} 1 & j2\pi f L_c \\ 0 & 1 \end{bmatrix}. \tag{10}$$

In (9) l denotes the section length, γ is the propagation constant [3], and Z_0 is the characteristic impedance [3]. Note that the frequency dependence of γ and Z_0 is omitted in the notation for simplicity. The numerical values of γ and Z_0 are taken from an assumed cable model, such as VUB [4], MAR [21], BT [21] or BT0$_\mathrm{H}$ [22]. All of these cable models have inherent electromagnetic and geometric parameters that characterize the cable insulation material, the resistivity, the wire diameter, etc. For a line composed of several sections, the chain rule [3] is applied to obtain the total transmission matrix $\mathbf{M}$.

That is, for a line with n_s number of line sections, the total (forward) transmission matrix yields

$$\mathbf{M} = \mathbf{M}^{(1)} \times \mathbf{M}^{(2)} \cdots \times \mathbf{M}^{(n_s)}, \tag{11}$$

where line section number s is represented by its transmission matrix $\mathbf{M}^{(s)}$. The input impedance of the line, associated with parameter vector $\boldsymbol{\theta}$, can be expressed as, [3],

$$Z_{in}(f, \boldsymbol{\theta}) = \frac{A(f, \boldsymbol{\theta})Z_T(f) + B(f, \boldsymbol{\theta})}{C(f, \boldsymbol{\theta})Z_T(f) + D(f, \boldsymbol{\theta})}, \tag{12}$$

where A, B, C and D are the elements of matrix $\mathbf{M}$ in (11). These four elements depend, as explicitly stated, on the frequency f and on the parameter vector $\boldsymbol{\theta}$. In (12), $Z_T(f)$ denotes the far-end termination impedance. Since the termination is assumed to be an on-hook POTS phone with approximately infinite impedance, a model for the line input impedance can be obtained by simplifying (12), *i.e.*,

$$Z_{model}(f, \boldsymbol{\theta}) = \frac{A(f, \boldsymbol{\theta})}{C(f, \boldsymbol{\theta})}. \tag{13}$$

Having defined a model for $Z_{in}(f)$ by (13), we now return to the minimization in (8).

Given a loaded line with n_s number of sections, it follows from (9)–(11) that substitution of (13) in (7) leads to a non-linear LS minimization problem in (8), since the model in (13) is not linear in the unknown parameters of $\boldsymbol{\theta}$. Although we propose stochastic optimization to solve (8), the minimization poses a challenge due to the multi-dimensional criterion function with multiple local optima. In general, the success of the solution to this kind of problem depends on several factors as *e.g.* the optimization algorithm, the number of unknown parameters (dimension), boundary constraints, and the amount of available *a priori* information. The strategy adopted herein to lower the complexity of the problem is as follows.

By utilizing the detected number of load coils, obtained with the method described in Section 4.1, the *structure* of the line topology is known prior to the minimization in (8). It thus remains to estimate the section lengths and the type of cables of the loaded line. With an assumed cable data base, as defined in *e.g.* [23], the number of unknown parameters is further reduced to one integer-value per cable type and one length-parameter per line section. That is, for N number of load coils there are $2(N + 1)$ parameters in $\boldsymbol{\theta}$ to be optimized, assuming the inductance of the load coils ($88\,\text{mH}$ or $66\,\text{mH}$) is known *a priori*. In general, one may extend $\boldsymbol{\theta}$ to include the inherent cable model parameters, but at the expense of added complexity of (8).

5 Indication of Line Symmetry

An indication of the level of line-symmetry can be obtained by comparing an (independent) estimate of the *total line length* with the corresponding CFE-based estimate $\hat{N}\hat{d}$, where $\hat{d}$ is the distance between two neighboring load coils and $\hat{N}$ denotes the number of detected load coils. In case these two estimates differ significantly, it is likely that the line under test is non-symmetric. A common way to estimate the total line length, here denoted d_{tot}, is to approximate the measured line input impedance with a capacitance, *i.e.*,

$$Z_{in}(f) \approx \frac{1}{j2\pi f C_{km} d_{tot}}. \tag{14}$$

The approximation in (14) is only valid for low frequencies. It thus follows from (14) that the total line length can be estimated by

$$\hat{d}_{tot} = \frac{-1}{\Im\{Z_{in}(f_{low})\}\, 2\pi f_{low} C_{km}}, \tag{15}$$

where f_{low} is the lowest available measured frequency in Hz and $\Im\{.\}$ denotes the imaginary part.

6 Computer Simulations

By computer simulations we validate the load coil detection and localization algorithms described in Section 4.1 and Section 4.2. The performance of the algorithms is evaluated in this section with simulated cables. We start out considering twisted-pair lines built according to the deployment rules in Section 2. Next, we introduce line asymmetries in terms of shorter/longer end-cables. In all cases, the standardized ETSI cables in [23] are considered, where the cable diameter defines all inherent parameters of the underlying BT [21] cable model. In total there are five ETSI cable types defined in [23]. However, the two extreme ones, *i.e.*, 0.32 mm and 0.90 mm, are normally not used with load coils. Hence, only the cable types denoted ETSI 0.4 mm, ETSI 0.5 mm and ETSI 0.63 mm [23] are used. For the simulations, the line input impedance is computed according to (11)–(12) at 128 equidistant points between 0 and 8 kHz with a frequency spacing of 62.5 Hz. A sampling frequency of 16 kHz is used.

6.1 Symmetric Lines

Table 1 summaries the estimation results for the CFE-based load coil locator applied to symmetric twisted-pair lines with cable type ETSI 0.4 mm.

For the load coil detection, the number of resonant peaks of line impedance spectrum $|Z_{in}(f)|$ is counted, where the highest resonant frequency is denoted $f_{r1}^{(N)}$. Here, N denotes the number of load coils with inductance 88 mH or 66 mH, corresponding to a load coil separation of $d = 1.8$ km and $d = 1.4$ km, respectively. By using (5), (19) and (21), an estimate $\hat{d}/2$ of the distance between the CO and the first load coil is obtained. From the assumption of line symmetry, an estimate $\hat{d}$ of the distance between two successive load coils follows. Similar estimation results as in Table 1 are achieved by instead detecting the zero-crossings of (6).

The estimation results in Table 1 indicate that $\hat{d}/2$ can be estimated with a relative error less than 3 % for all the test cases. It can also be noted that the estimation error is quantized to a finite set of levels due to the discrete frequency points. In fact, the relative error can be decreased for some of the cases in Table 1 if a denser frequency grid is used.

Table 1: ESTIMATION RESULTS OF CFE-BASED DETECTOR AND LOCATOR FOR SYMMETRIC LINES WITH ETSI 0.40 mm AND $C_{km} = 50$ nF/km

N	L_c [mH]	d [km]	$\hat{d}$ [km]	Rel. Error in $\hat{d}/2$ [%]	Res. Peak $f_{r1}^{(N)}$ [Hz]
1	88	1.8	1.814	-0.80	3562.5
1	66	1.4	1.397	0.19	4687.5
2	88	1.8	1.752	2.64	3625.0
2	66	1.4	1.397	0.19	4687.5
3	88	1.8	1.752	2.64	3625.0
3	66	1.4	1.361	2.80	4750.0
4	88	1.8	1.752	2.64	3625.0
4	66	1.4	1.397	0.19	4687.5
5	88	1.8	1.814	-0.80	3562.5
5	66	1.4	1.397	0.19	4687.5

Up to $N = 4$ load coils can robustly be detected with $L_c = 88$ mH and $d = 1.8$ km, for cable ETSI 0.40 mm, while with $N = 5$ only four resonant peaks of $|Z_{in}(f)|$ can be observed as shown in Fig. 5. From this figure it can also be seen that the two peaks around 3.5 kHz are overlapping. The corresponding CFE modeling, shown in Fig. 5, provides insight to where the closely-spaced peaks are located. However, despite the overlapping, the distance estimate becomes accurate with a relative error in $\hat{d}/2$ of only 0.19 %. Even with
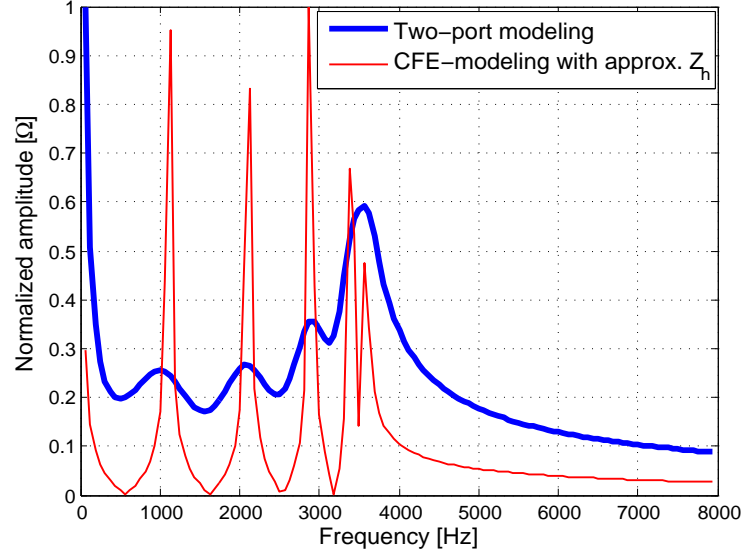
Figure 5: Line input impedance of a symmetric line with $N = 5$ number of load coils of $88\,\mathrm{mH}$, separated by $d = 1.8\,\mathrm{km}$, giving a total line length of $9\,\mathrm{km}$.

a denser frequency grid the two peaks are overlapping. With $L_c = 66\,\mathrm{mH}$ and $d = 1.4\,\mathrm{km}$, up to $N = 5$ load coils can be detected for ETSI cable $0.4\,\mathrm{mm}$. It should be noted that only the POTS frequency band, *i.e.,* up to $4\,\mathrm{kHz}$, is required for the load coil detection, as seen in Fig. 5. For the ETSI cables $0.5\,\mathrm{mm}$ and $0.63\,\mathrm{mm}$ similar results as in Table 1 are achieved, with $C_{km} = 45\,\mathrm{nF/km}$ for the latter cable type [23]. Moreover, for these cables up to $N = 5$ load coils can be detected with $L_c = 88\,\mathrm{mH}$ and $d = 1.8\,\mathrm{km}$.

6.2   Non-Symmetric Lines

Here the load coil locator in Section 4.1 and Section 4.2 are applied to non-symmetric lines. As in the previous section, the detection of load coils is based on counting the peaks of the line impedance spectrum.

6.2.1 Load Coil Location Using CFE

Table 2 shows the estimation results of the CFE-based load coil locator where the first/last cable is 20 % longer than for the symmetric case, *i.e.*, the longer cable is $1.2d/2$ while the other is $d/2$. For all cases, cable type ETSI $0.4\,\text{mm}$ is used. The load coil separation is fixed at $d = 1.8\,\text{km}$ and $L_c = 88\,\text{mH}$ for all cases.

The results in Table 2 highlights two important properties of the method. Firstly, the length estimate is independent of the placement of the asymmetry, *i.e.*, a shorter/longer first cable gives the same result as a shorter/longer last cable. Secondly, for a given level of asymmetry, practically the same distance estimate is achieved irrespectively of the number of load coils (up to number of detectable load coils).

Table 2: ESTIMATION RESULTS OF CFE-BASED LOCATOR FOR NON-SYMMETRIC LINES WITH ETSI 0.40 mm, $L_c = 88mH$, $d = 1.8\,\text{km}$, AND $C_{km} = 50\,\text{nF/km}$

N	First Cable [km]	Last Cable [km]	$\hat{d}$ [km]	Res. Peak $f_{r1}^{(N)}$ [Hz]
1	$1.2d/2$	$d/2$	1.948	3437.5
1	$d/2$	$1.2d/2$	1.948	3437.5
2	$1.2d/2$	$d/2$	1.814	3562.5
2	$d/2$	$1.2d/2$	1.814	3562.5
3	$1.2d/2$	$d/2$	1.814	3562.5
3	$d/2$	$1.2d/2$	1.814	3562.5
4	$1.2d/2$	$d/2$	1.814	3562.5
4	$d/2$	$1.2d/2$	1.814	3562.5

To evaluate the impact of line-asymmetry on the CFE-based locator estimate, the length of the first cable is varied from $0.5d/2$ to $1.5d/2$ while the other line parameters are fixed. This corresponds to varying the distance between the CO and the first load coil from $-50\,\%$ to $+50\,\%$ relative to the symmetric case of $d/2$. The so obtained results in Fig. 6 show, as expected, that the (percentage) error of the length (distance) estimate $\hat{d}/2$ increases with the length-deviation relative to the symmetric case. That is, given a loaded line where the first cable is *e.g.* $0.6d/2$, hence 40 % shorter than the symmetric case, the estimate becomes about 40 % higher than the true value $0.6d/2$. As seen from the figure, the impact is approximately linear with the deviation. From Fig. 6 it can also be noted that for distances larger than

$1.1d/2$ (+10 %), the slope of the curve decreases somewhat. The latter is caused by the highest resonance frequency becoming constant and independent of the increased distance to the first load coil.

In summary, for the considered non-symmetric cases, the CFE-based estimate gives a value somewhere between $d/2$ and the true value, for both positive and negative symmetry-deviations. Hence, accurate localization of the load coils is achieved mainly when the loaded line is fairly symmetric.

The estimator in (15) obtains an estimate of the total line length with an error less than 1 % for all the considered non-symmetric cases in Table 2 and in Fig. 6, given the true C_{km}. This confirms that estimation via (15) is independent of the line symmetry assumption (required by the CFE-based estimator).
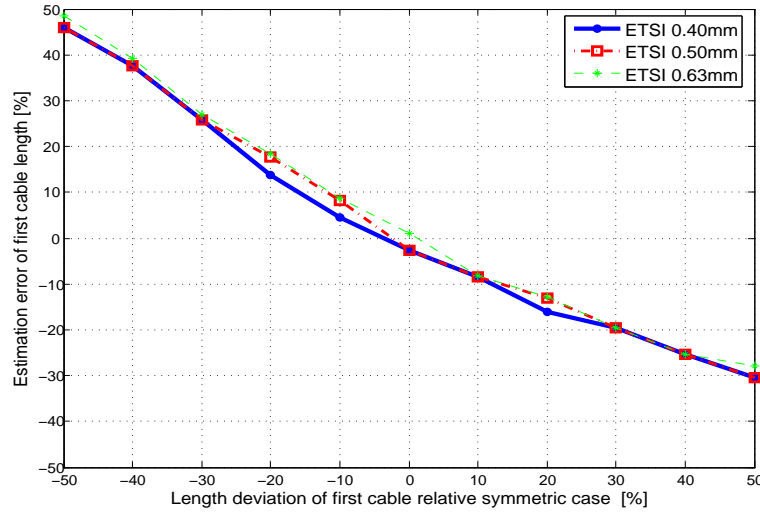
Figure 6: Estimation error of the CFE-based load coil locator for different levels of asymmetries of the loaded line. The distance from the CO to the first load coil is varied from $0.5d/2$ to $1.5d/2$ km, *i.e.,* from -50% to 50% relative to the symmetric case. Here $N = 2$, $L_c = 88mH$ and $d = 1.8$ km.

6.2.2   Load Coil Location Using Model-Based Optimization

For the model-based load coil locator, the minimization of (8) is performed using (ordinary) stochastic optimization with Gaussian adaptation. The employed cable data base consists of ETSI 0.4 mm, ETSI 0.5 mm and

ETSI $0.63\,\mathrm{mm}$ [23], which defines the set of γ and Z_0 for the impedance model in (13).

By using the number of detected load coils, obtained as previously described, the number of sections (cells) of the loaded line is known *a priori*. The applied optimization constraints define the acceptable length interval for the first and the last cables, and the inter-load coil spacing. To comply with network changes and the possible event of a missing load coil [17], we set the intervals for the first and the last cables to $0.3 - 3.0\,\mathrm{km}$ and $0.3 - 3.5\,\mathrm{km}$, respectively. The constrained length between two successive load coils is set to $1.5 - 3.8\,\mathrm{km}$ ($L_c = 88mH$). These optimization constraints are fixed for all test cases. Note that a comparison with [17] would not be meaningful since [17] is based on recognition of line faults rather than estimating the distances to the load coils.

Each test case defines the number of load coils, the cable types, and the length of each serial section counted from the CO towards the CP. For the test cases containing several cable types, the common rule of increasing the cable diameter with the distance from the CO is employed. The result-statistics of the stochastic optimization are assessed by simulating each test cases in Table 3 and Table 4 ten times. The estimation results are given in terms of the mean and the variance of each length estimate for the ten repeated trials. The values are rounded to two decimals and to the nearest power of ten, respectively.

The results in Table 3 validate the method for various simulated line topologies. As can be seen from Table 3, the error of the mean estimated length is less than $100\,\mathrm{m}$ for all cases and in several cases less than $50\,\mathrm{m}$. The low variances of the estimates indicate that the results are robust and that the same, or almost the same, "optimum" is reach for the ten independent runs. With our implementation, the time of convergence is in the order of a couple of seconds on a standard PC (year 2008).

Table 4 shows the estimation results on loaded lines with one load coil completely removed, leading to significantly longer first/last cable or a larger inter-distance between two neighboring load coils. Here $N' = N - 1$ denotes the number of present load coils. The results in Table 4 indicate that the location can be performed accurately also with one load coil missing.

The total line length estimated via (15) gives a relative error less than $3\,\%$ for all test cases in Table 3, with $C_{km} = 50\,\mathrm{nF/km}$. By comparing this estimate with the corresponding CFE-based estimate, which yields a total line length of $\hat{N}\hat{d}$, an indication of the level of symmetry for the line is obtained. More specifically, the CFE-based estimator gives a relative length error between $1.2\,\%$ and $30\,\%$ for Table 3. The lowest error is achieved for the second test case in Table 3 which is fairly symmetric, while the largest error

occurs for the third test case, reflecting the large level of asymmetry. For the test cases in Table 4, the total length estimation via (15) gives a maximum error of 1.4% while the CFE-based total length error lies between 12% and 32%.

Table 3: ESTIMATION RESULTS OF MODEL-BASED OPTIMIZATION FOR SIMULATED NON-SYMMETRIC LINES WITH $L_c = 88mH$

N	Cable Diameter [mm]	Cable Length [km]	Estimated Mean [km]	Estimated Variance [km^2]
1	0.4, 0.4	0.5, 1.2	0.54, 1.11	10^{-3}, 10^{-2}
1	0.4, 0.5	1.5, 1.2	1.49, 1.22	10^{-3}, 10^{-3}
1	0.4, 0.5	1.7, 0.5	1.70, 0.53	10^{-4}, 10^{-3}
2	0.4, 0.4, 0.4	0.5, 1.8, 0.9	0.50, 1.80, 0.92	10^{-4}, 10^{-4}, 10^{-3}
2	0.4, 0.4, 0.4	1.5, 1.7, 0.6	1.50, 1.71, 0.61	10^{-5}, 10^{-4}, 10^{-3}
2	0.4, 0.5, 0.5	1.0, 2.0, 1.0	1.00, 2.00, 1.01	10^{-4}, 10^{-6}, 10^{-3}
3	0.4, 0.4, 0.4, 0.4	0.9, 1.8, 1.5, 1.2	0.90, 1.80, 1.50, 1.20	10^{-13}, 10^{-13}, 10^{-11}, 10^{-11}
3	0.4, 0.5, 0.5, 0.5	1.5, 1.7, 2.0, 0.7	1.49, 1.69, 2.01, 0.72	10^{-4}, 10^{-4}, 10^{-4}, 10^{-3}
3	0.4, 0.4, 0.5, 0.63	0.9, 1.8, 1.9, 0.6	0.90, 1.80, 1.89, 0.56	10^{-7}, 10^{-7}, 10^{-5}, 10^{-3}
4	0.4, 0.4, 0.4, 0.4, 0.4	0.8, 1.8, 1.9, 2.0, 1.1	0.80, 1.80, 1.90, 2.01, 1.11	10^{-7}, 10^{-7}, 10^{-5}, 10^{-3}, 10^{-3}
4	0.4, 0.4, 0.4, 0.5, 0.63	0.7, 1.7, 2.0, 1.6, 1.0	0.70, 1.70, 1.99, 1.61, 0.95	10^{-7}, 10^{-6}, 10^{-5}, 10^{-3}, 10^{-3}
4	0.4, 0.4, 0.5, 0.5, 0.63	1.2, 1.7, 1.7, 1.9, 1.0	1.20, 1.70, 1.71, 1.86, 0.94	10^{-4}, 10^{-2}, 10^{-3}, 10^{-3}, 10^{-3}

Table 4: ESTIMATION RESULTS OF MODEL-BASED OPTIMIZATION FOR SIMULATED NON-SYMMETRIC LINES WITH ONE MISSING LOAD COIL, $L_c = 88mH$

N'	Cable Diameter [mm]	Cable Length [km]	Estimated Mean [km]	Estimated Variance [km^2]
1	0.40, 0.50	2.7, 1.0	2.70, 1.04	10^{-4}, 10^{-3}
1	0.40, 0.50	0.9, 3.2	0.90, 3.13	10^{-5}, 10^{-2}
2	0.40, 0.40, 0.50	2.7, 1.8, 1.0	2.80, 1.87, 1.00	10^{-2}, 10^{-2}, 10^{-3}
2	0.40, 0.40, 0.50	0.9, 1.8, 3.2	0.91, 1.78, 3.31	10^{-4}, 10^{-3}, 10^{-2}
2	0.40, 0.40, 0.50	0.9, 3.6, 1.2	0.89, 3.60, 1.14	10^{-3}, 10^{-2}, 10^{-1}
3	0.40, 0.40, 0.50, 0.63	2.7, 1.8, 1.8, 1.0	2.71, 1.79, 1.80, 0.97	10^{-2}, 10^{-2}, 10^{-2}, 10^{-2}
3	0.40, 0.40, 0.50, 0.50	0.9, 1.8, 1.8, 3.0	0.90, 1.79, 1.80, 2.98	10^{-5}, 10^{-4}, 10^{-5}, 10^{-2}
3	0.40, 0.40, 0.50, 0.50	0.9, 3.6, 1.8, 1.4	0.90, 3.55, 1.80, 1.36	10^{-6}, 10^{-3}, 10^{-2}, 10^{-3}
3	0.40, 0.40, 0.50, 0.50	0.9, 1.8, 3.6, 1.4	0.90, 1.80, 3.54, 1.31	10^{-6}, 10^{-5}, 10^{-3}, 10^{-3}

7   Laboratory Measurements

In this section, estimation results are presented based on laboratory measurements conducted with a traditional POTS transceiver through a splitter-filter limited to the $300 - 3800$ Hz frequency band.

7.1   Setup

The transceiver uses a sampling frequency of 8 kHz and measures the frequency response of the line input impedance at 32 equidistant points, with a frequency spacing of 125 Hz. Since many twisted-pair cables for telecommunication have a line capacitance between $40-50$ nF/km [23] we set parameter C_{km} to the average value of 45 nF/km. In order to validate the two load coil locator algorithms described in Section 4.1 and Section 4.2, the loaded lines are built according to the symmetric deployment rules in Section 2 with one,

two, and three 88 mH load coils, whose inductance L_c we assume known. Due to restrictions of the available cables, the shortest cable length is 1 km. This gives a line length of the first and last cable of $d/2 = 1$ km, respectively, and the length between two successive load coils is $d = 2$ km. Hence, the total line length is 2 km with one load coil, 4 km with two load coils, and 6 km with three load coils.

7.2   Estimation Using CFE

Fig. 7, 8 and 9 show the measured line input impedance and the corresponding approximative derivative in (6). The detected resonant frequencies are marked with circles at the zero-crossings of the derivative, where each circle corresponds to one detected load coil. The highest measured resonant frequency at the zero-crossing is: 3518 Hz, 3546 Hz and 3517 Hz, respectively. By using (5), (19) and (21), the estimate of the distance between the CO and the first load coil yields: 1034 m, 1017 m and 1034 m, respectively. Thus, the relative estimation error of the locator is in this case: 3.4 %, 1.7 % and 3.4 %, respectively. Since the loaded line is assumed symmetric it follows that the other load coils can be localized accurately too. For the used cable types and lengths, up to three load coils could robustly be detected.
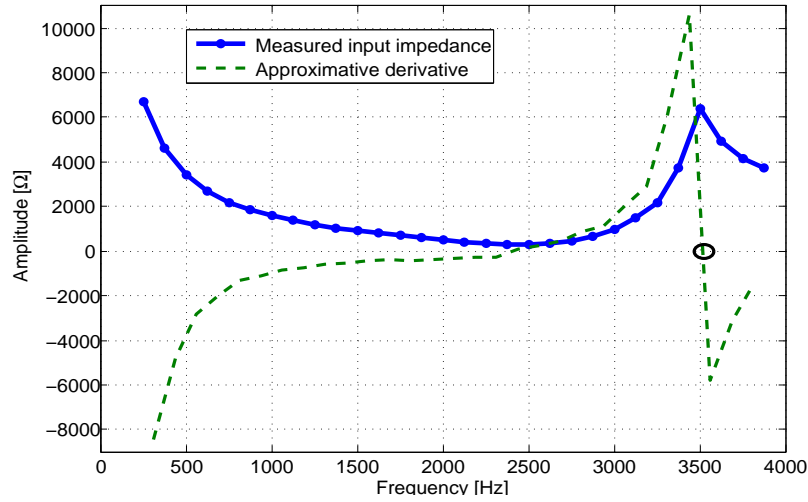
Figure 7: Line input impedance measured with a POTS transceiver for a symmetric line with one load coil and with a total line length of 2000 m ($d/2 = 1000$ km).
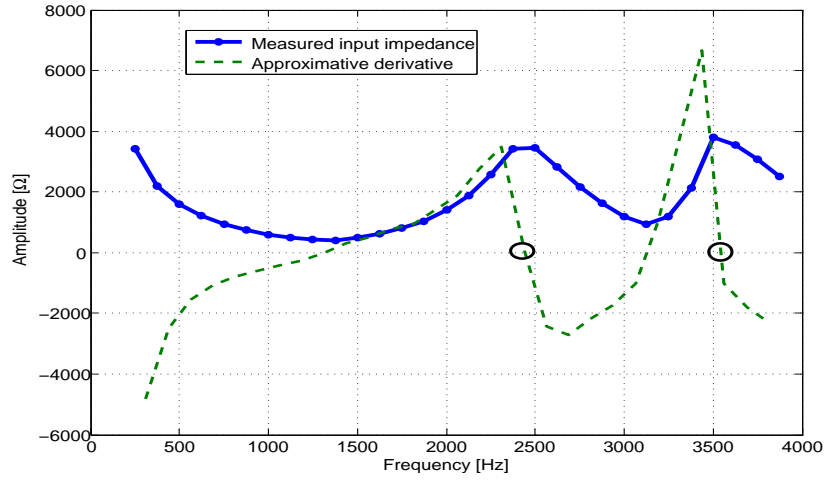
Figure 8: Line input impedance measured with a POTS transceiver for a symmetric line with two load coils and with a total line length of $4000\,\mathrm{m}$ ($d/2 = 1000\,\mathrm{km}$).
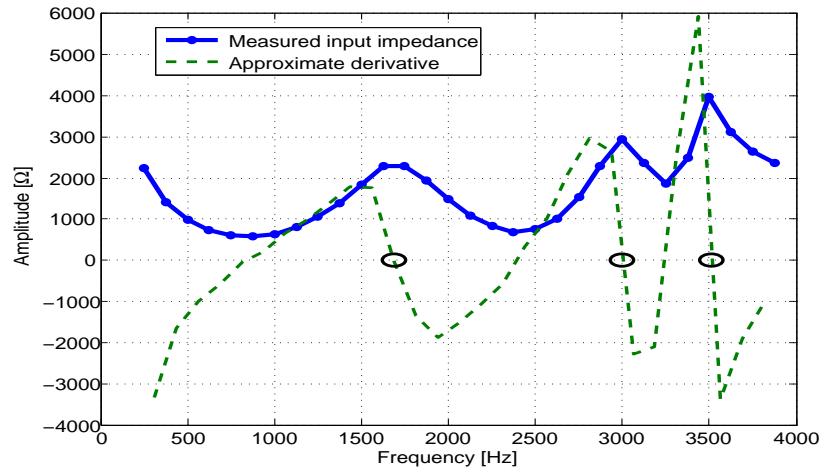
Figure 9: Line input impedance measured with a POTS transceiver for a symmetric line with three load coils and with a total line length of $6000\,\mathrm{m}$ ($d/2 = 1000\,\mathrm{km}$).

7.3 Estimation Using Model-Based Optimization

For the estimation on real cables, we employ the cable data base and the optimization constraints defined in Section 6. Fig. 10, 11 and 12 depict the measured line impedance and the corresponding estimated impedance of the optimized model after the convergence. From the figures it can be concluded that the optimized model follows the curvature of the measurement quite closely. The non-perfect model fit is mainly due to the difference between the real cables and the cable data base. The resulting length estimates are listed in Table 5. As in previous section, the mean value and the variance of each estimated section length is presented. From the results of Table 5 we note that the distance to the first load coil is within 100 m for all cases, *i.e.*, with a relative error less than 10 %. The same accuracy is achieved for the distances between two neighboring load coils. The length of the last cable seen from the CO is estimated with a relative error of maximum 2 %.
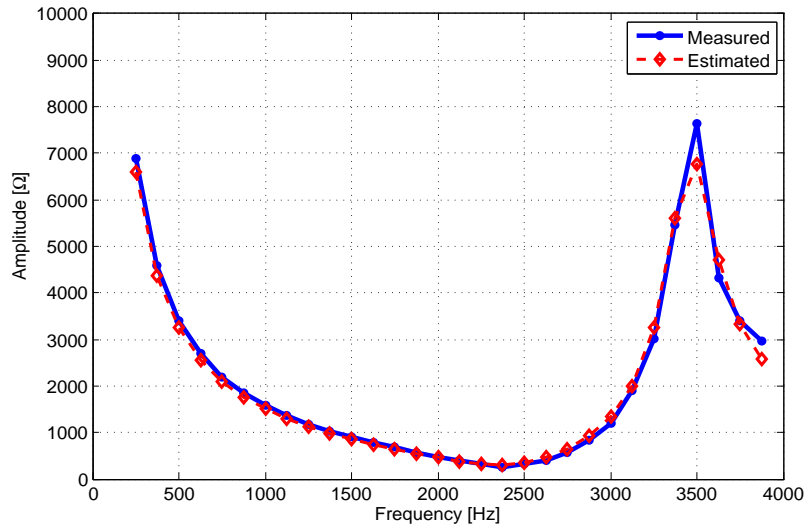
Figure 10: Line input impedance measured with a POTS transceiver and the corresponding estimate obtained with model-based optimization. The line has one load coil and a total line length of 2000 m ($d/2 = 1000$ km).
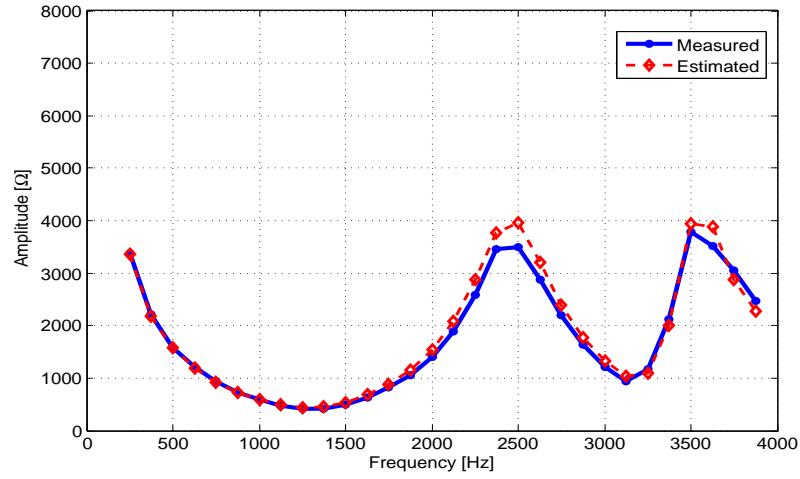
Figure 11: Line input impedance measured with a POTS transceiver and the corresponding estimate obtained with model-based optimization. The line has two load coils and a total line length of $4000\,\mathrm{m}$ ($d/2 = 1000\,\mathrm{km}$).
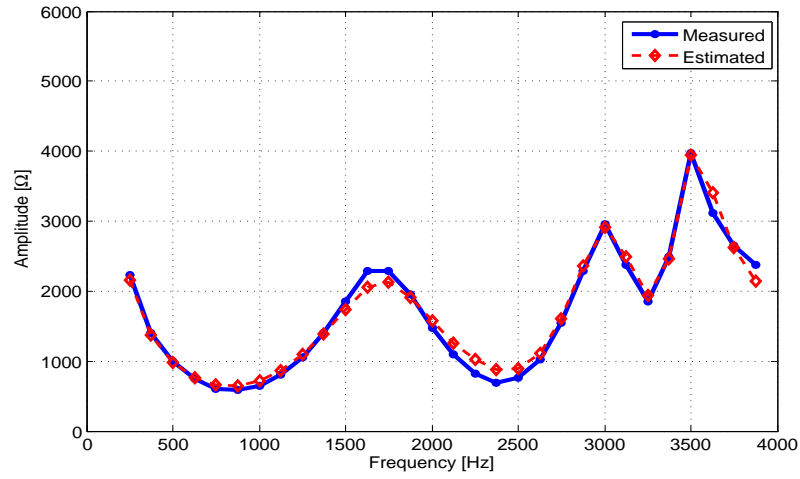
Figure 12: Line input impedance measured with a POTS transceiver and the corresponding estimate obtained with model-based optimization. The line has three load coils and a total line length of $6000\,\mathrm{m}$ ($d/2 = 1000\,\mathrm{km}$).

Table 5: ESTIMATION RESULTS OF MODEL-BASED OPTIMIZATION ON REAL CABLES WITH $L_c = 88mH$

| N	Cable Diameter [mm]	Cable Length [km]	Estimated Mean [km]	Estimated Variance [km^2]
1	0.40, 0.40	1.0, 1.0	0.94, 1.01	10^{-4}, 10^{-3}
2	0.40, 0.40, 0.40	1.0, 2.0, 1.0	0.91, 1.81, 0.98	10^{-14}, 10^{-14}, 10^{-14}
3	0.40, 0.40, 0.40, 0.40	1.0, 2.0, 2.0, 1.0	0.92, 1.83, 2.01, 0.99	10^{-4}, 10^{-4}, 10^{-3}, 10^{-3}

8   Summary and Conclusions

The proposed method detects the number of present load coils by counting the number of resonance frequencies in the one-port measurement of the line impedance spectrum. An approximative line model based on continued fraction expansion (CFE) of the input impedance of a symmetric loaded line was presented. From this model, a low-complexity load coil locator was derived. To handle non-symmetric loaded lines, caused by changes of the access network, a second load coil locator was described. This locator uses, combined with the detected number of load coils, a model-based approach with optimization. The load coil detector and locator algorithms were evaluated on simulated cables and on real cables with measurements obtained by a traditional (narrow-band) POTS transceiver. Up to three or five load coils, dependent on the cable type and length, could robustly be detected with the test-system. The load coil location estimation show accurate results for the tested lines. The CFE-based location estimates decrease, as expected, in case of non-symmetric loaded lines. An indicator for the level of line symmetry was described, showing satisfactory test results. Based on this indicator, an automated selection between the proposed algorithms seems feasible. Furthermore, the test results indicate that the model-based load coil locator is capable of locating all the load coils even when one load coil is missing (fault-case).

Appendix A

For a symmetric loaded line with *two-cells* ($N = 2$), the input impedance given by (3) yields

$$Z_{in}^{(2)} = \cfrac{1}{\cfrac{1}{Z_h} + \cfrac{1}{jwL_c + \cfrac{1}{\frac{1}{Z_s} + \frac{1}{jwL_c + Z_h}}}}$$

$$= \cfrac{1}{\cfrac{1}{Z_h} + \cfrac{jwL_c + Z_h + Z_s}{jwL_c(jwL_c + Z_h + Z_s) + Z_s(jwL_c + Z_h)}}. \qquad (16)$$

By introducing the notation $Z_{in}^{(2)} = \frac{N_Z^{(2)}}{D_Z^{(2)}}$, we find after some manipulations of (16) that the numerator can be expressed as

$$N_Z^{(2)} = Z_h(jwL_c(jwL_c + Z_h + Z_s) + Z_s(jwL_c + Z_h)),$$

and the denominator

$$\begin{aligned} D_Z^{(2)} &= jwL_c(jwL_c + Z_h + Z_s) + Z_s(jwL_c + Z_h) \\ &+ Z_h(jwL_c + Z_h + Z_s). \end{aligned} \qquad (17)$$

By using the fact that $Z_s = Z_h/2$, it follows that the denominator in (17) can be factored as

$$D_Z^{(2)} = (jwL_c + 2Z_h)(jwL_c + Z_h). \qquad (18)$$

By setting $D_Z^{(2)} = 0$, and substituting (4) in (18), we get the following two resonance frequencies, *i.e.,* pole frequencies,

$$f_{r1}^{(2)} = \frac{1}{2\pi}\sqrt{\frac{2}{L_c C_{km}(d/2)}}, \quad f_{r2}^{(2)} = \frac{1}{2\pi}\sqrt{\frac{1}{L_c C_{km}(d/2)}}, \qquad (19)$$

where C_{km} is the capacitance per km and d is the distance between the load coils. Similarly, for a loaded line with *three-cells* ($N = 3$) it can straightforwardly be shown that the denominator of $Z_{in}^{(3)} = \frac{N_Z^{(3)}}{D_Z^{(3)}}$ can be expressed as

$$D_Z^{(3)} = (jwL_c + 2Z_h)(jwL_c + 3Z_h/2)(jwL_c + Z_h/2). \qquad (20)$$

Hence, we get the following three resonance frequencies for the *three-cells* case

$$
\begin{aligned}
f_{r1}^{(3)} &= \frac{1}{2\pi}\sqrt{\frac{2}{L_c C_{km}(d/2)}}, \quad f_{r2}^{(3)} = \frac{1}{2\pi}\sqrt{\frac{3/2}{L_c C_{km}(d/2)}}, \\
f_{r3}^{(3)} &= \frac{1}{2\pi}\sqrt{\frac{1/2}{L_c C_{km}(d/2)}}.
\end{aligned}
\tag{21}
$$

It can be concluded from (2), (18) and (20) that the symmetric lines with $N = 1, 2$ and 3 have the factor $(jwL_c + 2Z_h)$ in common. Apparently, this factor corresponds to the highest resonance frequency of the input impedance.

In the following we show that the factor $(jwL_c + 2Z_h)$ is common for all symmetric loaded lines, independent of N. We already proved in (2) the base case of $N = 1$. Let us assume that the statement is also true for any arbitrary positive integer k, and we show that it is also true for $k + 1$. That is, for any integer $k > 0$ it follows from (3) that

$$
\begin{aligned}
Z_{in}^{(k+1)} &= \frac{1}{\frac{1}{Z_h} + \frac{1}{jwL_c + \frac{Z_h Z_{in}^{(k)}}{Z_h + Z_{in}^{(k)}}}} \\
&= \frac{jwL_c Z_h^2 + (jwL_c + Z_h)Z_h Z_{in}^{(k)}}{jwL_c Z_h + Z_h^2 + (jwL_c + 2Z_h)Z_{in}^{(k)}}.
\end{aligned}
\tag{22}
$$

By substituting $Z_{in}^{(k)} = \frac{N_Z^{(k)}}{D_Z^{(k)}}$ in (22) yields

$$
Z_{in}^{(k+1)} = \frac{D_Z^{(k)} jwL_c Z_h + N_Z^{(k)}(jwL_c + Z_h)Z_h}{D_Z^{(k)}(jwL_c Z_h + Z_h^2) + N_Z^{(k)}(jwL_c + 2Z_h)}.
\tag{23}
$$

From (23) it can be observed that if $Z_{in}^{(k)}$ has a pole at $w = w_0$, then the denominator of $Z_{in}^{(k+1)}$ yields $D_Z^{(k+1)} = N_Z^{(k)}(jw_0 L_c + 2Z_h)$. From this it follows that $(jw_0 L_c + 2Z_h)$ must also be a pole for $Z_{in}^{(k+1)}$. This completes the proof.

References

[1] ITU-T G.992.5, "Asymmetric digital subscriber line transceivers - extended bandwidth (adsl2plus)," 05/2003.

[2] ITU-T G.993.2, "Very high speed digital subscriber line transceivers 2 (vdsl2)," 2006.

[3] T. Starr, J.M. Cioffi, and P.J. Silverman, *Understanding digital subscriber line technology*, Prentice Hall, Upper Saddle River, 1999.

[4] T. Bostoen, P. Boets, M. Zekri, L. Van Biesen, T. Pollet, and D. Rabijns, "Estimation of the transfer function of a subscriber loop by means of one-port scattering parameter measurement at the central office," *IEEE Journal of Selected Areas in Communications*, vol. 20, No. 5, pp. 936–948, June 2002.

[5] S. Galli and D.L. Waring, "Loop makeup identification via single ended testing: beyond mere loop qualification," *IEEE Journal of Selected Areas in Communications*, vol. 20, No. 5, pp. 923–935, June 2002.

[6] K. Kerpez and S. Galli, "Single-ended loop make-up identification. Part I: A method of analyzing TDR measurements," *IEEE Transactions on Instrumentation and Measurement*, vol. 55, no. 2, pp. 528–537, Apr. 2006.

[7] K. Kerpez and S. Galli, "Single-ended loop make-up identification. Part II: Improved algorithms and performance results," *IEEE Transactions on Instrumentation and Measurement*, vol. 55, no. 2, pp. 538–549, Apr. 2006.

[8] T. Vermeiren, T. Bostoen, F. Louage, P. Boets, and X.O. Chehab, "Subscriber loop topology classification by means of time-domain reflectometry," *IEEE International Conference on Communications*, Anchorage, USA, 11-15 May, 2003.

[9] L. Van Biesen, P. Boets, F. Louage, and T. Bostoen, "Expert system for the identification and classification of the local loop," *10th IMEKO TC7 International Symposium*, Saint-Petersburg, Russia, June 30-July 2, 2004.

[10] P. Boets, L. Van Biesen, T. Bostoen, and D. Gardan, "Single-ended line testing - a white box approach," *Proceedings of the 4th IASTED International Multi-Conference, Wireless and Optical Communications*, July 8-10, 2004, Banff, Canada.

[11] Sunrise Telecom Incorporated, "SunSet xDSL application series: TDR - testing techniques for DSL circuits, publication number APP-XDSL-004 Rev.A," 2001.

[12] Godwin et al., "Method and apparatus to determine whether a subscriber line is loaded or non-loaded," US patent number 4620068, 1986.

[13] Jai H. Eu, "Digital measurement of amplitude and phase of sinusoidal signal and detection of load coil based on said measurement," US patent number 5404388, 1995.

[14] J. Kamali and B.H. Khalaj, "Single ended line probing in DSL system," US patent number 6668041, 2003.

[15] Sunrise Telecom Incorporated, "SunSet xDSL application series: load coil testing, publication number APP-XDSL-012 Rev.B," 2001.

[16] V. Demjanenko and A. Torres, "ITU - Telecommunication standardization sector temporary document WH-095," Study Group 15, Waikiki, Hawaii, USA, 29 June - 3 July, 1998.

[17] W.T. Bisignani, "Automated loaded transmission-line testing using pattern recognition techniques," *IEEE Transaction on Instrumentation and Measurement*, vol. IM-24, No.1, pp. 1–4, 1975.

[18] Cornet Technology Inc., "Digital subscriber line (DSL) testing," Web Forum Tutorial, http://www.iec.org, 2007.

[19] A. Fertner, et al., "Automated narrowband one-port measurements," *To be submitted*, .

[20] M. Abramowitz and I.A. Stengun, *Handbook of Mathematical Functions*, United States department of commerce, national bureau of standards, applied mathematics series 55, 9th printing, New York: Dover, 1972.

[21] R.F.M. van den Brink, "Cable reference models for simulating metallic access networks," Tech. Rep., ETSI STC TM6 Permanent document TM6(97)02, June 1998.

[22] F. Lindqvist, P.O. Börjesson, P. Ödling, S. Höst, K. Ericson, and T. Magesacher, "Low-order and causal twisted-pair cable modeling by means of the hilbert transform," *RVK08 - The twentieth Nordic Conference on Radio Science and Communications*, Växjö, Sweden, June 9-11, 2008. AIP Conference Proceeding, vol. 1106, pp 301-310.

[23] ITU-T G.996.1, "Test procedures for digital subscriber line (dsl) transceivers," 02/2001.

Paper V

Paper V

Line Topology Identification using Multi-Objective Evolutionary Computation

Abstract

The broadband capacity of the twisted-pair lines varies strongly within the copper access network. It is therefore important to assess the ability of a digital subscriber line (DSL) to support the DSL services prior to deployment. This task is handled by the line qualification procedures, where the identification of the *line topology* is an important part. The current work presents a new method, denoted TIMEC, for line topology identification where either one-port measurements or both one-port and two-port measurements are utilized. The measurements are input to a model-based multi-objective criterion that is minimized by a genetic algorithm in order to provide an estimate of the line topology. The inherent flexibility of the TIMEC enables incorporation of *a priori* information, as e.g. the total line length. The performance of the TIMEC is evaluated by computer simulations with varying degree of information. A comparison with a state-of-the-art method indicates that TIMEC achieves better results, for all the tested lines, when only one-port measurements are used. The results are improved when employing both one-port and two-port measurements. If a rough estimate of the total length is also used, near-perfect estimation is obtained for all tested lines.

1   Introduction

Throughout the years, several types of digital subscriber line (DSL) technologies have been standardized for broadband data transmission on the twisted-pair lines (loops), such as asymmetric digital subscriber line (ADSL) and very-high-bit-rate digital subscriber line (VDSL). The broadband capacity of the lines varies strongly within the copper access network since it was originally designed for narrowband analog transmission, i.e., plain old telephony service (POTS). Features such as bridged-taps, load coils and mixed cable types [1], have been introduced in the network to improve or extend the POTS. For DSL transmission, however, that exploits a much wider frequency range, these features affect the service quality. It is therefore important to assess the ability of a line to support the DSL services prior to deployment. This task is handled by the line qualification (LQ) procedures.

The existing POTS equipments are normally limited to the bandwidth from DC up to 4 kHz. This fact makes them less suitable for accurately qualifying a line for broadband transmission. Several new broadband techniques targeting LQ for DSL have therefore been proposed in e.g. [2–5]. The legacy POTS methods for LQ are typically restricted to estimating the total line length. Service activation is then based on pre-defined deployment rules, which define the maximum line lengths for proper deployment of a specific DSL service [6]. Alternatively, the topology of the line under test can be identified, which corresponds to the determination of the number of sections, wire diameter (gauge) and length of each section. The line topology identification also includes identifying the number of bridged-taps (if they exist), as well as their positions and lengths. Although this is a challenging task, an accurate estimate of the line topology enables efficient line qualification, whereupon any existing line databases can be corrected and updated. The databases can thereafter be used for support-engineering, provisioning and maintenance operations [4].

Line topology identification methods may employ two kinds of testing approaches: single-ended line testing (SELT), where one-port measurements are performed from e.g. the central office (CO) side of the line, and double-ended line testing (DELT) which is based on two-port measurements that require communication between the CO and the customer premises (CP) equipment. Most line topology identification methods presented in the literature are focused on SELT with time-domain reflectometry (TDR) or frequency-domain reflectometry (FDR). Both techniques are based on transmitting a probe signal followed by posterior analysis of the occurring reflection trace [4,7]. In [2], a model to analyze the real and spurious echoes is proposed, as well as a way to extract the intrinsic slowly decaying signal from the reflectogram.

This enables improved detection of weak echoes. In [4], an iterative de-embedding process for the TDR reflectogram is proposed, where the type of discontinuities is first identified, using a database and the mean squared error (MSE) criterion, followed by an estimate of the section lengths. In [8], the method in [4] is evaluated using measurements obtained via differential TDR. The line topology identification approach in [9] is based on the measured one-port scattering parameter $S_{11}(f)$. This approach utilizes pre-processing to obtain an appropriate time domain response $s_{11}(t)$ [5], from which important features are extracted such as time delay, amplitude, and energy, [9,10]. The extracted features are further used by an automated interpreting system, based on Bayesian networks, in order to estimate the line topology. In [3], a DELT method for bridged-tap location using transfer function measurements is described. Previously, this method would have been impractical for mass deployment due to the high cost of dedicated equipment necessary at the customer sides. However, with the recent advent of the ITU-T standards for ADSL2 and ADSL2+, [11,12], DELT has become a mandatory facility, denoted Loop Diagnostic in [11, 12]. Thus, standard compliant modems, located at the customer side, can communicate with the modem at the CO-side, in order to perform DELT. Measurements such as two-port channel transfer function $H(f)$ is possible via DELT, where the lower frequency part is measured from CP to CO and the upper part is measured from CO to CP.

Some of the previously published line topology identification methods rely on *a priori* information to achieve accurate results. This information can consists of e.g. a database of installed cables or the frequency-dependent velocity of propagation. It is intuitive that *a priori* information can be helpful, but in many practical applications such information is not available or not reliable. Hence, it is desirable to design methods that are not dependent on *a priori* information, but at the same time flexible to accommodate such information when available.

The present work describes a methodology for line topology identification employing SELT and, if supported, DELT. The proposed method utilizes the obtained one-port and two-port measurements in order to compose a model-based multi-objective criterion. The criterion is minimized by a specialized version of the non-dominated sorting genetic algorithm (NSGA-II) [13] that seeks the topology that best matches the defined criterion. The inherent flexibility of the proposed method allows integration of available *a priori* information. The proposed method is evaluated by computer simulations, based on either one-port measurements or both one-port and two-port measurements. The performance of the proposed method is evaluated by computer simulations with varying degree of information. By using simulated measurements, a controlled environment is established, suitable for result analysis.

The remainder of this paper is organized as follows: Section 2 provides a description of the proposed line topology identification method. Section 3 presents the specializations done on the conventional genetic algorithm (GA) in order to improve the rate of convergence and the accuracy. Section 4 presents the simulation results for the test lines. Finally, a summary and conclusions are given in Section 5.

2 Proposed Method

The proposed method estimates the line topology based on two frequency-dependent quantities: the SELT measured scattering parameter $\hat{S}_{11}$ and the DELT measured transfer function $\hat{H}$. The frequency-dependence of these quantities is omitted in the notation for simplicity. Alternatively, the SELT measured input impedance of the line could be used in place of $\hat{S}_{11}$, but this work will assume $\hat{S}_{11}$. In case only SELT measurements are available, the transfer function and associated formulas, described below, are not used. Specifically, the task is to estimate the set of parameters Θ that characterize (model) a given line. In this work, Θ is defined as the set containing:

- number of line sections, n_s;

- length of each section, l;

- gauge (diameter) of each section, g;

- type of each section (boolean), b, i.e. serial or bridged-tap;

as illustrated in Fig. 1. More specifically, Θ is a set of subsets, i.e., $\Theta = \left\{ \theta^{(1)}, \theta^{(2)}, ..., \theta^{(n_s)} \right\}$ where the subset $\theta^{(k)} = \left\{ l^k, g^k, b^k \right\}$ contains the length, gauge and type of the *k-th* section.
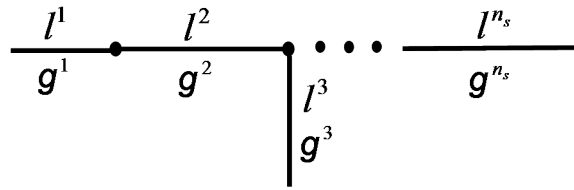
Figure 1: Set of parameters Θ of a given line to be determined. In this example, the third section of the illustrative line is a bridged-tap while the first, the second, and the last ones are *serial*.

For the estimation, an *analysis-by-synthesis* process is adopted in the current work. That is, for a given candidate solution Θ and an assumed cable model, the classic two-port network theory (see e.g., [1]) is used to derive the corresponding modeled S_{11} and H. These two quantities are then compared to the measured $\hat{S}_{11}$ and $\hat{H}$, using the objective (cost) functions $V_H(\Theta)$ and $V_{S_{11}}(\Theta)$. The true parameters will be denoted by $\Theta^\dagger$ while a candidate solution is denoted by Θ. A GA-based optimization routine then iteratively seeks the best solution Θ^* based on the two objective functions. The goal is to obtain $\Theta^* = \Theta^\dagger$, but imperfections on measurements and/or modeling can obviously impact the results. The current work considers only errors due to topology mismatch as measurements are replaced with noiseless computer simulations. The reader is referred to Appendix A for a more detailed error analysis.

The next three subsections provide a brief review of the two-port network theory and a description of the proposed method, called *topology identification via model-based evolutionary computation* (TIMEC). Evolutionary computation is the collective name for algorithms inspired by biological evolution. This paper discusses only genetic algorithms, but the proposed approach can be used with the optimization performed by other evolutionary algorithms as well.

2.1   Classic Two-port Network Theory

Each line section, represented by $\theta^{(k)}$ of a candidate solution Θ, is considered as a homogeneous transmission line and can therefore be modeled as a two-port network, represented by its frequency-dependent transmission (ABCD) matrix. Specifically, a serial section is modeled by [1, 14]

$$\mathbf{T}_s = \begin{bmatrix} A & B \\ C & D \end{bmatrix} = \begin{bmatrix} \cosh(\gamma l) & Z_0 \sinh(\gamma l) \\ \dfrac{\sinh(\gamma l)}{Z_0} & \cosh(\gamma l) \end{bmatrix} \tag{1}$$

while a bridged-tap is modeled by

$$\mathbf{T}_{bt} = \begin{bmatrix} A & B \\ C & D \end{bmatrix} = \begin{bmatrix} 1 & 0 \\ \dfrac{\tanh(\gamma l)}{Z_0} & 1 \end{bmatrix}, \tag{2}$$

where l is the corresponding section length, γ is the propagation constant, and Z_0 is the characteristic impedance. Note that γ and Z_0 are frequency-dependent complex values, but for simplicity this dependency is not indicated here as for H and S_{11}. The nominal values for γ and Z_0 are obtained from an assumed cable model, such as VUB [15], MAR [16], BT [16] or BT0$_{\mathrm{H}}$ [17]. These models have inherent electromagnetic and geometrical parameters that characterize the insulation material, the resistivity, etc. In the current work, however, we will only use the VUB [15] model with γ and Z_0 completely defined by the wire gauge, as described in Appendix B. It is therefore only necessary to include the wire gauge as a parameter in Θ. In general, one may extend Θ to also include some of the inherent cable parameters. However, this extension is beyond the scope of this work.

For a line composed of different sections, the chain rule [1] can be applied in order to obtain the overall transmission matrix. That is, for a line with n_s number of sections, the overall (forward) transmission matrix $\mathbf{T}_f$ is given by the following matrix product:

$$\mathbf{T}_f = \mathbf{T}^{(1)} \times \mathbf{T}^{(2)} \cdots \times \mathbf{T}^{(n_s)}. \tag{3}$$

From matrix $\mathbf{T}_f$, it is possible to derive the quantities of interest. Specifically, the scattering parameter S_{11} and the transfer function H, corresponding to Θ, can be formulated as [14]:

$$S_{11} = \frac{AZ_L + B - CZ_SZ_L - DZ_S}{AZ_L + B + CZ_SZ_L + DZ_S} \tag{4}$$

and

$$H = \frac{Z_L}{AZ_L + B + CZ_SZ_L + DZ_S}, \tag{5}$$

where Z_S and Z_L are the source and load impedances, respectively, and A, B, C and D are the frequency-dependent elements of the overall transmission matrix $\mathbf{T}_f$.

In summary, given a set of parameters Θ that describes a line, the two quantities H and S_{11} are generated by using the two-port network theory previously explained and a cable model. In this work, this generation process is represented by the operator $\mathcal{V}$ as

$$[H, S_{11}] = \mathcal{V}\{\Theta\}. \tag{6}$$

2.2   GA-based Optimization

Several optimization routines can be applied within the proposed analysis-by-synthesis framework. GA is chosen since it is flexible and well suited for optimization of multi-dimensional spaces with many local optima. GA does not require properties such as convexity, for example. On the other hand, the successful application of GA to a new problem typically depends on properly adapting the formalism to the specificities of the problem. This subsection briefly describes a general application of GA to the line topology identification problem while Section 3 describes the developed modifications to improve the accuracy and the convergence of the proposed method.

The DSL transceivers considered in this work employ discrete multi-tone modulation (DMT), where the measurement bandwidth is divided into K frequencies or tones [1] (e.g. $K = 512$ for ADSL2+). This enables measurement of the quantities $S_{11}(f_k)$ and $H(f_k)$, via SELT and DELT, at the frequency f_k, for $k = 1, 2, ..., K$. In this work, the quantities associated with a candidate line Θ are compared with the measured (*target*) quantities, as defined by the following objective functions [18]:

$$V_H(\Theta) = \sum_{k=1}^{K} \frac{\left| H\left(\Theta, f_k\right) - \hat{H}\left(f_k\right) \right|^2}{\sigma_{\hat{H}}^2\left(f_k\right)} \tag{7}$$

and

$$V_{S_{11}}(\Theta) = \sum_{k=1}^{K} \frac{\left| S_{11}\left(\Theta, f_k\right) - \hat{S}_{11}\left(f_k\right) \right|^2}{\sigma_{\hat{S}_{11}}^2\left(f_k\right)}, \tag{8}$$

where $\sigma_{\hat{S}_{11}}(f_k)$ and $\sigma_{\hat{H}}(f_k)$ are the standard deviations associated with the measured scattering parameter and the transfer function, respectively. These two standard deviations are used to weight the error along frequency according to the accuracy of the measurement, and are obtained by conducting several measurements of each quantity. In case only one measurement of each quantity is available, $\sigma_{\hat{S}_{11}}(f_k) = \sigma_{\hat{H}}(f_k) = 1, \forall f_k$ is assumed.

Since two objective functions are used in this work, multi-objective optimization is performed. Frequently, in multi-objective optimization, the defined objective functions are conflicting in the sense that there exist an ambiguity in the (final) optimum solution. For example, in our case with two objective functions, it is obvious that a solution Θ_a is better than Θ_b if $V_H(\Theta_a) < V_H(\Theta_b)$ and $V_{S_{11}}(\Theta_a) < V_{S_{11}}(\Theta_b)$. However, situations such as $V_H(\Theta_a) > V_H(\Theta_b)$ and $V_{S_{11}}(\Theta_a) < V_{S_{11}}(\Theta_b)$ are common. Thus, instead

of providing one final solution, the multi-objective optimization provides a set of (optimum) solutions, that reflects the interaction between the different objectives. To deal with this, the multi-objective optimization algorithm NSGA-II [13] is adopted in this work. The NSGA-II is based on Pareto front selection [13]. The sorting of solutions in Pareto fronts is a useful formalism for letting the optimum solutions evolve along the optimization process. Therefore, at the end of the optimization, a set Ψ corresponding to the solutions in the first Pareto front is selected, and a decision rule is employed to choose the final solution.

In this work, the following strategy is adopted. Firstly, the best candidate solution associated with each objective function is selected from all candidates Θ_r belonging to the first Pareto front. That is,

$$\Theta_H^* = \arg \min_{r=1,2,\,...\,|\Psi|} V_H(\Theta_r)$$

and

$$\Theta_{S_{11}}^* = \arg \min_{r=1,2,\,...\,|\Psi|} V_{S_{11}}(\Theta_r).$$

Then, the final solution is chosen as the one among these two options that has the smallest sum of the objective functions, i.e.,

$$\Theta^* = \arg \min_{\Theta=\Theta_H^*,\Theta_{S_{11}}^*} (V_H(\Theta) + V_{S_{11}}(\Theta)). \tag{9}$$

Alternative strategies that provide different weights to the two objective functions can also be used. A brute-force search for Θ^*, which exhaustively tries each possible set Θ, is unfeasible because of the huge size of the search space. However, GA avoids this by keeping a set (a *population* in GA terminology) Φ of candidates and iteratively improving them along the iterations (*generations* in GA terminology).

The next subsection provides a description oriented towards the implementation of the proposed method on a computer.

2.3   Implementation of TIMEC

A flowchart with a high-level description of TIMEC is shown in Fig. 2, in accordance with the definition of the parameters and variables in Table 1 and Table 2. At the initialization, the GA *control parameters* are initialized to their maximum values, i.e., $p_m = P_m$, $p_c = P_c$ and $\sigma_m = \Sigma_m$. If there is no *a priori* information about the line under test, Γ is initialized to the empty set, i.e., $\Gamma = \{\cdot\}$. An initial population Φ is randomly generated with size $R = |\Phi|$, where $|\cdot|$ is the number of elements (cardinality) of the set.

For dealing with the set of parameters Θ, GA requires mapping it into a coded structure called *chromosome*, which is composed of *genes*. The coding function $\mathcal{G}$ maps the line parameters Θ into the coded chromosome $\mathcal{G}(\Theta)$ and $\mathcal{G}^{-1}$ denotes the decoding operation. Since the initial population Φ is a set of chromosomes, the values of the objective functions related to them are calculated by applying the operator $\mathcal{V}$ in (6) to all decoded parameters $\mathcal{G}^{-1}(\Phi) = \{\Theta_1, \ldots, \Theta_R\}$, and then using (7) and (8). The values of the objective functions are organized in an objective matrix $\mathbf{Q}$ according to:

$$\mathbf{Q} = \begin{bmatrix} V_H(\Theta_1) & V_{S_{11}}(\Theta_1) \\ V_H(\Theta_2) & V_{S_{11}}(\Theta_2) \\ \vdots & \vdots \\ V_H(\Theta_R) & V_{S_{11}}(\Theta_R) \end{bmatrix} \tag{10}$$

with dimension $R \times 2$. Once the initial population of chromosomes Φ and the matrix $\mathbf{Q}$ have been generated, the first generation ($n = 1$) starts.
As shown in Fig. 2, NSGA-II iteratively improves Φ until the final solution Θ^* is found. Specifically, at each generation n the GA operators (selection, mutation and crossover) are applied to Φ to generate another population Φ'.

The control parameters p_m, p_c and σ_m are adapted using a novel algorithm, described in Section 3.2. In order to calculate the quantities H and S_{11} with $\mathcal{V}$ in (6), each chromosome $\mathcal{G}(\Theta)$ must be decoded into the corresponding line parameters Θ. A proper coding/decoding is therefore crucial and the proposed schemes are described in details in Section 3.1. If *a priori* information is available, i.e., $\Gamma \neq \{\cdot\}$, this information is used during the decoding process. The decoding block provides to the GA process both the new chromosomes Φ' and their decoded parameters $\mathcal{G}^{-1}(\Phi') = \{\Theta'_1, \ldots, \Theta'_R\}$. After the decoding, operator $\mathcal{V}$ in (6) is applied on the set $\{\Theta'_1, \ldots, \Theta'_R\}$, in order to calculate the corresponding quantities H and S_{11} associated with each chromosome in the set Φ'. The matrix $\mathbf{Q}'$ is obtained by comparing these quantities with the measured $\hat{H}$ and $\hat{S}_{11}$ through the respective objective function. Both the original and the new population, Φ and Φ', and their respective objective matrices, $\mathbf{Q}$ and $\mathbf{Q}'$, are used by the NSGA-II process to generate the resulting population Φ'' and its respective objective matrix $\mathbf{Q}''$.

   In this work, two stop conditions are employed. If the generation number n is larger than the maximum allowed number of generations N, i.e. $n > N$, the optimization is stopped. Moreover, if the sum of the objective functions associated with the best candidate solutions is less than an user-defined threshold δ, the optimization is stopped as well. In essence, parameter δ controls the trade-off between rate of convergence and accuracy of

optimization. If none of the stop conditions are satisfied, i.e., $n \leq N$ and $V_H(\tilde{\Theta}_H) + V_{S_{11}}(\tilde{\Theta}_{S_{11}}) \geq \delta$, the new population Φ'' and the objective matrix $\mathbf{Q}''$ replace the current population Φ and matrix $\mathbf{Q}$, and a new generation $n + 1$ takes place using the replaced entities. Here, $\mathcal{G}(\tilde{\Theta}_H)$ and $\mathcal{G}(\tilde{\Theta}_{S_{11}})$ denotes the best individuals of the population associated with H and S_{11}, respectively, at the current generation n. In case at least one of the two stop conditions are satisfied, the best chromosome from the current first Pareto front is selected based on (9), which is implemented at the block of decision rules in Fig. 2. The selected chromosome is then decoded, yielding the final solution Θ^* that contains the information about the identified topology.
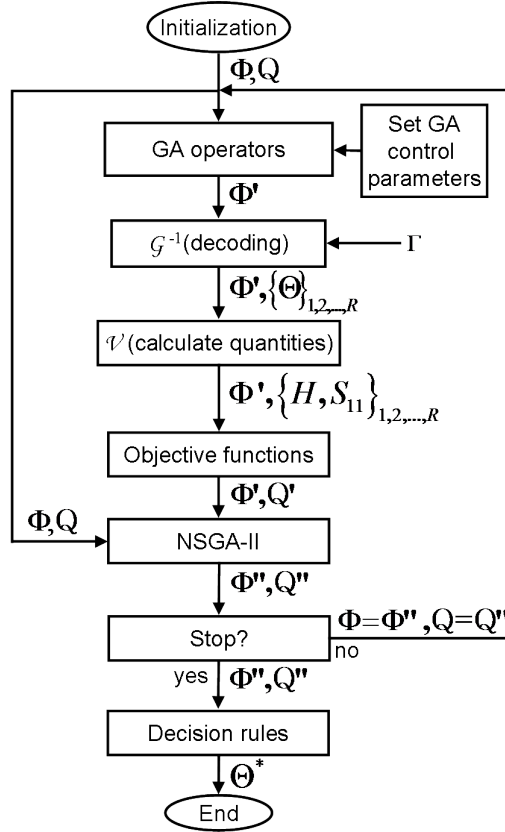
Figure 2: Flowchart of the proposed method for line topology identification.

Table 1: Brief description of the employed symbols.

Symbol	Data structures and variables
Γ	Store *a priori* information about the line under test
p_m	Current mutation probability
p_c	Current crossover probability
σ_m	Current standard deviation of mutation
Φ	Population (set) of chromosomes
Φ', Φ''	Temporary populations
$\mathbf{Q}$	Objective matrix. It stores the values of the objective functions related to the population Φ
$\mathbf{Q}'$, $\mathbf{Q}''$	Temporary objective matrices
n	Counter for the number of generations
$\tilde{\Theta}_H$	Candidate with current lowest value of the objective function related to the transfer function
$\tilde{\Theta}_{S_{11}}$	Candidate with current lowest value of the objective function related to the scattering parameter S_{11}
Θ^*	Final solution (identified topology of the line under test)
$\hat{H}$	Measured transfer function
H	Transfer function related to a certain candidate, calculated using the two-port network theory and a cable model
$\hat{S}_{11}$	Measured one-port scattering parameter S_{11}
S_{11}	One-port scattering parameter S_{11} related to a certain candidate, calculated using the two-port network theory and a cable model
Ω	Set containing the current values for the GA control parameters
Ψ	Solutions of the first Pareto front
n_s	Effective number of sections
n_b	Effective number of bridged-taps
c	Counter for the number of consecutive generations without evolution of the best chromosomes

3   Proposed Specializations of the GA Algorithm

This section describes the proposed schemes for the GA coding/decoding, a novel algorithm for adapting the GA control parameters, and the utilization

Table 2: Brief description of the employed symbols.

Symbol	User-defined parameters
Σ_m	Maximum standard deviation of mutation
P_m	Maximum mutation probability
P_c	Maximum crossover probability
w	Weight that affects the time-changes of the GA control parameters
R	Size of the populations (Φ, Φ' and Φ'')
N	Maximum number of generations to be executed. This value can be modified during the optimization process
ΔN	Increment of the number of generations
δ	Threshold for the sum of the two objective functions
δ_{pc}	Decreasing rate factor for crossover probability
δ_{pm}	Decreasing rate factor for mutation probability
δ_{σ_m}	Decreasing rate factor for standard deviation of mutation
N_s	Maximum number of sections
$N_s^{\min}$	Minimum number of sections
$N_b^{\min}$	Minimum number of bridged-taps

of the provided total line length (if used). The coding/decoding schemes are important to restrict the solution-space in order to obtain a feasible solution. The algorithm for adapting the GA control parameters aims at improving the convergence of the optimization process. The approach to utilize the line length handles the inherent uncertainty of the provided information.

3.1   Coding and Decoding

The coding/decoding connects the chromosomes of the GA population with line topology parameters in Θ, and determines the search-efficiency over the solution-space. The schemes considered in this work are described in the following.

3.1.1   Coding: The Constitution of the Chromosome

Each chromosome of the GA population has enough genes to store information about a line with N_s number of sections, where N_s is an user-defined parameter (see Table 2). More specifically, for each section three genes rep-

resent the section length, the gauge, and the type (serial or bridged-tap), respectively. For the first section, however, only two genes are needed since the section is defined as serial in this work. In addition, there are two genes to represent the effective number of bridged-taps n_b and the effective number of sections n_s that the decoded chromosome (candidate line) will have. In summary, each chromosome is composed of $3N_s + 1$ number of genes, as illustrated in Fig. 3.

Each gene carries a real-valued number between 0 and 1. At the initialization, the values of the genes are randomly set following the uniform distribution $U[0, 1]$. During the optimization process, these values are optimized via the GA operators of selection, crossover and mutation. Recall that $\mathcal{G}^{-1}$ denotes the decoding from a gene to the corresponding element of Θ, and that $\mathcal{G}$ denotes the coding of an element of Θ to the corresponding gene in the chromosome. In this way, a coded x-gene of the s-th line section of a certain line topology can be expressed as $\mathcal{G}(x^s)$, where $x \in \{l, g, b\}$. The next subsections provide details of the decoding schemes for each kind of parameter in Θ, followed by a decoding example.

3.1.2 Decoding of the Number of Sections

The first gene to be decoded in each chromosome is the one representing the effective number of sections, that is, $\mathcal{G}(n_s)$. This is essential since the decoded value of $\mathcal{G}(n_s)$, i.e. n_s, determines the remaining number of genes to be decoded for the considered chromosome. In other words, in case $n_s < N_s$, only the genes associated with the first n_s sections are used to generate the candidate line topology. The remaining $N_s - n_s$ genes are not taken in account.

The decoding of the gene $\mathcal{G}(n_s)$ is essentially a mapping of the gene value to the integer value n_s. The adopted strategy consists of dividing the interval $[0, 1]$ into $N_s - N_s^{\min} + 1$ equal sub-intervals, where $N_s^{\min}$ is the minimum number of sections and N_s is maximum number of sections. Each sub-interval is assigned one integer value within the range $[N_s^{\min}, N_s]$. That is, the first interval is assigned integer $N_s^{\min}$, the second interval is assigned integer $N_s^{\min} + 1$, and so on. Thus, the decoded value of the gene $\mathcal{G}(n_s)$ equals the integer that represents the sub-interval the gene value falls into. Typically $N_s^{\min}$ is set to 1, since one-section lines are considered. However, if there is trustful *a priori* information about the number of sections of the line under test, then restrictions to $N_s^{\min}$ and N_s can be employed to reduce the search space.

The mapping of a real-valued gene to an integer, via the sub-intervals described above, will be denoted in the following by the operator $\mathcal{M}$, defined

as

$$i = \mathcal{M}\left\{\mathcal{G}(x), [I_{min}, I_{max}]\right\}, \tag{11}$$

where the gene $\mathcal{G}(x)$ is mapped to integer i that represents the sub-interval, within $[0, 1]$, which $\mathcal{G}(x)$ falls into. In (11), $[I_{min}, I_{max}]$ denotes the interval of integers where I_{min} and I_{max} are the lower and upper bounds, respectively. With this notation at hand, the decoding of the effective number of sections can be expressed as

$$n_s = \mathcal{M}\left\{\mathcal{G}(n_s), [N_s^{\min}, N_s]\right\}. \tag{12}$$

3.1.3   Decoding of Length and Gauge

The decoding of a gene into the corresponding section length involves direct mapping of the gene value $\mathcal{G}(l^s) \in [0, 1]$ into the section length interval $[L_{\min}, L_{\max}]$. That is, for the s-th section, the decoding of the length yields

$$l^s = L_{\min} + (L_{\max} - L_{\min})\mathcal{G}(l^s), \tag{13}$$

where $L_{\min}$ and $L_{\max}$ are user-defined parameters that set the minimum and the maximum length of the section, respectively. The purpose of these bounds is to assure that the section lengths are within feasible range. Typically, different length bounds are employed for serial and bridged-tap sections.

For the decoding of the genes related to the gauges, it is not feasible to employ a similar mapping as in (13) since the gauges are represented as discrete values. For example, the gauges of the ETSI lines [19] are: $0.32, 0.4, 0.5, 0.63, 0.9$ mm. To take this into account, two different gauge-decoding algorithms, denoted *freegauge* and *gaugesort*, are considered in this work. As for the decoding of the number of sections, the *freegauge* consists of dividing the gene interval $[0, 1]$ into M equal sub-intervals, where M denotes the number of cable types in the assumed cable database. By applying the operator in (11), this decoding can be expressed as

$$i = \mathcal{M}\left\{\mathcal{G}(g^s), [1, M]\right\}, \tag{14}$$

where $\mathcal{G}(g^s)$ denotes the considered gauge-gene and integer i denotes the i-th element of the cable database. In this way, assuming the cable database is represented by the vector $\bar{G} = [G_1, \ldots, G_M]$, the decoded value of the gene $\mathcal{G}(g^s)$ is given by the i-th position of the cable database, i.e.,

$$g^s = \bar{G}(i). \tag{15}$$

The *gaugesort* is a more elaborated algorithm that aims to prevent repetition of gauges along the line and to assure that the gauges are always

increasing. That is, in order to decode each gauge-gene, *gaugesort* takes into account the gauge of the previous decoded section and the number of remaining sections to decode. Specifically, at each decoding iteration, the number of available gauges for the decoding of a certain gauge-gene $\mathcal{G}(g^s)$ is a sub-set of the assumed cable database, represented by the vector $\bar{G} = [G_1, \ldots, G_M]$. Algorithm 1 provides a formal description of the *gaugesort* algorithm, where i denotes the index of the previous used gauge and s is the number of the line section under decoding. At each iteration, the integer interval $[i + 1, i + S]$ represents the indices of the available gauges, in ascending order, and $(n_s - s)$ represents the number of remaining line sections to be decoded. It is important to note that *gaugesort* can only be used when the number of gauges in the cable database is larger than or equal to the effective number of sections n_s.

Algorithm 1: The *gaugesort* algorithm.

> **inputs** : n_s, $\{\mathcal{G}(g^1), \ldots, \mathcal{G}(g^{n_s})\}$, $[G_1, \ldots, G_M]$
> **outputs**: $\{g^1, \ldots, g^{n_s}\}$

$i = 0$;
$M = |\bar{G}|$;
for $s \leftarrow 1$ **to** n_s **do**
> $S = M - i - (n_s - s)$;
> $j = \mathcal{M}\{\mathcal{G}(g^s), [i + 1, i + S]\}$;
> $g^s = \bar{G}(j)$;
> $i = j$;
end

3.1.4   Decoding of the Type of Sections

This decoding is equivalent to establish whether a section is serial or a bridged-tap. The procedure starts by determining the effective number of bridged-taps n_b for each chromosome. By applying the operator in (11), the decoding of $\mathcal{G}(n_b)$ can be expressed as

$$n_b = \mathcal{M}\left\{\mathcal{G}(n_b), [N_b^{\min}, N_b]\right\}, \tag{16}$$

where $N_b^{\min}$ is the user-defined minimum number of bridged-taps. However, instead of being pre-defined, the maximum number of bridged-taps N_b is determined from the effective number of sections n_s as follows:

$$N_b = \text{round}\left[(n_s - 1)/2\right]. \tag{17}$$

Equation (17) reflects that the first section is defined as serial and that the bridged-taps must alternate between serial sections along the path from the CO to the CP. Having established that the effective number of bridged-taps $n_b > 0$, the next step is to determine the position of the bridged-tap(s).

The first decoded bridged-tap position is found from the index of the maximum type-gene of the chromosome (i.e. a max-search). In case $n_b > 1$, the position of the next bridged-taps is found by iteratively performing max-searches among the type-genes, but without taking into account the previously found type-gene and its two neighboring genes. In this way, the bridged-taps are alternating between serial sections. The decoding procedure is repeated until the n_b bridged-taps are found.

3.1.5   An Example of Decoding

A simple example shows how to obtain the line parameters of Θ from the chromosome depicted in Fig. 3. In this case, it is assumed that $N_s^{\min} = 1$, $N_s = 4$ and $N_b^{\min} = 0$.

First, the number of sections is decoded according to (12), which with the last gene $\mathcal{G}(n_s) = 0.56$ yields $n_s = 3$. Based on n_s, one obtains with (16) and (17) $n_b = 1$. The position of the bridged-tap is then determined according to the max-search described previously, which gives that the bridged-tap is located at the second section ($\mathcal{G}(b^2) = 0.56$). By assuming that $L_{\min} = 100\,\mathrm{m}$ and $L_{\max} = 4000\,\mathrm{m}$, the decoding of the length-genes $\mathcal{G}(l^1)$, $\mathcal{G}(l^2)$ and $\mathcal{G}(l^3)$ via (13) yields: $l^1 = 295\,\mathrm{m}$, $l^2 = 1387\,\mathrm{m}$ and $l^3 = 919\,\mathrm{m}$. For the decoding of the gauge-genes, it is assumed that *freegauge* is employed with a cable database consisting of $0.32, 0.4, 0.5, 0.63$ and $0.9\,\mathrm{mm}$. By applying (14) and (15), this results in: $g^1 = 0.4\,\mathrm{mm}$, $g^2 = 0.5\,\mathrm{mm}$ and $g^3 = 0.63\,\mathrm{mm}$.

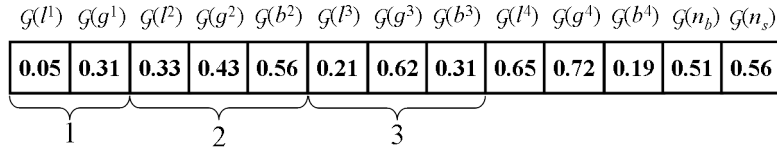| $\mathcal{G}(l^1)$	$\mathcal{G}(g^1)$	$\mathcal{G}(l^2)$	$\mathcal{G}(g^2)$	$\mathcal{G}(b^2)$	$\mathcal{G}(l^3)$	$\mathcal{G}(g^3)$	$\mathcal{G}(b^3)$	$\mathcal{G}(l^4)$	$\mathcal{G}(g^4)$	$\mathcal{G}(b^4)$	$\mathcal{G}(n_b)$	$\mathcal{G}(n_s)$
0.05	0.31	0.33	0.43	0.56	0.21	0.62	0.31	0.65	0.72	0.19	0.51	0.56

Figure 3: Illustration of a chromosome composed of 13 genes ($N_s = 4$) with $n_s = 3$ effective number of sections.

3.2   Self-Adaptation of the GA Parameters

The two main parameters that control the GA process are the crossover probability (p_c) and the mutation probability (p_m). The probability p_c con-

trols the crossover, which determines if two chromosomes will exchange their genetic information to generate two new chromosomes. The probability p_m controls the mutation, which is applied to each gene of a chromosome, and determines whether or not the gene will suffer mutation (modification). When a gene $\mathcal{G}(x)$ is selected to be modified, its new value $\mathcal{G}(x')$ is given by:

$$\mathcal{G}(x') = \mathcal{G}(x) + \mathcal{N}(0, \sigma_m),$$

where $\mathcal{N}(0, \sigma_m)$ denotes the normal distribution with mean equal to zero and standard deviation σ_m.

A general rule, widespread in the GA literature, is to use fixed (static) values for all parameters in the set $\Omega = \{p_c, p_m, \sigma_m\}$, which also include σ_m that has an impact on the diversity of the GA population. In addition, the maximum number of generations N is usually kept constant throughout the optimization process. However, for line topology identification and other applications, this can be inefficient and the algorithm may get stuck in local minima. Due to this, a self-adaptive control algorithm is proposed to determine the values for N and the GA parameters in Ω, along the optimization process.

The proposed strategy consists of sweeping the values of Ω, conditioned on the increase of the fitness[1] (*evolution* in GA terminology) of the best chromosomes. That is, the values of the GA parameters in Ω are maintained until they do not provide evolution anymore, whereupon they are changed. Additionally, whenever any evolution of the fitness of the best chromosomes occur, the maximum number of generations N is increased, giving the algorithm more time to improve the candidate solutions.

An algorithm that implements this self-adaptation is described in details in Algorithm 2, where p_c^n, p_m^n and σ_m^n are respectively the values of the crossover probability, mutation probability and standard deviation, at generation n. Here, P_c, P_m and Σ_m are the maximum values of the crossover probability, mutation probability and standard deviation, respectively (see Table 2). Variable c counts the number of consecutive generations without evolution and δ_{p_c}, δ_{p_m} and δ_{σ_m} indicate the decreasing rate of p_c, p_m and σ_m, respectively.

The algorithm can be summarized as follows. After calculating the objective matrix $\mathbf{Q}^n$ from the population Φ^n, at generation n, the best candidates $\tilde{\Theta}_H^n$ and $\tilde{\Theta}_{S_{11}}^n$ of the population have their values of the objective functions, $V_H(\tilde{\Theta}_H^n)$ and $V_{S_{11}}(\tilde{\Theta}_{S_{11}}^n)$, compared with $V_H(\tilde{\Theta}_H)$ and $V_{S_{11}}(\tilde{\Theta}_{S_{11}})$, respectively. Here, $\tilde{\Theta}_H$ and $\tilde{\Theta}_{S_{11}}$ denote the current best candidates so far (see

---

[1] *Fitness* is a figure or merit used in GA to classify the individuals of a population, and, in this work, its value will be the inverse of the value provided by the objective function.

Table 1). If any evolution in one of the current best GA solutions occur, i.e., if $V_H(\tilde{\Theta}_H^n) < V_H(\tilde{\Theta}_H)$ or $V_{S_{11}}(\tilde{\Theta}_{S_{11}}^n) < V_{S_{11}}(\tilde{\Theta}_{S_{11}})$, variable c is reset to 0 and N is increased by ΔN. Otherwise, c is increased by 1.

It can be noted from Algorithm 2 that the decision of changing the values of $\Omega = \{p_c, p_m, \sigma_m\}$ is determined by $c > w(N - n)$, where c counts the number of consecutive generations without evolution and $w(N - n)$ is a weighted number of remaining iterations. Specifically, the difference $(N - n)$ defines the rate of change of the GA parameters. In the beginning of the optimization process, the difference $(N - n)$ is high since n is low. This means that a greater number of generations without evolution will be necessary to change the values in Ω. On the other hand, close to the end of the optimization process, this difference is low since n is almost equal to N. The rate of change of the values in Ω is therefore increased.

Algorithm 2: Self-adaptive control algorithm for selecting the GA parameters.

> **Inputs** : p_c^{n-1}, p_m^{n-1}, σ_m^{n-1}, δ_{p_c}, δ_{p_m}, δ_{σ_m}
> **Outputs**: p_c^n, p_m^n, σ_m^n
>
> **for** $n \leftarrow 1$ **to** N **do**
> $\quad$ Calculate $\mathbf{Q}^n$ from Φ^n;
> $\quad \tilde{\Theta}_H^n = arg\min_{r=1,2,...,R} V_H(\Theta_r^n)$;
> $\quad \tilde{\Theta}_{S_{11}}^n = arg\min_{r=1,2,...,R} V_{S_{11}}(\Theta_r^n)$;
> $\quad$ **if** $V_H(\tilde{\Theta}_H^n) < V_H(\tilde{\Theta}_H)$ *or* $V_{S_{11}}(\tilde{\Theta}_{S_{11}}^n) < V_{S_{11}}(\tilde{\Theta}_{S_{11}})$ **then**
> $\quad\quad$ $N = N + \Delta N$;
> $\quad\quad$ $c = 0$;
> $\quad$ **else**
> $\quad\quad$ $c = c + 1$;
> $\quad$ **end**
> $\quad$ **if** $c > w(N - n)$ **then**
> $\quad\quad$ $p_m^n = p_m^{n-1} - p_m^{n-1}\delta_{p_m}$;
> $\quad\quad$ $p_c^n = p_c^{n-1} - p_c^{n-1}\delta_{p_c}$;
> $\quad\quad$ $\sigma_m^n = \sigma_m^{n-1} - \sigma_m^{n-1}\delta_{\sigma_m}$;
> $\quad\quad$ $c = 0$;
> $\quad$ **end**
> **end**

3.3   Utilization of Total Length Information

The objective of using the total length is to restrict the search space in order to improve the accuracy of the results and to improve the rate of convergence of the optimization process. The length-information can be obtained from e.g. a line data base or from the impulse response of the line under test, computed from the two-port measurements, i.e., via DELT.

The provided total line length can be considered fairly accurate, but not error free. More specifically, it is assumed in this work that the provided length is accurate within $\pm 10\%$. That is, the total length is represented as a stochastic variable following the uniform distribution $U[0.9l, 1.1l]$, where l denotes the true line length. In case the GA uses this information as completely trustful, there will potentially be an intrinsic gap between the true topology and the best candidate of the GA population. This gap could occur since the GA generates candidates with different topologies but with the same (static) total length. To handle this, the total lengths of each candidate is fine-tuned by the GA, as described in the following.

An additional gene is included in each chromosome of the GA population. This gene stores a percentage value related to the uncertainty of the total length given to GA. Just as for the other genes, the additional gene is tuned during the optimization process. The initial value E of this gene is generated according to the formula

$$E = E_{min} + (E_{max} - E_{min})\alpha, \tag{18}$$

where E_{min} and E_{max} are user-defined lower and upper bounds, and α is a chromosome-specific random number uniformly distributed as $U[0, 1]$. Under the given assumption of a total length uncertainty of $\pm 10\%$, it is natural to set E_{min} and E_{max} equal to $\pm 10\%$. However, to provide some extra freedom, we set $E_{min} = -0.15$ and $E_{max} = 0.15$, respectively. The percentage value E is used during the decoding process to calculate the total length $\hat{L}'_{tot}$ of each chromosome as follows:

$$\hat{L}'_{tot} = \hat{L}_{tot}(1 + E), \tag{19}$$

where $\hat{L}_{tot}$ is the length given to GA. The value of the so-obtained total length $\hat{L}'_{tot}$ of each chromosome is then divided among the serial sections of the line, taking into account the genes associated with the section lengths as follows:

$$l^s = \hat{L}'_{tot} \frac{\mathcal{G}(l^s)}{\mathcal{G}(l^1) + \mathcal{G}(l^2) + \ldots + \mathcal{G}(l^{n_s})}. \tag{20}$$

4   Simulation Results

This section presents simulation results to validate the proposed method: *topology identification via model-based evolutionary computation* (TIMEC). Here, instead of actually measuring $\hat{H}$ and $\hat{S}_{11}$ for a given line under test, these quantities are obtained using the operator $\mathcal{V}$ in (6), which employs a cable model, as described in Section 2.1. In other words, the correct set of parameters $\Theta^{\dagger}$ is used to generate the target functions, and consequently, $\hat{H} = H^{\dagger}$ and $\hat{S}_{11} = S_{11}^{\dagger}$. The same cable model is also used to generate the quantities associated with the candidates of the population. Under these controlled conditions, there are no measurement or modeling mismatches (see Appendix A). In this way, it is feasible to find exactly $\Theta^{*} = \Theta^{\dagger}$. Additionally, there is no uncertainty associated with the generation of the quantities, and hence, the variances in (7) and (8) are set to 1.

4.1   General Simulation Conditions

The simulations are organized according to the amount of available information, defined in Table 3. The aim is to investigate the performance of TIMEC based on either one-port measurements or both one-port and two-port measurements, and further employing information about the (total) line length. The TIMEC is evaluated for each of the four *test cases* in Table 3. For test case 1 and 2, TIMEC is compared with a reference method based on only one-port measurements, here denoted SELT-tdr. For test case 3 and 4, TIMEC is evaluated with different degree of accuracy in the line length information.

Table 3: Summary of the employed test cases and their respective result tables.

Method	Test Case	Available Information				Result Table
		One-port meas.	Two-port meas.	Total length (±10%)	True total length	
SELT-tdr		x				6, 7
TIMEC	1	x				6
	2	x	x			7
	3	x	x	x		8
	4	x	x		x	9

A comprehensive set of eight *test lines* is used for each test case. The selected test lines are: ETSI # 4, # 5, # 6, # 7, # 8, defined in [19], two test lines defined in [8] which are here called Loop G # 1, Loop G # 2, and one test line defined in [4], here called SBTS. The topologies of the test lines are described in the result Table 6–Table 9. All the test lines have an open-end termination at the remote side. The VUB [15] cable model, with the restrictions described in Appendix B, is used to generate the quantities of interest during the simulations via (6). The considered frequency band corresponds to the case of ADSL with 256 tones, ranging from 4.3125 kHz to 1.104 MHz.

Since the proposed method is based on GA, i.e. stochastic optimization, it is important to determine the statistics of the estimated section lengths, for independent simulations. The TIMEC is therefore applied ten times for each test line and test case, and each estimated section length is presented in the following result tables with its mean value and standard deviation. The employed GA uses the self-adaptive control algorithm described in Section 3.2 and the bounds for the line parameters are set as shown in Table 4.

The internal GA configuration is as follows. The population size (R) is set to 30, the maximum crossover probability $P_c = 0.85$, the maximum mutation probability $P_m = 0.85$ and the maximum standard deviation of mutation $\Sigma_m = 0.75$. The threshold δ for the sum of the objective functions is set to 10^{-7}. These values were determined from empirical experiments, that provides trade-off between accuracy and rate of convergence, suitable for the test cases in this paper. Additionally, $\Delta N = 50$, w is equal to 0.05, δ_{p_c} and δ_{p_m} are set to 0.005, and δ_{σ_m} is set to 0.01.

The usage of the decoding algorithms *gaugesort* and *freegauge*, described in Section 3.1.3, is as follows. The TIMEC uses as default the *freegauge*. In case no bridged-taps are detected, TIMEC is executed with *gaugesort* to improve the accuracy.

Table 4: Upper and lower bounds for the line parameters.

Parameter	Bounds	
	lower	upper
Serial section length (km)	$L_{\min} = 0.02$	$L_{\max} = 7$
Bridged-tap section length (km)	$L_{\min} = 0.05$	$L_{\max} = 0.8$
Number of sections	$N_s^{\min} = 1$	$N_s = 5$
Number of bridged-taps	$N_b^{\min} = 0$	$N_b = 2$

4.2   TIMEC for Test Case 1 and 2

This subsection presents a comparison between TIMEC and the state-of-the-art TDR-based reference method in [4], here denoted *SELT-tdr*. More specifically, TIMEC for test case 1 and 2 in Table 3 is compared with SELT-tdr, for all eight test lines. Before presenting the test results, the reference method is briefly described.

The TDR-based method in [4] was selected since it has documented good results for different line topologies, as described in [8] (Table II, page 545). For the current work, the method was implemented strictly following the process described in [4], except for their technique for detecting singularities in the so-called reflectogram [4]. This is unfortunately not described in [4]. We therefore employ derivatives to detect those singularities. Our implementation of SELT-tdr was tested with the lines defined in [8], obtaining similar results as the reported ones. It is also worth mentioning that our implementation uses a velocity of propagation set to 68.7 % of the speed of light in vacuum, calculated according to the description in [4].

4.2.1   Test Case 1: TIMEC Based on One-port Measurements

The results for this test case are summarized in Table 6, which shows the estimated length and the percentage error $\Delta l(\%)$ of the sections for SELT-tdr. For the TIMEC, the mean estimated length, the mean percentage error $\overline{\Delta l(\%)}$ and the standard deviation σ for each section, calculated from ten independent simulations, are given. For all result tables, the estimated lengths are rounded to integer values, $\Delta l(\%)$ and $\overline{\Delta l(\%)}$ are rounded to two decimals, and σ is rounded to four decimals.

The results provided by the SELT-tdr method highlight two main features of such method: it is well-suited for detecting bridged-taps but is not successful in detecting all kinds of gauge changes. A gauge change constitutes an impedance change that is often small in comparison to e.g. the impedance change due to a bridged-tap. Some gauge changes yield a more prominent reflection coefficient than others, as shown in Fig. 4. In this figure, the magnitude of the reflection coefficients for all gauge changes present in the considered test lines are plotted as function of frequency. It can be seen from the figure that especially the gauge changes 0.32/0.4 mm, 0.32/0.5 mm and 0.5/0.9 mm provide large impedance changes, for a broad frequency range. Consequently, these gauge changes are easier to detect. This is confirmed for ETSI # 7, which has two large impedance changes (0.32/0.5 mm and 0.5/0.9 mm). The results in Table 6 shows that the line topology of ETSI # 7 is correctly detected with SELT-tdr except for the gauge type of the second section. It can also be observed from Fig. 4 that the gauge changes
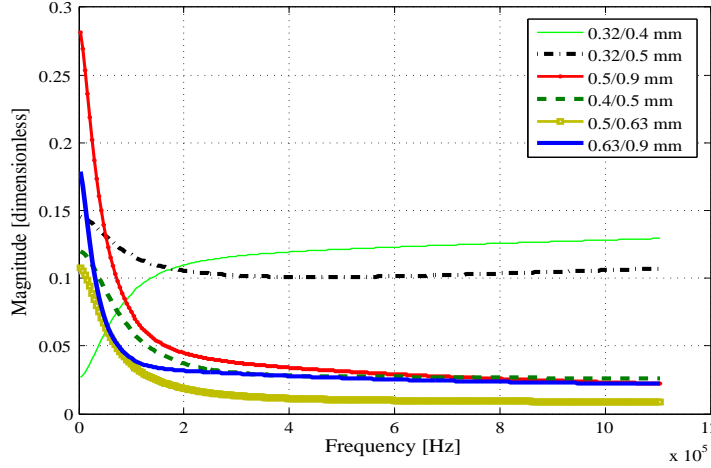
Figure 4: Magnitude of the reflection coefficients related to all impedance mismatches present in the considered test lines.

0.5/0.63 mm and 0.63/0.9 mm have the lowest impedance changes. The latter is reflected in the results of SELT-tdr for ESTI # 4, ESTI # 5 and ESTI # 6 where only one or two serial sections are detected, with an estimation error on the total length of about 26 %, 13 % and 4 %, respectively. Note that the total length estimations are not shown in the result table(s) but can be calculated as a sum of the estimated sections lengths. For the one-section lines, i.e., Loop G # 1 and Loop G # 2, SELT-tdr has an error on the total length estimates below 8 %.

For the TIMEC, the results of Table 6 show that the estimation errors are negligible for Loop G # 1, Loop G # 2 and SBTS. The last sections of ETSI # 4, # 5, # 6, and # 8 are not detected, but the percentage error of length for the first section(s) of these lines are small. In addition, for these lines the estimated length of the last detected section is almost equal to the sum of the two last sections of the true line, yielding a mean estimate of the total length less than 0.5 %. For ETSI # 7, the TIMEC results are accurate with a mean percentage error of the section lengths less than 0.1 %.

In summary, Table 6 indicates that the results provided by TIMEC, using only one-port measurements with one objective function, are equal to or better than those ones provided by the SELT-tdr method. For the lines with incorrectly detected topologies, the TIMEC provides an accurate estimate of the first section(s) and the total line length. For both methods, the test lines

containing small impedance changes prove to be more difficult to estimate. The standard deviations in Table 6 are all small, indicating that the same (local) optimum is found for the repeated trials with TIMEC. Furthermore, in case only one-port measurements are used with *a priori* information about the total line length (not described above), no significant improvements could be observed with TIMEC.

4.2.2 Test Case 2: TIMEC Based on Both One-port and Two-port Measurements

The results with TIMEC for test case 2 are listed in Table 7 where for convenience the SELT-tdr results for test case 1 are repeated. Here, two objective functions based on both the one-port and the two-port measurements are used by the TIMEC. From Table 7 we note that the number of line sections for all test lines are correctly estimated with TIMEC, except for ETSI # 5. A perfect topology estimation is obtained for ETSI # 8, where the bridged-taps are found at their correct positions, i.e., at the second and the fourth line sections. For ETSI # 4, the length of the third and the fourth line sections are somewhat *over* and *under* estimated, respectively, yielding a mean percentage error of the total length of 2.0 %. For ETSI # 5, the last line section is not detected, but the mean percentage error of the total length is only 1.3 %. For ETSI # 6, the gauge of the last line section is incorrectly estimated and the mean percentage error of the total length is 1.24 %.

In summary, the TIMEC based on both one-port and two-port measurements improves the estimation results compared to only using one-port measurements, as expected. As for test case 1, the estimation of the last section(s) fails for the lines with small impedance changes, although the mean percentage error of the total length is small. The standard deviations for TIMEC with repeated trials are small or zero, except for last section of ETSI # 5, indicating that the same (local) optimum is found.

4.3 TIMEC for Test Case 3 and 4

This section presents the performance results of TIMEC using two objective functions based on one-port and two-port measurements, as well as using a measure of the total line length.

4.3.1 Test Case 3: Inaccurate Total Length Information

For this test case, the TIMEC is provided with the total length of each test line, offset by $+10\%$ relative the total length. That is, the provided input to the TIMEC is $1.1l$ m for a line with the total length of l m. In order to

handle this, the TIMEC uses the approach and associed settings described in
Subsection 3.3. The results for this test case are shown in Table 8, from which
it can be seen that the topological structures (number of sections, section
types and gauges) of all considered lines are accurately detected by TIMEC.
In particular the topology identification of ETSI # 5 have been significantly
improved compared to previous test cases. The mean error on the total length
estimation is negligible (i.e. $< 0.1\%$) for all test lines, which means that
TIMEC is able to fine-tune the provided (errornously) total length values.

4.3.2   Test Case 4: Perfect Total Length Information

For test case 4, the total length information is assumed free of error. In this
case, the GA considers the length information as trustful, i.e., the approach
described in Subsection 3.3 is not employed. In other words, unlike test case
3, all candidate lines generated during the optimization process have the same
total length, equal to the given value. As indicated by Table 9, the results
are slightly better than those ones for test cases 1 and 2. As for test case 3,
the topological structure is accurately detected by TIMEC for all considered
lines. However, it can be noted from Table 9 that for some of the lines, the
mean percentage error of the section lengths is somewhat increased compared
to test case 3.

5   Summary and Conclusions

This paper presents a new method for line topology identification. The pro-
posed model-based method, called TIMEC, takes advantage of both con-
ventional one-port measurements (S_{11}) and two-port measurements (transfer
function). The latter measurement is obtained via the line-diagnostic func-
tionality defined in the ITU-T G.992.3 and G.992.5 standards. These mea-
surement quantities are used in two objective functions that are optimized
with a version of the Non-dominated Sorting Genetic Algorithms (NSGA-II).
In addition, specialized schemes for coding/decoding are adopted together
with an algorithm for self-adaptation of the GA parameters. An important
property of the chosen GA-based approach is its flexibility, which permits
incorporation of additional measurements or *a priori* line information, such
as the total line length. However, though the TIMEC method based on
only the one-port S_{11} measurements, utilizes the same information as the
SELT-tdr method, it performs slightly better. Including also the two-port
measurements (transfer function), the difference in performance between the
TIMEC and SELT-tdr is increased considerably. Finally, when information

about the total line length is included, the TIMEC method correctly determines all considered test-line topologies in terms of number of sections, types, gauges and lengths.

Appendix A

This appendix tries to clearly distinguish the sources of errors in the proposed model-based analysis-by-synthesis. Assuming $\hat{H}$ is a measured quantity (the same reasoning is valid for $\hat{S}_{11}$), one wants to find a line Θ with minimum error Δ_v, where

$$H = \mathcal{V}\{\Theta\} = \hat{H} + \Delta_v.$$

The error Δ_v can be decomposed into the parcels:

$$\Delta_v = \Delta_v^n + \Delta_v^m + \Delta_v^t + \Delta_v^s + \Delta_v^p,$$

which can be summarized as follows:

- Statistical measurement errors Δ_v^n: Errors due to internal measurement noise as thermal noise, and external noise as RF interference etc. These can normally be suppressed by averaging;

- Systematic measurement errors Δ_v^m: Errors due to an imperfect measurement setup and calibration procedure;

- Topology error Δ_v^t: Error due to an incorrect topology assumption, i.e., when Θ is not the correct $\Theta^\dagger$;

- Structural error Δ_v^s: Error due to a bad choice of the cable model. For example, a VUB cable model cannot fully describe a BT-modeled line;

- Parameter error Δ_v^p: Error due to imperfect translation of line gauge into the cable model parameters. For example, two cables of the same diameter could have a difference in one or more of the other model parameters.

The parcels Δ_v^n and Δ_v^m are not relevant in the present paper since simulated measurement-data is used. Moreover, Δ_v^p is zero since the cable database defined in Appendix B is used for the simulated measurement-data and employed by TIMEC. On the other hand, the parcels Δ_v^t, Δ_v^s exist because of the adopted model-based approach and deserve further discussion. For example, the BT $\#1$ cable model [16] provides a result $H = \mathcal{V}_{\mathrm{BT}}(\Theta)$ based on a set Λ_{BT} with $|\Lambda_{\mathrm{BT}}| = 13$ parameters. Assuming the other parcels are

zero, i.e. $\Delta_v^n = \Delta_v^m = \Delta_v^t = \Delta_v^p = 0$, and a cable model that provides Λ, Δ_v^s is defined as the error $\Delta_v^s = \arg\min_\Lambda V(\Theta(\Lambda))$, where the dependence on Λ is made explicit in $\Theta(\Lambda)$ for readability and where $V(\Theta(\Lambda))$ is given by (7). In other words, if one assumes the BT model, Δ_v^s should be obtained by trying all possible (an infinite number) sets $\Lambda_{\mathrm{BT}} \in \mathbb{C}^{|\Lambda_{\mathrm{BT}}|}$. This error is called structural because $\Delta_v^s \neq 0$ means that the model is not able to fit to the measured $\hat{H}$ even after trying all possible combinations of parameters with $\Delta_v^t = \Delta_v^n = \Delta_v^m = 0$.

One may account for the total $\Delta_v^t + \Delta_v^s + \Delta_v^p$ but not be able to estimate each parcel individually. In simulations though, all these parcels can be accounted for. This is a motivation for starting the validation of the proposed TIMEC method from a well-controlled simulation setup, where $\Delta_v^s = \Delta_v^p = \Delta_v^n = \Delta_v^m = 0$ and the only error is Δ_v^t, i.e., the topology error.

Appendix B

This appendix presents the values of the geometrical and electromagnetic parameters adopted for the VUB cable model used in the current work.

The VUB model is based on geometrical assumptions and models the propagation constant and characteristic impedance (γ and Z_0) of a cable by using parameterized equations. These equations are stated as function of parameters, here called the VUB parameters. These parameters, in turn, depend on geometrical and electromagnetic parameters associated with the conductor and the insulation materials. The geometrical parameters are: radius of the conductors (a), insulation thickness of the conductor (i) and distance between center of the conductors (D). The electromagnetic parameters are: the relative permeability (μ_r) and the relative permittivity (ϵ_r) of the insulation, and the conductor conductivity (σ). It is assumed that the insulation material is polyethylene, the conductor material is copper and the cables are twisted-pair-structured. The values for a, i, σ, μ_r and ϵ_r are extracted from [19].

The way the cable is structured determines the calculation of the variable D, as illustrated by Fig. 5. For a twisted-pair-structured cable of certain gauge g, D is expressed by

$$D = 2\left[a(g) + i(g)\right].$$

Table 5 summarizes the values for the geometrical and electromagnetic parameters associated with a certain diameter, adopted for the VUB cable model in the simulations.
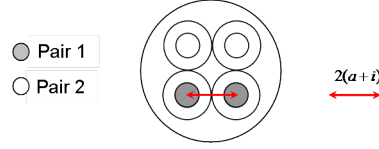
Figure 5: Distance between the center of the conductors for a twisted-pair structure.

Table 5: Geometrical and electromagnetic parameters for the considered cable types, adopted for the VUB cable model in the simulations.

Parameters	0.32 mm	0.4 mm	0.5 mm	0.63 mm	0.9 mm
$a\ (mm)$	0.16	0.2	0.25	0.315	0.45
$i\ (mm)$	0.05	0.13	0.15	0.2	0.27
$D\ (mm)$	0.42	0.66	0.8	1.03	1.44
$\sigma\ (S/m)$	5.8×10^{7}				
μ_r	1				
ϵ_r	2.26				

Acknowledgment

Table 6: Results for test case 1. Here, T=Type, S=Serial, G=Gauge, L=Length, BT=Bridged-tap.

Loop	Actual Topology			Estimated - SELT-tdr				Estimated - TIMEC (S_{11})				
	T	G (mm)	L (m)	T	G (mm)	L (m)	Δl (%)	T	G (mm)	Mean L (m)	Δl (%)	σ (m)
G#1	S	0.4	164	S	0.4	152	7.50	S	0.4	164	0.05	0.0002
G#2	S	0.5	195	S	0.5	195	0.01	S	0.5	195	0.01	0.0000
ETSI #4	S	0.32	200	S	0.32	217	8.35	S	0.32	200	0.00	0.0000
	S	0.4	900	S	0.4	2535	181.69	S	0.40	900	0.04	0.0005
	S	0.5	1500	—	—	—	—	S	0.50	1986	32.43	0.0010
	S	0.63	500	—	—	—	—	—	—	—	—	—
ETSI #5	S	0.4	1450	S	0.4	2362	62.89	S	0.4	1448	0.17	0.0011
	S	0.5	750	—	—	—	—	S	0.5	947	26.28	0.0050
	S	0.63	500	—	—	—	—	S	0.9	800	60.01	0.0048
	S	0.9	500	—	—	—	—	—	—	—	—	—
ETSI #6	S	0.4	1300	S	0.4	2664	104.90	S	0.4	1299	0.05	0.0001
	S	0.5	1250	—	—	—	—	S	0.5	1736	38.90	0.0003
	S	0.63	500	—	—	—	—	—	—	—	—	—
ETSI #7	S	0.32	200	S	0.32	217	8.35	S	0.32	200	0.03	0.0001
	S	0.5	600	S	0.4	672	11.95	S	0.4	600	0.07	0.0005
	S	0.9	4000	S	0.9	3099	22.54	S	0.9	4001	0.04	0.0023
ETSI #8	S	0.4	750	S	0.4	737	1.77	S	0.4	750	0.01	0.0001
	BT	0.4	500	BT	0.4	108	78.34	BT	0.4	500	0.07	0.0003
	S	0.4	1100	S	0.63	390	64.55	S	0.4	1601	45.58	0.0020
	BT	0.4	500	BT	0.4	87	82.60	—	—	—	—	—
SBTS	S	0.5	300	S	0.5	303	1.07	S	0.5	300	0.07	0.0003
	BT	0.5	300	BT	0.5	303	1.07	BT	0.5	300	0.08	0.0003
	S	0.5	900	S	0.5	910	1.06	S	0.5	900	0.02	0.0002

Table 7: Results for test case 2. Here, T=Type, S=Serial, G=Gauge, L=Length, BT=Bridged-tap.

	Actual Topology			Estimated - SELT-tdr				Estimated - TIMEC (S_{11},H)				
Loop	T	G (mm)	L (m)	T	G (mm)	L (m)	Δl (%)	T	G (mm)	Mean L (m)	$\overline{\Delta l}$ (%)	σ (m)
G#1	S	0.4	164	S	0.4	152	7.50	S	0.4	164	0.03	0.0001
G#2	S	0.5	195	S	0.5	195	0.01	S	0.5	195	0.03	0.0001
ETSI#4	S	0.32	200	S	0.32	217	8.35	S	0.32	200	0.00	0.0000
	S	0.4	900	S	0.4	2535	181.69	S	0.4	900	0.00	0.0000
	S	0.5	1500	S	–	–	–	S	0.5	1563	4.20	0.0763
	S	0.63	500	S	–	–	–	S	0.63	404	19.20	0.1109
ETSI#5	S	0.4	1450	S	0.4	2362	62.89	S	0.4	1450	0.00	0.0000
	S	0.5	750	–	–	–	–	S	0.5	925	23.60	0.0854
	S	0.63	500	–	–	–	–	S	0.63	769	55.00	0.1354
	S	0.9	500	–	–	–	–	–	–	–	–	–
ETSI#6	S	0.4	1300	S	0.4	2664	104.90	S	0.4	1300	0.00	0.0000
	S	0.5	1250	–	–	–	–	S	0.5	1401	12.24	0.1072
	S	0.63	500	–	–	–	–	S	0.9	387	23.00	0.1120
ETSI#7	S	0.32	200	S	0.32	217	8.35	S	0.32	200	0.00	0.0000
	S	0.5	600	S	0.4	672	11.95	S	0.5	600	0.00	0.0000
	S	0.9	4000	S	0.9	3099	22.54	S	0.9	4000	0.00	0.0000
ETSI#8	S	0.4	750	S	0.4	737	1.77	S	0.4	750	0.00	0.0000
	BT	0.4	500	BT	0.4	108	78.34	BT	0.4	500	0.00	0.0000
	S	0.4	1100	S	0.63	390	64.55	S	0.4	1100	0.00	0.0000
	BT	0.4	500	BT	0.4	87	82.60	BT	0.4	500	0.00	0.0000
SBTS	S	0.5	300	S	0.5	303	1.07	S	0.5	300	0.03	0.0000
	BT	0.5	300	BT	0.5	303	1.07	BT	0.5	300	0.04	0.0000
	S	0.5	900	S	0.5	910	1.06	S	0.5	900	0.02	0.0000

Table 8: Results for test case 3. Here, T=Type, S=Serial, G=Gauge, L=Length, BT=Bridged-tap.

Actual Topology				Estimated - TIMEC (S_{11},H)				
Loop	**T**	**G**	**L**	**T**	**G**	**Mean L**	$\overline{\Delta l}$	σ
		(mm)	**(m)**		**(mm)**	**(m)**	**(%)**	**(m)**
G # 1	S	0.4	164	S	0.4	164	0.00	0.0000
G # 2	S	0.5	195	S	0.5	195	0.00	0.0000
ETSI # 4	S	0.32	200	S	0.32	200	0.05	0.0002
	S	0.40	900	S	0.40	905	1.36	0.0124
	S	0.50	1500	S	0.50	1486	2.06	0.0300
	S	0.63	500	S	0.63	509	3.88	0.0207
ETSI # 5	S	0.4	1450	S	0.4	1449	0.24	0.0047
	S	0.5	750	S	0.5	752	0.91	0.0086
	S	0.63	500	S	0.63	497	1.91	0.0113
	S	0.9	500	S	0.9	501	1.31	0.0073
ETSI # 6	S	0.4	1300	S	0.4	1302	0.29	0.0042
	S	0.5	1250	S	0.5	1244	0.85	0.0107
	S	0.63	500	S	0.63	503	1.45	0.0074
ETSI # 7	S	0.32	200	S	0.32	200	0.04	0.0001
	S	0.4	600	S	0.4	600	0.21	0.0014
	S	0.9	4000	S	0.9	4000	0.04	0.0019
ETSI # 8	S	0.4	750	S	0.4	750	0.05	0.0007
	BT	0.4	500	BT	0.4	500	0.22	0.0016
	S	0.4	1100	S	0.4	1100	0.06	0.0009
	BT	0.4	500	BT	0.4	499	0.23	0.0019
SBTS	S	0.5	300	S	0.5	300	0.01	0.0000
	BT	0.5	300	BT	0.5	300	0.02	0.0001
	S	0.5	900	S	0.5	900	0.00	0.0000

Table 9: Results for test case 4. Here, T=Type, S=Serial, G=Gauge, L=Length, BT=Bridged-tap.

Actual Topology				Estimated - TIMEC (S_{11},H)				
Loop	T	G	L	T	G	Mean L	$\overline{\Delta l}$	σ
		(mm)	(m)		(mm)	(m)	(%)	(m)
G # 1	S	0.4	164	S	0.4	164	0.00	0.0000
G # 2	S	0.5	195	S	0.5	195	0.00	0.0000
ETSI # 4	S	0.32	200	S	0.32	200	0.00	0.0000
	S	0.40	900	S	0.40	900	0.00	0.0000
	S	0.50	1500	S	0.50	1524	2.13	0.0470
	S	0.63	500	S	0.63	476	6.40	0.1010
ETSI # 5	S	0.4	1450	S	0.4	1450	0.00	0.0000
	S	0.5	750	S	0.5	754	1.33	0.0092
	S	0.63	500	S	0.63	495	4.20	0.0300
	S	0.9	500	S	0.9	503	3.00	0.0161
ETSI # 6	S	0.4	1300	S	0.4	1300	0.00	0.0000
	S	0.5	1250	S	0.5	1270	1.60	0.0600
	S	0.63	500	S	0.63	487	2.60	0.0390
ETSI # 7	S	0.32	200	S	0.32	200	0.00	0.0000
	S	0.4	600	S	0.4	598	0.33	0.0040
	S	0.9	4000	S	0.9	3996	0.10	0.0092
ETSI # 8	S	0.4	750	S	0.4	750	0.00	0.0000
	BT	0.4	500	BT	0.4	500	0.00	0.0000
	S	0.4	1100	S	0.4	1100	0.00	0.0000
	BT	0.4	500	BT	0.4	500	0.00	0.0000
SBTS	S	0.5	300	S	0.5	300	0.04	0.0002
	BT	0.5	300	BT	0.5	300	0.09	0.0002
	S	0.5	900	S	0.5	900	0.02	0.0003

References

[1] T. Starr, J.M. Cioffi, and P.J. Silverman, *Understanding digital subscriber line technology*, Prentice Hall, Upper Saddle River, 1999.

[2] S. Galli and D.L. Waring, "Loop makeup identification via single ended testing: beyond mere loop qualification," *IEEE Journal of Selected Areas in Communications*, vol. 20, No. 5, pp. 923–935, June 2002.

[3] J.L. Fang, C. Zeng, and J.M. Cioffi, "Bridged tap location estimation," *preprint*.

[4] K. Kerpez and S. Galli, "Single-ended loop make-up identification. Part I: A method of analyzing TDR measurements," *IEEE Transactions on Instrumentation and Measurement*, vol. 55, no. 2, pp. 528–537, Apr. 2006.

[5] P. Boets, T. Bostoen, L. Van Biesen, and T. Pollet, "Preprocessing of signals for single-ended subscriber line testing," *IEEE Transactions on Instrumentation and Measurement*, vol. 55, no. 5, pp. 1509–1518, Oct. 2006.

[6] J. Rius i Riu, "Position paper on loop qualification and monitoring outlining general features the developed loop qualification and monitoring solution should fulfil," Report, Ericsson AB, Nov. 2004.

[7] G. Long and J. Kamali, "Single-ended line probing helps speed up DSL mass deployment," in *IIC-China/ESC China Conference*, 2002, pp. 57–60.

[8] K. Kerpez and S. Galli, "Single-ended loop make-up identification. Part II: Improved algorithms and performance results," *IEEE Transactions on Instrumentation and Measurement*, vol. 55, no. 2, pp. 538–549, Apr. 2006.

[9] T. Vermeiren, T. Bostoen, P. Boets, X.O. Chehab, and F. Louage, "Subscriber loop topology classification by means of time-domain reflectometry," in *Proceedings of the IEEE International Conference on Communications. ICC '03.*, May 2003, vol. 3, pp. 1998–2002.

[10] C. Neus, P. Boets, and L. Van Biesen, "Feature extraction of one port scattering parameters for single ended line testing," *XVIII IMEKO World Congress*, 2006.

[11] ITU-T G.992.3, "Asymmetric digital subscriber line transceivers 2 (adsl2)," 07/2002.

[12] ITU-T G.992.5, "Asymmetric digital subscriber line transceivers - extended bandwidth (adsl2plus)," 05/2003.

[13] K. Deb, A. Pratap, S. Agarwal, and T. Meyarivan, "A fast and elitist multiobjective genetic algorithm: NSGA-II," *IEEE Transactions on Evolutionary Computation*, vol. 6, no. 2, pp. 182–197, Apr. 2002.

[14] P. Golden, H. Dedieu, and K. Jacobsen, *Fundamentals of DSL technology*, Auerbach Publications, Taylor & Francis Group, 2006.

[15] P. Boets, M. Zekri, L. Van Biesen, T. Bostoen, and T. Pollet, "On the identification of cables for metallic access networks," in *Proceedings of the 18th IEEE Instrumentation and Measurement Technology Conference. IMTC '01.*, May 2001, vol. 2, pp. 1348–1353.

[16] R.F.M. van den Brink, "Cable reference models for simulating metallic access networks," Tech. Rep., ETSI STC TM6 Permanent document TM6(97)02, June 1998.

[17] F. Lindqvist, P.O. Börjesson, P. Ödling, S. Höst, K. Ericson, and T. Magesacher, "Low-order and causal twisted-pair cable modeling by means of the hilbert transform," *RVK08 - The twentieth Nordic Conference on Radio Science and Communications*, Växjö, Sweden, June 9-11, 2008. AIP Conference Proceeding, vol. 1106, pp 301-310.

[18] T. Bostoen, P. Boets, M. Zekri, L. Van Biesen, T. Pollet, and D. Rabijns, "Estimation of the transfer function of a subscriber loop by means of one-port scattering parameter measurement at the central office," *IEEE Journal of Selected Areas in Communications*, vol. 20, No. 5, pp. 936–948, June 2002.

[19] ITU-T G.996.1, "Test procedures for digital subscriber line (dsl) transceivers," 02/2001.

Paper VI

Paper VI

Crosstalk Channel Estimation via Standardized Two-Port Measurements

Abstract

The emerging multi-user transmission techniques for enabling higher data rates in the copper access network relies upon accurate knowledge of the twisted-pair cables. In particular the square-magnitude of the crosstalk channels between the transmission lines are of interest for crosstalk-mitigation techniques. Acquiring such information normally requires dedicated apparatus since crosstalk-channel measurement is not included in the current digital subscriber line (DSL) standards. We address this problem by presenting a standard-compliant estimator for the square-magnitude of the frequency-dependent crosstalk channels, that uses only functionality existing in today's standards. The proposed estimator is evaluated by laboratory experiments with standard-compliant DSL modems and real copper access network cables. The estimation results are compared with both reference measurements and with a widely-used crosstalk model. The results indicate that the proposed estimator obtains an estimate of the square-magnitude of the crosstalk channels with a mean deviation from the reference measurement less than $3\,\mathrm{dB}$ for most frequencies.

1 Introduction

One of the main impairments for high-speed digital subscriber line (DSL) systems is the destructive crosstalk from neighboring DSL systems. The interfering crosstalk occurs when neighboring systems transmit in the same spectrum due to the inherent electromagnetic coupling between the twisted-pair cables co-located in the same copper access binder (bundle). Both near-end crosstalk (NEXT) and far-end crosstalk (FEXT) occur, where FEXT (NEXT) refers to the crosstalk caused by the transmitter(s) on the opposite (same) side of the line. The NEXT and FEXT interferences in a copper access binder are illustrated in Fig. 1. In order to achieve higher data rates in the access network, many new proposed multi-user transmission techniques utilize accurate knowledge of the transmission paths in the cable binder.
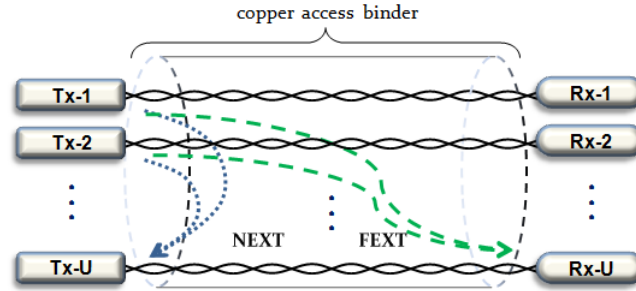
Figure 1: NEXT and FEXT interferences in a copper cable binder for a DSL network with U number of near-end transmitters (Tx) and far-end receivers (Rx).

An important multi-user transmission approach that has received a lot of attention recently is *Dynamic Spectrum Management (DSM)* [1–4]. For DSM aiming at *crosstalk mitigation* [5–11], the power spectral density (PSD) of the individual transmitters is usually optimized in such a way that *e.g.* the total data rate (throughput) is maximized, and/or the total transmitted power is minimized. Most of the spectrum management algorithms have been developed assuming perfect (crosstalk) channel information. Especially the square-magnitude of the FEXT channels, *i.e.* the attenuation, is assumed known *a priori*. The NEXT is of less concern for DSM due to the usage of frequency division duplex (FDD) for separation of the upstream and down-stream frequency bands, employed by the majority of all ADSL [12, 13] and VDSL [14] connections. It is worth noting that for crosstalk *cancellation* methods, which are not considered in this work, the phase also has to be

estimated or assumed known.

One option to create up-to-date information about the transmission lines is to use one-port measurements referred to as Single-Ended Line Testing (SELT) [15–20]. From the SELT measurement the line length can be estimated, which together with a length-dependent crosstalk model [21, 22] can be used to roughly estimate the square-magnitude of the NEXT/FEXT channel. However, as reported in *e.g.* [23, 24], the frequency-dependent crosstalk channels can vary significantly, and in a stochastic way, between different twisted-pair lines of the same length. This fact was considered in [24] which extends the standardized crosstalk model [21, 22], based on measurements and stochastic analysis, by including phase information and variation of the coupling functions. However, given only the length of the line, the accuracy is still not satisfying.

A general drawback with one-port based methods, applied to crosstalk channel estimation, is the high attenuation of the crosstalk channel, which becomes a major drawback since the SELT signal has to travel back and forth. In the literature, several two-port estimation methods have been considered [25–29]. In [25] an impartial third party site identifies the crosstalk channels of the binder. Transmitted and received signals from all modems in the binder are collected during a given time span. Initially, a cross-correlation technique is applied to estimate the timing differences between the signals from different providers in the same binder. Thereafter, a least-squares method is used to jointly estimate the crosstalk channels and to further improve the timing offsets. In [26] the NEXT crosstalk sources are identified in the frequency domain by finding the maximum correlation with a "basis set" of representative measured crosstalk couplings. However, this method does not apply to FEXT estimation. In [27], a real-time FEXT crosstalk identification is proposed by using the initialization procedure of a newly activated modem and applying a least-squares estimator. The authors of [28] derive "blocked state-space models" for multirate xDSL networks and set up the mapping relationship between available input and output data. The least-squares principle is further used to identify the crosstalk channels. In [29] an iterative method is described that estimates the FEXT channels based on measured and reported signal-to-noise ratios. The purpose in [29] is to cancel the self-FEXT by precoding, and therefore, both amplitude and phase of the channels are estimated.

This paper describes an estimator for simultaneously obtaining the square-magnitude of the FEXT and NEXT channels of a copper access cable binder. More specifically, the aim is to estimate the multiple-input multiple-output (MIMO) FEXT and NEXT channel matrices. By employing a sequential single-input multiple-output (SIMO) estimation procedure, as illustrated in

Fig. 2, we provide an accurate estimate of the crosstalk channels which commonly are assumed known *a priori* by the published DSM crosstalk mitigation techniques. In contrast to [25–28], the proposed estimator requires no hardware or software changes of the DSL modems, and utilizes only measurements available via the existing DSL standards [12–14]. Thus, the estimator provides an immediately available low-cost solution based on standardized signals and protocols. In line with [25], we propose a co-ordinated measurement period during a given time span where the estimation is carried out. Since the square-magnitude of the crosstalk channels does not (normally) vary with time, at least not significantly, the estimation only has to be done once or seldom.

The paper is organized as follows. In Section 2 we introduce the system and signals used by the proposed estimator, followed by the MIMO and the SIMO modeling applied in this work. Based on these transmission models, Section 3 describes the proposed estimator for obtaining the square-magnitude of FEXT and NEXT channels. A practical implementation of the estimator is described in Section 4. The FEXT model used for the evaluation is described in Section 5. Laboratory experiments are presented and evaluated in Section 6 followed by an error analysis in Section 7. Finally, a summary and conclusions are provided in Section 8.
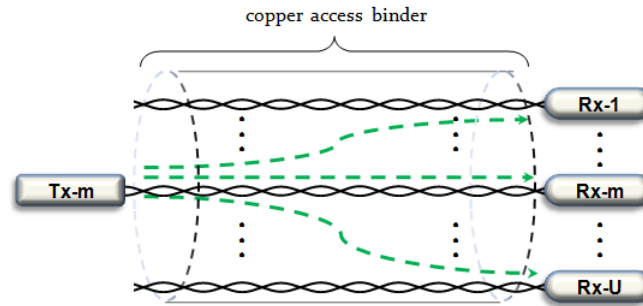
Figure 2: Sequential SIMO transmission with only one active transmitter (Tx) per estimation sequence $m = 1, 2, ..., U$. The far-end receivers (Rx) measure the FEXT for each sequence, whereupon the MIMO FEXT channel matrix can be estimated. The MIMO NEXT channel matrix can be estimated in the same way by using Rx:s located at the same side of the binder as Tx.

2   System Model

In this section we first describe the concept of DMT-based transmission [30] and the accompanying system and signals used throughout this work. Secondly, the MIMO and the SIMO transmission models are introduced to compactly represent the transmission on a complete cable binder. Any reader familiar with these topics could skip directly to Section 3, where these transmission models are used for deriving the proposed estimator.

2.1   Discrete Multitone Transmission

Consider the DSL system depicted in Fig. 3, which consists of a transmitter and a receiver located in an ADSL2/2+ [12, 13] or VDSL2 [14] modem-pair. The transceivers are connected to a twisted-pair line and employ Discrete Multitone (DMT) modulation. Without loss of generality, we assume in this section that the same number of subcarriers are used in the downstream and in the upstream direction, *i.e.*, the system uses symmetric transmission bandwidths. The DMT-based transceivers use $N/2 + 1$ frequency domain subcarriers denoted X^k, where k is the subcarrier (subchannel) number, $k = 0, 1, 2, ..., N/2$. The carriers are quadrature-amplitude modulated (QAM) and Hermitian extended before being converted to a time-domain DMT symbol (waveform) by an N-point inverse discrete Fourier transform (IDFT)[1]. A cyclic prefix (CP) of L samples is added to the beginning of the time domain symbol before transmission. Hence, by denoting the transmitted frequency domain DMT symbol with the complex vector $\bar{X} = [X^0\, X^1\, \cdots\, X^{N-1}]^T$, the cyclic prefix extended time domain symbol can be expressed as (omitting symbol number)

$$\bar{x} = \mathbf{T}\bar{X}, \tag{1}$$

where $\bar{x} = [x_{-L}\, \cdots\, x_0\, x_1\, \cdots\, x_{N-1}]^T$. The matrix $\mathbf{T}$ denotes the normalized and extended IDFT-matrix defined as

$$\mathbf{T} = \left(\begin{array}{c} \mathbf{Q_{cp}} \\ \mathbf{Q} \end{array} \right). \tag{2}$$

Here, sub-matrix $\mathbf{Q_{cp}}$ is of size $L \times N$ and contains the L last rows of the $N \times N$ normalized IDFT-matrix $\mathbf{Q}$. A real-valued time domain signal is obtained due to the Hermitian extension of the subcarriers, defined as

$$X^k = (X^{k-N/2})^*, \quad \text{for } k = N/2 + 1, ..., N - 1 , \tag{3}$$

---

[1]In practice the IDFT/DFT transform is normally implemented with fast Fourier transform (FFT) techniques.
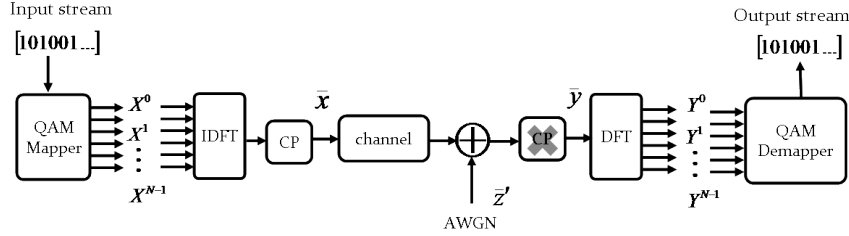
Figure 3: DMT transmission over a twisted-pair channel with additive white Gaussian noise (AWGN). The figure shows the basic transmitter and receiver blocks of the modem-pair.

where * denotes the complex conjugate. Since X^0 and $X^{N/2}$ (the Nyquist carrier) carry no information they are here set to zero. The transmission channel in Fig. 3 is represented by a stationary impulse response of M samples, denoted by vector $\bar{p} = [p_0\, p_1\, ... \, p_{M-1}]^T$. The disturbance on the line is modeled as additive white Gaussian noise (AWGN) where each noise sample has mean value zero and variance σ^2. Hence during the symbol transmission, the $(N + L) \times 1$ noise vector $\bar{z}'$ is added to the received signal, where $\bar{z}' \in \mathcal{N}(\bar{0}, \sigma^2 I')$ and I' is the identity matrix of size $(N + L) \times (N + L)$.

The receiver removes the CP of the received time domain signal. By exploiting the cyclic nature of the added prefix, i.e., $x_n = x_{N-n}$, for $n = -L, ..., -1$, the received signal vector, after removal of CP, can be expressed as

$$\bar{y} = \mathbf{P}\bar{x} + \bar{z} = \mathbf{P}\mathbf{T}\bar{X} + \bar{z} \ , \tag{4}$$

where $\bar{y} = [y_0\, y_1\, ... \, y_{N-1}]^T$, $\bar{z}$ is $N \times 1$ since no CP, and $\mathbf{P}$ is the $N \times (N + L)$ channel convolution matrix. The receiver demodulates the received signal by calculating the discrete Fourier transform (DFT) of the received vector $\bar{y}$. Thus, the received frequency domain vector $\bar{Y} = [Y^0\, Y^1\, \cdots\, Y^{N-1}]^T$ can, with (4), be expressed as

$$\bar{Y} = \mathbf{R}\bar{y} = \mathbf{R}\mathbf{P}\mathbf{T}\bar{X} + \bar{Z} \ , \tag{5}$$

where $\mathbf{R} = \mathbf{Q}^H$ denotes the $N \times N$ normalized DFT-matrix, and $\bar{Z}$ is the received frequency domain complex noise vector. Since $\bar{z}$ is uncorrelated, real-valued $\mathcal{N}(\bar{0}, \sigma^2 I)$, where I is the identity matrix of size $N \times N$, it follows that $\bar{Z}$ is complex Gaussian, i.e. $\mathcal{CN}(\bar{0}, \sigma^2 I)$, due to the transformation by the normalized DFT-matrix.

It can be shown [30] that if $L > M - 1$, matrix $\mathbf{RPT}$ becomes a diagonal

matrix $\boldsymbol{\Lambda}$. Thus, for $L > M - 1$, we can rewrite (5) as

$$\bar{Y} = \boldsymbol{\Lambda}\bar{X} + \bar{Z} \ , \tag{6}$$

where matrix $\boldsymbol{\Lambda} = \mathbf{RPT}$ is an $N \times N$ diagonal matrix with the channel frequency response on the main diagonal. In other words, equation (6) shows that each transmitted subcarrier is independently affected by the transfer function of the channel and no intercarrier interference (ICI) occurs. This property is assumed in this work and can be obtained in practice as is described in the following.

For the purpose of estimating the channel, an ADSL / VDSL transmitter repeats the same transmitted DMT symbol. This corresponds to the transmission of the repetitive pseudo-random signal called *Reverb* in the standards [12, 13]. An advantage of using the Reverb signal is the inherent low peak-to-average-power-ratio (PAR) [30]. This type of repetitive transmission can be interpreted as if the cyclic prefix were a multiple of N samples long rather than L, where normally $L << N$. Thus, for the case of repeated signals the channel matrix $\mathbf{RPT}$ becomes diagonalized, and hence, the subchannels become independent. In this work, we will utilize repetitive DMT transmission signals like the Reverb signal, in order to obtain independent subchannels. Hence, the destructive effects of ICI or intersymbol interference (ISI) are of no concern here.

2.2   MIMO Transmission

The proposed estimator in Section 3 takes advantage of the MIMO structure of the copper access network, where the underlying MIMO transmission model is described in the following. Fig. 1 shows a cable binder with U number of users on each side of the binder, where the twisted-pair lines in the binder are denoted by $u = 1, 2, ..., U$. Although the DMT subchannels on a single line are independent under the conditions described in Section 2.1, the electromagnetic coupling between the lines of the binder results in frequency-dependent crosstalk. In fact, the transmitted signal from user u couples (leaks) into all other lines and contribute to the total received crosstalk at the victim receivers. Both near-end crosstalk (NEXT) and far-end crosstalk (FEXT) occur.

In MIMO mathematical modeling for DSL, each user is allocated a user-specific $K_u \leq N/2$ number of subchannels (ignoring DC tone) that depends on the line conditions. However, we will assume in the following description, without loss of generality, that all users are allocated the same number of subchannels, denoted K, where $k = 1, 2, ..., K$. In order to model the FEXT channels, we introduce the three-dimensional MIMO FEXT channel

matrix $\mathbf{H}$ of size $U \times U \times K$, which characterizes the transmission through the whole binder from the near-end transmitters to the far-end receivers, *i.e.*, the direct channel-paths and the FEXT paths. The matrix channel element $H_{n,m}^k$, as seen in Fig. 4, represents the complex-valued FEXT coupling from transmitter m to receiver n, for subchannel k. Each complex vector

Figure 4: MIMO channel matrix $\mathbf{H}$ with dimension $U \times U \times K$, where U is the number of lines in the cable binder and K is the number of subchannels in a MIMO group.

$\bar{H}_{n,m} = \left[H_{n,m}^1, H_{n,m}^2, \ldots, H_{n,m}^K \right]^T$ represents the frequency-dependent FEXT transfer function from near-end transmitter m to far-end receiver n. For the case where $m = n$, the vectors $\bar{H}_{1,1}, \bar{H}_{2,2}, \ldots, \bar{H}_{U,U}$ correspond to the direct transfer functions of the individual lines of the binder. Similarly, for $m \neq n$, the off-diagonal elements $\bar{H}_{n,m}$ correspond to the FEXT transfer functions between the lines. In an analogous way to the FEXT, we introduce the three-dimensional MIMO NEXT channel matrix $\mathbf{G}$ of size $U \times U \times K$, which characterizes the channel from the near-end transmitters to the near-end receivers. The complex vector $\bar{G}_{n,m} = \left[G_{n,m}^1, G_{n,m}^2, \ldots, G_{n,m}^K \right]^T$ represents the frequency-dependent NEXT transfer function from near-end transmitter m to near-end receiver n. For $n = m$, the element $G_{n,n}^k$ is by definition zero and of no interest.

In line with Section 2.1, superscript and subscript are used in the following to denote *subchannel*, and *user (line)* number, respectively. Thus, for subchannel k the transmitted frequency-domain signals on the U lines can be represented by the complex vector $\bar{X}^k = [X_1^k \, X_2^k \, \cdots \, X_U^k]^T$. Since the subchannels are assumed independent in this work, we can extend (6) for the MIMO scenario by formulating it as

$$\bar{Y}^k = \mathbf{H}^k \bar{X}^k + \bar{Z}^k, \quad \text{for } k = 1, 2, \ldots, K , \tag{7}$$

where $\mathbf{H}^k$ is the two-dimensional $U \times U$ matrix representing $\mathbf{H}$ at subchannel k. Here $\bar{Y}^k = [Y_1^k \, Y_2^k \, \cdots \, Y_U^k]^T$ denotes the received (complex) FEXT vector

for subchannel k and $\bar{Z}^k = [Z_1^k \, Z_2^k \, \cdots \, Z_U^k]^T$ is the (complex) noise vector for subchannel k. In the same way, we model the received NEXT signal as

$$\bar{V}^k = \mathbf{G}^k \bar{X}^k + \bar{W}^k \ \text{ for } k = 1, 2, \ldots, K \ , \tag{8}$$

where $\bar{V}^k = [V_1^k \, V_2^k \, \cdots \, V_U^k]^T$ is the received (complex) NEXT vector in sub-channel k, and $\bar{W}^k$ is the (complex) noise vector for subchannel k. From (7) we observe that the received subcarrier Y_n^k, at user n, can be expressed as

$$Y_n^k = H_{n,n}^k X_n^k + \sum_{m=1, m \neq n}^{U} H_{n,m}^k X_m^k + Z_n^k, \tag{9}$$
$$k = 1, 2, \ldots, K \ , \quad n = 1, 2, \ldots, U \ .$$

Hence, the received subcarrier Y_n^k consists of the direct-component $H_{n,n}^k X_n^k$ and the summation of the FEXT contributions from the far-end transmitters, plus the additive noise. From (8) it follows that the received subcarrier V_n^k consists of the summation of NEXT contributions from the near-end trans-mitters plus additive noise. Thus, in order to estimate the crosstalk channels it is desirable to somehow separate the transmitted signals in *e.g.* time-, frequency-, and/or code-domain. In this paper, however, we restrict our-selves to the standardized DMT-based DSL systems [12–14], in which case only the time- and frequency-domain can be utilized for signal separation. Since an efficient frequency-separation method would require a co-ordination of the different transmitted signals we instead choose time-separated trans-mitted signals, as will be described in the following section.

2.3   SIMO Transmission

The proposed estimator in Section 3 computes the crosstalk channels of $\mathbf{H}$ and $\mathbf{G}$ by exploiting single-input multiple-output (SIMO) transmission instead of MIMO. This corresponds to the case where the transmitted signals are separated in time-domain, as discussed in previous section. Fig. 2 illustrates the SIMO transmission scenario for a cable binder. By using one transmitter at a time, let say m, we simultaneously excite the FEXT and NEXT channels: $\bar{H}_{1,m}, \bar{H}_{2,m}, ..., \bar{H}_{U,m}$ and $\bar{G}_{1,m}, \bar{G}_{2,m}, ..., \bar{G}_{U,m}$. Thus, with only transmitter m active, it follows from (9) that the received FEXT at far-end receiver n yields

$$Y_n^k = H_{n,m}^k X_m^k + Z_n^k, \tag{10}$$
$$k = 1, 2, \ldots, K \ , \ n = 1, 2, \ldots, U.$$

In an analogous way, the received NEXT at the near-end receiver n can be expressed as

$$V_n^k = G_{n,m}^k X_m^k + W_n^k,$$

$$k = 1, 2, \ldots, K \ , \ n = 1, 2, \ldots, U. \tag{11}$$

By sequentially activating one transmitter at a time, *i.e.*, transmitter $m = 1, 2, ..., U$, all channels (elements) of the MIMO matrix $\mathbf{H}$ and $\mathbf{G}$ are excited. This sequential-transmission scheme is exploited by the proposed estimator, as described next.

3 Crosstalk Channel Estimation

Based on the SIMO transmission model described in previous section, we derive the optimal NEXT/FEXT estimator in the least-squares sense. As the FEXT channels are most important for spectrum management applications, the SIMO FEXT channel estimator is the main focus, but the description applies in general also to NEXT channel estimation.

The SIMO system described by (10) and (11) represents a (complex) linear model with additive noise. In contrast to the MIMO case, it is here convenient to consider the transmission from one user at a time and for all K subchannels. In order to simplify the notation, we let transmitter m be active at estimation sequence m. Hence, for estimation sequence m, the SIMO system can be expressed as follows with matrix notation

$$\mathbf{Y}(m) = \mathbf{X}(m)\mathbf{H}(m) + \mathbf{Z}(m), \tag{12}$$

where $\mathbf{Y}(m) = [\bar{Y}_1(m) \, \bar{Y}_2(m) \ldots \bar{Y}_U(m)]$ is the $K \times U$ matrix containing the received FEXT in all K subchannels and for all U receivers. The $K \times U$ SIMO channel matrix in (12) is represented by $\mathbf{H}(m) = [\bar{H}_{1,m} \, \bar{H}_{2,m} \ldots \bar{H}_{U,m}]$, which corresponds to column m of $\mathbf{H}$ along the K-dimension. Recall that $\mathbf{H}$ has three dimensions while $\mathbf{H}(m)$ has two. The known $K \times K$ signal matrix from transmitter m yields

$$\mathbf{X}(m) = \begin{pmatrix} X_m^1 & 0 & 0 & 0 \\ 0 & X_m^2 & \ddots & 0 \\ \vdots & \ddots & \ddots & \vdots \\ 0 & \cdots & \cdots & X_m^K \end{pmatrix},$$

and the added (complex) noise in (12) is denoted by the $K \times U$ matrix $\mathbf{Z}(m) = [\bar{Z}_1(m) \, \bar{Z}_2(m) \ldots \bar{Z}_U(m)]$. In the following we assume that the probability

density function (PDF) of the noise is unknown, *i.e.*, we assume no *a priori* information about the mean value or the covariance of the noise. Moreover, we assume that the noise is uncorrelated between the receivers since they are (typically) placed at different locations. Subsequently, we choose to apply a least-squares (LS) estimator for the SIMO system in (12), which permits an independent processing among the far-end receivers. That is, for estimation sequence m, the received $K \times 1$ FEXT vector at user n yields

$$\bar{Y}_n(m) = \mathbf{X}(m)\bar{H}_{n,m} + \bar{Z}_n(m), \quad \text{for } n = 1, 2, \ldots, U. \tag{13}$$

By minimizing the LS criterion

$$J(\bar{H}_{n,m}) = \left(\bar{Y}_n(m) - \mathbf{X}(m)\bar{H}_{n,m}\right)^H \left(\bar{Y}_n(m) - \mathbf{X}(m)\bar{H}_{n,m}\right), \tag{14}$$

the following LS estimator $\widehat{\bar{H}}_{n,m}(m)$ can be derived, [31],

$$\begin{aligned}
\widehat{\bar{H}}_{n,m}(m) &= \left(\mathbf{X}(m)^H\mathbf{X}(m)\right)^{-1}\mathbf{X}(m)^H\bar{Y}_n(m) \\
&= \mathbf{X}(m)^{-1}\bar{Y}_n(m),
\end{aligned} \tag{15}$$

where ^{H} denotes the Hermitian transpose, and where the last step of (15) utilizes that $\mathbf{X}(m)$ is a square matrix with full rank. It now follows from (15) that the LS estimator for the SIMO FEXT channel matrix $\mathbf{H}(m)$ can be expressed as

$$\widehat{\mathbf{H}}(m) = \mathbf{X}(m)^{-1}\mathbf{Y}(m). \tag{16}$$

Thus, by sequentially activating transmitter $m = 1, 2, ..., U$, the three dimensional MIMO FEXT channel matrix $\mathbf{H}$ can be estimated via (16). For subchannel k, the LS estimation of the FEXT channel between transmitter m and receiver n can be expressed with (13) and (15) as

$$\widehat{H}_{n,m}^k = \frac{Y_n^k(m)}{X_m^k} = H_{n,m}^k + \frac{Z_n^k(m)}{X_m^k}, \ k = 1, 2, \ldots, K . \tag{17}$$

When the (complex-valued) noise sample $Z_n^k(m)$ is considered CAWGN $\mathcal{CN}(0, \sigma^2)$ and uncorrelated with the transmitted signal, it follows from (17) that the estimate $\widehat{H}_{n,m}^k$ is unbiased $\mathcal{CN}(H_{n,m}^k, \sigma^2)$ with $|X_m^k|^2 = 1$. By averaging the estimate over M number of DMT symbols it can be shown that $\widehat{H}_{n,m}^k \in \mathcal{CN}(H_{n,m}^k, \sigma^2/M)$. Hence, the variance of the estimate is reduced by a factor of M in this case. In Appendix A we consider the optimum minimum variance unbiased (MVU) estimator for the SIMO system in (12) with CAWGN.

In what follows, we extend the LS estimator in (16) to the case where the phase of the received frequency-domain signal $\mathbf{Y}$ is *not* known. This corresponds to the perspective of an access network operator where only the standardized interfaces of the DMT-based modems [12–14] are accessible. It is therefore interesting to consider an estimator based on *e.g.* the power spectral density (PSD) of standardized transmit and receive signals. Thus, the intention is to derive an estimator for the square-magnitude of the crosstalk channels, *i.e.*, an estimator for the attenuation of the crosstalk channels.

From (12) we note that the received PSD can be expressed as

$$\mathbf{P}_y(m) = \mathbf{P}_x(m)|\mathbf{H}|^{\mathbf{2}}(m) + \mathbf{P}_z(m), \tag{18}$$

where $\mathbf{P}_y(m)$, $\mathbf{P}_x(m)$, and $\mathbf{P}_z(m)$ are the corresponding PSD matrices obtained by taking the absolute-squared value of the elements of $\mathbf{Y}(m)$, $\mathbf{X}(m)$, and $\mathbf{Z}(m)$, respectively. Here, $|\mathbf{H}|^{\mathbf{2}}(m)$ denotes the $K \times U$ FEXT attenuation matrix at estimation sequence m, where matrix element (r, c) of $|\mathbf{H}|^{\mathbf{2}}(m)$ is equal to $|H_{c,m}^r|^2$. Since (18) constitutes a linear model with real-valued additive noise, the LS estimator in (16) provides the PSD-based estimator of $|\mathbf{H}|^{\mathbf{2}}(m)$ by

$$\widehat{|\mathbf{H}|}^{\mathbf{2}}(m) = \mathbf{P}_x(m)^{-1}\mathbf{P}_y(m). \tag{19}$$

Hence, for subchannel k, the PSD-based LS estimate of the square-magnitude of the FEXT channel between transmitter m and receiver n is given by (19) as

$$\left|\widehat{H_{n,m}^k}\right|^2 = \frac{|Y_n^k(m)|^2}{|X_m^k|^2} = |H_{n,m}^k|^2 + \frac{|Z_n^k(m)|^2}{|X_m^k|^2}, \ k = 1, 2, \ldots, K \ . \tag{20}$$

From (20) we note that the estimate $\left|\widehat{H_{n,m}^k}\right|^2$ becomes biased even if the noise can be considered uncorrelated, normally distributed, and with a mean value of zero. To simplify the notation, we select the estimation sequences equidistant in time, *i.e*, we let the estimation sequence number $m = 1, 2, ..., U$ also denote the corresponding normalized time instance. This allows the same notation for both estimation sequence-number and measurement time instance. Moreover, we let m_0 denote the time instance between the time instances $m - 1$ and m, where $m_0 = m - \frac{1}{2}$ for $m = 1, 2, ..., U$.

In order to mitigate the biased PSD-based estimate of (19)–(20), we assume that the noise PSD is stationary over a time span of at least two measurement intervals, which corresponds in practice to a couple of seconds. Before activating transmitter m, the noise PSD is measured with all transmitters silent. The so-obtained (background) noise PSD is denoted $\mathbf{P}_z(m_0)$, where m_0 can be viewed as an initial measurement time instance for sequence

m. Transmitter m is thereafter activated and $\mathbf{P}_y(m)$ is measured. Due to the assumed temporarily-stationary condition we have $\mathbf{P}_z(m) \approx \mathbf{P}_z(m_0)$. An unbiased PSD-based estimate $\widetilde{|\mathbf{H}|}^{\mathbf{2}}(m)$ can be formulated by modifying (19) accordingly

$$\begin{aligned}
\widetilde{|\mathbf{H}|}^{\mathbf{2}}(m) &= \widehat{|\mathbf{H}|}^{\mathbf{2}}(m) - \mathbf{P}_x(m)^{-1}\mathbf{P}_z(m_0) \\
&= |\mathbf{H}|^{\mathbf{2}}(m) - \mathbf{P}_x(m)^{-1}\Big(\mathbf{P}_z(m) - \mathbf{P}_z(m_0)\Big) \\
&= \mathbf{P}_x(m)^{-1}\Big(\mathbf{P}_y(m) - \mathbf{P}_z(m_0)\Big).
\end{aligned} \tag{21}$$

From the second row of (21) we conclude that the estimate $\widetilde{|\mathbf{H}|}^{\mathbf{2}}(m)$ becomes unbiased if $\mathbf{P}_z(m) = \mathbf{P}_z(m_0)$. The temporary stationarity assumption is reasonable from at least two aspects: in the SIMO case no other active disturber is present, and the twisted-pair channel is non time-varying.

We end this section by emphasizing that the square-magnitude of the NEXT channels $\mathbf{G}$ can be estimated with the same estimator as (21) if $\mathbf{P}_y$ and $\mathbf{P}_z$ are interpreted as the received *near-end* signal PSD and *near-end* noise PSD, respectively. In line with Section 2.3 we denote the near-end received $K \times U$ NEXT matrix $\mathbf{P}_v$ and the $K \times U$ near-end noise PSD-matrix $\mathbf{P}_w$. It then follows from (19)–(21) that the corresponding PSD-based estimator for the square-magnitude of the NEXT channels yields

$$\widetilde{|\mathbf{G}|}^{\mathbf{2}}(m) = \mathbf{P}_x(m)^{-1}\Big(\mathbf{P}_v(m) - \mathbf{P}_w(m_0)\Big). \tag{22}$$

4   Implementation

In this section we outline a practical crosstalk channel estimator that *simultaneously* implements (21) and (22) by using only standardized signals and protocols, supported by off-the-shelf DSL modems compliant with *e.g.* [12,13]. Thus, the focus is on an estimator that can be deployed with equipment already available to the copper access network operator.

The estimator(s) described by (21)–(22) utilize the PSD of the near-end and far-end signals. A standardized DSL protocol that contains the measurement of both the far-end and the near-end PSD is the *Loop Diagnostic* (LD) functionality [12, 13], which is a so-called double-ended line testing (DELT) protocol. The LD procedure is performed synchronously by the near-end and far-end modem for the purpose of line qualification and fault localization. The test requires that the data traffic on the line is temporarily stopped for a couple of seconds while the LD test is performed.
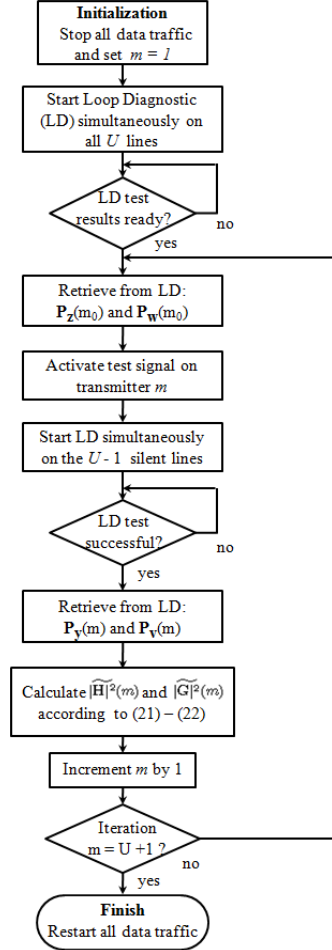
Figure 5: Flow chart of the FEXT and NEXT channel estimator, based on the two-port Loop Diagnostic (LD) protocol.

In the following description we consider the Central Office (CO) side as the near-end side. The proposed sequential estimation scheme works as illustrated in Fig 5. First in the sequence, the data traffic on all U lines in the binder is stopped. Thereafter, LD is started on all lines simultaneously. The retrieved LD test results contain the measured near-end and far-end PSDs on all U lines. The obtained far-end PSDs is denoted by matrix $\mathbf{P}_z(m_0)$ and the

near-end PSDs is denoted by $\mathbf{P}_w(m_0)$. As in Section 3, m_0 denotes the initial measurement time instance at sequence number m, where $m = 1, 2, ..., U$. Next, transmitter m is activated and a known test signal is transmitted.

The test signal is preferably a pseudo-random repetitive signal which excites the bandwidth of interest with a time period equal to the length of a DMT symbol. Here we assume the Reverb signal in [12, 13] is used since it is available as a test signal. With this type of signal the measured sub-channels become independent as described in Section 2.1. After activation of the test signal, LD is started on all the other silent $U - 1$ lines. The now obtained far-end and near-end PSDs correspond to $\mathbf{P}_y(m)$ and $\mathbf{P}_v(m)$, respectively. Based on the measured PSDs, (21) and (22) are used to calculate the estimated FEXT and NEXT attenuation matrices $\widetilde{|\mathbf{H}|}^2(m)$ and $\widetilde{|\mathbf{G}|}^2(m)$. The sequential procedure is repeated for $m = 1, 2, ..., U$. After the last sequence, the U lines are available for data traffic. It should be noted that the crosstalk channels are estimated only for those frequencies that are common for both transmitter m and the receivers in case of different transmit and receive bandwidths.

The LD protocol contains both a silent period, where the *quite-line* PSDs are measured, and a non-silent period with transmission of signals. Hence, it is important that the simultaneously started LD sessions are fairly synchro-
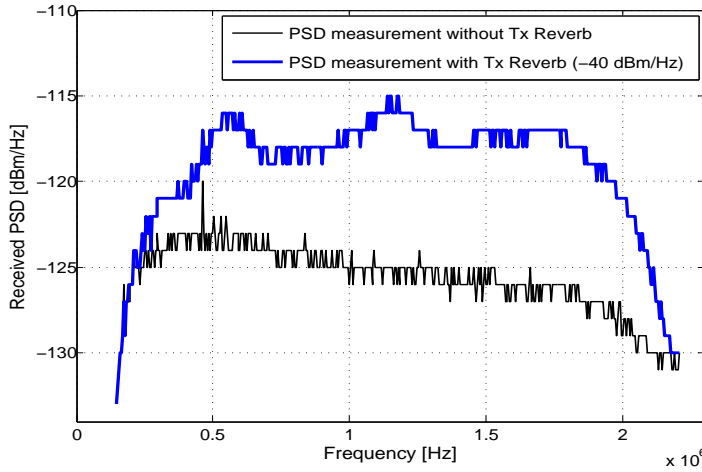
Figure 6: FEXT PSD measurements performed via Loop Diagnostic (LD) with and without transmitting the Reverb test signal on a neighboring line.

nized on the U lines. Alternatively one may choose to start LD sequentially on line $1, 2, ..., U$ in order to prevent the requirement of synchronization. Furthermore, every time LD is started the direct transfer function of the channel between the two modems is also estimated by the protocol. Hence the diagonal elements of the FEXT matrix, which represent the direct channels, are measured at time instance m_0 with high accuracy for both amplitude and phase. It should be emphasized that the described estimation procedure is not restricted to LD since it is based on only PSD measurements. LD is merely a convenient standardized protocol that provides means for executing and retrieving the measurements from a network management level at the CO side.

Fig. 6 shows an example of the measured FEXT PSDs, when measured by standardized modems, with and without activation of the Reverb test signal on a neighboring line. The figure also shows the quantization effects of the measured PSDs, where each PSD sample from the LD measurement is represented as an integer in dBm/Hz. The impact of this PSD quantization on the estimation performance is analyzed in Section 7.

5 Crosstalk Models

Commonly the NEXT/FEXT channels of a cable binder is represented by the deterministic so-called 99% worst-case model[2] [21] or by any of the more recently published models [24, 32–37]. These models predict the frequency-dependent square-magnitude of the NEXT/FEXT channels but require *a priori* information about the line lengths and the line insertion loss or the geometry descriptions of the cable. These properties of the lines, especially the length, may be obtained from a network database or from measurements. However, as can be seen from the measurements of *e.g.* [23], the FEXT channels between individual lines of the same cable type and length can vary more than $10\,\mathrm{dB}$. Hence, these models are for many crosstalk channels too simple for accurately predicting the crosstalk.

Some of the models [24, 32] are stochastic in the sense that they generate, based on a set of parameters, a random coupling function that represents the NEXT/FEXT channel. The stochastic nature of these kind of models make them less attractive for our needs since a deterministic comparison is desirable. In Section 6 we compare the obtained FEXT channels of the standardized 99% worst-case model with both a reference measurement and

---

[2]The 99% worst-case model is sometime also referred to as the 1% worst-case model. This model has been designed to represent the worst-case of 99% of all the measured crosstalk channels.

the corresponding channels obtained with the proposed estimator in Section 4. In this paper the 99% worst-case model represents the square-magnitude of the FEXT channels as, [21],

$$|H_{model}[f,n,l]|^2 = |\text{IL}(\text{f})|^2 \cdot X_F \cdot l \cdot c \cdot f^2 \tag{23}$$

where

- $|\text{IL}(\text{f})|^2$ denotes the channel insertion loss [30];

- f is the frequency (in Hertz);

- $X_F = 7.74 \times 10^{-21}$ is a coupling constant;

- l is the coupling path length;

- c is a distance conversion constant. For l in unit meters $c = 1$, and for l in unit feet, $c = 3.28\,\text{ft/m}$.

For the comparison in Section 6 we employ the model in (23) with the true, (*i.e.* measured) coupling length l and insertion loss $|\text{IL}(\text{f})|^2$. It should be noticed that the model in (23) disregards the phase information of the channel.

6 Laboratory Experiments

By means of laboratory experiments on real twisted-pair cables, we investigate the performance of the PSD-based FEXT channel estimator, described in Section 4. As NEXT is of less importance for crosstalk mitigation with FDD-based systems, we concentrate the experiments on FEXT channel estimation. The estimation results are compared with the corresponding results obtained with the FEXT model in Section 5 and reference measurements conducted with a network analyzer (NA). The three access network scenarios depicted in Fig. 7, Fig. 8, and Fig. 9 are considered in the comparison. For each scenario there are two FEXT channels, the *upper* and the *lower* channel, which for scenarios II and III have unequal lengths. The access binders consist of ten 0.40 mm (26 AWG) twisted-pair copper cables of lengths 200 m, 500 m, 700 m and 1500 m. In Fig. 7–Fig. 9, the transmitter and receiver units are denoted Tx and Rx, respectively.

Two laboratory setups are used: one modem-based setup for the FEXT channel estimator and a reference setup. The reference setup is used for the purpose of measuring the "true" square-magnitude of the FEXT channels, which the estimation results are compared with. In both setups the frequency band from 142 kHz to 2.2 MHz is measured with a frequency spacing
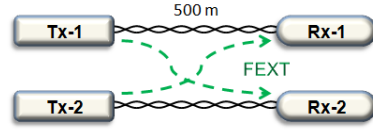
Figure 7: Access network scenario I with two FEXT channels of equal length.
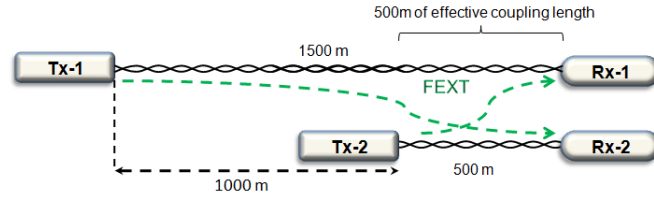
Figure 8: Access network scenario II with two FEXT channels of unequal lengths.
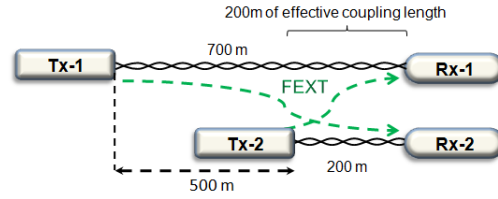

Figure 9: Access network scenario III with two FEXT channels of unequal lengths.

of $4.3\,$kHz. This corresponds to the downstream band of ADSL2+. Hence the Tx:s are located at the Central Office and the Cabinet side of the cable binder while the Rx:s are located at the customer-premises side. The modem-based setup provides an estimate of the square-magnitude of the *total* FEXT channel. That is, the estimate includes the extra attenuation introduced by the low-pass and the high-pass filters of the two DSL transceivers in addition to the physical crosstalk channel. This total channel is the channel of interest for DSM. However, the used FEXT model and the reference measurements are not able to capture the additional attenuation caused by the transceivers. We therefore compensate the FEXT model and the reference measurements by including the measured zero-line (*i.e.* zero-meter) attenuation obtained from LD with the two DSL modems directly connected back-to-back.

6.1 Modem-based Setup

The modem-based setup consists of ADSL2+ modems where $100\,\Omega$ resistors are used to represent the termination of the non-active modems of the multi-pair binder. For all experiments, sequential estimation is employed rather than simultaneous estimation of all SIMO crosstalk channels. The procedure follows the flow chart depicted in Fig. 5 and the estimation of the square-magnitude of the FEXT channel is calculated via (21).

6.2 Reference Setup

The setup used for the reference measurements is shown in Fig. 10. This setup constitutes an established way of measuring the transfer functions of the FEXT channels. The output power of the *HP 4395A Network Analyzer* (NA) is set to 15 dBm (maximum). The *HP 87512A/B Transmission/Reflection Test Set* is used for splitting the signal into two signals: a reference signal and a test signal that is applied to the twisted-pair cable. Hence, the effective power of the inserted test signal is about 7.5 dBm. In order to assure the impedance match, the cable to be measured is connected to the instrument through two baluns (North Hills, wide band transformer, 0311LB, $10\,\mathrm{kHz} - 60\,\mathrm{MHz}, 50\,\Omega$ UNB, $100\,\Omega$ BAL). As before, $100\,\Omega$ resistors are connected to the unused cable ends.
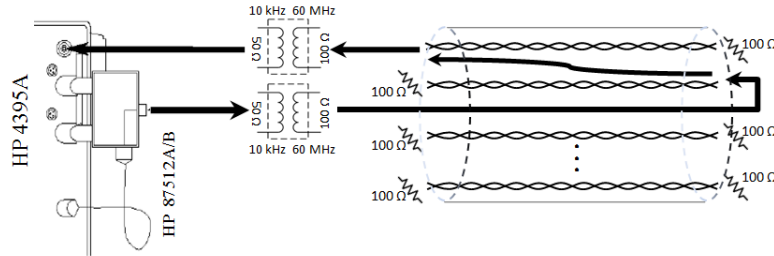
Figure 10: Reference setup for measuring the FEXT transfer functions with a Network Analyzer (NA).

6.3 Results and Comparison

The estimation via (21) can result in negative values for some frequencies due to the variance of the PSDs. Since the attenuation is always positive for passive networks we consider these negative values as *missing data* rather than

zeros, since the latter introduces a too large error. As shown in Fig. 6, the measured FEXT PSD is quantized by the modem to integer-values in units of dBm/Hz, according to the LD protocol. From repeated measurements on the same crosstalk channel, it can be concluded that the obtained FEXT PSDs varies with time in integer steps for a given frequency. The PSD variation between the maximum and the minimum value for a given frequency is typically $1 - 3$ dBm/Hz with our setup. At the measurement band-edges a variation up to $4 - 6$ dBm/Hz can be observed for some crosstalk channels. From the measurements it can also be concluded that the level of variation is independent of the magnitude of the received PSD. The impact of the time-variation on the FEXT channel estimate is analyzed further in Section 7 and provides some insight to the estimation errors.

For each access network scenario in Fig. 7, Fig. 8, and Fig. 9, the square-magnitude of the two FEXT channels are estimated and measured with the modem-based setup and the reference setup, respectively. Fig. 11–Fig. 16 show the estimation results of the two FEXT channels in access network scenario I, II, and III, respectively. The corresponding worst-case FEXT model in (23) is also plotted in Fig. 11–Fig. 16 for comparison, given the true line length and insertion loss.

For all scenarios it can be observed, as expected, that the difference between the NA measurement and the FEXT model is larger than the corresponding difference between the NA measurement and the proposed FEXT estimator. This is true for all used frequencies. The transceiver-filter compensation of the NA measurement and the FEXT model can be seen as increasing (more negative) attenuation at the band edges, *i.e.*, high-pass and low-pass filtering. Except for a small estimation offset for scenario I at certain frequencies, the shape of the estimation curve follows the curvature of the NA measurement quite well. This ability of the estimator is especially important for DSM algorithms that exploit the peaks and the valleys of the FEXT channels in the search for the optimum transmission PSDs.

It can be noted that the estimation results contain a few number of missing data points for all scenarios at the lower frequency-band edge. This is due to the high-pass filter of the transceiver(s) which causes the received signal, measured with active test-signal, to drown in the background noise. This can also be seen for the typical FEXT channel in Fig. 6 where the received signal PSDs are overlapping at frequencies below 250 kHz. Hence, at these frequencies no estimation via (21) is possible due to power limitation of maximum -40 dBm/Hz regulated by the DSL standards [12, 13]. It is, however, possible to use interpolation and/or extrapolation of the estimation results in order to recapture the missing data.
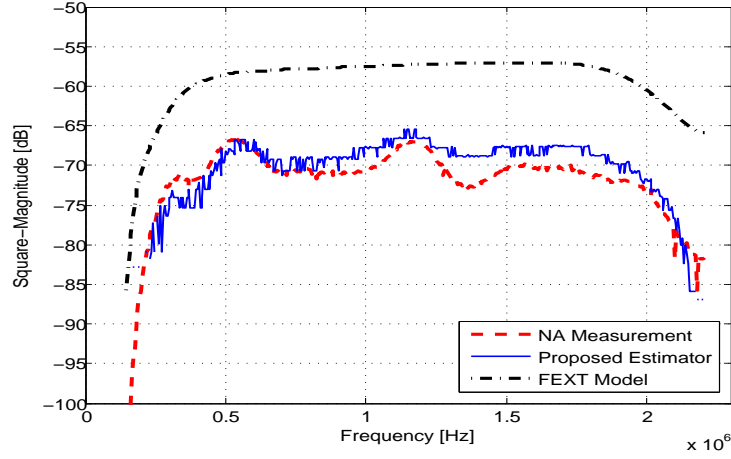
Figure 11: Square-magnitude of the upper FEXT channel in access network scenario I obtained with the NA, the FEXT model and the proposed Estimator.
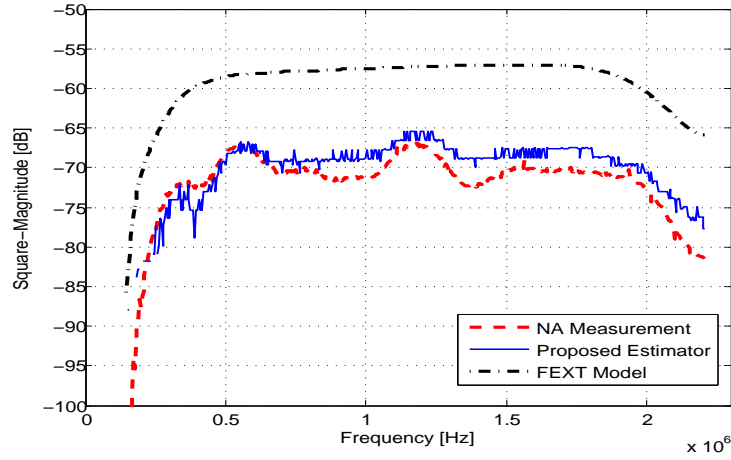

Figure 12: Square-magnitude of the lower FEXT channel in access network scenario I obtained with the NA, the FEXT model and the proposed Estimator.
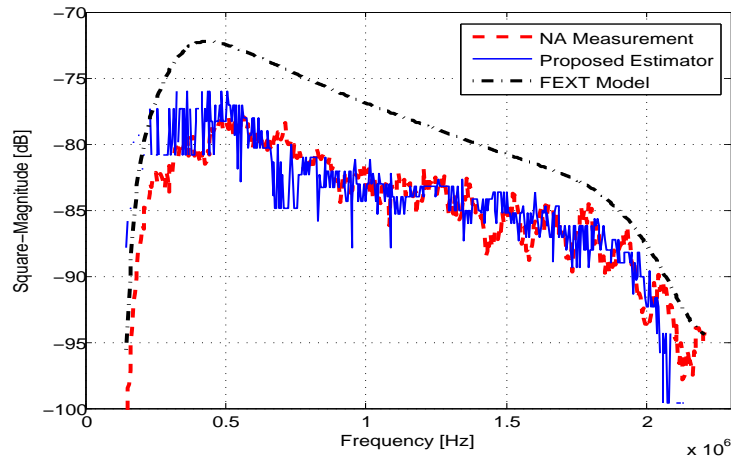
Figure 13: Square-magnitude of the upper (longer) FEXT channel for access network scenario II obtained with the NA, the FEXT model and the proposed Estimator.
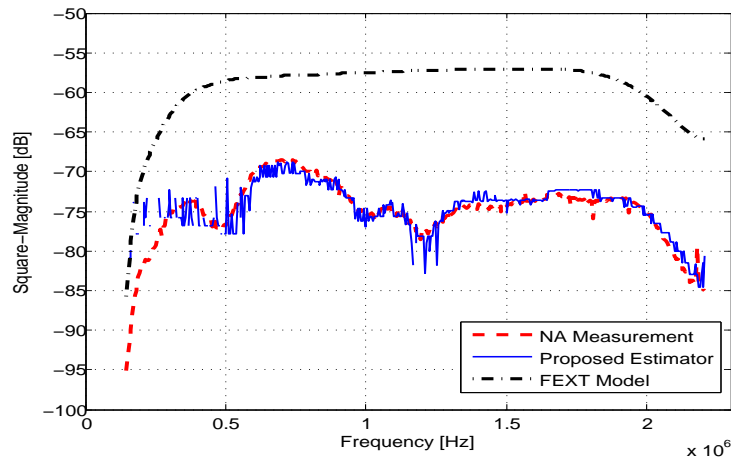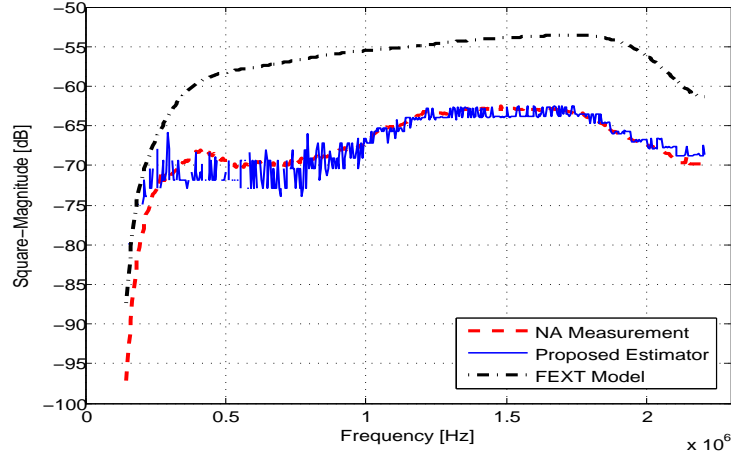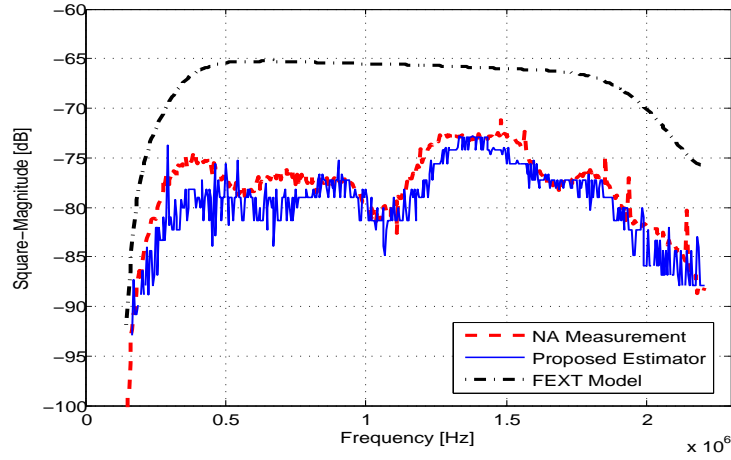

Figure 14: Square-magnitude of the lower (shorter) FEXT channel for access network scenario II obtained with the NA, the FEXT model and the proposed Estimator.

Figure 15: Square-magnitude of the upper (longer) FEXT channel for access network scenario III obtained with the NA, the FEXT model and the proposed Estimator.

Figure 16: Square-magnitude of the lower (shorter) FEXT channel for access network scenario III obtained with the NA, the FEXT model and the proposed Estimator.

Although the variance of the estimates is different for the considered FEXT channels, as seen in Fig. 11–Fig. 16, we can state that the proposed FEXT estimator has a mean deviation less than 3 dB relative to the NA measurements for most frequencies. In fact, pre-processing of the estimation results with *e.g.* a moving average filter reduces the variance of the estimates and gives a mean deviation typically less than 2 dB. The change in the variance of the estimates is analyzed further in the following section.

7   Error Analysis

The internal (thermal) noise of the transceivers, and extrinsic noise, causes the obtained PSDs to vary (slightly) with time. The impact of this PSD variation, combined with the measurement quantization, is analyzed in this section. In the following we focus on the FEXT estimator in (21), but the analysis is also valid for the NEXT estimator in (22).

The estimator(s) described by (21) and (22) rely on the assumption of stationary background noise PSD during the two consecutive measurements at time instance m_0 and m, *i.e.*, it is assumed that $\mathbf{P}_z(m) \approx \mathbf{P}_z(m_0)$ for the FEXT case, and $\mathbf{P}_w(m) \approx \mathbf{P}_w(m_0)$ for the NEXT case. As before, we use the same notation for estimation sequence number and measurement time instance. Without loss of generality, we simplify the notations by consider only one subcarrier (frequency) and a certain FEXT channel, *i.e.*, scalar quantities are used in this section.

With an implementation of the estimator according to Section 4, the PSD is measured as integer values in units of dBm/Hz [3]. Let us denote the true received PSD at estimation sequence m by $P_{dBmHz}(m)$, where the frequency dependence is omitted. Before calculating the FEXT channel estimate, the obtained PSDs are converted to linear scale by

$$P(m) = 10^{(P_{dBmHz}(m,f)-30)/10}B, \tag{24}$$

where B is the measurement bandwidth in Hz. After this conversion the FEXT channel estimate in (21) yields

$$\widetilde{|H|}^2(m) = \frac{P_y(m) - P_z(m_0)}{P_x(m)}, \tag{25}$$

where all quantities are scalar-values in linear scale. Furthermore, $P_z(m_0)$ is the PSD-measurement of the background noise at time instance m_0, and

---

[3]The unit dBm/Hz is a power-measure that expresses the transmit/receive power relative to 1 mW, in logarithmic scale.

$P_y(m)$ is the corresponding PSD-measurement with an active Reverb test-signal on a neighboring line. Here, $P_x(m)$ is the (known) PSD of the test signal. The measurement quantization due to the LD protocol [12, 13], in combination with the additive noise, causes the obtained PSD values (in logarithmic scale) to fluctuate in integer steps around the mean value. The PSD-measurements can therefore be described as

$$\widehat{P}_{dBmHz}(m) = P_{dBmHz}(m) + \Delta_{dBmHz}(m), \tag{26}$$

where $P_{dBmHz}(m)$ is the non-quantized PSD and $\Delta_{dBmHz}(m)$ is the quantized measurement error, modeled as a discrete integer-valued random variable with uniform distribution, i.e., $\Delta_{dBmHz}(m) \in \{-\delta, -\delta+1, ..., 0, ..., \delta\}$ dBm/Hz. From Section 6.3 we know that δ is typically in the order of $1-3$ dBm/Hz, and independent of the magnitude of the received PSD. Consequently, for the case where the received FEXT is (significantly) larger than the background noise, i.e. $P_y(m) >> P_z(m_0)$, the measurement error of $P_z(m_0)$ has little or no impact on the FEXT channel estimate compared to the error of $P_y(m)$. With this assumption, the measurement error at time instance m_0 can be neglected, and the FEXT channel estimate of (25) yields, with (24) and (26),

$$\widetilde{|H|}^2(m) = \frac{P_y(m)\Delta(m) - P_z(m_0)}{P_x(m)}, \tag{27}$$

where $\Delta(m)$ is the corresponding measurement error in linear scale. Expressed in decibel the FEXT channel estimate is $\widetilde{|H|}_{dB}^2(m) = 10\log_{10}\widetilde{|H|}^2(m)$. Subsequently, the estimation error defined as the ratio of (25) and (27), in logarithmic scale, can be formulated as

$$
\begin{aligned}
Error_{dB}(m) &= 10\log_{10}\frac{P_y(m) - P_z(m_0)}{P_y(m)\Delta(m) - P_z(m_0)} \\
&= 10\log_{10}\frac{1 - P_z(m_0)/P_y(m)}{\Delta(m) - P_z(m_0)/P_y(m)}. \tag{28}
\end{aligned}
$$

Equation (28) shows that the measurement error affects the FEXT channel estimate in a nonlinear way. Of particular interest is the fact that the estimation error is a function of the ratio (in linear scale) between the two consecutive measurements at time instance m_0 and m.

However, with the assumption $P_y(m) >> P_z(m_0)$ the estimation error becomes $Error_{dB}(m) \approx 10\log_{10}\frac{1}{\Delta(m)}$, which has a linear dependence on the measurement error in logarithmic scale. Note that error-free measurements correspond to $\Delta_{dBmHz}(m) \to -\infty$, which with (24) gives $\Delta(m) \to 1$.
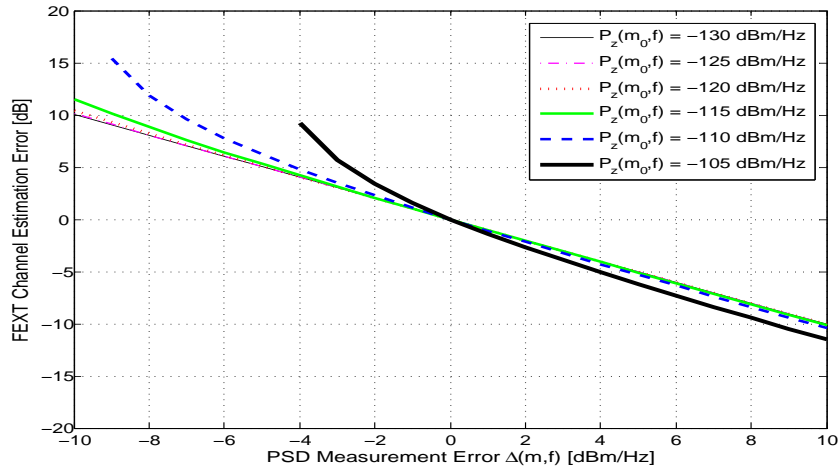
Fig. 17 shows the FEXT channel estimation error in (28) as a function of the measurement error $\Delta(m)$ and the background noise $P_z(m_0)$. The received FEXT PSD $P_y(m)$ with active test signal is here fixed to $-100\,\mathrm{dBm/Hz}$, which corresponds to a transmitted test signal $P_x(m)$ of $-40\,\mathrm{dBm/Hz}$ and a FEXT channel attenuation of $60\,\mathrm{dB}$. Fig. 17 suggests that the estimation

Figure 17: The FEXT channel estimation error in equation (28) as a function of the PSD measurement error $\Delta(m)$ and the received background noise $P_z(m_0)$. The received FEXT PSD $P_y(m)$ from the neighboring line is here fixed to $-100\,\mathrm{dBm/Hz}$.

error increases more than linearly when the level of the background noise $P_z(m_0)$ approaches $P_y(m)$. When the difference between $P_y(m)$ and $P_z(m_0)$ becomes larger than $5\,\mathrm{dBm/Hz}$ the estimation error is approximately linear with the measurement error. For the case $P_z(m_0) \geq P_y(m)$, no estimation is possible which is depicted in Fig. 17 as missing data.

The changes in the estimation variance, seen in *e.g.* Fig. 15 as a larger variance for frequencies below $1\,\mathrm{MHz}$, can be explained with the analysis above. In fact, a closer inspection of the measured PSDs for the FEXT channel in Fig. 15 reveals that $P_y(m) \approx P_z(m_0)$ for frequencies below $1\,\mathrm{MHz}$ while $P_y(m) >> P_z(m_0)$ for frequencies above $1\,\mathrm{MHz}$. Thus in line with (28), the measurement error becomes amplified in the FEXT channel estimate for frequencies below $1\,\mathrm{MHz}$ in Fig. 15. The same increase in estimation variance can be observed for the other scenarios where $P_y(m) \approx P_z(m_0)$.

8 Summary and Conclusions

DSM crosstalk mitigation techniques for the copper access network requires information about the *square-magnitude* (attenuation) of the crosstalk channels. The paper addresses this issue by proposing an estimator that is capable of simultaneously obtain the square-magnitude of the FEXT and NEXT channels. The proposed estimator is derived from least-squares (LS) estimation of a linear SIMO system with AWGN. The additional requirement of only utilizing PSD-signals for the LS estimator results in a biased estimate. However, by assuming stationary conditions during the short estimation period, the estimator is made unbiased by subtracting the measured background PSD at the receiver.

The proposed estimator requires no hardware or software changes of the used DSL modems and utilizes only measurements available via the existing DSL standards. An implementation based on the standardized *Loop Diagnostic* (LD) functionality was described and evaluated by laboratory experiments on three access network scenarios, built-up with twisted-pair copper cables. A comparison with reference measurements indicate that the mean deviation of the estimator is less than $3\,\mathrm{dB}$ for most frequencies. In particular the ability of the estimator to follow the curvature of the FEXT channels was demonstrated, which is an important property for DSM that the compared FEXT channel model is missing.

Appendix A

Here we consider the optimum minimum variance unbiased (MVU) estimator for the SIMO linear model of (12) with complex AWGN. The noise is assumed uncorrelated between different receivers, and hence, independent between receivers for the Gaussian case. We may therefore study (12) from a single-receiver perspective. Thus, with only transmitter m active at estimation sequence m, the (complex) FEXT at receiver n can be expressed as

$$\bar{Y}_n(m) = \mathbf{X}(m)\bar{H}_{n,m} + \bar{Z}_n(m), \quad \text{for } n = 1, 2, \ldots, U \quad, \tag{29}$$

where $\bar{Y}_n(m)$ is the $K \times 1$ received FEXT vector from transmitter m, $\bar{H}_{n,m}$ is the FEXT channel from transmitter m to receiver n, and $\mathbf{X}(m)$ denotes the $K \times K$ transmit matrix, all defined in Section 3. Here, $\bar{Z}_n(m) \in \mathcal{CN}(\bar{0}, \mathbf{C})$ where the mean-value vector is zero and the $K \times K$ positive definite covariance matrix is denoted by $\mathbf{C}$. In order to simplify the notation we drop the subscript and the sequence number in the following analysis. Under the

assumed conditions, the PDF of the received vector is given by

$$f_Y(\bar{H}) = \frac{1}{\pi^K \det \mathbf{C}} \exp\left(-\frac{1}{2}(\bar{Y} - \mathbf{X}\bar{H})^H \mathbf{C}^{-1}(\bar{Y} - \mathbf{X}\bar{H})\right). \qquad (30)$$

The maximum likelihood estimator (MLE) maximizes $\ln f_Y(\bar{H})$ which is equivalent to minimize the exponent of (30). Hence, the MLE minimizes

$$J = (\bar{Y} - \mathbf{X}\bar{H})^H \mathbf{C}^{-1}(\bar{Y} - \mathbf{X}\bar{H}), \qquad (31)$$

where ^{H} denotes the Hermitian transpose. Since $\mathbf{C}^{-1}$ is a positive definite matrix and J is a quadratic function of the elements of $\bar{H}$, the global minimum is obtained by expanding (31) and completing the square, *i.e.*

$$\begin{aligned} J \;=\; & \left(\bar{H} - (\mathbf{X}^H \mathbf{C}^{-1}\mathbf{X})^{-1}\mathbf{X}^H \mathbf{C}^{-1}\bar{Y}\right)^H \mathbf{X}^H \mathbf{C}^{-1}\mathbf{X} \\ & \cdot\left(\bar{H} - (\mathbf{X}^H \mathbf{C}^{-1}\mathbf{X})^{-1}\mathbf{X}^H \mathbf{C}^{-1}\bar{Y}\right) + \bar{Y}^H \mathbf{C}^{-1}\bar{Y} \\ & -\bar{Y}^H \mathbf{C}^{-1}\mathbf{X}(\mathbf{X}^H \mathbf{C}^{-1}\mathbf{X})^{-1}\mathbf{X}^H \mathbf{C}^{-1}\bar{Y}. \end{aligned} \qquad (32)$$

The quadratic term in (32) is always non-negative and thus J is minimized for

$$\bar{H}_{MLE} = (\mathbf{X}^H \mathbf{C}^{-1}\mathbf{X})^{-1}\mathbf{X}^H \mathbf{C}^{-1}\bar{Y}, \qquad (33)$$

where the index MLE stands for maximum likelihood estimator. It can further be shown [31] that the PDF of the MLE is complex normal distributed as

$$\bar{H}_{MLE} \in \mathcal{CN}(\bar{H}, (\mathbf{X}^H \mathbf{C}^{-1}\mathbf{X})^{-1}). \qquad (34)$$

For a general linear model with complex AWGN, as (29) represents, it can be shown [31] that the MLE is a MVU estimator as well as an efficient estimator in that it attains the Cramer-Rao lower bound. However, the estimator in (33) requires the inverted noise covariance matrix $\mathbf{C}^{-1}$ which is not available from an network operator's point of view, where only standardized signals can be retrieved. In case the noise is uncorrelated, $\mathbf{C}$ becomes a diagonal matrix and the MLE in (33) is reduced to $\mathbf{X}^{-1}\bar{Y}$, provided $\mathbf{X}$ has full rank. This case corresponds to the least-squares estimator in (15).

References

[1] K. Kerpez, "DSL spectrum management standard," *IEEE Commun. Mag.*, vol. 40, no. 11, Nov. 2002.

[2] K. Kerpez, D. Waring, S. Galli, J. Dixon, and P. Madon, "Advanced DSL management," *IEEE Commun. Mag.*, vol. 41, no. 9, pp. 116 – 123, Sept. 2003.

[3] J. Verlinden, T. Bostoen, and G. Ysebaert, "Dynamic spectrum management for digital subscriber lines - edition 2," *Technology White Paper - Alcatel*, 2005.

[4] NIPP-NAI-2007-038 R3, "Draft Dynamic Spectrum Management technical report for second default ballot.," 2007.

[5] R. Cendrillon and M. Moonen, "Iterative spectrum balancing for digital subscriber lines," *IEEE International Communications Conference (ICC)*, May 2005.

[6] R. Cendrillon, W. Yu, M. Moonen, J. Verlinden, and T. Bostoen, "Optimal multiuser spectrum balancing for digital subscriber lines," *IEEE Trans. Commun.*, vol. 54, no. 5, pp. 922–933, May 2006.

[7] J. Papandriopoulos and J.S. Evans, "Low-complexity distributed algorithms for spectrum balancing in multi-user DSL networks," *IEEE International Conference on Communications (ICC)*, Jun. 2006.

[8] R. Cendrillon, J. Huang, M. Chiang, and M. Moonen, "Autonomous spectrum balancing for digital subscriber lines," *IEEE Transactions on Signal Processing*, vol. 55, no. 8, pp. 4241–4257, Aug. 2007.

[9] D. Statovci, T. Nordström, and R. Nilsson, "Dynamic spectrum management for standardized VDSL," *IEEE International Conference on Acoustics, Speech, and Signal Processing (ICASSP), Honolulu, Hawaii, USA*, 2007.

[10] J.M. Cioffi, S. Jagannathan, W. Lee, H. Zou, A. Chowdhery, W. Rhee, G. Ginis, and P. Silverman, "Greener copper with dynamic spectrum management," *AccessNets, Las Vegas, NV, USA*, 2008.

[11] S. Jagannathan, C.S. Hwang, and J.M. Cioffi, "Margin optimization in digital subscriber lines employing level-2 dynamic spectrum management," *IEEE International Conference on Communications (ICC), Beijing, China*, May 2008.

[12] ITU-T G.992.3, "Asymmetric digital subscriber line transceivers 2 (adsl2)," 07/2002.

[13] ITU-T G.992.5, "Asymmetric digital subscriber line transceivers - extended bandwidth (adsl2plus)," 05/2003.

[14] ITU-T G.993.2, "Very high speed digital subscriber line transceivers 2 (vdsl2)," 2006.

[15] T. Bostoen, P. Boets, M. Zekri, L. Van Biesen, T. Pollet, and D. Rabijns, "Estimation of the transfer function of a subscriber loop by means of one-port scattering parameter measurement at the central office," *IEEE Journal of Selected Areas in Communications*, vol. 20, No. 5, pp. 936–948, June 2002.

[16] S. Galli and D.L. Waring, "Loop makeup identification via single ended testing: beyond mere loop qualification," *IEEE Journal of Selected Areas in Communications*, vol. 20, No. 5, pp. 923–935, June 2002.

[17] T. Vermeiren, T. Bostoen, F. Louage, P. Boets, and X.O. Chehab, "Subscriber loop topology classification by means of time-domain reflectometry," *IEEE International Conference on Communications*, Anchorage, USA, 11-15 May, 2003.

[18] P. Boets, L. Van Biesen, T. Bostoen, and D. Gardan, "Single-ended line testing - a white box approach," *Proceedings of the 4th IASTED International Multi-Conference, Wireless and Optical Communications*, July 8-10, 2004, Banff, Canada.

[19] K. Kerpez and S. Galli, "Single-ended loop make-up identification. Part I: A method of analyzing TDR measurements," *IEEE Transactions on Instrumentation and Measurement*, vol. 55, no. 2, pp. 528–537, Apr. 2006.

[20] K. Kerpez and S. Galli, "Single-ended loop make-up identification. Part II: Improved algorithms and performance results," *IEEE Transactions on Instrumentation and Measurement*, vol. 55, no. 2, pp. 538–549, Apr. 2006.

[21] American National Standard for Telecommunications, "Spectrum Management for Loop Transmission Systems, T1.417-2003, (issue 2)," 2003.

[22] ITU-T G.996.1, "Test procedures for digital subscriber line (dsl) transceivers," 02/2001.

[23] N. Fonseca, D. Neves, A.C. Gomes, M. Conte, B. Dortschy, K. Ericson, J. Rius i Riu, E. Pelaes, and A. Klautau, "Evaluation of DSM performance with mixed DSL services and measured crosstalk channels,"

XXV Simpósio Brasileiro de Telecomunicações - SBrT 2007, Recife, PE., Brazil, 2007.

[24] M. Sorbara, P. Duvaut, F. Shmulyian, S. Singh, and A. Mahadevan, "Construction of a DSL-MIMO channel model for evaluation of FEXT cancellation systems in VDSL2," *Sarnoff Symposium, 2007 IEEE*, Apr. 2007.

[25] C. Zeng, C. Aldana, A.A. Salvekar, and J.M. Cioffi, "Crosstalk identification in xDSL systems," *IEEE J. Sel. Areas Commun.*, vol. 19, pp. 1488–1496, 2001.

[26] S. Galli, C. Valenti, and K. Kerpez, "A frequency-domain approach to crosstalk identification in xDSL Systems," *IEEE J. Sel. Areas Commun.*, vol. 19, no. 8, pp. 1497–1506, Aug. 2001.

[27] N. Papandreou and T. Antonakopoulos, "Far-End Crosstalk Identification Method Based on Channel Training Sequences," *IEEE Transactions on Instrumentation and Measurement*, vol. 54, pp. 2204–2212, 2005.

[28] Y. Shi, F. Ding, and T. Chen, "Multirate Crosstalk Identification in xDSL Systems," *IEEE Trans. Commun.*, vol. 54, no. 10, pp. 1878–1886, 2006.

[29] ITU-T Study Group 15, "G.vector: Draft Recommendation," Dec. 2008.

[30] T. Starr, J.M. Cioffi, and P.J. Silverman, *Understanding digital subscriber line technology*, Prentice Hall, Upper Saddle River, 1999.

[31] S.M. Kay, *Fundamentals of Statistical Signal Processing: Estimation Theory*, Prentice Hall Signal Processing Series. Alan V. Oppenheim, Series, 1993.

[32] C. Valenti, "NEXT and FEXT models for twisted-pair north american loop plant," *IEEE J. Sel. Areas Commun.*, vol. 20, pp. 893–900, 2002.

[33] S. Galli and K. Kerpez, "Methods of summing crosstalk from mixed sources - part I: theorectical analysis," *IEEE Transactions on Communications*, vol. 50, pp. 453–461, Mar. 2002.

[34] K. Kerpez and S. Galli, "Methods of summing crosstalk from mixed sources - part II: performance results," *IEEE Transactions on Communications*, vol. 50, pp. 600–607, Apr. 2002.

[35] E. Karipidis, N. Sidiropoulos, A. Leshem, L. Youming, R. Tarafi, and M. Ouzzif, "Crosstalk models for short VDSL2 lines from measured 30MHz data," *EURASIP Journal on Applied Signal Processing*, p. , 2006.

[36] B. Lee, J.M. Cioffi, S. Jagannathan, K. Seong, Y. Kim, M. Mohseni, and M.H. Brady, "Binder MIMO Channels," *IEEE Transactions on Communications*, vol. 55, no. 8, pp. 1617–1628, 2007.

[37] ITU-T Study Group 15 - Contribution 30, "Status of ATIS NIPP-NAI Technical Report on MIMO Crosstalk Channel Model," Nov. 2008.

Paper VII

Paper VII

Impact of Crosstalk Channel Estimation on the DSM Performance for DSL Networks

Abstract

The development and assessment of spectrum management methods for the copper access network are usually conducted under the assumption of accurate channel information. Acquiring such information implies, in practice, estimation of the crosstalk coupling functions between the twisted-pair lines in the access network. This type of estimation is not supported or required by current digital subscriber line (DSL) standards. In this work, we investigate the impact of the inaccuracies in crosstalk estimation on the performance of dynamic spectrum management (DSM) algorithms. A recently proposed crosstalk channel estimator is considered and a statistical sensitivity analysis is conducted to investigate the effects of the crosstalk estimation error on the bitloading and on the achievable data rate for a transmission line. The DSM performance is then evaluated based on the achievable data rates obtained through experiments with DSL setups and computer simulations. Since these experiments assume network scenarios consisting of real twisted-pair cables, both crosstalk channel estimates and measurements (for a reference comparison) are considered. The results indicate that the error introduced by the adopted estimation procedure does not compromise the performance of the DSM techniques, *i.e.*, the considered crosstalk channel estimator provides enough means for a practical implementation of DSM.

1   Introduction

High-speed communication over digital subscriber lines (DSL) can be severely limited by interference from adjacent copper twisted-pair lines in the access network. This destructive crosstalk between neighboring systems is considered as one of the most dominant impairments and consequently poses a limit for performance improvements [1, 2].

Dynamic spectrum management (DSM) is a promising resource management approach to optimize the transmission and improve the data throughput of DSL networks. In summary, DSM is based on improving the spectral utilization by adapting the transmit signals to the slowly time-varying channel conditions. Moreover, DSM algorithms exploit multi-user cooperation in order to mitigate or cancel multi-user interference [3–8]. The DSM techniques are commonly organized into three levels depending on the amount of multi-user coordination [5, 7]. For DSM level 1 [9], no crosstalk coupling information is used to optimize the DSL network performance. In DSM level 2 [10–14], the magnitude of the direct and the crosstalk transfer functions are used in order to mitigate the crosstalk. For DSM level 3 (Vectoring), which employs crosstalk cancellation, the crosstalk channel phase information is also required [15–17].

The acquisition of information about the crosstalk channels in the network is usually a demanding task, which may require additional measurement apparatus that are costly to deploy [18]. In *e.g.* [19–21], different crosstalk estimation solutions have been proposed. However, up to now, the standardization bodies have not yet defined any DSL standard with specific support to estimate the coupling relation between the twisted-pairs in a cable binder. With off-the-shelf modems not offering a specific method for estimating the crosstalk channels, various DSM algorithms have been developed and evaluated assuming perfect crosstalk channel information [3, 7, 10, 12]. Moreover, these evaluations adopt standardized channel models, which are typically based on statistics and reflect a worst-case scenario [1, 22, 23].

A practical implementation of DSM level 2 and level 3 algorithms must cope with eventual inaccuracies in the crosstalk channel estimation. This is also valid for the stage when evaluating DSM algorithms through computer simulations. Motivated by this fact, the present work investigates the impact of non-ideal crosstalk channel estimation on the DSM performance. For this purpose, the crosstalk channel estimator in [24] is considered, since it is a standard-compliant method and does not require costly DSL hardware/software changes or dedicated measurement apparatus for deployment.

A statistical sensitivity analysis is provided to gain insight of how the crosstalk estimation error affects the frequency-dependent bitloading and the

resulting data rate for a transmission line, under the exposure of different background noise levels. It is worth to notice that, in general, the level 2 DSM algorithms are formulated in order to optimize the *bitloading*, or equivalently the *power loading*, and generate a solution for the spectrum management problem (see *e.g.* [25]).

Since the presence of the crosstalk estimation error impacts the final solution of the DSM algorithms, the DSM performance is evaluated based on the achievable data rates obtained through DSL network simulations. For these simulations, network scenarios consisting of real twisted-pair cables are considered and in addition, both crosstalk-channel estimates and reference measurements are used for the comparison. The crosstalk channel reference-measurements are conducted in a laboratory using a network analyzer and ordinary twisted-pair cables. For each scenario, three state-of-the-art DSM algorithms are simulated and the results in terms of achievable data rate region curves are analyzed.

The remainder of this work is organized as follows. Section 2 presents the system model and defines the notation. Section 3 describes the principles of the power spectrum density (PSD) level optimization applied by DSM algorithms as a solution to the spectrum management problem. In Section 4, the employed crosstalk channel estimation is introduced. Section 5 is dedicated to the proposed statistical sensitivity analysis. Details about the network scenarios, laboratory setup and obtained measurements are given in Section 6. The DSM performance evaluation assuming the crosstalk channel estimation is presented in Section 7. Finally, a summary and conclusions are provided in Section 8.

2   System Model

Traditionally, DSL broadband access networks have been analyzed from a single-user system perspective. However, for DSM-enabled systems, such as the ones considered here, the DSL lines are used in a multi-user context. This perspective requires a multi-user or a multiple-input multiple-output (MIMO) channel model,[1] which permits the joint-user coordination concept utilized by the DSM techniques.

In this work, DSM algorithms are applied on a copper access binder, which consists of N users (*i.e.* lines) equipped with DSL transceivers. Each transceiver employs discrete multitone modulation (DMT) and operates over a twisted-pair line with K independent and parallel subchannels (tones) over

---

[1]This should not be confused with the concept of MIMO or vectoring DSM, related to DSM level 3 algorithms [3, 15].
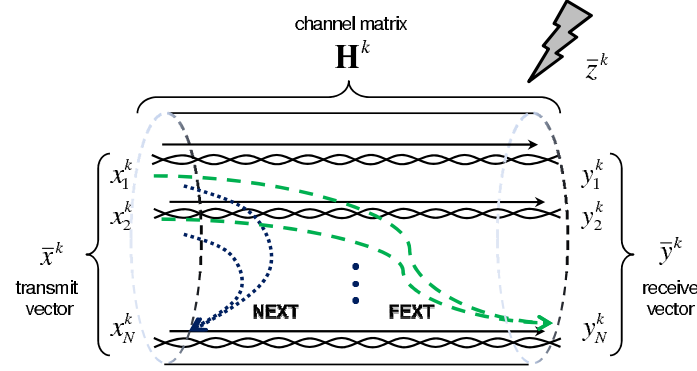
Figure 1: Illustration of DMT transmission and occurring NEXT and FEXT interference on a copper access binder.

the frequency band plan [1]. This means that the received signal vector on tone k can be modeled as [1,5],

$$\bar{y}^k = \mathbf{H}^k \bar{x}^k + \bar{z}^k, \quad \text{for } k = 1, 2, \ldots, K, \tag{1}$$

where

- $\bar{x}^k = \left[x_1^k, x_2^k, \ldots, x_N^k\right]^T$ is the transmitted signal vector on tone k for all N users;

- $\bar{y}^k = \left[y_1^k, y_2^k, \ldots, y_N^k\right]^T$ is the received signal vector on tone k for all N users;

- $\bar{z}^k = \left[z_1^k, z_2^k, \ldots, z_N^k\right]^T$ is the additive noise vector on tone k including the extrinsic network impairment, *e.g.* impulse noise, radio frequency interference (RFI), thermal noise and alien crosstalk [1];

- $\mathbf{H}^k$ corresponds to a $N \times N$ matrix containing the channel transfer functions on tone k.

The DMT transmission for tone k in a cable binder, represented by (1), is illustrated in Fig. 1. Basically two types of crosstalk are present in the DSL network: the far-end (FEXT) and the near-end (NEXT) crosstalk, shown in Fig. 1. By assuming only frequency division duplex DMT transmission, where upstream and downstream frequency bands are non-overlapping, it is reasonable to neglect the weak NEXT influence [1]. The channel matrix

Figure 2: MIMO channel matrix $\mathbf{H}$ of dimension $N \times N \times K$.

$\mathbf{H}$ characterizes the binder by representing both the direct and the FEXT coupling transfer functions, and can be interpreted along the three dimensions $N \times N \times K$, as illustrated in Fig. 2.

Each channel vector $\bar{h}_{n,m} = \left[h_{n,m}^1, h_{n,m}^2, \ldots, h_{n,m}^K \right]^T$ represents the transfer function of the channel from transmitter m to receiver n, over the tones. For the case where $m = n$, the diagonal vectors $\bar{h}_{1,1}, \bar{h}_{2,2}, \ldots, \bar{h}_{N,N}$ correspond to the direct transfer functions of the twisted-pair lines. Similarly, the off-diagonal vectors $\bar{h}_{n,m}$ for $n \neq m$, correspond to the FEXT transfer functions between the lines.

3 PSD Level Optimization and the Spectrum Management Problem

DSM level 1 and level 2 employ PSD level optimization aiming to assign a transmit PSD for each user, within the DSL network, in order to minimize the crosstalk interference. The PSD assignment is conducted according to a set of predefined criteria and constraints, *e.g.* maximize the user rates under power limitation. For the nth user, the PSD of the transmitted signal on tone k is here defined by $E \left\{ \left| x_n^k \right|^2 \right\}$, whose maximum value is specified by the DSL standard(s), where $E \left\{ \cdot \right\}$ denotes the statistical mean value. Hence the transmit power on tone k for user n can be expressed as $s_n^k = \Delta_f E \left\{ \left| x_n^k \right|^2 \right\}$, where Δ_f is the tone spacing. The transmit power vector with K tones for user n can be represented by $\bar{s}_n = \left[s_n^1, s_n^2, \ldots, s_n^K \right]^T$.

The PSD level optimization allows the transmitter to adaptively vary the number of transmitted bits per tone according to the characteristics of the channel. This practice avoids the use of fixed transmit PSDs for all users and thereby prevents a loss in performance [5, 7]. The final result of the PSD level optimization is a dynamic shaping of the transmit PSDs

according to the interference levels within the used frequency band. The PSD dynamic shaping is possible due to the bitloading concept exploited by DMT [1]. This allocation of bits per tone is performed for each subchannel and can be expressed as follows

$$b_n^k \quad = \quad \log_2 \left[1 + \frac{s_n^k \left| h_{n,n}^k \right|^2}{\Gamma \left(\sigma_{k,n}^2 + \sum_{m \neq n} s_m^k \left| h_{n,m}^k \right|^2 \right)} \right], \tag{2}$$

where

- b_n^k is the achievable bitloading on tone k for user n;

- $\sigma_{k,n}^2$ is defined as $\Delta_f E \left\{ \left| z_n^k \right|^2 \right\}$ and represents the additive noise power, *i.e.* the background noise level, on tone k at receiver n, which coincides with the noise variance given that $E \left\{ z_n^k \right\} = 0$. It is assumed that $\sigma_{k,n}^2$ contains the thermal noise, alien crosstalk and radio frequency interference;

- Γ denotes the signal-to-noise (SNR) ratio *gap*, which is a function of the desired bit error rate (BER). The *gap* is an indicator of how closely the bit rate comes to the theoretical channel capacity [1, 2].

Considering that each transceiver (modem) treats the interference from the other transceivers as noise, the achievable bit rate of user n can be formulated as [1, 2]

$$R_n = f_{\text{sym}} \sum_{k=1}^{K} b_n^k, \tag{3}$$

where f_{sym} represents the symbol rate of the DMT transceivers [5]. Similarly, the total power assigned to the nth user can be expressed as

$$P_n = \sum_{k=1}^{K} s_n^k. \tag{4}$$

The total data throughput is an often used performance measure for communication networks. In the context of DSM, we can assume that the optimization of a multi-user DMT (multicarrier) system corresponds to the problem of maximizing the total throughput subject to system resource-constraints. Thus, the spectrum management problem is commonly formulated as a maximization problem of the weighted sum-rate, subject to a power

constraint per user. That is,

$$\text{maximize} \qquad \sum_{n=1}^{N} \omega_n R_n \qquad\qquad\qquad (5)$$

$$\text{subject to} \qquad \sum_{k=1}^{K} s_n^k \leqslant P_n^{\max} \quad n = 1, 2, ..., N; \ s_n^k \geq 0,$$

where ω_n is the non-negative constant for user n that provides different priorities (or weights) for users and $P_n^{\max}$ is the maximum available power for user n.

The optimization problem represented by (5) can be interpreted as a search to find a set of non-negative s_n^k values, under a trade-off between maximizing the data rate R_n and avoiding crosstalk interference. Generally, in the context of a solution for the spectrum management problem, the DSM algorithms aim to find the optimum values for the transmit power allocation (power loading) s_n^k, which is equivalent to find the optimum values for the bit allocation (bitloading) b_n^k, both for $n = 1, 2, ..., N$ and for $k = 1, 2, ..., K$.

In this work, DSM algorithms [10, 12] formulated to solve the weighted sum-rate maximization problems (rate adaptive) are considered. Therefore, the sensitivity analysis performed in the forthcoming section is based on the bitloading formulation. However, this analysis could also be cast in a power loading framework without loss of generality, due to the equivalence of the rate and power adaptive problems [25].

4   Crosstalk Channel Estimation

The DSM level 2 compliant algorithms used in this work provide a solution to the spectrum management problem formulated in (5). These algorithms require channel information about the square-magnitude of the direct and crosstalk channels. As mentioned before, the corresponding channel phase information can be neglected for DSM level 2 applications. The channel matrix $\mathbf{H}$, introduced in Section 2, characterizes the access cable binder and contains the direct and the FEXT transfer functions. It can be presumed that the direct transfer functions are known *a priori*, since the procedures to obtain them are supported by the current DSL standards [26].

In this work, the square-magnitude of the off-diagonal elements of channel matrix $\mathbf{H}$ are obtained by the crosstalk channel estimation procedure described in [24]. Since the transmitted PSD for each user is assumed known, the total received crosstalk can be calculated from the crosstalk channel es-

timates. Thus, throughout the paper we define the method proposed in [24] as the *Crosstalk Estimator*, where no *a priori* channel information is used.

In the following subsection a brief summary of the *Crosstalk Estimator* is given with focus on the behavior of the estimation error [24]. This provides the fundamental understanding of the error to expect when estimating the FEXT with the employed estimator. This is further elaborated on in Section 5 where a statistical sensitivity analysis of the achievable bitloading and data rate is presented.

4.1   Crosstalk Channel Estimation Error

The *Crosstalk Estimator* presented in [24] relies only on standardized DSL signals and protocols, *e.g.* the two-port measurement procedure referred to as Loop Diagnostic [26], which are supported by off-the-shelf DSL modems that are DSL standard compliant. More specifically, the estimator is based on sequential PSD measurements at the far-end side of the lines with only one near-end transmitter active per measurement sequence. The procedure is typically executed and coordinated from a network management system with independent processing among the far-end receivers. It should be emphasized that the FEXT channel estimation has to be performed only once, or seldom, since the FEXT channels do not (normally) vary significantly over time.

The sequential PSD-based estimate of the FEXT channel attenuation $|h_{n,m}^k|^2$ can be formulated as, [24],

$$\widetilde{|h_{n,m}^k|^2} \quad = \quad \frac{P_y^k - P_z^k}{P_x^k}, \tag{6}$$

where P_x^k, P_y^k and P_z^k are the transmit PSD on line m, the receive FEXT PSD on line n, and the additive noise PSD on line n, respectively, for tone k and in unit Watts. In practice, however, the PSD measurements via the Loop Diagnostic protocol is not error-free due to the fact that *e.g.* the PSD measurements are quantized and, in combination with the additive noise, fluctuate in discrete steps around the mean values. That is, for tone k the obtained PSD measurements can be expressed as

$$\hat{P}_{\text{dBm/Hz}}^k = P_{\text{dBm/Hz}}^k + \Delta_{\text{dBm/Hz}}, \tag{7}$$

where $P_{\text{dBm/Hz}}^k$ denotes the non-quantized PSD and $\Delta_{\text{dBm/Hz}}$ is the quantized measurement error modeled as a discrete integer-valued random variable with uniform distribution, *i.e.*, $\Delta_{\text{dBm/Hz}} \in \{-\delta, \delta+1, \ldots, 0, \ldots, \delta\}$ dBm/Hz. The PSD measurements are converted to unit Watts according to

$$P = 10^{\left(P_{\text{dBm/Hz}}^k - 30\right)/10} B, \tag{8}$$

where B is the measurement bandwidth in Hz. It is known from the experiments in [24] that it is reasonable to consider δ as typically varying in the range of 1 to 3 dBm/Hz, independently of the magnitude of the measured PSD. Moreover, for the case where the measured FEXT is much larger than the background noise level, that is, $P_y \gg P_z$, the measurement error associated with P_z has essentially no impact when compared to the measurement error of P_y. Consequently, the measurement error of P_z can be neglected. Based on these assumptions, the obtained FEXT channel estimate can straightforwardly be derived from (6)–(8) and yields

$$\widetilde{|h_{n,m}^k|}^2 = \frac{P_y^k \Delta - P_z^k}{P_x^k},$$ (9)

where both the FEXT channel estimate given by (9) and the measurement error Δ are in linear scale. The resulting FEXT channel estimation error in dB, denote by $\widetilde{\Delta}_{\mathrm{dB}}$, can be defined as the ratio between (6) and (9), that is,

$$\widetilde{\Delta}_{\mathrm{dB}} = 10 \log_{10} \left(\frac{1 - \frac{P_z}{P_y}}{\Delta - \frac{P_z}{P_y}} \right),$$ (10)

which shows that the PSD measurement error Δ affects the FEXT channel estimate in a non-linear way. It should be noticed the difference between the *PSD measurement error* Δ and the *FEXT channel estimation error* $\widetilde{\Delta}$.

Under the given assumption that $P_y \gg P_z$, the estimation error in (10) yields

$$\widetilde{\Delta}_{\mathrm{dB}} \approx 10 \log_{10} \frac{1}{\Delta}.$$ (11)

Equation (11) indicates that the estimation error $\widetilde{\Delta}_{\mathrm{dB}}$ has an approximative linear dependence on the PSD measurement error Δ (in logarithmic scale) when $P_y \gg P_z$. The experimental results in [24] suggests that the linear error approximation is reasonable if the difference between P_y and P_z corresponds to at least 5 dB, in which case the estimation error $\widetilde{\Delta}_{\mathrm{dB}}$ is typically confined to the interval $[-3, 3]$ dB. Hence, in line with [24] this work assumes a FEXT channel estimation error uniformly distributed within $[-3, 3]$ dB.

5 Statistical Sensitivity Analysis

This section provides a statistical sensitivity analysis of the achievable bit-loading, represented by (2), as a function of the FEXT channel estimation

error parameter $\widetilde{\Delta}$. The purpose of this analysis is to gain insight of how the bitloading and the data rate are affected by the FEXT channel estimation error.

Firstly, the probability density function (PDF) of the bitloading b_n^k, for line n and tone k, is derived given that the FEXT channel estimation error is modeled as an uniform random variable according to Section 4.1. Secondly, we derive the PDF of the data rate achieved on line n, resulting from the uniformly distributed estimation error. Thirdly, numerical results for the above mentioned PDFs are presented based on measured FEXT couplings of an ordinary twisted-pair cable.

5.1   Deriving the PDF of b_n^k

The relation between the bitloading and the crosstalk estimation error $\widetilde{\Delta}$ reveals a variation in the assignment of bits per tone caused by the non-perfect crosstalk channel estimation. Such variation in the number of bits is also reflected in the final solutions of the DSM algorithms in terms of a spread in the achievable data rate, given by (3). Motivated by this fact, the PDF of b_n^k as a function of the random variable $\widetilde{\Delta}$ is derived in the sequel while the PDF of the data rate is derived in Section 5.2.

We start out defining the relation between the bitloading b_n^k and the crosstalk estimation error $\widetilde{\Delta}$ by reformulating the expression in (2) as

$$b_n^k = \log_2\left[1 + \frac{s_n^k\left|h_{n,n}^k\right|^2}{\Gamma\left(\sigma_{k,n}^2 + \sum_{m \neq n} s_m^k \widetilde{\Delta}\left|h_{n,m}^k\right|^2\right)}\right]. \tag{12}$$

It can be noted that the estimation error parameter $\widetilde{\Delta}$ appears in (12) as a factor that multiplies with $\left|h_{n,m}^k\right|^2$, where the latter corresponds to the FEXT channel attenuation between lines m and n. For convenience, we also define the following non-negative quantities:

$$A = \frac{s_n^k\left|h_{n,n}^k\right|^2}{\Gamma}, \qquad B = \sum_{m \neq n} s_m^k\left|h_{n,m}^k\right|^2. \tag{13}$$

With the help of these two constants, b_n^k can be written as a function $g\left(\widetilde{\Delta}\right)$ according to

$$b_n^k = g\left(\widetilde{\Delta}\right) = \log_2\left[1 + \frac{A}{\sigma_{k,n}^2 + \widetilde{\Delta}B}\right]. \tag{14}$$

By defining the inverse function $g^{-1}\left(b_n^k\right)$, the parameter $\widetilde{\Delta}$ can be expressed as

$$\widetilde{\Delta} = g^{-1}\left(b_n^k\right) = \frac{A - \sigma_{k,n}^2 \left(2^{b_n^k} - 1\right)}{B\left(2^{b_n^k} - 1\right)}. \tag{15}$$

Thus, the PDF of b_n^k, denoted by $f_{b_n^k}\left(b_n^k\right)$, can be formulated as, [27],

$$f_{b_n^k}\left(b_n^k\right) \quad = \quad \left|\frac{\partial\left(g^{-1}\left(b_n^k\right)\right)}{\partial b_n^k}\right| f_{\widetilde{\Delta}}\left(g^{-1}\left(b_n^k\right)\right), \tag{16}$$

where $f_{\widetilde{\Delta}}$ is the PDF of $\widetilde{\Delta}$ and the derivative of $g^{-1}\left(b_n^k\right)$ is

$$\frac{\partial\left(g^{-1}\left(b_n^k\right)\right)}{\partial b_n^k} \quad = \quad \frac{-A 2^{b_n^k} \ln 2}{B\left(2^{b_n^k} - 1\right)^2}. \tag{17}$$

Hereafter the PDF of $\widetilde{\Delta}$ (in linear scale) is determined. In line with [24], we assume that the measurement error $\widetilde{\Delta}_{\mathrm{dB}}$ is uniformly distributed (in unit dB), *i.e.*,

$$f_{\widetilde{\Delta}_{\mathrm{dB}}}\left(\widetilde{\Delta}_{\mathrm{dB}}\right) = \begin{cases} 0, & \widetilde{\Delta}_{\mathrm{dB}} < c_1 \\ \frac{1}{(c_2 - c_1)}, & c_1 \leq \widetilde{\Delta}_{\mathrm{dB}} \leq c_2 \\ 0, & \widetilde{\Delta}_{\mathrm{dB}} > c_2 \end{cases}, \tag{18}$$

where c_1 and c_2 are constants in dB. It now follows directly from (18) that the PDF of $\widetilde{\Delta}$ yields

$$f_{\widetilde{\Delta}}\left(\widetilde{\Delta}\right) = \begin{cases} 0, & \widetilde{\Delta} < 10^{c_1/10} \\ \left|\frac{10}{\widetilde{\Delta} \ln 10}\right| \cdot \frac{1}{(c_2 - c_1)}, & 10^{c_1/10} \leq \widetilde{\Delta} \leq 10^{c_2/10} \\ 0, & \widetilde{\Delta} > 10^{c_2/10} \end{cases}. \tag{19}$$

Thus, from the combination of (16)–(19), it follows that the PDF of b_n^k can be expressed as

$$f_{b_n^k}\left(b_n^k\right) = \begin{cases} 0, & b_n^k < \gamma_2 \\ \frac{A\, 2^{b_n^k}\, 10\, \ln 10}{(c_2 - c_1)\left(2^{b_n^k} - 1\right)\left[A - \sigma_{k,n}^2\left(2^{b_n^k} - 1\right)\right]}, & \gamma_2 \leq b_n^k \leq \gamma_1 \\ 0, & b_n^k > \gamma_1 \end{cases}, \tag{20}$$

where

$$\gamma_1 \;=\; \log_2\left[1 + \frac{A}{\sigma_{k,n}^2 + 10^{c_1/10}B}\right] \tag{21}$$

$$\gamma_2 \;=\; \log_2\left[1 + \frac{A}{\sigma_{k,n}^2 + 10^{c_2/10}B}\right] . \tag{22}$$

Finally, by replacing A and B in expression (20) according to (13), the PDF of b_n^k is obtained in the form

$$f_{b_n^k}\left(b_n^k\right) = \begin{cases} 0, & b_n^k < \gamma_2 \\ \dfrac{s_n^k\left|h_{n,n}^k\right|^2 2^{b_n^k}\,10\,\ln 10}{(c_2-c_1)\left(2^{b_n^k}-1\right)\left[s_n^k\left|h_{n,n}^k\right|^2 - \Gamma\,\sigma_{k,n}^2\left(2^{b_n^k}-1\right)\right]}, & \gamma_2 \le b_n^k \le \gamma_1 , \\ 0, & b_n^k > \gamma_1 \end{cases} \tag{23}$$

where

$$\gamma_1 \;=\; \log_2\left[1 + \frac{s_n^k\left|h_{n,n}^k\right|^2}{\Gamma\left(\sigma_{k,n}^2 + 10^{c_1/10}\sum_{m\neq n} s_m^k\left|h_{n,m}^k\right|^2\right)}\right] \tag{24}$$

$$\gamma_2 \;=\; \log_2\left[1 + \frac{s_n^k\left|h_{n,n}^k\right|^2}{\Gamma\left(\sigma_{k,n}^2 + 10^{c_2/10}\sum_{m\neq n} s_m^k\left|h_{n,m}^k\right|^2\right)}\right] . \tag{25}$$

The PDF $f_{b_n^k}(b_n^k)$ in (23) represents the variation of the number of bits for tone k and line n due to the presence of the crosstalk estimation error $\widetilde{\Delta}$ through the constants c_1 and c_2. The interval for the number of bits assigned per tone, *i.e.*, the interval of existence of the PDF, is limited by γ_1 and γ_2 defined in (24) and (25), respectively. It can be noted from (23) that the shape of the PDF does not depend on the FEXT crosstalk channel values, *i.e.* $\left|h_{n,m}^k\right|^2$ for $m \neq n$, which are present only in the definition of γ_1 and γ_2.

5.2   Deriving the PDF of R_n

In the previous subsection the PDF $f_{b_n^k}(b_n^k)$ was derived in order to gain insight of the variation in the number of allocated bits (per tone) due to the presence of $\widetilde{\Delta}$. In the following, the variation in the data rate R_n achieved by a line n as a function of the crosstalk estimation error $\widetilde{\Delta}$ is analyzed through the derivation of the PDF of the data rate R_n, denoted by $f_{R_n}(R_n)$.

The achievable data rate for an user n, as introduced in (3), can be reformulated according to (12) as

$$
\begin{aligned}
R_n &= f_{\text{sym}} \sum_{k=1}^{K} b_n^k \\[2mm]
&= f_{\text{sym}} \sum_{k=1}^{K} \log_2 \left[1 + \frac{s_n^k \left|h_{n,n}^k\right|^2}{\Gamma \left(\sigma_{k,n}^2 + \sum_{m \neq n} s_m^k \widetilde{\Delta} \left|h_{n,m}^k\right|^2 \right)} \right].
\end{aligned}
\tag{26}
$$

Hence the PDF of the data rate $f_{R_n}(R_n)$ is obtained as

$$
f_{R_n}(R_n) = f_{sym}[f_{b_n^k}(b_n^1) \otimes f_{b_n^k}(b_n^2) \otimes \ldots \otimes f_{b_n^k}(b_n^K)],
\tag{27}
$$

where $\otimes$ denotes the convolution operator. Instead of performing the cumbersome repeated convolutions, we resort to the Central Limit Theorem (CLT) [27], given that R_n is a sum of random variables. It should be noted that b_n^k for $k = 1, \ldots, K$ are in general not $i.i.d.$ variables since the PDF $f_{b_n^k}(b_n^k)$ is determined by the frequency-dependent properties of the cable binder, the background noise, etc., as seen in (23). However, it is well know that the CLT often (approximately) applies for non $i.i.d.$ cases as the number of random variables goes to infinity. The results in Section 5.3 confirm that the PDF $f_{R_n}(R_n)$ is approximately Gaussian for our test case, $i.e.$, for the cable binder and system considered. Thus, the PDF of the data rate can be approximated by the Gaussian PDF

$$
f_{R_n}(R_n) = f_{\text{sym}} \frac{1}{\sqrt{2\pi\, \sigma_{R_n}^2}} e^{\frac{-(R_n - E\{R_n\})^2}{2\, \sigma_{R_n}^2}},
\tag{28}
$$

where the mean $E\{R_n\}$ and the variance $\sigma_{R_n}^2$ are obtained as

$$
E\{R_n\} = f_{\text{sym}} \sum_{k=1}^{K} E\{b_n^k\}, \quad \sigma_{R_n}^2 = f_{\text{sym}}^2 \sum_{k=1}^{K} \sigma_{b_n^k}^2.
\tag{29}
$$

5.3   Numerical Results

The FEXT coupling functions measured on $N = 20$ twisted-pairs of an ordinary 500 m long (26 AWG) telephone cable are considered for our study case. Since the knowledge of the FEXT distribution behavior is helpful in understanding the forthcoming results, the histogram of the measured attenuation values $\left|h_{n,m}^k\right|^2$ for tone $k = 33, 34, \ldots, K$, and line $n = 1, 2, \ldots, N$, is shown

in Fig. 3, assuming the ADSL2+ downstream frequency bandplan [26] where $K = 512$. From Fig. 3 we note that the majority of the values $\left|h_{n,m}^k\right|^2$ are within the interval from -50 dB to -80 dB. This reflects a typical behavior of the crosstalk channels for such cable type and length. Thus, given a transmit PSD of -40 dBm/Hz [26], the received FEXT levels are mainly within -90 dBm/Hz to -120 dBm/Hz.
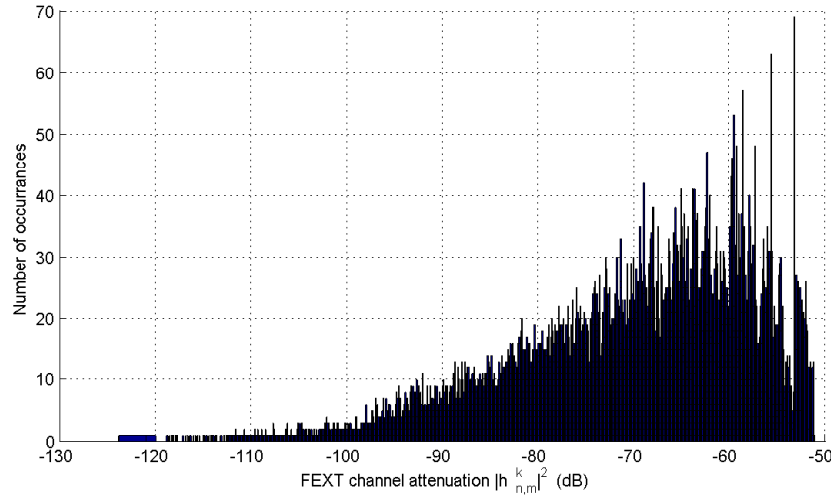

Figure 3: Histogram of the measured FEXT channel attenuation $\left|h_{n,m}^k\right|^2$ for an ordinary 500 m long 26 AWG cable of 20 twisted-pairs and assuming downstream ADSL2+ frequency bandplan.

In the following we consider a specific transmission line $n = 1$ among the $N = 20$ twisted-pairs of the 500 m cable (26 AWG), a SNR-gap Γ of 12.8 dB and a frequency-flat transmit PSD s_n^k set to -40 dBm/Hz for all the ADSL2+ modems. Fig. 4 demonstrates an application of (23) for an arbitrary tone $k = 300$ and line $n = 1$ of our cable binder. Here, for different background noise levels, the corresponding PDF $f_{b_n^k}(b_1^{300})$ given by (23) is compared with the achievable number of bits b_n^k calculated using (2), where the latter are indicated by the vertical lines. Under the described conditions, it can be observed that for low background noise levels, *i.e.*, when the channel is mainly crosstalk-limited, the PDF of $f_{b_n^k}(b_1^{300})$ is approximately uniformly distributed. However, a change in the PDF shape occurs if the background noise level is greater than (roughly) -100 dBm/Hz, since the channel then also becomes background noise-limited, resulting in that the PDF $f_{b_n^k}(b_1^{300})$
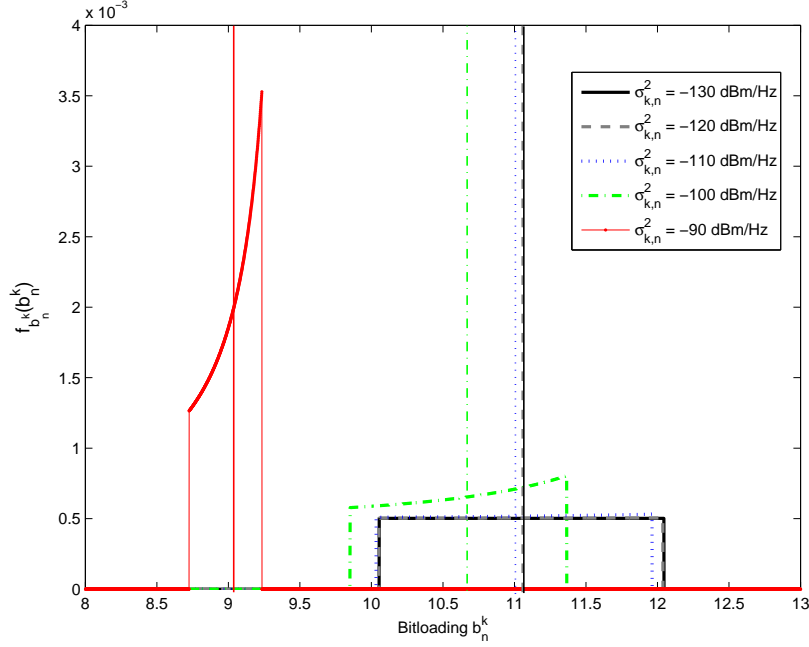
Figure 4: The PDF $f_{b_n^k}\left(b_n^k\right)$ for a tone $k = 300$ and for different background noise $\sigma_{k,n}^2$ levels. The bitloading calculated with (2), corresponding to $\tilde{\Delta} = 1$, are represented by the vertical lines.

tends to be non-uniformly distributed.

The PDF $f_{R_n}(R_n)$ in (28) for transmission line $n = 1$ is shown in Fig. 5 with red dashed lines for different background noise $\sigma_{k,n}^2$ levels. The corresponding Monte Carlo simulations, for each background noise level, is also shown according to the legend. In addition, the data rate calculated with (3), which corresponds to $\tilde{\Delta} = 1$ ($\tilde{\Delta}_{\mathrm{dB}} = 0$), is depicted in Fig. 5 by the vertical lines.

If a comparison is made between the PDFs calculated with (28) and the corresponding Monte Carlo simulations, it is clear from Fig. 5 that the CLT applies and that the PDF can be considered Gaussian, for our study case. Furthermore, according to Fig. 5, the maximum spread in the data rate caused by $\tilde{\Delta}$ is approximately 400 kbps, for the considered background noise levels. This corresponds to an uncertainty of less than 2 % of the mean data rate for the considered line. Moreover, the PDF $f_{R_n}(R_n)$ becomes slightly biased as the $\sigma_{k,n}^2$ level increases, in the sense that the mean value $E\{R_n\}$
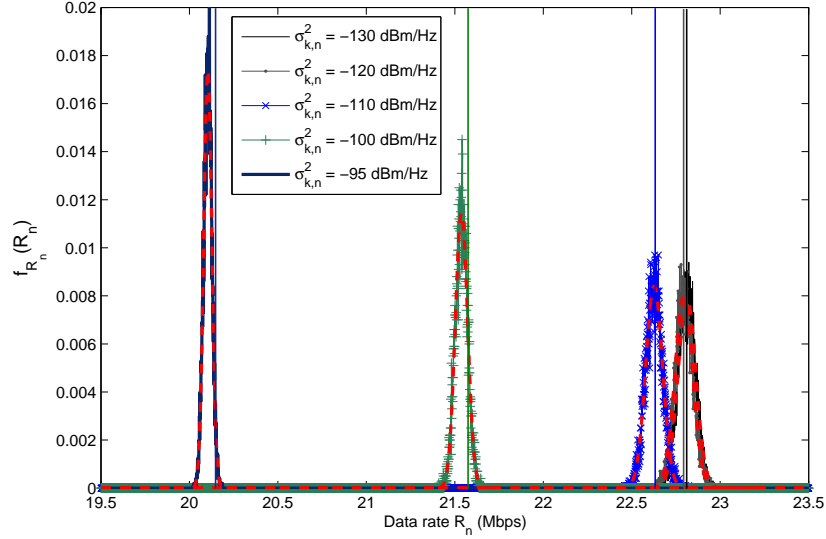
Figure 5: The PDF $f_{R_n}(R_n)$ for a transmission line $n = 1$, and for different background noise levels, are depicted by the dashed red lines. The curves following the legend are the corresponding Monte Carlo simulations. The data rates calculated with (3) are represented by the vertical lines.

does not correspond (exactly) to the case where $\tilde{\Delta} = 1$. This corresponds to a scenario which is not only limited by the crosstalk, whereas the assumed uniform error model of the *Crosstalk Estimator* is no longer valid as described in Section 4.1.

6   Laboratory Setup for DSM Simulations

This section describes the laboratory setup utilized to obtain the two network scenarios and their respective channel measurements and estimates, which are used during the DSM simulations. The used access network *Scenario I* and *Scenario II* are depicted in Fig. 6 and Fig. 7, respectively. Both networks comprise transmitter units (TU) located at the central office (CO) and at the cabinet (CAB) side. The receiver units (RU) are located at the customer premises (CP) side. All considered DSL transceiver units correspond to ADSL2+ modems [26]. The access binder in Fig. 6 and Fig. 7 are built-up with real twisted-pair cables consisting of 0.40 mm (26 AWG) copper
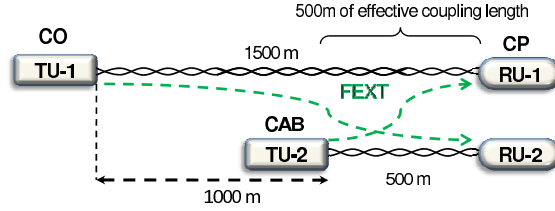
Figure 6: Access network *Scenario I.*
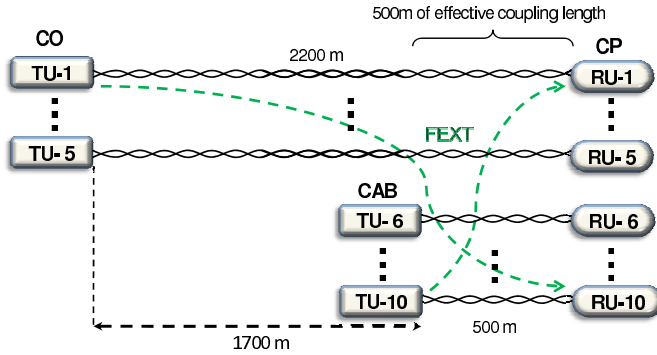
Figure 7: Access network *Scenario II.*

lines of lengths 500 m, 1500 m and 2200 m.

For the purpose of establishing a reference, a network analyzer (NA) is used to measure the "ideal" square-magnitude of the FEXT channels. This measurement is performed by connecting the NA equipment directly to the cable ends, *i.e.*, no DSL modems are involved in the measurement setup. The NA also provides the square-magnitude of the direct channels used in the forthcoming DSM performance simulations. The ADSL2+ downstream band from frequency 142.31 kHz to 2.208 MHz is considered and a tone spacing of $\Delta_f = 4.3125$ kHz is employed in order to comply with the DMT tone spacing used for ADSL2+ [26]. Fig. 8 shows the square-magnitude of the FEXT channels for *Scenario I* obtained with the NA, the *Crosstalk Estimator* [24], and with the so-called 99 % worst-case FEXT model [22]. The FEXT model is only used for comparison and is calculated based on the true line-length and the measured insertion loss. Similar measurements and estimation results are also obtained for *Scenario II.*

In Fig. 8, the estimates acquired with the *Crosstalk Estimator* are pre-

sented in the forms of raw data and processed data. The raw data are the primary estimation results and include a small number of missing data points. The missing data occur mainly at the lower frequencies due to the presence of high-pass filters in the transceivers, which in turn attenuates the received signal to the level of the background noise, preventing those channel-values to be estimated (see [24] for details). Interpolation and extrapolation are therefore applied in order to recover the missing data and overcome this problem, as shown by the curves representing the processed data in Fig. 8. In addition, a moving average (MA) filter is employed to smooth the curves prior to executing the DSM algorithms. Furthermore, it should be noted that the (reference) NA measurements and the FEXT model do not describe the complete FEXT channels seen by the *Crosstalk Estimator*, since the two former quantities do not include the effects of the transceiver filters and the analog front-ends of the DSL modems. Due to this, the obtained NA measurements and the FEXT-model values are compensated with the transceiver characteristics, as described in [24], providing a more fair comparison. The effects of the transceiver-filter compensation is especially noticeable at the
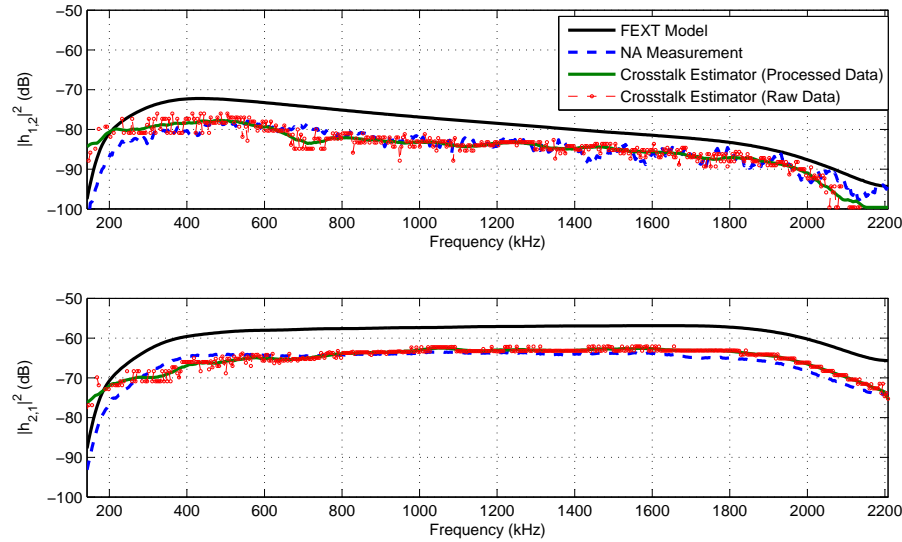
Figure 8: Square-magnitude of the FEXT channels for *Scenario I* representing: the worst-case FEXT model; the NA measurements; and the *Crosstalk Estimator* estimates in the form of raw data and smoothed curves with the application of a MA filter.

frequency-band edges in Fig. 8, *i.e.,* high-pass and low-pass filtering.

The deviations of the FEXT channel estimates in Fig. 8 indicate, as expected, that the FEXT model over-estimates the FEXT influence. The *Crosstalk Estimator*, however, is able to follow the shape of the NA measurements quite well. This ability of the estimator is of particular interest for the DSM approach. More specifically, the *Crosstalk Estimator* provides an estimate of the FEXT channels for *Scenario I* and *II* with a mean deviation less than 3 dB relative to the the NA measurements for most frequencies. Thus, the accuracy of the estimation results are in line with [24].

7 Impact of Crosstalk Channel Estimation on DSM Performance

In this section we present a simulation-based investigation of the impact of non-ideal FEXT channel estimation on the DSM performance. The *Crosstalk Estimator* described in Section 4 is applied for the two access network scenarios shown in Fig. 6 and Fig. 7. Based on the obtained estimates of the FEXT channels, we evaluate the performance of the two DSM algorithms *Iterative Spectrum Balancing (ISB)* [10] and *Successive Convex Approximation for Low-complExity (SCALE)* [12].

The DSM simulations utilize the measured direct channel-gains and the PSD of the background noise, obtained with a network analyzer (NA) and with the Loop Diagnostic procedure [24], [26], respectively. The simulations further assumes: SNR-gap of 9.8 dB, noise margin of 6 dB, coding gain of 3 dB, BER of 10^{-7}, transmit power for each modem of 19.4 dBm, and a maximum of 15 bits per tone.

7.1 Results for *Scenario I*

The DSM algorithms are first executed using the FEXT channels provided by the (transceiver-compensated) NA measurements described in previous section. The so-obtained DSM results are considered as the (true) reference values. Thereafter is the DSM algorithms executed based on the FEXT channels from the *Crosstalk Estimator* and from the (transceiver-compensated) FEXT model. Fig. 9 and Fig. 10 show the obtained rate regions for the 2-users *Scenario I* (Fig. 6) using the DSM algorithms ISB and SCALE. It should be understood that the rate region consists of a set of points representing possible transmission-rate combinations between the two users, where the points belonging to the outermost border-line indicates the maximum achievable data rate calculated according to (3).
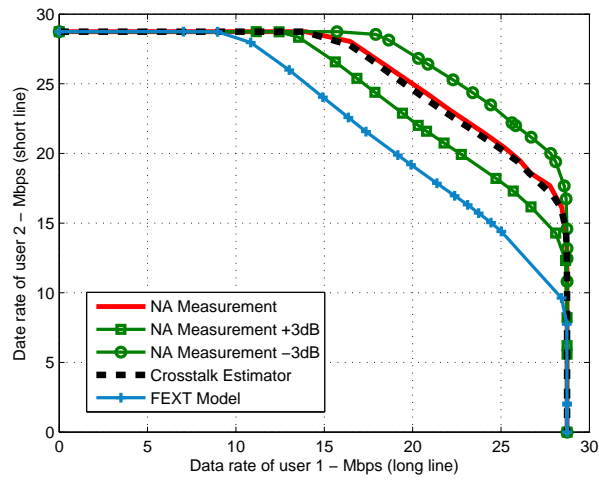
Figure 9: Simulation results obtained with the ISB algorithm.
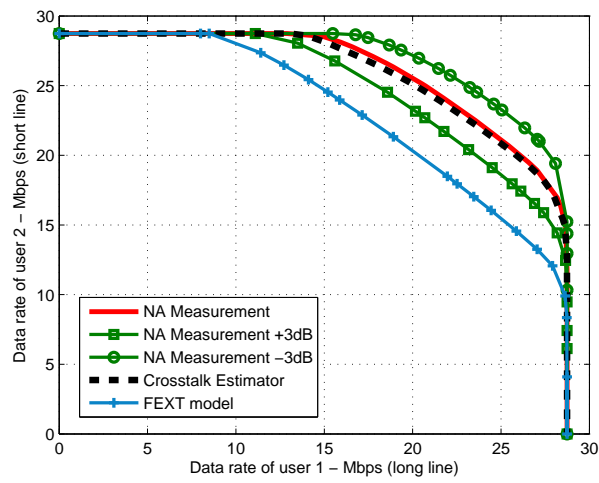

Figure 10: Simulation results obtained with the SCALE algorithm.

The results plotted in Fig. 9 and Fig. 10 show that for both the ISB and the SCALE algorithms, the FEXT channel estimates are accurate enough to provide values close to the reference (NA measurements) values. That is, the deviation in data rates obtained with the *Crosstalk Estimator* and the NA measurement are less than 500 kbps. It is worth to notice that this deviation is in the same order as the spread in that rate found in Section 5.3, even though the scenarios are not the same. The rate region obtained with the FEXT model demonstrates, as expected, that the user data rates are significantly underestimated with the model.

To further investigate the confidence region of data rates achieved with the *Crosstalk Estimator*, the DSM algorithms are once more simulated based on the NA measurements, but now with an assumed error-offset of $+3$ dB and -3 dB for each tone, representing the extreme values of the estimation error. From Fig. 9 and Fig. 10 it can be noted that the so-obtained confidence region spans roughly data rates from -3 Mbps to $+3$ Mbps relative the reference data rates. It is interesting to note that even though the borders of the confidence regions should correspond to the unlikely worst-case for the *Crosstalk Estimator*, the achieved data rates are still closer to the reference values than the rates obtained with the FEXT model.

7.2   Results for *Scenario II*

The 10-users *Scenario II* depicted in Fig. 7 is evaluated by using the DSM algorithm SCALE. In order to evaluated the DSM performance for a 10-users case and still holding the achievable data rate per user as a metric, Fig. 11 and Fig. 12 represent two sections of the 10-dimensional rate region curve that isolates the relation between 2 arbitrary users, reducing then the graph to a 2-dimensional case. In Fig. 11, the rate region for the NA channel measurement case and the corresponding confidence region are plotted for 2 users (out of 10 users) with non-equal length lines. Similarly, Fig. 12 also shows the NA FEXT channel measurement case and the confidence region for 2 users, but for equal length lines (2200 m). Unlike the results shown in Subsection 7.1, both cases show that some of the NA measurements border points are close to the confidence rate region limits. These fact arises from the non-linear data rate relation between the users, that is dependent of *e.g.* different users priorities, channel states, etc. However, the data rates based on the NA measurements do not cross the confidence region limits.

Assuming now the total data throughput of *Scenario II* as a metric to evaluate the SCALE performance for this 10-users case, Fig. 13 shows the total data rate for different profiles. In this work, the term profile stands for a predefined set of different user priorities given to the DSM algorithms.
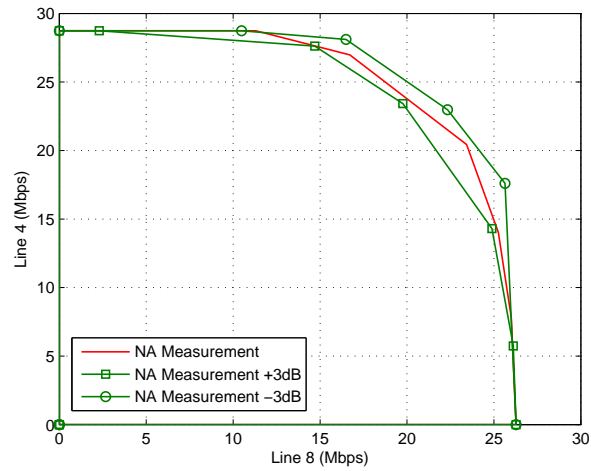
Figure 11: Section of the 10-dimensional rate region curve, obtained with SCALE, for 2 users (out of 10 users) with non-equal length lines.
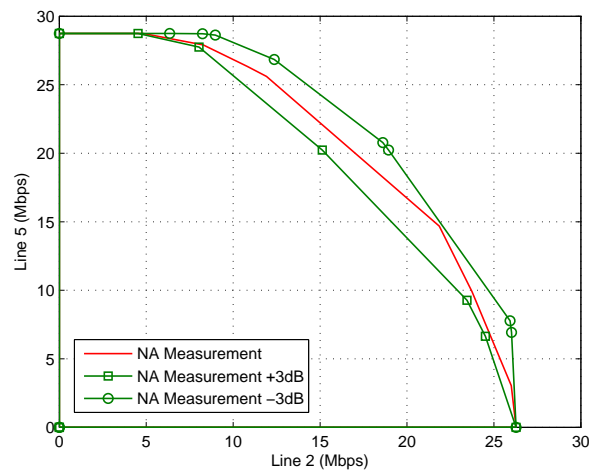

Figure 12: Section of the 10-dimensional rate region curve, obtained with SCALE, for 2 users (out of 10 users) with equal length lines (2200m).

In other words, varying the users priorities, *i.e*, defining different profiles, we provide a diversity of data rate combinations between the users. For a 2-users case, which comprises a two dimensional rate region, this diversity corresponds to almost equally distributed (scattered points) along the rate region curves (border). The 10-users simulation using the ISB, comprising the same number of profiles (approximately 100 profiles), was skipped due to complexity issues, since it would required several days to be performed. However, it is believed that both ISB and SCALE presents similar performances, as indicated by the results for *Scenario I*.

In Fig. 13, the total data rate values obtained by the SCALE, based on the NA measurements and the confidence rate region limits, are sorted separately in an ascending order, *i.e.*, the best/worst values of a curve are compared with the relative best/worst values of the other curves. The results in Fig. 13 indicate that a variation of ± 3 dB in the FEXT crosstalk channel estimates can result in a spread of the total data throughput of ± 10 Mbps, for the specific 10-users scenario considered. On the other hand, this represents the extreme cases where all the crosstalk channel estimates for the 10 users, and for all the tones, assume an error $\widetilde{\Delta}_{\mathrm{dB}} = \pm 3$ dB. Thus, we can interpret these extreme cases as limits for a total data throughput confidence region.
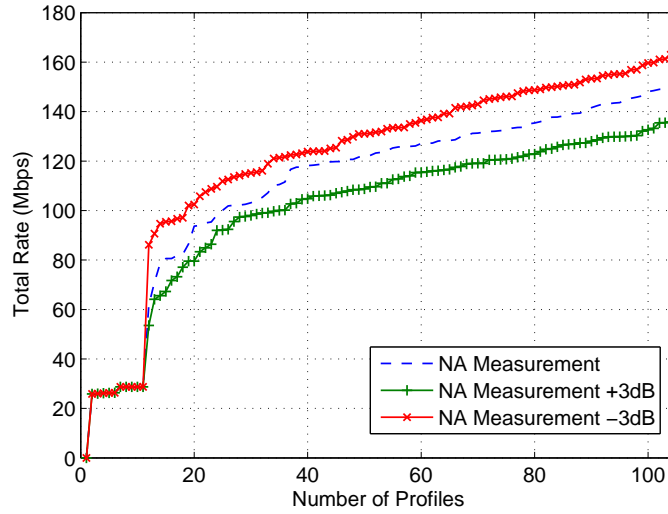

Figure 13: Total data throughput for the 10-users *Scenario II* using the SCALE algorithm, comprising approximately 100 profiles.

8   Summary and Conclusions

The paper provides a statistical sensitivity analysis of the achievable bit-loading assuming an uniformly distributed FEXT channel estimation error. The analysis comprises the derivation of the bitloading PDF and the data rate PDF resulting from the non-perfect FEXT channel estimation. The so-obtained data rate PDF is approximated by the Gaussian distribution with the use of the Central Limit Theorem. The validation of this approximation is numerically verified by comparing the derived PDF with the corresponding Monte Carlo simulations for measured FEXT channels of an ordinary twisted-pair cable. For the study case, a maximum spread of approximately 400 kbps in the data rate could be observed due to the FEXT channel estimation error. This corresponds to an uncertainty of less than 2 % of the mean data rate for the considered line. Moreover, it could be noted that the data rate PDF becomes slightly biased when the background noise level is in the same range as the FEXT, in the sense that the mean data rate differs from the estimation error-free case. This is equivalent to a scenario that is also limited by the background noise, rather than just FEXT, whereas the assumed estimation error model is no longer valid.

The impact of the crosstalk channels estimation on the DSM performance was evaluated by means of computer simulations of the DSM algorithms ISB and SCALE. For the latter, measured channel information from different network scenarios, consisting of real twisted-pair cables, was used. From the achieved rate region curves, the following conclusions can be made. Using the worst-case FEXT model, the DSM performance is under-estimated compared to the one obtained with the *Crosstalk Estimator* [24], as expected. The ISB and SCALE algorithms achieved practically the same performance with both the *Crosstalk Estimator* and the reference measurements. The results for the considered 10 users scenario applying the SCALE algorithm and assuming the total data throughput as a metric, indicate that the non-perfect FEXT channel estimates lead to a spread in the total data throughput of ± 10 Mbps, for the specific scenario considered. However, this should be considered as the extreme case, where all the crosstalk channel estimates for the 10 users, and for all the tones, assume an error-offset of ± 3 dB.

References

[1] T. Starr, J.M. Cioffi, and P.J. Silverman, *Understanding Digital Subscriber Line Technology*, Prentice-Hal, Upper Saddle Riverl, 1999.

[2] P. Golden, H. Dedieu, and K. Jacobsen, *Fundamentals of DSL technology*, Auerbach Publications, Taylor & Francis Group, 2006.

[3] Dynamic Spectrum Management Technical Report, "ATIS committee NIPP pre-published document ATIS-PP-0600007," May 2007.

[4] K.B. Song, S.T. Chung, G. Ginis, and J.M. Cioffi, "Dynamic spectrum management for next-generation DSL systems," *IEEE Communications Magazine*, vol. 40, no. 10, pp. 101–109, 2002.

[5] T. Starr, M. Sorbara, J.M. Cioffi, and P.J. Silverman, *DSL Advances*, Prentice-Hall, 2003.

[6] R. Cendrillon, *Multi-user Signal and Spectra Co-Ordination for Digital Subscriber Lines*, Ph.D. thesis, Katholieke Universiteit Leuven, Dec. 2004.

[7] J. Verlinden, T. Bostoen, and G. Ysebaert, "Dynamic spectrum management for digital subscriber lines - edition 2," *Technology White Paper - Alcatel*, 2005.

[8] P. Golden, H. Dedieu, and K. Jacobsen, *Implementation and Applications of DSL Technology*, Auerbach Publications, Taylor & Francis Group, 2007.

[9] W. Yu, G. Ginis, and J.M. Cioffi, "Distributed power control for digital subscriber lines," *IEEE J. Select. Areas Commun.*, vol. 20, no. 5, pp. 1105–15, June 2002.

[10] R. Cendrillon and M. Moonen, "Iterative spectrum balancing for digital subscriber lines," *IEEE International Communications Conference (ICC)*, May 2005.

[11] R. Cendrillon, W. Yu, M. Moonen, J. Verlinden, and T. Bostoen, "Optimal multiuser spectrum balancing for digital subscriber lines," *IEEE Trans. Commun.*, vol. 54, no. 5, pp. 922–933, May 2006.

[12] J. Papandriopoulos and J.S. Evans, "Low-complexity distributed algorithms for spectrum balancing in multi-user DSL networks," *IEEE International Conference on Communications (ICC)*, Jun. 2006.

[13] D. Statovci, T. Nordström, and R. Nilsson, "Dynamic spectrum management for standardized VDSL," *IEEE International Conference on Acoustics, Speech, and Signal Processing (ICASSP), Honolulu, Hawaii, USA*, 2007.

[14] R. Cendrillon, J. Huang, M. Chiang, and M. Moonen, "Autonomous spectrum balancing for digital subscriber lines," *IEEE Transactions on Signal Processing*, vol. 55, no. 8, pp. 4241–4257, Aug. 2007.

[15] G. Ginis and J.M. Cioffi, "Vectored transmission for digital subscriber line systems," *IEEE Journal on Selected Areas in Communications*, vol. 20, no. 5, pp. 1085–1104, June 2002.

[16] R. Cendrillon, G. Ginis, E. van den Bogaert, and M. Moonen, "A near-optimal linear crosstalk canceler for upstream VDSL," *IEEE Transactions on Signal Processing*, vol. 54, no. 8, pp. 3136–3146, 2006.

[17] R. Cendrillon, G. Ginis, E. van den Bogaert, and M. Moonen, "A near-optimal linear crosstalk precoder for downstream VDSL," *IEEE Transactions on Communications*, vol. 55, no. 5, pp. 860–863, 2007.

[18] J.W. Cook, R.H. Kirkby, M.G. Booth, K.T. Foster, D.E.A. Clarke, and G. Young, "The noise and crosstalk environment for ADSL and VDSL systems," *IEEE Communications Magazine*, vol. 37, no. 5, pp. 73–78, May 1999.

[19] S. Galli, C. Valenti, and K. Kerpez, "A frequency-domain approach to crosstalk identification in xDSL Systems," *IEEE J. Sel. Areas Commun.*, vol. 19, no. 8, pp. 1497–1506, Aug. 2001.

[20] C. Zeng, C. Aldana, A.A. Salvekar, and J.M. Cioffi, "Crosstalk identification in xDSL systems," *IEEE J. Sel. Areas Commun.*, vol. 19, pp. 1488–1496, 2001.

[21] Y. Shi, F. Ding, and T. Chen, "Multirate Crosstalk Identification in xDSL Systems," *IEEE Trans. Commun.*, vol. 54, no. 10, pp. 1878–1886, 2006.

[22] American National Standard for Telecommunications, "Spectrum Management for Loop Transmission Systems, T1.417-2003, (issue 2)," 2003.

[23] ETSI, "Std. TS 101 270-1 v1.3.1. Transmission and multiplexing, access transmission systems on metallic access cables, very high speed digital subscriber lines (VDSL), part 1: Functional requirements," 2003-07.

[24] F. Lindqvist, N. Lindqvist, B. Dortschy, P. Ödling, P.O. Börjesson, K. Ericsson, and E. Pelaes, "Crosstalk channel estimation via standardized two-port measurements," *EURASIP Journal on Advances in Signal Processing*, vol. 2008, Article ID 916865, 14 pages, 2008.

[25] M. Monteiro, N. Lindqvist, and A. Klautau, "Spectrum balancing algorithms for power minimization in DSL networks," *IEEE International Conference on Communications ICC '09. Dresden, Germany*, 2009.

[26] ITU-T Standard G.992.5, "Asymmetric Digital Subscriber Line (ADSL) transceivers - Extended bandwidth ADSL2 (ADSL2plus)," 01/2005.

[27] A. Papoulis, *Probability Random Variables and Stochastic Process - Third Edition*, McGraw-Hill, 1991.

Paper VIII

Paper VIII

Frequency Domain
Echo Canceller

Abstract

An echo canceller reduces an echo signal produced when the transmitted signal leaks back into the receiver via a hybrid. The echo canceller estimates the echo signal from the transmitted signal, and then subtracting the estimated echo signal from the received signal. In practice, the echo path channel for a DMT-modem is much longer than the cyclic prefix, and therefore, the received echo signal will be subjected to both ISI (inter-symbol-interference) and ICI (inter-carrier-interference). A traditional echo canceller, designed for a xDSL-modem, uses either a time domain adaptive FIR-filter or a combined echo canceller implemented in both time and frequency domain. A matrix-based adaptive echo canceller is implemented in the frequency domain. Various example embodiments are disclosed.

1

FREQUENCY DOMAIN ECHO CANCELLER

FIELD OF THE INVENTION

The invention relates to digital communication systems. One application of the invention is systems that use multicarrier modulation methods, such as DMT (Discrete

5   Multitone) where DSL (Digital Subscriber Lines) twisted pair subscriber lines are employed for high speed data transmission. Another application of the invention is OFDM (Orthogonal Frequency Division Multiplexing) based systems.

BACKGROUND AND SUMMARY OF THE INVENTION

Referring to Fig. 1, a DSL modem consists of a transmitter 12 and a

10   receiver 14 connected to the subscriber line's twisted-pair 18 (telephone line) via a so-called hybrid circuit 16. The hybrid 16 is a two-to-four wire interface that connects the twisted-pair subscriber line 18 to the four-wire modem (two-wire transmitter and two-wire receiver). An ideal hybrid is exactly matched to the impedance of the subscriber line and transports the transmitter signal only to the subscriber line and the received signal only to

15   the receiver.

A problem with matched hybrids (non-adaptive) is that different subscriber lines have different impedances, and temperature variations make the impedances slowly time-varying. Consequently, the hybrid cannot be exactly matched to the impedance of the subscriber line, and the transmitted signal "leaks" back into the receiver through the

20   hybrid creating an echo signal as shown in Fig. 1. From the receiver's point of view, the echo signal acts like a powerful noise source reducing the signal-to-noise ratio (SNR) and therefore reduces the performance of the receiver. An echo canceller may be used to reduce the influence of the echo in the received signal.

The main purpose of the echo canceller is to reduce the echo signal

25   produced when the transmitted signal "leaks" back into the receiver via the hybrid. The echo canceller works by first estimating the echo signal from the transmitted signal, and

2

then subtracting the estimated echo signal from the received signal. In order to estimate the echo signal, the echo canceller must model the echo path channel. Generally speaking, the echo canceller performs a "system estimation," where the system to be estimated is the echo path channel. Due to the slowly time-varying nature of the echo path channel, the
5   echo canceller must continuously, but infrequently, update the echo path channel estimation. This update is typically accomplished with an adaptive finite impulse response (FIR) filter to continuously track the slowly time-varying echo path channel.

        The echo canceller operates in two different modes: the training mode and the echo cancellation mode. In the training mode, the far-end transmitter is forced to be
10   silent while the near-end modem transmits a training sequence in order to estimate the echo path channel. The estimation of the echo path channel may be accomplished using a fast training algorithm followed by an adaptive algorithm such as the LMS-algorithm. After the echo canceller finishes the training mode, it jumps into the echo cancellation mode where the echo canceller performs echo cancellation, i.e. it subtracts the echo signal
15   from the received signal.

        Discrete Multi-tone (DMT) modulation is one form of multicarrier modulation that is attractive because of its ability to utilize, and be implemented by, efficient digital signal processing techniques. The basic idea of DMT modulation is to partition the communication channel into orthogonal and memoryless subchannels using
20   the digital signal processing technique known as the Fast Fourier Transform and the Inverse Fast Fourier Transform (FFT/IFFT). Data transmitted through one subchannel is independent of other subchannels under some orthogonal conditions that will be described later. DMT also allows for efficient and flexible allocation of power and bits to each subchannel.

25   The DMT modulated signal can be described as a composition of $N/2$ independent carriers, where each carrier has equal bandwidth and a center frequency f_i, where $i = 1... N/2$. For example, ADSL uses 255 carriers (subchannels) downstream and 31 carriers upstream. Each one of the carriers is a Quadrature Amplitude Modulated (QAM) signal with an assigned amplitude and phase. The assigned values for the

3

amplitude and the phase are determined by a signal constellation containing a set of complex values. During start-up, the DMT-system measures the signal-to-noise ratio in each subchannel and assigns different numbers of bits to each subchannel (carrier) to maximize performance. This process is known as adaptive bitloading. A subchannel with

5   low signal-to-noise (SNR) is assigned a small number of bits or no bits, and a subchannel with high SNR is assigned many bits. This technique is robust in a typical Digital Subscriber Line scenario where the line conditions are unknown and slowly time-varying.

A DMT signal that is filtered through a physical channel will be subjected to inter-symbol-interference (ISI) because all practical physical channels have a memory.

10   (The impulse response of the channel is non-zero for more than one point in time). This impairment of the physical channel causes the transmitted DMT symbols to interfere with each other (ISI). Furthermore, the transitions between the DMT symbol cause transients in the received signal. These transients cause interference between the carriers in the same DMT symbol. This type of interference is known as inter-channel interference (ICI),

15   where the "channel" refers to the subchannel. The ISI and ICI imply that the received subchannels do not remain orthogonal (independent) to each other, and therefore, the received data will be corrupted.

The received echo signal, like the received data signal, will also be affected by the ISI and ICI, because all practical physical echo path channels have memory. Thus,

20   the echo from one carrier will leak into every other carrier within the same DMT symbol and the next transmitted DMT symbol.

One way to circumvent, or at least reduce, the ISI and ICI in a DMT-based system is to add a cyclic prefix (guard time) to the beginning of each transmitted DMT symbol. The cyclic prefix (CP) is a mechanism to make the subchannels independent of

25   each other, or in other words, memory-less. A cyclic prefix of L samples means that the last L samples of the N samples long time domain symbol is copied to the beginning of the time domain symbol. Thus, the total length of the prefixed time domain symbol is $L + N$ samples. Figure 3 illustrates the cyclic prefixing.

4

If the length of the cyclic prefix is greater than the length of the channel memory, then all ISI and all transients causing ICI will be contained within the cyclic prefix. The receiver can then remove all ISI and ICI by simply discarding the cyclic prefix. This means that the channel will only affect the amplitude and the phase of each

5   transmitted carrier, and different subchannels will remain independent (no ISI or ICI). Unfortunately, increasing the length of the cyclic prefix reduces the data rate. For example, suppose that one time domain symbol is N samples long, and the length of the cyclic prefix is L samples. The data rate is reduced by a factor of $N/(N+L)$.

In a practical DMT-system the echo path channel is much longer than the

10   cyclic prefix, and therefore, the received echo signal is subjected to both ISI and ICI. Hence, the part of the echo signal that corresponds to both ISI and ICI must be estimated and subtracted as well. The present invention provides an echo canceller that takes into account intersymbol interference and interchannel interference when estimating an echo signal to be removed from a received signal. The echo canceller calculates the received

15   echo signal completely in the frequency domain, which is particularly beneficial in a DMT type system because the transmitted data is already available in the frequency domain. Accordingly, the echo estimate is determined using a frequency domain model of an echo path channel that includes the effects of interference like ISI and ICI.

In a first example embodiment, the frequency domain model of the echo

20   path channel is determined using a first matrix of coefficients and a second matrix of coefficients. The first matrix is combined with a current transmitted symbol, and the second matrix is combined with a previously transmitted symbol. The sum of these two combinations is used to estimate the echo signal. The coefficients of the first matrix represent how an echo from a currently transmitted frequency domain signal affects a

25   received signal. The coefficients of the second matrix represent how an echo from a previously transmitted domain symbol affects the received symbol. The coefficients of the first and second matrices are adjusted using a difference between the received signal and the estimated signal.

5

In a second example embodiment, the current transmitted symbol and the previously transmitted symbol are partitioned into real and imaginary parts before being combined with matrices as described in the first example embodiment. This operation reduces the computational complexity by a factor of two compared to the first example

5   embodiment.

In a third example embodiment, the currently transmitted symbol is combined with a first column vector. The previously transmitted symbol is multiplied with a complex exponential term, in order to compensate for the cyclic prefix, and then subtracted from the current transmitted symbol. The resulting signal is combined with a

10   matrix. The vector and matrix combinations are summed and used to estimate the echo signal to be removed from the received symbol. This third example embodiment reduces the computational complexity approximately by a factor of two compared to the first example embodiment.

In a fourth example embodiment, the operations described in the second

15   and third example embodiments are combined resulting in a reduction of computational complexity approximately by a factor of four compared to the first example embodiment.

In a fifth example embodiment, when the transmitter of a transceiver has a lower sampling rate than its receiver, the received echo signal is interpolated at the receiver. The interpolation may also be combined with the operations described in the

20   second example embodiment to reduce the computational complexity by a factor of four compared to the first example embodiment.

In a sixth example embodiment, when the transmitter has a higher rate than the receiver, the echo signal is decimated at the receiver. The decimation may also be combined with the operations described in the second example embodiment to reduce the

25   computational complexity by a factor of four compared to the first example embodiment.

In a seventh example embodiment, when the transmitted symbols are not aligned in time with the received symbols or frames, an asynchronous echo canceller may

6

be used. The asynchronous echo canceller may be combined with any of the previously-described example embodiments.

In a DMT type modem, because all of the data is already available in the frequency domain, there is no need to do any additional Fourier transform or inverse

5   Fourier transform operations, except for the asynchronous echo canceller embodiment which requires one extra IDFT. Moreover, some of the coefficients in the matrices may be very small and ignored, further reducing the computational complexity and memory required.

BRIEF DESCRIPTION OF THE DRAWINGS

10   The foregoing and other objects, features, and advantages of the invention will be apparent from the following description of preferred, non-limiting example embodiments, as well as illustrated in the accompanying drawings. The drawings are not necessarily to scale, emphasis instead being placed upon illustrating the principles of the invention.

15   Fig. 1 illustrates a *symmetric-rate DMT transceiver where the hybrid is* unmatched to the subscriber line;

Fig. 2 illustrates cyclic prefixing;

Fig. 3 shows a symmetric-rate DMT transceiver with an echo canceller;

Fig. 4 shows a symmetric-rate DMT transceiver with one example

20   embodiment of a frequency domain echo canceller;

Fig. 5 shows a flowchart of procedures performed by the echo canceller in Fig. 4;

Fig. 6 shows a symmetric-rate DMT transceiver with another example embodiment of a domain echo canceller;

7

Fig. 7 shows a flowchart of procedures performed by the echo canceller of
Fig. 6;

Fig. 8 shows another example embodiment of the invention as applied to
asymmetric data rate transceiving situations;

5   Fig. 9 shows a symmetric-rate DMT transceiver with another example
embodiment of the invention as applied to asynchronous data transceiving situations; and

Figs. 10 and 11 show the learning curve of the echo canceller of Fig. 6
implemented in a DMT-based, symmetric-rate DSL transceiver, using a simple lowpass
model of the echo path channel.

10   DETAILED DESCRIPTION OF THE DRAWINGS

In the following description, for purposes of explanation and not limitation,
specific details are set forth, such as particular embodiments, protocols, data structures,
and techniques, in order to provide a thorough understanding of the present invention.
However, it will be apparent to one skilled in the art that the present invention may be
15   practiced in other embodiments that depart from these specific details. In other instances,
detailed descriptions of well-known methods, systems, and devices are omitted so as not to
obscure the description of the present invention with unnecessary detail. Moreover,
individual function blocks are shown in some of the figures. Those skilled in the art will
appreciate that the functions may be implemented using individual hardware circuits, using
20   software functioning in conjunction with a suitably programmed digital microprocessor or
general purpose computer, using an Application Specific Integrated Circuit (ASIC), and/or
using one or more Digital Signal Processors (DSPs).

A discrete multi-tone modem 20 in which the present invention may be
employed is illustrated in Fig. 3. The DMT modem includes a DMT transmitter 22 and a
25   DMT receiver 26 coupled to the subscriber line via a hybrid 24. Serial input data are
grouped into blocks, converted into parallel form, and encoded by an encoder 28. Each
one of $N/2$ active subchannels contains a number of bits allocated to that subchannel.

8

Each block of bits is mapped into a two-dimensional signal constellation point (i.e., a complex number). The output from the encoder 28 is $N/2$ complex numbers (i.e., subsymbols), one for each block of bits. The $N/2$ complex subsymbols constitute a DMT symbol in the frequency domain and are extended to Hermitian symmetry (i.e., conjugate

5   symmetry) before being input to block 30, which calculates the inverse discrete Fourier transform (IDFT). Due to the Hermitian symmetry property, the N-IDFT output is a sequence consisting of N real samples. The output sequence consists of the superposing of the $N/2$ modulated orthogonal carriers. The parallel N-IDFT output is converted to a serial stream by a parallel-to-serial converter 32. The digital modulated data stream is

10   cyclically prefixed in the Add CP block 34, converted to analog form by digital-to-analog converter 36, filtered at the transmit filter 38, and passed to the hybrid 24 for transmission over the subscriber line.

At the receiver end, the received analog signal from the hybrid 24 is filtered in receive filter 40, converted to digital form in the analog to digital converter 42, and

15   stripped of the cyclic prefix in the Remove CP block 44. The resulting digital signals are converted to parallel format in the serial-to-parallel converter 46. The parallel digital signals are demodulated in the N-DFT block 48. The frequency domain echo canceller 50 estimates the echo caused by the reflected signals from the DMT transmitter 22, and those echo signal estimates are removed from the demodulated signal at block 52. The

20   remaining frequency domain signal is equalized, decoded, and converted back to a serial form by decoder 54.

The remaining description will focus on the frequency domain echo canceller 50. To understand the mathematical foundation for the echo canceller of the present invention, a mathematical expression of the received echo signal in the frequency

25   domain is derived as a function of the transmitted frequency domain signal and the echo path channel. A significant feature of the invention echo canceller is that the received echo signal is cancelled completely in the frequency domain. This is particularly beneficial in a DMT transceiver where the transmitted data is already available in the frequency domain. There is no need to do any extra DFT or IDFT calculations except for the later-

9

described asynchronous echo cancellation embodiment which requires only one extra IDFT.

As explained above, the received echo signal includes ISI and ICI because of the long impulse response of the echo path channel. In order to estimate the received
5   echo signal, a frequency domain model of the echo path channel should include the effects of the ISI and the ICI.

The following notations are introduced:

$$\mathbf{X}_i = [X_i(0), X_1(1), \ldots, X_i(N-1)]^T \qquad (1)$$

$\mathbf{X}_i$ denotes the i:th transmitted frequency domain symbol containing the N transmitted
10   frequency subsymbols $X_i(k)$,where subscript i denotes the DMT symbol number and k denotes the frequency sample number. Note that the vector $\mathbf{X}_i$ is Hermitian symmetric in order to obtain a real-valued sequence after the IDFT.

The Hermitian symmetry of the vector $\mathbf{X}_i$ is defined as

$$X_i(k) = X_i^*(N-k), \text{ for } k = N/2+1, N/2+2, \ldots, N-1, \qquad (2)$$

15   where * denotes complex conjugate. Furthermore, the DC term $X_i(0)$ and the Nyquist term $X_i (N/2)$ must both be real-valued. Note that $\mathbf{X}_i$ is the transceiver's own transmitted signal that generates the echo signal $\mathbf{Y}_i$. The vector

$$\mathbf{Y}_i = [Y_i(0), Y_i(1), \ldots, Y_i(N-1)]^T \qquad (3)$$

denotes the i:th received frequency domain (Hermitian symmetric) echo symbol containing
20   the received frequency subsymbols $Y_i(k)$. Only the received echo signal is considered, and the far-end data signal is ignored. Thus, the scenario emulates the echo canceller training mode where the far-end modem is silent.

The N-point IDFT of $\mathbf{X}_i$ can be expressed by

$$\mathbf{s}_i = \mathbf{Q}\mathbf{X}_i, \qquad (4)$$

25   where $\mathbf{Q}$ is the IDFT matrix defined by

$$[\mathbf{Q}]_{n,k} = \frac{1}{N} e^{j\frac{2\pi}{N}nk}, \text{ for } n = 0, 1, \ldots, N-1 \text{ and } k = 0, 1, \ldots, N-1. \qquad (5)$$

10

Defining Q_{cp} as a matrix containing the last L rows of Q, i.e. for $n = 0, 1,$
... L -1 results in the following:

$$[\mathbf{Q}_{cp}]_{n,k} = [\mathbf{Q}]_{N-L+n,k} \qquad (6)$$

The transmitted, prefixed time domain symbol x_i is written as:

$$\mathbf{x}_i = \begin{bmatrix} \mathbf{Q}_{cp} \\ \mathbf{Q} \end{bmatrix} \mathbf{X}_i. \qquad (7)$$

The sequence consisting of the i -1:th and i:th prefixed time domain DMT-
symbol can be written as:

$$\mathbf{x} = \begin{bmatrix} \mathbf{Q}_{cp} & \varnothing_{LxN} \\ \mathbf{Q} & \varnothing_{NxN} \\ \varnothing_{LxN} & \mathbf{Q}_{cp} \\ \varnothing_{NxN} & \mathbf{Q} \end{bmatrix} \begin{bmatrix} \mathbf{X}_{i-1} \\ \mathbf{X}_i \end{bmatrix} = \mathbf{Q}_{tot}\mathbf{X}, \qquad (8)$$

where $\varnothing_{LxN}$ denotes a matrix with L rows and N columns consisting of zero-valued
elements.

The length of the echo path channel is assumed to be M samples long, and
the impulse response of the echo path channel is denoted with the convolution matrix, G,
which is of size $(2N+2L) \times (2N+2L)$.

$$\mathbf{G} = \begin{bmatrix} g(0) & 0 & \dots & 0 & \dots & 0 & \dots & 0 & 0 \\ g(1) & g(0) & \dots & 0 & \dots & 0 & \dots & 0 & 0 \\ \dots & \dots & \dots & \dots & \dots & \dots & \dots & \dots & \dots \\ g(M-1) & g(M-2) & \dots & g(0) & \dots & 0 & \dots & 0 & 0 \\ 0 & g(M-1) & \dots & g(1) & \dots & 0 & \dots & 0 & 0 \\ \dots & \dots & \dots & \dots & \dots & \dots & \dots & \dots & \dots \\ 0 & 0 & \dots & 0 & \dots & g(M-1) & \dots & g(1) & g(0) \end{bmatrix} \qquad (9)$$

The received time domain echo signal equals

$$\mathbf{y} = \mathbf{GQ}_{tot}\mathbf{X} \qquad (10)$$

11

In the receiver, only the i:th DMT-symbol is of interest. It contains both ISI and ICI. The cyclic prefix (CP) is discarded, and the received vector y is multiplied with the DFT matrix R of size (NxN), defined as

$$[\mathbf{R}]_{n,k} = e^{-j\frac{2\pi}{N}nk} \qquad (11)$$

With $\mathbf{R}_{tot}$ defined as $\mathbf{R}_{tot} = [\mathit{0}_{Nx(N+L)} \quad \mathit{0}_{NxL} \quad \mathbf{R}]$, the received i:th frequency domain DMT-symbol (vector of size $Nx1$) is obtained as:

$$\mathbf{Y}_i = \mathbf{R}_{tot}\mathbf{GQ}_{tot}\mathbf{X} = \mathbf{AX} = [\mathbf{A}_{prev}\mathbf{A}_{current}]\begin{bmatrix}\mathbf{X}_{i-1}\\ \mathbf{X}_i\end{bmatrix}. \qquad (12)$$

This can also be written as

$$\mathbf{Y}_i = \mathbf{A}_{prev}\mathbf{X}_{i-1} + \mathbf{A}_{current}\mathbf{X}_{i,} \qquad (13)$$

where the following matrices of size $(N \, xN)$ are defined:

$$\mathbf{A}_{prev} = \begin{bmatrix} p_{0,0} & p_{0,1} & \cdots & \cdots & p_{0,N-1} \\ p_{1,0} & p_{1,1} & \cdots & & \\ \cdots & & \cdots & & \\ \cdots & & & \cdots & \\ p_{N-1,0} & \cdots & \cdots & & p_{N-1,N-1} \end{bmatrix} \qquad (14)$$

$$\mathbf{A}_{current} = \begin{bmatrix} c_{0,0} & c_{0,1} & \cdots & \cdots & c_{0,N-1} \\ c_{1,0} & c_{1,1} & \cdots & & \\ \cdots & & \cdots & & \\ \cdots & & & \cdots & \\ c_{N-1,0} & \cdots & \cdots & & c_{N-1,N-1} \end{bmatrix} \qquad (15)$$

Thus, the k:th received frequency echo sample in the i:th symbol can be written as

$$Y_i(k) = c_{k,k}X_i(k) + \sum_{\substack{m=0\\m\neq k}}^{N-1} c_{k,m}X_i(m) + \sum_{m=0}^{N-1} p_{k,m}X_{i-1}(m). \qquad (16)$$

<div align="center">12</div>

From equation (16), the first term $c_{k,k}X_i(k)$ describes the direct echo from

the carrier number k in the symbol number i. The second term $\sum_{\substack{m=0 \\ m\neq k}}^{N-1} c_{k,m}X_i(m)$ describes

the ICI from symbol number i. The third term $\sum_{m=0}^{N-1} p_{k,m}X_{i-1}(m)$ describes the combined ICI

and ISI from the previously transmitted symbol number i-1. If the cyclic prefix was longer

5   than the echo channel memory, then only the first term would be non-zero, and there

would not be ISI or ICI terms because the matrix $A_{current}$ will only have non-zero values at

the main diagonal (upper left corner to the lower right corner), and the matrix A_{prev} would

contain only zeros.

Hence, the matrix A_{prev} describes how the echo from the previously

10   transmitted frequency domain symbol leaks into or distorts the received symbol. The

matrix $A_{current}$ describes how the echo from the currently transmitted frequency domain

symbol leaks into or distorts the received symbol. Accordingly, the two matrices A_{prev} and

$A_{current}$ model how ISI and ICI will affect the echo signal completely in the frequency

domain. By determining the coefficients for the matrices A_{prev} and $A_{current}$, the echo in the

15   frequency domain will be known and can then be subtracted from the received signal. The

coefficients of the unknown matrices A_{prev} and $A_{current}$ can be adaptively identified in order

to estimate the received echo signal. Matrices A_{prev} and $A_{current}$ can also be calculated from

equation (12) by estimating the echo path channel impulse response (matrix G).

Fig. 4 shows a transceiver using Discrete Multitone (DMT) as a modulation

20   scheme with a first, non-limiting, example embodiment of a matrix-based frequency

domain echo canceller (MBAEC) structure. There are two complex matrices H_i and W_i,

numbered 62 and 64, respectively. Each matrix has a size of $(N \times N)$, where N is the size

of the IDFT and DFT. The received echo signal is estimated in the frequency domain by

multiplying the matrix H_i with the currently transmitted frequency domain symbol (an

25     $N \times 1$ vector), X_i, output by the encoder, and multiplying the matrix W_i with the previously

transmitted frequency domain symbol (an $N \times 1$ vector), X_{i-1}, ou tput from delay 60. The

two products H_iX_i and W_iX_{i-1} are added together, i.e.,

13

$$\hat{\mathbf{Y}}_i = \mathbf{H}_i\mathbf{X}_i + \mathbf{W}_i\mathbf{X}_{i-1} \qquad (17)$$

where

$$\mathbf{H}_i = \begin{bmatrix} H_{0,0} & H_{0,1} & \cdots & \cdots & H_{0,N-1} \\ H_{1,0} & H_{1,1} & \cdots & & \\ \cdots & & \cdots & & \\ \cdots & & & \cdots & \\ H_{N-1,0} & \cdots & \cdots & & H_{N-1,N-1} \end{bmatrix} \qquad (18)$$

and

$$\mathbf{W}_i = \begin{bmatrix} W_{0,0} & W_{0,1} & \cdots & \cdots & W_{0,N-1} \\ W_{1,0} & W_{1,1} & \cdots & & \\ \cdots & & \cdots & & \\ \cdots & & & \cdots & \\ W_{N-1,0} & \cdots & \cdots & & W_{N-1,N-1} \end{bmatrix} \qquad (19)$$

Thus, the *k*:th estimated frequency echo sample in the *i:th* symbol is

$$\hat{Y}_i(k) = H_{k,k}X_i(k) + \sum_{\substack{m=0 \\ m\neq k}}^{N-1} H_{k,m}X_i(m) + \sum_{m=0}^{N-1} W_{k,m}X_{i-1}(m) \qquad (20)$$

The hat symbol of $\hat{Y}_k(k)$ indicates that it is an estimation of the received echo signal $Y_i(k)$

The estimated echo signal is subtracted from the received frequency domain symbol, and the resulting error vector $\mathbf{E}_i = \mathbf{Y}_i - \hat{}_i$ is used by an adaptive algorithm, e.g., Least Mean Square (LMS), to adjust the matrix elements of $\mathbf{H}_i$ and $\mathbf{W}_i$. In regular operation, (after training) the error signal is also the desired data signal. Adjusting $\mathbf{H}_i$ and $\mathbf{W}_i$ with the LMS-algorithm yields:

$$\mathbf{H}_{i+1} = \mathbf{H}_i + \mu\mathbf{E}_i\left(\mathbf{X}_i^*\right)^T \qquad (21)$$

$$\mathbf{W}_{i+1} = \mathbf{W}_i + \mu\mathbf{E}_i\left(\mathbf{X}_{i-1}^*\right)^T \qquad (22)$$

where $\mathbf{E}_i = \mathbf{Y}_i - \hat{\mathbf{Y}}_i = \left[E_i(0), E_i(1), \ldots E_i(N-1)\right]^T$ is the *i*:th received frequency domain error vector and μ is the step size of the LMS algorithm. One can prove that the LMS

14

algorithm will adapt the coefficients of H_i to an estimate of $A_{current}$ and the coefficients of W_i to an estimate of A_{prev}. Most of the coefficients of the matrices H_i and W_i are complex-valued. Hence, all arithmetic computations are complex additions, subtractions, and multiplications.

5   Some of the coefficients (elements) in $A_{current}$ and A_{prev} will be almost zero and can therefore be neglected to reduce the computational complexity in equations (21) and (22). This will also reduce the amount of memory. In fact, Acurrent and Aprev may often be band matrices meaning that mainly the strong diagonal (left to right) and some of the upper and lower diagonals have non-zero values. The number of diagonals to be taken

10   into account depends on the echo path channel (ISI and ICI) and the desired level of echo cancellation.

The operation of an echo canceller in accordance with the first, non-limiting, example embodiment and illustrated in Fig. 4 is now described in conjunction with the MBAEC routine (block 70) shown in flowchart format in Fig. 5. A signal to be

15   transmitted X_i is detected in the frequency domain (block 72). That signal is multiplied by matrix H_i 62 and the previously transmitted frequency domain signal X_{i-1} is multiplied by matrix W_i (block 74). The matrix products are summed together, i.e., $H_iX_i + W_iX_{i-1}$, to estimate the current echo $\hat{Y}_i$ (block 76). The estimated echo $\hat{Y}_i$ is subtracted from the actually received symbol Y_i to determine an error E_i (block 78). The coefficient values of

20   the H and W matrices are then adjusted for the next signal period $i+1$ with the detected error E_i using for example the LMS algorithm (block 78).

When the transmitted time domain signal is real valued, e.g., in the case of DMT, it is possible to avoid the use of complex arithmetic. In order to obtain a real-valued, time domain signal, the frequency data must be Hermitian symmetric, and the DC

25   and Nyquist terms must both be real-valued. In a second, non-limiting, example embodiment of the present invention, a real-valued implementation of the MBAEC reduces computational complexity by a factor of two compared to the general case described above. A real-valued vector is introduced as

15

$$\widetilde{\mathbf{X}}_i = \begin{bmatrix} \mathbf{X}_{real,i} \\ \mathbf{X}_{imag,i} \end{bmatrix}, \qquad (23)$$

where the vectors $\mathbf{X}_{real,i}$ and $\mathbf{X}_{imag,i}$ are defined as

$$\mathbf{X}_{real,i} = [X_i(0), X_{real,i}(1), X_{real,i}(2), ..., X_{real,i}(N/2-1), X_i(N/2)]^T \qquad (24)$$

and

$$\mathbf{X}_{imag,i} = [X_{imag,i}(1), X_{imag,i}(2), ..., X_{imag,i}(N/2-1)]^T \qquad (25)$$

In equations (24) and (25), $X_{real,i}(n) = \mathrm{Re}\{X_i(n)\}$ and $X_{imag,i}(n) = \mathrm{Im}\{X_i(n)\}$ are defined. Furthermore, $X(0)$ is the DC term, and $X(N/2)$ is the Nyquist term of $\mathbf{X}_i$. The vector $\widetilde{\mathbf{X}}_i$ contains exactly the same information as the vector $\mathbf{X}_i$ defined in equation (1), but in a slightly different order.

The matrices $\mathbf{Q}_{cos}$ and $\mathbf{Q}_{sin}$ are defined for $k = 0,1,...,N/2-1$ and $n = 0,1,...,N-1$ as

$$[\mathbf{Q}_{cos}]_{n,k} = \frac{2}{N}\cos\left(\frac{2\pi}{N}kn\right), \quad for \ k = 0,1,...,N/2 \qquad (26)$$

$$[\mathbf{Q}_{sin}]_{n,k} = \frac{2}{N}\sin\left(\frac{2\pi}{N}(k+1)n\right), \quad for \ k = 0,1,...,N/2-2 \qquad (27)$$

Furthermore, the matrix $\widetilde{\mathbf{Q}}$ is defined as

$$\widetilde{\mathbf{Q}} = \begin{bmatrix} \mathbf{Q}_{cos} & \mathbf{Q}_{sin} \end{bmatrix} \qquad (28)$$

Equation (4) may be rewritten

$$\mathbf{s}_i = \widetilde{\mathbf{Q}}\widetilde{\mathbf{X}}_i \qquad (29)$$

$\widetilde{\mathbf{Q}}_{cp}$ is further defined as a matrix containing the last L rows of $\widetilde{\mathbf{Q}}$, i.e. for $n = 0,1,...L-1$ we have

16

$$\left[\widetilde{\mathbf{Q}}_{cp}\right]_{n,k} = \left[\widetilde{\mathbf{Q}}\right]_{n-L+n,k} \tag{30}$$

The transmitted prefixed time domain symbol $\mathbf{x}_i$ may now be written as

$$\mathbf{x}_i = \begin{bmatrix} \widetilde{\mathbf{Q}}_{cp} \\ \widetilde{\mathbf{Q}} \end{bmatrix} \widetilde{\mathbf{X}}_i \tag{31}$$

As in equation (8), the sequence of the i-1:th and i:th prefixed time domain DMT symbols can be written as

$$\mathbf{x} = \begin{bmatrix} \widetilde{\mathbf{Q}}_{cp} & \mathcal{O}_{LxN} \\ \widetilde{\mathbf{Q}} & \mathcal{O}_{NxN} \\ \mathcal{O}_{LxN} & \widetilde{\mathbf{Q}}_{cp} \\ \mathcal{O}_{NxN} & \widetilde{\mathbf{Q}} \end{bmatrix} \begin{bmatrix} \widetilde{\mathbf{X}}_{i-1} \\ \widetilde{\mathbf{X}}_i \end{bmatrix} = \widetilde{\mathbf{Q}}_{tot}\widetilde{\mathbf{X}} \tag{32}$$

With $\mathbf{G}$ defined in equation (9), the received time domain signal may be written as

$$\mathbf{y} = \mathbf{G}\widetilde{\mathbf{Q}}_{tot}\widetilde{\mathbf{X}} \tag{33}$$

In the receiver, we are only interested in the i:th DMT symbol which contains both ISI and ICI. The cyclic prefix is discarded, the received vector $\mathbf{y}$ is multiplied with the matrix $\widetilde{\mathbf{R}}_{tot}$ defined as

$$\widetilde{\mathbf{R}}_{tot} = \begin{bmatrix} \mathcal{O}_{Nx(N+L)} & \mathcal{O}_{NxL} & \widetilde{\mathbf{R}} \end{bmatrix} \tag{34}$$

where

$$\widetilde{\mathbf{R}} = \begin{bmatrix} \mathbf{Q}_{cos} & -\mathbf{Q}_{sin} \end{bmatrix} \tag{35}$$

The received i:th frequency domain data vector is now expressed as

$$\widetilde{\mathbf{Y}}_i = \widetilde{\mathbf{R}}_{tot}\mathbf{G}\widetilde{\mathbf{Q}}_{tot}\widetilde{\mathbf{X}} = \widetilde{\mathbf{A}}\widetilde{\mathbf{X}} = \begin{bmatrix} \widetilde{\mathbf{A}}_{prev} & \widetilde{\mathbf{A}}_{current} \end{bmatrix} \begin{bmatrix} \widetilde{\mathbf{X}}_{i-1} \\ \widetilde{\mathbf{X}}_i \end{bmatrix}. \tag{36}$$

where we have defined

17

$$\widetilde{\mathbf{Y}}_i = \begin{bmatrix} \mathbf{Y}_{real,i} \\ \mathbf{Y}_{imag,i} \end{bmatrix}. \qquad (37)$$

and

$$\mathbf{Y}_{real,i} = \left[Y_i(0), Y_{real,i}(1), Y_{real,i}(2), ..., Y_{real,i}(N/2-1), Y_i(N/2) \right]^T \qquad (38)$$

$$\mathbf{Y}_{imag,i} = \left[Y_{imag,i}(1), Y_{imag,i}(2), ..., Y_{imag,i}(N/2-1) \right]^T \qquad (39)$$

Comparing equations (36) and (12), in equation (36) we have to perform $2N^2$ real-valued multiplications, and in equation (12), we need to perform $2N \times (N/2)$ complex-valued multiplications. Since one complex-valued multiplication requires four real-valued multiplications, the total number of real-valued multiplications is reduced by a factor of two in equation (36) compared to equation (12).

A third, non-limiting, example embodiment of an MBAEC is shown in Fig. 6. The H_i matrix of size $(N \times N)$ is replaced by a vector V_i 94 of size $(N \times 1)$. A matrix also includes single column or row vectors, although the term vector is used here to distinguish from the $N \times N$ matrix of the embodiments described above. Furthermore, the matrix W_i is replaced by another matrix Z_i 96 of size $(N \times N)$. In this example embodiment, the previously transmitted frequency domain symbol X_{i-1} is multiplied in multiplier 90 by a complex exponential term to compensate for the cyclic prefix, which has a length of L samples, i.e., $e^{j2\pi Lk/N}$. The product output from multiplier 90 is subtracted from X_i, and the difference is multiplied by matrix Z_i 96. The vector and matrix products are summed in summer 98 to estimate the echo.

The following equations describe the algorithm:

$$\hat{\mathbf{Y}}_i = \mathbf{V}_i \bullet \mathbf{X}_i + \mathbf{Z}_i \left(\mathbf{X}_i - \overline{\mathbf{X}}_{i-1} \right), \qquad (40)$$

where

$$\left[\overline{\mathbf{X}}_{i-1} \right]_k = \left[\mathbf{X}_{i-1} \right]_k e^{j\frac{2\pi}{N}Lk}, \text{ for } k = 0, ..., N-1 \qquad (41)$$

$\mathbf{X}_i$ is the i:th transmitted frequency domain symbol, $(N \times 1)$ vector, defined above.

18

$\hat{Y}_i$ is the i:th estimated echo signal in frequency domain, $(N x \ 1)$ vector.

V_i and Z_i is frequency domain vector and matrix of size $(N x \ 1)$ and $(N x \ N)$.

Adjusting column vector V_i and matrix Z_i with the LMS algorithm yields:

$$V_{i+1} = V_i + \mu E_i \bullet \left(X_i^*\right)^T \qquad (42)$$

$$Z_{i+1} = Z_i + \mu E_i \left(X_i^* - \overline{X}_{i-1}^*\right)^T \qquad (43)$$

5   where $E_i = Y_i - \hat{Y}_i$ is the i:th received frequency domain error, $(N x \ 1)$ vector, μ is the

stepsize of the LMS algorithm, and $\bullet$ denotes element-by-element vector multiplication.

Example procedures for the operation of the third example embodiment
MBAEC shown in Fig. 6 are now described in conjunction with the routine 100 shown in
flowchart form in Fig. 7. The signal to be transmitted X_i is detected in the frequency

10   domain (block 120). That signal is multiplied by the column vector V_i. The previously
transmitted signal X_{i-1} is multiplied by a cyclic prefix compensating complex factor, which
in this example embodiment is $e^{j2\pi Lk/N}$. That product is subtracted from the current signal
to be transmitted X_i, and the difference is multiplied by the $(N x \ N)$ matrix Z_i (block 104).
The products $V_i \bullet X_i$ and $Z_i\left(X_i - \overline{X}_{i-1}\right)$ are summed to estimate the echo $\hat{Y}_i$ (block 106).

15   The estimated echo $\hat{Y}_i$ is subtracted from the actually received symbol Y_i to determine an
error E_i (block 108). The coefficients of the column vector V_i and the matrix Z_i are
adjusted with the current error E_i using the LMS algorithm (block 110).

As a fourth example, non-limiting embodiment, the operations described in
the second and third example embodiments may be combined. Specifically, the real and

20   imaginary parts of the current and prior symbols are determined and used to simplify the
column vector V_i and the matrix multiplication with matrix Z_i in accordance with
equations (23)-(39) set forth above. As a result, the computational complexity for
performing the necessary data manipulations is reduced appropriately by a factor of four
compared to the first example embodiment.

19

In a DMT application, the vectors $\mathbf{X}_i$, $\mathbf{Y}_i$, $\hat{\mathbf{Y}}_i$, and $\mathbf{E}_i$ all have Hermitian symmetry. This property can be used to reduce the number of computations needed by only calculating the first $N/2 + 1$ coefficients of the vectors. Furthermore, the matrices $\mathbf{V}_i$ and $\mathbf{Z}_i$ need only be calculated and stored for the first $N/2 + 1$ rows. Moreover, the

5   computational complexity may be further reduced by partitioning the vectors X_i, $\overline{X}_{i-1}$, Y_i, and E_i into real and imaginary parts in accordance with equations (23)-(39).

An MBAEC may be used in an asymmetric transceiver, such as an ADSL transceiver, with the modifications now described. When the modem's transmitter has a *lower* sampling rate than its receiver, the echo signal is interpolated at the receiver (a fifth,

10   non-limiting, example embodiment). When the modem's transmitter has a *higher* sampling rate than the receiver, the echo signal will be decimated at the receiver (a sixth, non-limiting, example embodiment).

For an interpolated MBAEC, assume the size of the IDFT in the transmitter is N and the size of the DFT in the receiver is qN, where $q = 8$ in ADSL . Thus, the

15   received symbol contains q times more samples than the transmitted symbol. The received echo is therefore interpolated q times in the receiver. As one example interpolated asymmetric MBAEC, equation (40) is modified as follows:

$$\hat{\mathbf{Y}}_i = \mathbf{V}_i \bullet \mathbf{X}rep_i + \mathbf{Z}_i\left(\mathbf{X}_i - \overline{\mathbf{X}}_{i-1}\right), \qquad (44)$$

where

20   $$\left[\overline{\mathbf{X}}_{i-1}\right]_k = \left[\mathbf{X}_{i-1}\right]_k e^{j\frac{2\pi}{N}Lk}, \text{for } k = 0,\ldots,N-1 \qquad (45)$$

$\mathbf{X}_i$ is the i:th transmitted frequency domain symbol, $(N \times 1)$ vector.

$\mathbf{X}rep_i$ is equal to the vector $\mathbf{X}_i$ replicated q times, forming a block vector of contiguous vectors. For example, if $q = 4$ then is $\mathbf{X}rep_i = [\mathbf{X}_i^T \mathbf{X}_i^T\mathbf{X}_i^T \mathbf{X}_i^T]^T$.

$\hat{\mathbf{Y}}_i$ is the ith estimated echo signal in frequency domain, $(qN \times 1)$ vector.

25   $\mathbf{V}_i$ and $\mathbf{Z}_i$ is frequency domain vector and matrix of size $(qN \times 1)$ and $(qN \times N)$.

20

Adjusting V_i and Z_i with the proposed LMS-algorithm yields:

$$V_{i+1} = V_i + \mu E_i \bullet \left(Xrep_i^*\right)^T \qquad (46)$$

$$Z_{i+1} = Z_i + \mu E_i \left(X_i^* - \overline{X}_{i-1}^*\right)^T \qquad (47)$$

where $E_i = Y_i - \hat{Y}_i$ is the i:th received frequency domain error, μ is the stepsize of the

LMS algorithm, and   denotes element-by-element vector multiplication.

5   Hence, the only differences from equation (40) are the replication of X_i and

the size of the matrices and the vectors. Some of the coefficients in the vectors and in the

matrices will be small and can be neglected to reduce the computational complexity and

the required memory. In addition, the computational complexity in the interpolated

MBAEC may be further reduced by partitioning the vectors X_i, X_{rep_i}, $\overline{X}_{i-1}$, Y_i, and E_i

10   into real and imaginary parts in accordance with equations (23)-(39).

For a decimated MBAEC, assume the size of the IDFT in the transmitter is

qN and the size of the DFT in the receiver is N, where $q = 8$ in ADSL. Thus, the

transmitted symbol contains q times more samples than the received symbol. This means

that the received echo will be decimated q times in the receiver. Equation (40) is modified

15   as follows.

$$\hat{Y}_i = Decimate\left\{(V_i \bullet X_i), q\right\} + Z_i\left(X_i - \overline{X}_{i-1}\right), \qquad (48)$$

where

$$\left[\overline{X}_{i-1}\right]_k = \left[X_{i-1}\right]_k e^{j\frac{2\pi}{N}Lk}, \text{for } k = 0,...,N-1 \qquad (49)$$

X_i is the i:th transmitted frequency domain symbol, $(N \times 1)$ vector.

20          $Decimate\left\{(V_i \quad X_i), q\right\}$ means that the vector $V_i \quad X_i$ is decimated q times

in the frequency domain. In other words the frequency domain vector $V_i \quad X_i$ is blocked

into q contiguous vectors of N points each. These smaller vectors are then added together

forming one vector of size $(Nx1)$.

$\hat{Y}_i$ is the i:th estimated echo signal in frequency domain, $(N \times 1)$ vector.

21

V_i and Z_i is frequency domain vector and matrix of size $(qN \times 1)$ and $(N \times q N)$.

Adjusting V_i and Z_i with the proposed LMS-algorithm yields:

$$V_{i+1} = V_i + \mu Erep_i \bullet \left(X_i^*\right)^T \qquad (50)$$

$$Z_{i+1} = Z_i + \mu Erep_i \left(X_i^* - \overline{X}_{i-1}^*\right)^T \qquad (51)$$

where $E_i = Y_i - \hat{Y}_i$ is the i:th received frequency domain error, $Erep_i$ is of size $(qNx1)$ and is equal to the vector E_i replicated q times, forming a block vector of q contiguous vectors, μ is the stepsize of the LMS algorithm, and denotes element-by-element vector multiplication.

Again, the only differences to equation (40) are the decimation of V_i X_i, the replication E_i, and the size of the matrices and the vectors. Some of the coefficients in the vectors and in the matrices will be very small and can be neglected to reduce the computational complexity and the required memory.

An asymmetric MBAEC routine (block 120) is now described in Fig. 8. A decision is made in block 122 whether the modem transmitter sampling rate is less than the sampling rate at the modem transceiver. If so, the symbol to be transmitted is interpolated at the modem receiver, e.g., at the analog-to-digital converter, and the estimated echo $\hat{Y}_i$ is calculated using the following equation:

$$\hat{Y}_i = V_i \bullet Xrep_i + Z_i \left(X_i - \overline{X}_{i-1}\right) \qquad (52)$$

(block 128). If the modem transmitter sampling rate is greater than that for the modem receiver, the symbol to be transmitted is decimated at the receiver, e.g., at the analog-to-digital converter, and the estimated echo $\hat{Y}_i$ is calculated in accordance with the following formula:

$$\hat{Y}_i = \text{Decimate}\{(V_i \bullet X_i), q\} + Z_i \left(X_i - \overline{X}_{i-1}\right) \qquad (53)$$

For both the interpolation and decimation cases, the estimated echo $\hat{Y}_i$ is subtracted from the received signal Y_i to determine the error E_i (block 132). The coefficients of the

22

column vector $\mathbf{V}_i$ and the matrix $\mathbf{Z}_i$ are adjusted with the error $\mathbf{E}_i$ using for example the LMS algorithm (block 134).

A seventh, non-limiting, example embodiment of an echo canceller in accordance with the present invention may be used in an asynchronous transceiver, such as
5   an ADSL transceiver at the Central Office, with the modifications now described. In an asynchronous transceiver, the transmitted and received frames or symbols are not aligned in time. Hence, there is a time offset between the transmitter and receiver symbols. In this seventh embodiment, the echo canceller is de-coupled from the receiver. Nevertheless, asynchronous MBAEC may be applied to any one of the previously-
10   described embodiments with a small modification. Instead of removing the echo in the frequency domain, the estimated echo signal is first transformed to the time domain by an IDFT operation, and then removed in the time domain sample-by-sample. The asynchronous MBAEC is illustrated in Fig 9. The estimated echo signal $\hat{Y}_i$ output from MBAEC is transformed into the time domain by an $N - IDFT$ block 140 to produce an
15   estimated echo in the time domain $\hat{y}_i$ which is then removed in the time domain sample-by-sample from the received echo y_i. The time domain difference or error e_i is transformed into the complex domain in the $N - DFT$ block which is located after the summation stage rather than before it as shown in Figs. 4 and 6. In addition, the computational complexity in the decimated MBAEC may be further reduced by
20   partitioning the vectors X_i, $\bar{X}_{i-1}$, Y_i, and E_i into real and imaginary parts in accordance with equations (23)-(39).

The proposed matrix-based adaptive echo canceller (MBAEC) has been implemented and simulated in different DMT-based transceivers such as a symmetric-rate DSL transceiver, an ADSL central office end transceiver, and an ADSL Subscriber end
25   transceiver. Figs. 10 and 11 show the learning curve of the matrix-based adaptive echo canceller (MBAEC), implemented in a DMT-based Symmetric-rate DSL transceiver, using a simple lowpass model of the echo path channel. The learning curve illustrates how the mean-square-error, MSE, is reduced during adaptation with the LMS-algorithm. The

23

simulation results indicate that the present invention is reliable, accurate and performs according to theoretical expectations.
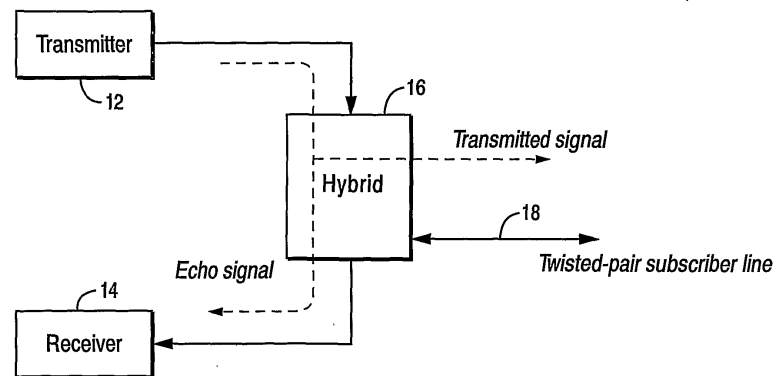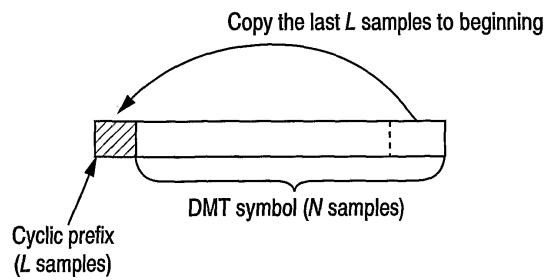
The matrix-based adaptive echo canceller is well-suited to follow slow channel fluctuations during transmission because the transmitted signal is used to adapt
5 matrix coefficients. An echo canceller in accordance with the present invention is particularly efficient in a DMT system employing FDM (Frequency Division Multiplexing) because echo cancellation is only needed for a few carriers which leads to less computational complexity. Moreover, because the needed data are already available in the frequency domain, so there is no need to do any extra DFT or IDFT operations to
10 implement the MBAEC, except for the asynchronous MBAEC, which requires one extra IDFT. Furthermore, some of the coefficients in the matrices and in the vectors will be zero or quite small, and therefore, can be ignored, which means that the computational complexity of and the required memory for the echo canceller will be reduced.

While the present invention has been described with respect to a particular
15 embodiment, those skilled in the art will recognize that the present invention is not limited to the specific embodiments described and illustrated herein. Different formats, embodiments, and adaptations besides those shown and described as well as many modifications, variations, and equivalent arrangements may also be used to implement the invention. Therefore, while the present invention has been described in relation to its
20 preferred embodiments, it is to be understood that this disclosure is only illustrative and exemplary of the present invention and is merely for the purposes of providing a full and enabling disclosure of the invention. Accordingly, it is intended that the invention be limited only by the scope of the claims appended hereto.

1/8

Fig. 1

Fig. 2

2/8

Fig. 3

3/8

Fig. 4

Fig. 5

4/8

Fig. 6

5/8


```
      ┌──────────────┐
      │    MBAEC     │──── 100
      └──────────────┘
             │
             ▼                                          ┌─102
┌────────────────────────────────────────────────────────┐
│ Detect in the frequency domain a symbol to be transmitted (Xᵢ) │
└────────────────────────────────────────────────────────┘
             │
             ▼                                          ┌─104
```

Detect in the frequency domain a symbol to be transmitted (X_i)

Multiply X_i by Vector V_i. Multiply X_{i-1} by a complex factor ($e^{j2\pi Lk/N}$), subtract the product from X_i, and multiply the difference by matrix Z_i

Add the products $X_i V_i + Z_i [X_i - X_{i-1}(k) \, e^{j2\pi Lk/N}]$ to estimate the echo $\hat{Y}_i$

Subtract the estimated echo $\hat{Y}_i$ from the actually received symbol Y_i to determine an error E_i

Adjust V_i and Z_i using the error E_i, e.g., using the LMS algorithm

Fig. 7

6/8

Fig. 8

7/8

Fig. 9

8/8

Fig. 10

Fig. 11